

**DENSITY-INDUCED SPIN-NEMATIC SQUEEZING IN A SPIN-1  
BOSE-EINSTEIN CONDENSATE**

A Dissertation  
Presented to  
The Academic Faculty

By

Maryrose Barrios

In Partial Fulfillment  
of the Requirements for the Degree  
Doctor of Philosophy in the  
School of Physics  
College of Sciences

Georgia Institute of Technology

May 2024

© Maryrose Barrios 2024

**DENSITY-INDUCED SPIN-NEMATIC SQUEEZING IN A SPIN-1  
BOSE-EINSTEIN CONDENSATE**

Thesis committee:

Dr. Michael Chapman, Advisor  
School of Physics  
*Georgia Institute of Technology*

Dr. Itamar Kimchi  
School of Physics  
*Georgia Institute of Technology*

Dr. Martin Mourigal  
School of Physics  
*Georgia Institute of Technology*

Dr. Creston Herold  
Georgia Tech Research Institute  
*Georgia Institute of Technology*

Dr. Colin Parker  
School of Physics  
*Georgia Institute of Technology*

Date approved: May 1, 2024

Measure twice. Cut once.

*My Dad*

For the ones who came before me, and the ones who will come after.

## ACKNOWLEDGMENTS

As an eager, young student, I took AP Physics in high school. I had a teacher there, Mr. Mark Fairbank, who provided wonderful demos that helped to illustrate the seemingly magical nature of physics. One of the most important lessons he taught me though, was that anyone could learn physics, and that just because it is a struggle at first, doesn't mean you can't or shouldn't do it. I didn't know then how much that lesson would ring true for me throughout my journey.

When college came around, I received a scholarship from my tribe, the Tule River Band of Indians, to attend the University of California, Berkeley. Without them, I wouldn't be able to attend an elite school like UC Berkeley. The Native community at UC Berkeley, as well as my own, were instrumental in making campus feel more like a home to me. A special thanks must be noted to Diana Lizarraga who found me funding to get a research position, and ran the NERDS program at Cal, and Bridget Wilson who facilitated many of the Native student organizations on campus.

In the classroom, college was challenging, and I often struggled to find myself and my place in the physics community. One of the chief reasons I stayed with physics in this time, was because of the research I pursued as an undergraduate. Working with Dr. Carl Haber, I learned the potential impacts a physics career could have on communities like my own. I will always be indebted to his early mentorship and the opportunities he gave me as a budding physicist. Working in Professor Stamper-Kurn's lab, I felt myself grow exponentially, both as a scientist and as a person. I not only fell in love with atomic and quantum physics there, but I also started to see myself as a physicist. Graduate students Sydney Schreppler, Ed Marti, Jennie Guzman, Ryan Olf, Claire Thomas, and my other fellow Ultracold Lab contemporaries gave me invaluable knowledge, and an inexpressible amount of gratitude towards them for their investment and belief in me. Had it not been for this experience, I could easily have not chosen the career path I'm on today.

I took a detour from going straight to graduate school, and did a two year post-baccalaureate program at Harvard University, thanks to funding initiatives through the Harvard Graduate School of Arts and Sciences Research Scholar Initiative. I made many good friends there, such as Andrew Chael, Olivia Miller, James Mitchell, Ronald Alexander, Cris Panda, Michael Rowan, and Aavishkar Patel (to name a few). Their peer acceptance and friendship made the late nights and long hours pass a lot easier. Working in the laboratory of Professor Gerald Gabrielse, I acquired a new set of skills in low-temperature physics and precision measurements. My lab mates Ronald Alexander, Cris Panda, Elise Novitski, Mason Marshall, and Kathryn Marable all provided me with fond memories and valuable experimental skills. Machine shop instructor, Stan Cotreau, taught me many machining techniques, and reminded me a lot of my dad; he was a welcome friend, while I was so far from home. I will always be thankful that Professor Gabrielse invited me to join his lab, and that I was able to use my experiences at Harvard to apply to Georgia Tech's physics PhD program.

My time at Georgia Tech has been long, but it didn't always feel that way, largely through the experiences I had with many of my peers and lab mates at Georgia Tech. I was very grateful to have made many great friends who would last throughout my time at Tech and beyond. Friends like Natalie Brown, Hema Selvakumar, Logan Kageorge, Shashank Markande, Bhavesh Khamesra, Ashley Coenen, Matthew Johnson, Adrien Saremi, Zackary Jackson, Chris Tung, and Matthew Gudorf all provided invaluable friendship that got us through the many stresses of graduate school. I also found refuge in the aquatics community at Georgia Tech. I played on both the Georgia Tech Women's Water Polo Club team, as well as the Atlanta Rainbow Trout Water Polo masters team for most of my graduate career. Both provided me with lifelong friends in teammates Alex Crowley, Christine Hsieh, Sydney Gathe, Sarah Demsky, Nicole Hughes, Tina Hilko, and many others! Additionally, GT Scuba is an amazing program, which allowed me to become an advanced certified diver. Learning from Debbie Dorsey, Marty Ade, and Jen Ade, and having the best dive buddies, Christine, Sarah, and Nicole, I expanded my personal horizons and my

lifelong love of the ocean.

I was happy to find a home in Professor Michael Chapman's lab. I worked with many talented colleagues and friends over the years. Martin Anquez was a congenial lab mate who worked with me early on with the 2D-MOT testing. Bharath Hebbe Madhusudhana spent the most time teaching me to run and troubleshoot the BEC experiment. Were it not for his mentorship and friendship, I would have struggled a lot longer to learn the ways of the experiment. Matthew Boguslawski had a great penchant and skill for tinkering with things. His technical skills were very useful to the experiment that I inherited. Lin Xin is a fastidious worker who shared many of the burdens of the experimental maintenance with me, especially during the pandemic. Julia Cohen and Shane Carter have become fast experts on the inner workings of the experiment. It has been a pleasure to watch their growth and persistence. I know they will do great things with the experiment's future. I have learned many things from each of my lab mates, and have benefited greatly from their camaraderie and expertise. Lastly, I would like to thank Professor Chapman. Throughout the ups and downs of the experiment, I always knew that he wanted the best for each of his students. His guidance in the lab, from the large things to the small things, meant you always had someone to come to with your questions. I'm grateful for his support over the years. Additionally, I'm very grateful to my thesis committee for being a source of support and guidance throughout my career, and especially in this thesis endeavor.

Last and never least, I have to thank my incredibly supportive family. My parents Peter and Fidela always instilled in me a belief and confidence in myself. They taught me the values of hard work, humility, faith, and love. They always had my back and were always with me on each leg of my journey. I would not have made it far without their love and devotion. My brother, James, was my first student and I recall the nights at home helping him with his school work. He and his wife, Nancy, have been wonderful family members in my life. To my partner, Rafael Araica, though you have been a more recent addition to our family, you have provided me with so much love and support. Your friendship, love,

care, and belief in me have helped push me through many a tough lab day. With all this love, I am truly blessed. I thank Creator for all He has given me.

I'm grateful to my ancestors who were strong enough to survive three waves of colonization to allow me to be here today. *Ayemxo nim yokitsa*. I'm thankful to the broader Native community I've found in the American Indian Science and Engineering Society and with my fellow Lighting the Pathway participants, Dr. Jessica Hernandez, Dr. Kali Dale, and (soon-to-be Dr.) Jocelyn Painter, to name but a few. My involvement with this organization has taught me how amazing and important indigenous scholars are in this world. I'm privileged to be one of them and I hope there will be many more. I'm grateful to the Mvskoke and Cherokee nations whose land I have worked and lived on for my entire graduate career. There are many who are not explicitly thanked here, but know I am forever grateful for the support that has helped me be where I am today. I hope to help others who wish to attain the same. *Waki insis* (thank you).

## TABLE OF CONTENTS

<b>Acknowledgments</b> . . . . .	v
<b>List of Tables</b> . . . . .	xiv
<b>List of Figures</b> . . . . .	xv
<b>List of Acronyms</b> . . . . .	xix
<b>Summary</b> . . . . .	xx
<b>Chapter 1: Introduction and Background</b> . . . . .	1
1.1 Density and Pressure-Tuned Quantum Phase Transitions . . . . .	2
1.2 Spinor BECs and Our Work . . . . .	4
1.2.1 Quantum Phase Transitions in Cold Atomic Systems . . . . .	5
1.3 Thesis Organization and Contribution . . . . .	9
<b>Chapter 2: Spinor BECs: Background and Theory</b> . . . . .	10
2.1 Gross-Pitaevski Equation and our Simplified Hamiltonian . . . . .	10
2.1.1 Our Hamiltonian . . . . .	10
2.1.2 Single Mode Approximation . . . . .	12
2.2 Quantum Mechanical Description . . . . .	14
2.3 Mean-Field Approach . . . . .	17

2.4	Phase Space and Spin-1 Pictures . . . . .	18
<b>Chapter 3: Experimental Apparatus . . . . .</b>		<b>24</b>
3.1	Lasers . . . . .	24
3.1.1	Experimental Diode Lasers . . . . .	24
3.1.2	Frequency Stabilization of Diode Lasers Used in the Experiment . . . . .	25
3.1.3	MOT and Imaging Beams . . . . .	29
3.1.4	Optical Layout . . . . .	35
3.2	Optical Trapping Lasers . . . . .	40
3.2.1	Trap Properties . . . . .	41
3.2.2	CO <sub>2</sub> and Cross Trapping Lasers . . . . .	43
3.3	Vacuum Chamber . . . . .	47
3.4	Magnetic Coils . . . . .	49
3.4.1	MOT Coils . . . . .	51
3.4.2	Trim Coils . . . . .	52
3.4.3	Auxiliary Gradient Coils . . . . .	53
3.4.4	Stern-Gerlach Gradient Coils . . . . .	56
3.5	Control System . . . . .	61
3.5.1	Data Acquisition . . . . .	61
3.5.2	Data Analysis . . . . .	65
3.6	Imaging . . . . .	66
3.6.1	Imaging Optics and Masks . . . . .	66
3.6.2	Fluorescence Imaging . . . . .	66

3.6.3	Absorption Imaging . . . . .	71
3.6.4	Realistic Fluorescence Imaging Calculations . . . . .	74
3.6.5	RF Calibration . . . . .	76
3.7	State Interaction and Preparation . . . . .	78
3.7.1	Microwave Fields . . . . .	78
3.7.2	Radio-Frequency Fields . . . . .	80
3.8	BEC Experimental Stages . . . . .	82
3.8.1	MOT . . . . .	82
3.8.2	Dark MOT . . . . .	83
3.8.3	Optical Dipole Trap and Evaporation . . . . .	84
3.8.4	State Preparation and Cross Trap . . . . .	86
3.8.5	Imaging the BEC . . . . .	86
3.9	Typical Experiments and Diagnostics . . . . .	87
3.9.1	Measuring the Temperature of the Cloud . . . . .	87
3.9.2	Lifetimes . . . . .	91
3.9.3	Critical Field Scan . . . . .	91
3.9.4	Coherent Oscillations . . . . .	94
3.9.5	Spin Mixing . . . . .	95
3.9.6	Number Squeezing . . . . .	98
<b>Chapter 4: Density-Induced Squeezing . . . . .</b>		<b>101</b>
4.1	Quantum Phase Transitions . . . . .	101
4.2	Ways to Cross our Quantum Phase Transition . . . . .	102

4.2.1	Conventional Magnetic Field Quenching . . . . .	103
4.2.2	Optical Trapping Modulation . . . . .	106
4.2.3	Simulation of Density-Quench . . . . .	109
4.3	Checking for Effects of the Density-Increasing Ramp . . . . .	114
4.3.1	Coherent Oscillations of Energy Gap . . . . .	116
4.3.2	Density-Induced Spin Mixing . . . . .	120
4.4	Density-Induced Spin-Nematic Squeezing . . . . .	123
4.4.1	Imaging Calibration . . . . .	126
4.5	Outlook and Conclusion . . . . .	128
 <b>Chapter 5: Other Experimental Pursuits . . . . .</b>		<b>130</b>
5.1	Finite Energy Gap for Small Numbered Condensates . . . . .	130
5.1.1	QPT for Finite Numbers of Atoms . . . . .	131
5.1.2	Adiabatic Crossing of the QPT . . . . .	132
5.1.3	Preliminary Data for Making Small Condensates . . . . .	136
5.2	2D-MOT . . . . .	141
5.2.1	Preliminary 2D-MOT Experiments . . . . .	142
5.2.2	New Vacuum Designs with 2D-MOT Source . . . . .	150
5.3	Imaging Improvements . . . . .	154
5.3.1	Current Imaging Limitations . . . . .	154
5.3.2	Realistic CPA Estimates and Improvements . . . . .	159
 <b>Chapter 6: Conclusion and Outlook . . . . .</b>		<b>161</b>
6.1	Future Directions . . . . .	162

6.1.1	New Atom Source and Vacuum Upgrades . . . . .	162
6.1.2	Reducing Scatter and Improving Squeezing Detection . . . . .	163
6.1.3	Studying the Finite Energy Gap . . . . .	165
<b>References</b>	. . . . .	<b>166</b>

## LIST OF TABLES

2.1	Spin-1 Operators and Matrices . . . . .	14
2.2	Spin-1 Nematic, Quadrapole Matrices . . . . .	15
2.3	Commutation relations for the spin-1 operators. . . . .	23
3.1	Diode Lasers and FM Modulation . . . . .	26
3.2	Frequency shifts for the cycling light used to generate the MOT and imaging light for the experiment . . . . .	31
3.3	Frequency shifts for the cycling light used to generate the probe light for the experiment . . . . .	33
3.4	Typical powers as measured through the MOT fibers . . . . .	40
5.1	Optimal 2D-MOT+ Loading Curves . . . . .	146
5.2	Table of 2D-MOT varieties and relevant data . . . . .	149
5.3	Scatter noise analysis for the imaging masks . . . . .	157
5.4	Potential imaging modification and their effect on the CPA . . . . .	160

## LIST OF FIGURES

2.1	Energy contours in the spinor phase space . . . . .	20
2.2	Energy contours in the spin-nematic phase space. . . . .	22
3.1	DBR cycling laser saturation absorption signal . . . . .	26
3.2	FM locking electronics circuit used to lock the ECDLs . . . . .	27
3.3	FM locking electronics circuit used to lock the DBRs . . . . .	28
3.4	MOT Transitions in Rubidium-87 . . . . .	30
3.5	Net Frequency shift for the cycling DBR detuning as a function of experimental control voltage . . . . .	32
3.6	Probe saturation absorption and locking error signal . . . . .	34
3.7	DBR Repump saturation absorption spectrum and error signal . . . . .	34
3.8	Probe Optical Layout . . . . .	36
3.9	DBR Cycling Laser Optical Layout . . . . .	37
3.10	DBR Repump Laser Optical Layout . . . . .	38
3.11	Tapered amplifiers and MOT fibers for experiment . . . . .	39
3.12	Optical layout for the 10.6 $\mu\text{m}$ trapping laser. . . . .	44
3.13	Crossed dipole trap layout . . . . .	45
3.14	Schematic for crossed optical dipole traps in the chamber . . . . .	46
3.15	Schematic of BEC experiment . . . . .	50

3.16 Schematic of coil layouts on the BEC experiment . . . . .	51
3.17 Spin Mixing in the primary ODT for different auxiliary coil voltages . . . .	54
3.18 Average amount of spin mixing in the ODT for one second of evolution time	55
3.19 Condensate appearance in absorption as a function of lens mover distance .	57
3.20 Auxiliary gradient fit to measured magnetic field gradients for different cur- rents . . . . .	57
3.21 SG pulses taken with the new and current IGBT circuit . . . . .	59
3.22 Schematic of current IGBT circuit on experiment that controls the SG pulses for imaging. . . . .	60
3.23 Cloud separation in absorption with new SG circuit . . . . .	61
3.24 Labview front panel of control computer . . . . .	62
3.25 Labview errors when AO1 board not attached properly . . . . .	63
3.26 Demonstration of lens mover error . . . . .	64
3.27 Top down view of BEC experiment and the imaging setup . . . . .	67
3.28 Schematic of BEC fluorescence imaging setup. . . . .	69
3.29 Schematic of BEC absorption imaging setup . . . . .	74
3.30 RF Calibration for 200 $\mu$ s at 500 mG . . . . .	77
3.31 Imaging mask adjustments . . . . .	79
3.32 RF spectrum and rate . . . . .	81
3.33 DarkMOT images with top (iXon) and FLIR cameras . . . . .	83
3.34 Temperature and number measurements for a MOT . . . . .	89
3.35 Number and temperature comparisons for different 10.6 $\mu$ m ramps . . . . .	90
3.36 Single focus trap lifetime measurements . . . . .	92
3.37 Crossed trap alignment in absorption . . . . .	93

3.38	Critical field scan for the cross trap . . . . .	93
3.39	Coherent oscillations in the crossed dipole trap in the BA and Polar phase . . . . .	95
3.40	Coherent oscillations and energy gap measurements in the crossed trap . . . . .	96
3.41	RF pulse and measuring a ground state coherent oscillation . . . . .	97
3.42	Spin mixing in the crossed trap for different crossed trap powers . . . . .	97
3.43	Number squeezing data taking in the crossed trap . . . . .	99
3.44	Number squeezing analysis in the crossed trap . . . . .	100
4.1	Normal high density spin mixing from a magnetic quench . . . . .	104
4.2	Normal SN squeezing in the crossed dipole trap . . . . .	105
4.3	Experimental timings used to generate mean-field spin mixing dynamics using density modulation . . . . .	111
4.4	Mean-field spin mixing simulations averaging over 1000 samples and 27,000 atoms. . . . .	115
4.5	Measurement of coherent oscillations of density-induced shift in energy gap. . . . .	117
4.6	Depiction of the relevant experimental parameters for the density quench performed using a second laser trap . . . . .	119
4.7	The quantum phase diagram for our system of spin-1 atoms in a bias magnetic field. . . . .	120
4.8	Spin mixing evolution for two clouds confined to two different final densities. . . . .	122
4.9	Spin-nematic squeezing performed for condensates ramped up to different final densities . . . . .	124
5.1	Quantum calculated energy gap for finite numbers of atoms . . . . .	133
5.2	Noise estimates for crossing the quantum critical point with different ramp speeds and finite numbers of atoms . . . . .	135
5.3	Measured $c$ values for different final $10.6 \mu\text{m}$ powers and final atom numbers . . . . .	137

5.4	Absorptive images for the 10.6 $\mu\text{m}$ laser ramped to high power in various times . . . . .	138
5.5	Absorptive images of small condensates . . . . .	139
5.6	Spin mixing with 100s of atoms . . . . .	140
5.7	Coherent oscillations with 100s of atoms . . . . .	141
5.8	Existing double-MOT experimental setup . . . . .	143
5.9	2D-MOT beam looking down the longitudinal axis of the 2D-MOT to 3D-MOT experiment. . . . .	145
5.10	2D-MOT loading curves . . . . .	147
5.11	Possible new double MOT designs 1 . . . . .	151
5.12	Possible new double MOT designs 2 . . . . .	152
5.13	Vertical, MOT 1 mask adjustment . . . . .	156
5.14	Imaging with all six beams, using long and short exposure times . . . . .	157
5.15	Imaging with all six beams, using long exposure times and large detunings .	158



## SUMMARY

Density or pressure modulation of materials is an important method for tuning and engineering interactions within materials studied in condensed matter systems. This tuning is often used to alter or modify the underlying properties of the material, leading to the crossing of a phase transition or enhanced chemical or mechanical properties. This thesis investigates the possibility of whether a similar approach might be employed in the study of ultracold atoms present within a spinor condensate. In our system we use the confining trap potential to modulate and increase the density of the system in such a way as to push the cloud of atoms from non-interacting to interacting, and across a quantum critical point. By crossing over into this new phase, we are able to perform a constant magnetic field quench to observe both spin mixing and spin-nematic squeezing. This allows us to achieve  $-8.4 \pm 0.8$  dB of squeezing and shows promise for future density-driven interactions.

# CHAPTER 1

## INTRODUCTION AND BACKGROUND

From the macroscopic transformation of ice to water to steam, to the microscopic creation of a superconductor, phase transitions are a part and parcel of our daily lives. The same can be said for quantum phase transitions [1]. From a thermodynamic perspective, the crossing of a critical point from one phase to another occurs from the increase in thermal fluctuations. In the case of quantum phase transitions, these transitions are driven by quantum fluctuations. Just like in conventional, thermodynamic phase transitions, these transitions can be first order or second order (continuous) [2]. Continuous phase transitions often exhibit other interesting properties, such as spontaneous symmetry breaking. It stands to reason then, that with the advent of cold atomic systems and their high degrees of control-ability, that one natural avenue of research would be to try and employ these tools to explore quantum phase transitions. These endeavors have probed the many-body behavior of quantum gases in a variety of contexts.

A large aspect of experimentation in the field of condensed matter is designing desirable samples to study. One way to explore particular types of transitions, is to choose a material with the desired properties or phase transition. This however, may still present experimental challenges if the interesting aspects of the material are still outside the available experimental controls, such as a phase transition that occurs at absolute zero or a material with only weak to moderate structural coupling. However, if one could take a material that has close to the desired qualities, one might be able to devise a way to slightly alter its properties to achieve more manageable outcomes. This is where the technique of pressure-tuning comes into play. A technique often used in condensed matter, it can be utilized to change the structure and correlations in a given material, allowing for critical points and in some cases, exotic phases, to become accessible. We use this to draw parallels to our

own system where we have devised a means of traversing the quantum critical point in our system using density modulation. This will involve us briefly reviewing the background of our spinor BEC system, as well as touch on how pressure-tuning can be used in condensed matter systems, before we return to the question of how cold atoms can be used to study the behavior of quantum phase transitions.

## 1.1 Density and Pressure-Tuned Quantum Phase Transitions

As mentioned, many condensed matter studies revolve around the types of materials used or created. These studies center around a wide-range of topics from the practical to the purely scientific. However in many of these areas, pressure tuning has been found to be a useful tool both for the engineering and the testing of the properties of a material.

In the realm of quantum studies, many studies have used pressure-induced QPT's in the study of quantum and fundamental scientific studies [3, 5, 6, 7, 8, 9, 10, 11, 12, 4]. Pressure tuning, along with other types of experimental tuning such as temperature, voltage, doping, or magnetic field, can be used to look at a wide range of phenomenon. One early example of this are studies investigating Mott transitions [5], in which pressure was used to search for the first order phase metal to Mott insulator transition in  $(V_{1-x}Cr_x)_2O_3$  materials. This work has been extended to other studies of similar systems [11]. Mott insulators are important in the studies of superconductivity, and the transition between metal to Mott insulator is a first-order transition. A similar study was performed in an organic material [7], and showed a similar relationship to pressure tuning that the original metallic studies had shown. This largely has to do with the role that pressure and temperature play in the tuning of these transitions which look at the correlations of electrons. In these studies, doping has nearly the same effect as pressure-tuning [11, 5]. Additionally, some of these materials also touch on other interesting topics, as the organic material  $(\kappa - (BEDT-TTF_4)Hg_{289}B_8)$  in [12] is additionally a quantum spin liquid candidate material.

The studies of Mott insulators using pressure and doping as experimental knobs show

us there are even more complex topics to study using pressure-tuning of transitions. Topics involving superconducting to charge-density wave phases have been explored in [8] using rare-earth materials. For the spin-1/2 ladder compound  $C_9H_{18}N_2CuBr_4$ , pressure tuning affected the magnetic structure and spin dynamics [9] in such a way as to exhibit rarely seen fractionalization from an organized Neel order when the continuous quantum phase transition is crossed using high pressures.

Different types of material geometry also exhibit interesting collective behavior, when tuned with pressure. The triangular lattice system found in  $Cs_2CuCl_4$  [10] shows that the application of pressure at low temperature leads to field-induced magnetic phases; furthermore, high pressures can be used to suppress quantum fluctuations for precise measurement. The hexagonal, kagome lattice found in  $Co_3Sn_2S_2$  undergoes a magnetic-topological phase transition when tuned with pressure and appropriate temperature, opening a new avenue to investigate potential Weyl semimetal and 3D topological insulator transitions.

The effects pressure has on the creation of frustrated magnets in the spin dimer system,  $TiCuCl_3$ , is also a very interesting system [13, 14, 7]. It has a continuous transition which goes from disordered (spin liquid) to ordered (antiferromagnetic) for a critical pressure. This critical pressure point can be similarly shifted using other external parameters, as the point where the spin energy gap is closed is between the singlet and triplet states.

Other applications of pressure-tuning involve engineering a material's properties for more practical purposes, such as changing the band gap and absorption profiles of quantum dots to create more favorable photovoltaic structures [15], or changing the magnetic and electronic properties of nanoribbons [15, 16].

These examples underpin the importance of pressure-tuning in condensed matter systems. We draw analogy from this and compare it to the quantum phase transition in our own system. For us, the "pressure-tuning" is performed by the increase in the trap power, which increases the density of the cloud of atoms trapped in its minimum potential. The density in our system is a tuning parameter, as the relationship for the quantum critical point

(QCP) occurs when the density is equal to the quadratic magnetic field divided by two. For sufficiently high densities, we are able to cross our quantum critical point to induce spin interactions in the cloud. In the next section, we will outline the previous quantum work that has lead up to the work presented in this thesis.

## 1.2 Spinor BECs and Our Work

Describing the quantum phase transition of our system, requires us to first describe the creation and evolution of our spinor BEC work. Spinor BEC's are so termed because they involve atoms cooled to quantum degeneracy that still retain their spin degrees of freedom. BEC's were famously first created in 1995 [17, 18, 19] in a Nobel Prize-winning invention. Owing to their ease of controllability and relative theoretical simplicity, BECs have been an important tool for many researchers investigating many-bodied effects and phenomena. Early experiments with BECs studied the coherent nature of the condensate itself [20, 21], as well as designing atom-optics with them [22, 23, 24]. The quantum properties of the macroscopic condensates were also investigated, looking at their quantized angular momentum [25, 26, 27] and quantum tunneling [28, 29].

Many of these early condensates were created by performing evaporative cooling in magnetic traps. The first optical confinement of BEC was in 1998, but was not created in the optical trap itself [30]. All-optical evaporation first occurred in our lab in 2001 [31]. From there, many experiments developed looking at the spin domain formation [32, 33, 34], spin mixing [35, 36], and mean-field formulation of the ground states [37, 38]. The quantum formalism for these spinor collisional interactions for an optical potential were further elaborated on by the Bigelow group [39, 40, 41].

In our lab, we looked at the mean-field dynamics of the hyperfine levels through theoretical description [42, 43], and experimental observation in rubidium-87. Our lab looked at the interactions within the  $F = 1$  ground state [44, 45]. The excited manifold of  $F = 2$  states were studied by the Sengstock group [46, 47, 48]. Other groups also began to look at

the collisional properties of BECs in optical lattices [49, 50]. More complex studies of spin and spatial structures were looked at with larger rubidium condensates [51, 52], magnetic trap studies in the  $F = 2$  manifold [53], and spin wave demonstrations [54].

By looking at higher spin in spinor condensates [51, 52], studies grew involving quantum phase transitions present in several spin-1 species. This was investigated early on [35], but the observation of polar and ferromagnetic regions in rubidium [44], and later the measurement of an antiferromagnetic transition in sodium [55], led to theoretical explorations of the effects of magnetic field quenches [56] and ferromagnetic spinor BECs [57] in the context of a quantum phase transition. The ferromagnetic quantum phase transition in rubidium is the heart of this thesis and will be described in the next section, along with a brief overview of explorations of quantum phase transitions in cold atoms.

### 1.2.1 Quantum Phase Transitions in Cold Atomic Systems

Early work involving the study of quantum phase transitions with ultracold atoms began with the use of the optical lattices [58]. The interactions between the atoms in the lattice are controlled by changing the trap depth by changing the laser potential, allowing the system to be driven from the Mott to superfluid phase, as described by the Bose-Hubbard model. The Bose-Hubbard model describes the occupation and tunnelling between lattice sites for bosonic atoms. These experiments [59] offered insight into the simulation power of cold atoms, and led to further studies such as the Fermi-Hubbard model [60], two-component quantum magnetism [61, 62] and nematic spinor phases with spin-1 gases [63].

In the case of spinor BECs, the mean-field theories referenced in the previous section lead to phase diagrams for our particular quantum phase transition. These can be used to study the many-body behavior of the system, by looking at the change in the order parameter across the transition. This has been looked at in a number of different dimensions as well, including studies dealing with QPTs in zero-dimensions [64, 65, 66, 67, 68]. Zero-dimensionality is a feature by which the spatial evolution of a system is inhibited, such

that the other degrees of freedom carry the dynamics. In our case, the interactions of the system are restricted to the spin variables under a simplified Hamiltonian (see chapter 2 for details).

Our system exhibits a continuous transition which results in a change in the spin symmetry of the ground state when quenched into the broken-axis symmetry phase (or BA phase) [57]. The effective potential for the system, when written in terms of the collective atomic spin, exhibits a potential of the form of a Landau, or double-well, potential [69]. The choice of what well to occupy creates a simultaneous breaking of a  $U(1)$  symmetry. This has been shown experimentally for rubidium and has been investigated in detail in the Chapman lab's work, as will be touched on in the next section.

#### *Previous Chapman Lab BEC Work*

From our early, innovative work on all-optical BEC formation [31], to our description and understanding of the mean-field dynamics [70, 71, 72, 73], our many efforts greatly enhanced our current understanding of ferromagnetic, spin-1 BECs. Other important works as a result of these findings led to the description of the mean-field dynamics as an inverted, unstable pendulum [73]. Meanwhile, the evolution of the state across the quantum critical point, was described to lead to "number suppression" in the magnetization, as pair-wise, spin-interacting collisions led to the formation of correlated pairs [74]. We were able to measure this phenomenon experimentally leading to an effect called "number squeezing." This has become a standard protocol on our experiment and has given us a clear way to measure our detection system to determine our overall detection limit.

Likewise, a short time after, formulism for the understanding of spin-squeezing was developed and measured in our lab as well [75]. With the ability to accurately determine our detection limits, we were able to measure a high degree of squeezing called "spin-nematic" squeezing. Using a magnetic field quench to lower the quadratic Zeeman energy, the spin contact interaction dominates to create correlated pairs. The tomography of this

state is then performed to measure the degree of spin-nematic squeezing. Its development is crucial to the current understanding of what squeezing in higher spin systems looks like. We were able to measure a high degree of squeezing in that system, as well as develop a deeper theoretical understanding of the spin-1 space. This has also become a standard experiment to attempt to replicate for our system.

### *Quantum Kibble-Zureck Mechanism*

A more recent and important work for the study of crossing the quantum phase transition (QPT) in our rubidium spin-1 BEC, is our work investigating the quantum version of the Kibble-Zurek mechanism. This investigates the effects the speed of a quench has on the system dynamics as it crosses the quantum critical point (QCP). The affect applies to continuous QPTs, such as our spin-1 polar to broken-axis transition, to the Kibble-Zurek Mechanism (KZM) [56, 76]. It was originally studied with cold atoms initially in the context of the Mott to superfluid transition in optical lattices, but did not show good agreement with the KZM predicted behavior [77]. However, the transition to the broken-axis phase was a good candidate for observing the quantum KZM dynamics [78, 56, 57, 77], as it restricts the experiment to a zero-dimensional system. The first evidence of the quantum KZM was measured and confirmed in our lab, showing good agreement with the predicted theory [79]. A key development out of this experiment was the ability to measure the spin interaction energy ( $c$ ) of the system, using a critical magnetic field scan (see Sub-Section 3.9.3). This is currently used in the lab to measure the critical field at which the quadratic energy is equal to two times the spin interaction energy of the condensate – the critical point of our system (see Chapter 2). This is a fast and reliable tool that we employ often in our daily measurements.

### *Adiabatic Passage of a QPT*

A particularly relevant work is the adiabatic passage and characterization of our spin-1 quantum phase transition [69]. This work used coherent oscillations to measure the energy gap and gave predictions for potential finite-numbered condensate studies in the future (see Section 5.1). Additionally, this work looked at a piece-wise optimized magnetic field quench to cross the QCP with minimal disruptions to the ground state. Unfortunately, the atom loss due to the finite lifetime of the trap lead to too many atoms being lost for an accurate number of highly entangled pairs to be counted, but this would also be a future goal from this work. Measuring the coherent oscillations of the energy gap is an important tool in our experiments for confirming and checking the stability of the spinor dynamics.

### *Other Recent Chapman Lab Efforts*

Other recent experiments that the lab has been involved in is the study of the measurement of geometric phases in spin-1 atoms [80], and the development of a circular polarized antenna used to selectively drive individual microwave transitions [81]. While these studies did not necessarily use condensates for their work, their theoretical understanding and experimental demonstration help illustrate the versatility of the spin-1 system for addressing and solving both theoretical and technical challenges. The study of geometric phases demonstrates the existence of topological phases in our experiments, and how we might measure and control them. Our microwave work is a very interesting technique which could be used in quantum state preparation for quantum engineering. The ability to individually drive transitions and suppress off-resonant excitations is very important to performing precise computations with microwaves which provide low fault occurrences.

Our most recent work involves using the changing of the ground state near the critical point to engineer a partially squeezed state [82]. This state can be preserved because it never actually crosses the critical point, meaning that it does not exponentially evolve away. By timing the quench sequence appropriately, we can create and preserve a squeezed state for

the duration of the lifetime of the condensate. This is an experimentally interesting result as it demonstrates the ability to create a long-lived squeezed state which could prove a useful tool for future metrological applications which may hope to utilize spin squeezed states.

### **1.3 Thesis Organization and Contribution**

The structure of this thesis starts out with an overview of spin-1, spinor BEC theory. In Chapter 2, we will introduce the mean-field description of the dynamics and how it is used in our experiments. A quantum description of the spin interactions is also presented, along with a discussion of the connection to our semi-classical representations.

Next, we build on this understanding in Chapter 3, as we highlight the key aspects of the experimental apparatus which creates our spinor condensates. Furthermore, we describe several procedures performed routinely on the experiment, and how they demonstrate our control and understanding of the spin interactions.

The content of Chapter 4 contains the main thrust of this thesis's work, as we present the technique of density modulation of the condensate. We are able to do this to a precise degree and use trap modulation shift the quantum phase transition of the system. Doing so, allows us to control the interactions of the system and to observe these interactions through spin mixing and spin-nematic squeezing.

The final chapter, Chapter 5, details previous, relevant investigations performed on the experiment. The descriptions of our work involving finite-numbered condensates demonstrate the motivations behind these investigations and the progress we've made in beginning this work. A technical upgrade to our experiment with the potential addition of a 2D-MOT as a cold atom source is also discussed. We examine the main results of our previous studies and present future designs where a 2D-MOT could be readily incorporated into the experiment. The final section of this chapter relates improvements to our imaging system and how it could impact our current studies, as well as our future studies of condensates involving finite atoms.

## CHAPTER 2

### SPINOR BECS: BACKGROUND AND THEORY

#### 2.1 Gross-Pitaevski Equation and our Simplified Hamiltonian

In order to understand our contributions to the understanding of quantum phase transitions, it is important to contextualize the experimental system with which we work. Our laboratory specializes in working with what are now termed as “spinor Bose-Einstein condensates” or “spinor BECs.” BECs were originally Nobel prize-winning inventions, first created in 1995 [18, 19, 17] by cooling a bosonic atomic species to quantum degeneracy, as predicted by Bose-Einstein statistics [2]. Over the years, they have proven their utility in many fundamental and applied fields of physics, owing to their ease of theoretical description and range of experimental control. While BECs were first created through evaporative cooling in a magnetic trap, the innovation of trapping and creating a BEC using all-optical means (first pioneered in our lab [31]) allows all (hyperfine) atomic spins in the ground state to be preserved. In our lab, our rubidium BEC is called a “spin-1” BEC, as the hyperfine ground state of the atom is in  $F = 1$ , leaving the  $m_f = -1, 0, 1$  Zeeman sublevels to interact. As we will demonstrate, this creates a rich environment in which to study the behaviors of more complex topics, such as the connection between quantum and semi-classical theories, and the crossing of quantum phase transitions.

##### 2.1.1 Our Hamiltonian

The Hamiltonian for  $N$ -identical atoms in an optical potential, or dipole trap, can be written in the form known as the Gross-Pitaevskii equation:

$$H = \sum_{i=1}^N \left( -\frac{\hbar^2}{2m} \nabla_i^2 + V_T(\vec{r}_i) \right) + U. \quad (2.1)$$

Here, the terms summed over  $N$  pertain to the kinetic energy of the atoms and the trapping potential energy of the optical dipole trap.  $U$  represents a psuedo-potential term which arises from the two-body contact interaction between the atoms. The form of this contact interaction depends greatly on the properties of the particles themselves. For example, because our system reaches such low temperature, the effective scattering of the system is dominated by s-wave scattering. Likewise, as the system consists of bosonic particles, only values of the total hyperfine spin state (the combined hyperfine values of the two atoms colliding), are allowed. This yields for our  $f = 1$  bosons, a total spin  $F$  channel of 0 or 2, where  $F = f_1 + f_2$  represents the sum of the atoms' maximum hyperfine spin value. This allows us to represent the psuedo-potential  $U$  as,

$$U = \sum_{i < j} \delta(\vec{r}_i - \vec{r}_j) \sum_{F=0,2} g_F \sum_{m_F=-F} |F, m_F\rangle \langle F, m_F| \quad (2.2)$$

Here,  $g_F = 4\pi\hbar^2 a_F/M$ , where  $a_F$  is the s-wave scattering length used to describe the two-body coupling strength of the total spin channel. Expanding the outer product summation we obtain a number of terms which, in combination with the other terms in our original Hamiltonian, can be rewritten in the form of symmetric spin-preserving terms, and asymmetric spin-dependent terms. Doing so, we find:

$$H = H_{symm} + H_{asym}, \quad (2.3)$$

where for  $i = 0, \pm 1$ ,

$$H_{symm} = \sum_i \int d^3r \hat{\Psi}_i^\dagger \left( -\frac{\hbar^2}{2m} \nabla_i^2 + V_T \right) \hat{\Psi}_i + \frac{c_0}{2} \sum_{ij} \int d^3r \hat{\Psi}_i^\dagger \hat{\Psi}_j^\dagger \hat{\Psi}_i \hat{\Psi}_j \quad (2.4)$$

and,

$$\begin{aligned}
H_{asym} = \frac{c_2}{2} \int d^3r & (\hat{\Psi}_1^\dagger \hat{\Psi}_1^\dagger \hat{\Psi}_1 \hat{\Psi}_1 + \hat{\Psi}_{-1}^\dagger \hat{\Psi}_{-1}^\dagger \hat{\Psi}_{-1} \hat{\Psi}_{-1} \\
& - 2\hat{\Psi}_1^\dagger \hat{\Psi}_{-1}^\dagger \hat{\Psi}_1 \hat{\Psi}_{-1} + 2\hat{\Psi}_1^\dagger \hat{\Psi}_0^\dagger \hat{\Psi}_1 \hat{\Psi}_0 \\
& + 2\hat{\Psi}_{-1}^\dagger \hat{\Psi}_0^\dagger \hat{\Psi}_{-1} \hat{\Psi}_0 + 2\hat{\Psi}_0^\dagger \hat{\Psi}_0^\dagger \hat{\Psi}_1 \hat{\Psi}_{-1} \\
& + 2\hat{\Psi}_1^\dagger \hat{\Psi}_{-1}^\dagger \hat{\Psi}_0 \hat{\Psi}_0)
\end{aligned} \tag{2.5}$$

Note that the symmetric and asymmetric expressions of the Hamiltonian share their own coupling strengths denoted by  $c_0 = (2g_2 + g_0)/3$  and  $c_2 = (g_2 - g_0)/3$ . Both arising from a linear combination of the coupling strengths,  $g_F$ , listed above and grouped into spin preserving (symmetric) and spin-dependent (asymmetric) channels. Thus,  $H_{sym}$  describes the spatial dynamics of the atoms, and  $H_{asym}$  describes the spin exchanges.

### 2.1.2 Single Mode Approximation

Using these expressions, one can now describe the spatial and spin evolution of the system of spin-1 bosons in an optical potential. However, if we would like to consider a subset of the dynamics, say solely the spin interactions, we need to compare the relative length scales of the respective Hamiltonians. In the case of the spin-dependent Hamiltonian, the relevant length scale is defined by the so-called spin-healing length,  $\xi = 2\pi\hbar/\sqrt{2m|c_2|n}$ , where  $n$  is the number density, and  $c_2$  is as defined above. This defines the characteristic scale in which spin domains in the clouds of atoms are formed. For typical densities and our rubidium-87 atoms, this value is typically on the order of  $\sim 10 \mu\text{m}$ . That means for clouds smaller than this size, all atomic spins will reside within the same domain, and be allowed to interact [38]. Such is the case in our all-optical, spin-1 BEC which typically consists of 40,000  $^{87}\text{Rb}$  atoms in a  $10.6 \mu\text{m}$  dipole trap, crossed with an additional 850 nm laser to create a roughly spherical trap. The trap volume is such that these spin domains are inhibited, and the spatial degrees of freedom can be largely ignored in the problem,

consistent with what's known as the single-mode approximation (or SMA)[38, 83, 39, 84].

The SMA allows us to write all the spin components into the a single wave function of the form

$$\hat{\psi}_i \approx \hat{a}_i \phi(\vec{r}), \quad (2.6)$$

where  $\hat{a}_i = |1, i\rangle$  is defined as a bosonic annihilation operator for each spin component, and  $\phi(\vec{r})$  is the spatial wave function. This spatial wave function is a simultaneous solution of the symmetric Hamiltonian,  $H_{symm}$ , defined above. This is the dominant term, as the coupling constants for the Hamiltonians have the relationship where  $c_0 \gg |c_2|$  determined by the scattering lengths for Rb<sup>87</sup> which has  $a_0 > a_2$  by about a 2% difference [85].

We can now define the spin mixing Hamiltonian by taking the mean-field form of the Gross-Pitaevskii equation written as:

$$\hat{H}_{sym} \phi = \left( -\frac{\hbar^2}{2m} \nabla^2 + V_T + c_0 N |\phi|^2 \right) \phi = \mu \phi, \quad \int d^3 r |\phi(\vec{r})|^2 = 1, \quad (2.7)$$

and integrate over the condensate. Neglecting the kinetic energy in our low momentum, ultracold case, we arrive at the SMA Hamiltonian in the symmetric and asymmetric forms:

$$\hat{H}_{sym} = \mu \hat{N} - \tilde{c} \hat{N} (\hat{N} - 1) \quad (2.8)$$

$$\begin{aligned} \hat{H}_{asym} = & \tilde{c}_2 (\hat{a}_1^\dagger \hat{a}_1^\dagger \hat{a}_1 \hat{a}_1 + \hat{a}_{-1}^\dagger \hat{a}_{-1}^\dagger \hat{a}_{-1} \hat{a}_{-1} - 2 \hat{a}_1^\dagger \hat{a}_{-1}^\dagger \hat{a}_1 \hat{a}_{-1} \\ & + 2 \hat{a}_1^\dagger \hat{a}_0^\dagger \hat{a}_1 \hat{a}_0 + 2 \hat{a}_{-1}^\dagger \hat{a}_0^\dagger \hat{a}_{-1} \hat{a}_0 \\ & + 2 \hat{a}_0^\dagger \hat{a}_0^\dagger \hat{a}_1 \hat{a}_{-1} + 2 \hat{a}_1^\dagger \hat{a}_{-1}^\dagger \hat{a}_0 \hat{a}_0). \end{aligned} \quad (2.9)$$

In the above case,  $\hat{N} = \hat{a}_1^\dagger \hat{a}_1 + \hat{a}_0^\dagger \hat{a}_0 + \hat{a}_{-1}^\dagger \hat{a}_{-1}$  represents the total number of atoms, and  $\tilde{c}_i = \frac{c_i}{2} \int |\phi(\vec{r})|^4 d^3 r$  is the spatially integrated interaction strength. If the total number of atoms is constant, along with the trap potential, then  $H_{sym}$  is constant, and the dynamics

Table 2.1: Spin-1 Operators and Matrices. Matrices are in the spherical polar basis of  $|f, m_F\rangle$ .

$$\begin{aligned}
 S_x &= \frac{1}{\sqrt{2}} \begin{pmatrix} 0 & 1 & 0 \\ 1 & 0 & 1 \\ 0 & 1 & 0 \end{pmatrix}, & \hat{S}_x &= \frac{1}{\sqrt{2}} \left( \hat{a}_{+1}^\dagger \hat{a}_0 + \hat{a}_0^\dagger \hat{a}_{+1} + \hat{a}_0^\dagger \hat{a}_{-1} + \hat{a}_{-1}^\dagger \hat{a}_0 \right) \\
 S_y &= \frac{i}{\sqrt{2}} \begin{pmatrix} 0 & -1 & 0 \\ 1 & 0 & -1 \\ 0 & 1 & 0 \end{pmatrix}, & \hat{S}_y &= \frac{i}{\sqrt{2}} \left( -\hat{a}_{+1}^\dagger \hat{a}_0 + \hat{a}_0^\dagger \hat{a}_{+1} - \hat{a}_0^\dagger \hat{a}_{-1} + \hat{a}_{-1}^\dagger \hat{a}_0 \right) \\
 S_z &= \begin{pmatrix} 1 & 0 & 0 \\ 0 & 0 & 0 \\ 0 & 0 & -1 \end{pmatrix}, & \hat{S}_z &= \left( \hat{a}_{+1}^\dagger \hat{a}_{+1} - \hat{a}_{-1}^\dagger \hat{a}_{-1} \right)
 \end{aligned}$$

can be attributed solely to the spin-dependent Hamiltonian,  $H_{asym}$ .

This simplified case can now be looked at through the lenses of both mean field and quantum mechanical approaches.

## 2.2 Quantum Mechanical Description

The quantum representation of the asymmetric, spin-dependent Hamiltonian is made possible by expressing the states of the system in terms of second-quantized operators [75, 86, 87, 88]. This is written as,

$$\hat{H}_{asym} = \tilde{c}_2 \left( \hat{S}^2 - 2\hat{N} \right), \quad (2.10)$$

where  $\hat{S}^2 = \hat{S}_x^2 + \hat{S}_y^2 + \hat{S}_z^2$  and can be shown to be written as spin-1 dipole operators [86] (see Table 2.1).  $\hat{N}$  is as defined above. The final consideration we must look at involves the addition of the magnetic field interaction to our system, given by the linear and quadratic Zeeman effects.

This becomes easier to see when we note that the quadratic moment operator can be defined as  $\hat{Q}_{zz} = 2 \left( \hat{N}_1 + \hat{N}_{-1} \right) - \frac{4}{3} \hat{N}$  (see Table 2.2) and can be used to represent the quadratic Zeeman interaction, while  $\hat{S}_z = \hat{N}_1 + \hat{N}_{-1}$  represents the linear Zeeman terms. This gives,

Table 2.2: Spin-1 Nematic, Quadrapole Matrices. Matrices are in the spherical polar basis of  $|f, m_F\rangle$ .

$$\begin{aligned}
Q_{xx} &= \frac{1}{3} \begin{pmatrix} -1 & 0 & 3 \\ 0 & 2 & 0 \\ 3 & 0 & -1 \end{pmatrix}, & \hat{Q}_{xx} &= -\frac{1}{3}\hat{a}_{+1}^\dagger\hat{a}_{+1} + \frac{2}{3}\hat{a}_0^\dagger\hat{a}_0 - \frac{1}{3}\hat{a}_{-1}^\dagger\hat{a}_{-1} + \hat{a}_{+1}^\dagger\hat{a}_{-1} + \hat{a}_{-1}^\dagger\hat{a}_{+1} \\
Q_{yy} &= \frac{1}{3} \begin{pmatrix} -1 & 0 & -3 \\ 0 & 2 & 0 \\ -3 & 0 & -1 \end{pmatrix}, & \hat{Q}_{yy} &= -\frac{1}{3}\hat{a}_{+1}^\dagger\hat{a}_{+1} + \frac{2}{3}\hat{a}_0^\dagger\hat{a}_0 - \frac{1}{3}\hat{a}_{-1}^\dagger\hat{a}_{-1} - \hat{a}_{+1}^\dagger\hat{a}_{-1} - \hat{a}_{-1}^\dagger\hat{a}_{+1} \\
Q_{zz} &= \frac{1}{3} \begin{pmatrix} 2 & 0 & 0 \\ 0 & -4 & 0 \\ 0 & 0 & 2 \end{pmatrix}, & \hat{Q}_{zz} &= \frac{2}{3}\hat{a}_{+1}^\dagger\hat{a}_{+1} - \frac{4}{3}\hat{a}_0^\dagger\hat{a}_0 + \frac{2}{3}\hat{a}_{-1}^\dagger\hat{a}_{-1} \\
Q_{xy} &= i \begin{pmatrix} 0 & 0 & -1 \\ 0 & 0 & 0 \\ 1 & 0 & 0 \end{pmatrix}, & \hat{Q}_{xy} &= i \left( -\hat{a}_{+1}^\dagger\hat{a}_{-1} + \hat{a}_{-1}^\dagger\hat{a}_{+1} \right) \\
Q_{xz} &= \frac{1}{\sqrt{2}} \begin{pmatrix} 0 & 1 & 0 \\ 1 & 0 & -1 \\ 0 & -1 & 0 \end{pmatrix}, & \hat{Q}_{xz} &= \frac{1}{\sqrt{2}} \left( \hat{a}_{+1}^\dagger\hat{a}_0 + \hat{a}_0^\dagger\hat{a}_{+1} - \hat{a}_0^\dagger\hat{a}_{-1} - \hat{a}_{-1}^\dagger\hat{a}_0 \right) \\
Q_{yz} &= \frac{i}{\sqrt{2}} \begin{pmatrix} 0 & 1 & 0 \\ 1 & 0 & -1 \\ 0 & -1 & 0 \end{pmatrix}, & \hat{Q}_{yz} &= \frac{i}{\sqrt{2}} \left( -\hat{a}_{+1}^\dagger\hat{a}_0 + \hat{a}_0^\dagger\hat{a}_{+1} + \hat{a}_0^\dagger\hat{a}_{-1} - \hat{a}_{-1}^\dagger\hat{a}_0 \right)
\end{aligned}$$

$$\hat{H}_{asym} = \tilde{c}_2 \left( \hat{S}^2 - 2\hat{N} \right) + p\hat{S}_z + \frac{q}{2}\hat{Q}_{zz} \quad (2.11)$$

with  $p = \mu_B B_z g_F$  and  $q = \mu_B^2 B_z^2 / (\hbar^2 \Delta E_{hf}) = q_z B_z^2$ , defined with constants the Bohr magneton ( $\mu_B$ ), the Landé g-factor ( $g_F$ ), and the hyperfine energy gap ( $\Delta E_{HF}$ ). This Hamiltonian is nontrivial to find simultaneous eigenstates for, as not all of the operators commute with each other, namely  $\hat{Q}_{zz}$  and  $\hat{S}^2$  (see Table 2.3). This can be further simplified by noting that both the magnetization ( $\hat{S}_z = M = 0$ ) and the atom number ( $N$ ) are conserved, and so won't affect the dynamics. The simplified version of this Hamiltonian ( $\hat{H}$  becomes:

$$\hat{H}_{asym} = \tilde{c}_2 \hat{S}^2 - \frac{q}{2} \hat{Q}_z, \quad (2.12)$$

as we define the new variable,  $\hat{Q}_z = -\frac{\hat{N}}{3} - \hat{Q}_{zz}$ . This version of the Hamiltonian is

useful in our simulations and depictions of the dynamics in the spin-1 space.

Looking back at Equation 2.11, the asymmetric Hamiltonian was constructed in the spin-1 Fock basis,  $|N_{-1}, N_0, N_{+1}\rangle$ . This can equivalently be transformed to be written in terms of  $|N, M, k\rangle$ , where  $N$  is the total number of atoms,  $M$  is the magnetization, and  $k$  is the number of pairs of atoms in the  $m_f = \pm 1$  state. As we will see, this basis is convenient due to several conserved quantities.

The total atom number can be assumed to be a constant throughout our experiments. Likewise, the magnetization, defined as  $M = N_1 - N_{-1}$ , is also conserved; this leaves the parameter  $k$  as the single parameter over which the Hamiltonian can be solved. The Fock states therefore have a dimensionality of  $N/2 + 1$ , as it spans the number of available pairs for  $k \in [0, \frac{N}{2}]$ .

Taking this, we can write Equation 2.11 in the Fock number basis as,

$$\begin{aligned}
H_{asym} = & \tilde{c}_2 \left( \left( \hat{N}_1 - \hat{N}_{-1} \right)^2 + \left( 2\hat{N}_0 - 1 \right) \left( \hat{N}_1 + \hat{N}_{-1} \right) \right) \\
& + \tilde{c}_2 \left( 2\hat{a}_1^\dagger \hat{a}_{-1}^\dagger \hat{a}_0 \hat{a}_0 + 2\hat{a}_0^\dagger \hat{a}_0^\dagger \hat{a}_1 \hat{a}_{-1} \right) \\
& + p \left( \hat{N}_1 - \hat{N}_{-1} \right) + q \left( \hat{N}_1 + \hat{N}_{-1} \right) + \hat{N} E_0.
\end{aligned} \tag{2.13}$$

From the above equation, noting again that  $\Delta M = 0$  and the initial state for the atomic cloud is  $|f, m_f = 0\rangle$ , we gather that the elemental form of the Hamiltonian matrix follows as [75],

$$\begin{aligned}
H_{k,k'} = & (2\tilde{c}_2 k (2(N - 2k) - 1) + 2qk) \delta_{k,k'} \\
& + 2\tilde{c}_2 [(k' + 1) \sqrt{(N - 2k')(N - 2k' - 1)} \delta_{k,k'+1} \\
& + k' \sqrt{(N - 2k' + 1)(N - 2k' + 2)} \delta_{k,k'-1}].
\end{aligned} \tag{2.14}$$

These elements form a symmetric, tridiagonal matrix. Using this form, we can numerically integrate the Schrödinger equation of the form  $i\hbar \frac{\partial}{\partial t} \psi = H\psi$ , to look at the dynamics of the system in the quantum formulation.

### 2.3 Mean-Field Approach

In the mean field description, we can describe a large number  $N$  of atoms in the form of  $N$ -independent wavefunctions which satisfy the constraints given by the solution to the Gross-Pitaevski equation [39]. For our tightly confining trap, our system satisfies the single mode approximation (or SMA) [39] and we can consider the whole condensate to be in the same spatial state. This allows us to write a spinor wavefunction of the form,

$$\psi_i = \sqrt{N}|\zeta_i\rangle e^{i\theta_i} \quad (2.15)$$

where  $|\zeta_i|^2 = \rho_i = N_i/N$  are the fractional spin populations and  $\theta_i$  are the phases for the  $m_F = 0, \pm 1$  modes. This can be written as a form of coupled Gross-Pitaevskii equations, which we can use to simulate the evolution of the states in time. They take the form:

$$\begin{aligned} i\hbar \frac{\partial \zeta_1}{\partial t} &= E_1 \zeta_1 + c[(\rho_1 + \rho_0 - \rho_{-1})\zeta_1 + \zeta_0^2 \zeta_{-1}^*] \\ i\hbar \frac{\partial \zeta_0}{\partial t} &= E_0 \zeta_0 + c[(\rho_1 + \rho_{-1})\zeta_0 + 2\zeta_1 \zeta_{-1} \zeta_0^*] \\ i\hbar \frac{\partial \zeta_{-1}}{\partial t} &= E_{-1} \zeta_{-1} + c[(\rho_{-1} + \rho_0 - \rho_1)\zeta_{-1} + \zeta_0^2 \zeta_1^*] \end{aligned} \quad (2.16)$$

with  $c = 2\tilde{c}N$  (the spinor dynamical rate) and  $E_{m_F} = -(m_F)p + q$  (the expression for the linear ( $p = p_z B$ ) and quadratic ( $q = q_z B^2$ ) magnetic field energy shifts felt by each hyperfine sublevel ( $m_F$ )) being defined above. This allows us to write the wavefunction:

$$\psi = (\zeta_1, \zeta_0, \zeta_{-1})^T. \quad (2.17)$$

Additional constraints further simplify our expression, as we take into account the conservation of magnetization ( $m = \rho_1 - \rho_{-1}$ ) and the normalization condition  $\sum_{i=1}^3 \rho_i = \sum_{i=1}^3 |\zeta_i|^2 = 1$ . This leads us to rewrite the order parameter by defining  $\chi^\pm = \theta_{\pm 1} - \theta_0$  to

give:

$$\psi = \left( \sqrt{\frac{(1 - \rho_0 + m)}{2}} e^{ix_+}, \sqrt{\rho_0}, \sqrt{\frac{(1 - \rho_0 - m)}{2}} e^{ix_-} \right). \quad (2.18)$$

Defining the spinor phase,  $\theta_s = \theta_{+1} + \theta_{-1} - 2\theta_0$  and the magnetization phase,  $\theta_m = \theta_{+1} - \theta_{-1}$ , we can write the mean field spinor energy per particle [72]:

$$\mathcal{E} = \frac{c}{2} m^2 + c\rho_0 \left[ (1 - \rho_0) + \sqrt{(1 - \rho_0)^2 - m^2} \cos \theta_s \right] + pm + q(1 - \rho_0). \quad (2.19)$$

As will be seen in the next section, the mean-field description can be linked to the quantum formulism to provide a semi-classical picture, making it easier to simulate the complex dynamics for our ensemble of atoms.

## 2.4 Phase Space and Spin-1 Pictures

Several useful pictures can be described using the mean-field and quantum descriptions. They help us visualize the space and dynamics in which our spin dynamics reside. The first of which is obtained by looking at the phase space created by the conjugate variables  $\rho_0$  and  $\theta_s$  [72]. These can be obtained by taking the derivative of the energy functional in Equation 2.19:

$$\dot{\rho}_0 = \frac{2}{\hbar} \frac{\partial \mathcal{E}}{\partial \theta_s}, \quad (2.20)$$

giving,

$$\dot{\rho}_0 = \frac{2c}{\hbar} \rho_0 \sqrt{(1 - \rho_0)^2 - m^2} \cos \theta_s. \quad (2.21)$$

Likewise,

$$\dot{\theta}_s = \frac{2}{\hbar} \frac{\partial \mathcal{E}}{\partial \rho_0} \quad (2.22)$$

yields,

$$\dot{\theta}_s = -\frac{2q}{\hbar} + \frac{2c}{\hbar} \left[ (1 - 2\rho_0) + \frac{(1 - \rho_0)(1 - 2\rho_0) - m^2}{\sqrt{(1 - \rho_0)^2 - m^2}} \cos \theta_s \right]. \quad (2.23)$$

As will be discussed below, our system undergoes a change in observable behaviors for certain values of spin collision energy ( $\tilde{c}_2$ , hereafter simplified to “ $c$ ”) and quadratic Zeeman energy ( $q$ ). Using the  $\rho_0, \theta_s$  phase space, we can simulate the mean-field behavior of a collection of atoms for various  $q/c$  values. These dynamics follow orbits around constant energy contours, and give us insight into how the semi-classical phase space changes. We can express the mean-field variables  $\rho_0, \theta_s, \chi$ , and  $m$  in terms of the expectation values of the spin-1 operators presented earlier as [86, 88]:

$$\begin{aligned}
\tan \chi_+ &= -\frac{S_y + Q_{yz}}{S_x - Q_{xz}} \\
\tan \chi_- &= \frac{S_y - Q_{yz}}{S_x - Q_{xz}} \\
\rho_0 &= \frac{1}{2} \left[ 1 + \sqrt{1 - \frac{1}{2} \left( \left( \frac{S_x + Q_{xz}}{\cos \chi_+} \right)^2 + \left( \frac{S_x - Q_{xz}}{\cos \chi_-} \right)^2 \right)} \right] \\
m &= \frac{1}{8\rho_0} \left( \left( \frac{S_x + Q_{xz}}{\cos \chi_+} \right)^2 - \left( \frac{S_x - Q_{xz}}{\cos \chi_-} \right)^2 \right) \\
\theta_s &= \chi_+ + \chi_-
\end{aligned} \tag{2.24}$$

Furthermore, we can use the  $\rho_0$  and  $\theta_s$  variables to create a spherical projection of the spin-1 space. We call this the “spin-nematic” (SN) sphere. Remembering the operator  $\hat{Q}_z$  presented in our Hamiltonian (Equation 2.12), we note that we can define a sphere with the normalized, mean-field relation:

$$1 = S_{\perp}^2 + Q_{\perp}^2 + Q_z^2. \tag{2.25}$$

This incorporates the definitions of the transverse spin,  $S_{\perp}^2 = S_x^2 + S_y^2$ , and the off-diagonal quadrupole moments,  $Q_{\perp}^2 = Q_{xz}^2 + Q_{yz}^2$ . These equations take the form [86, 88]:

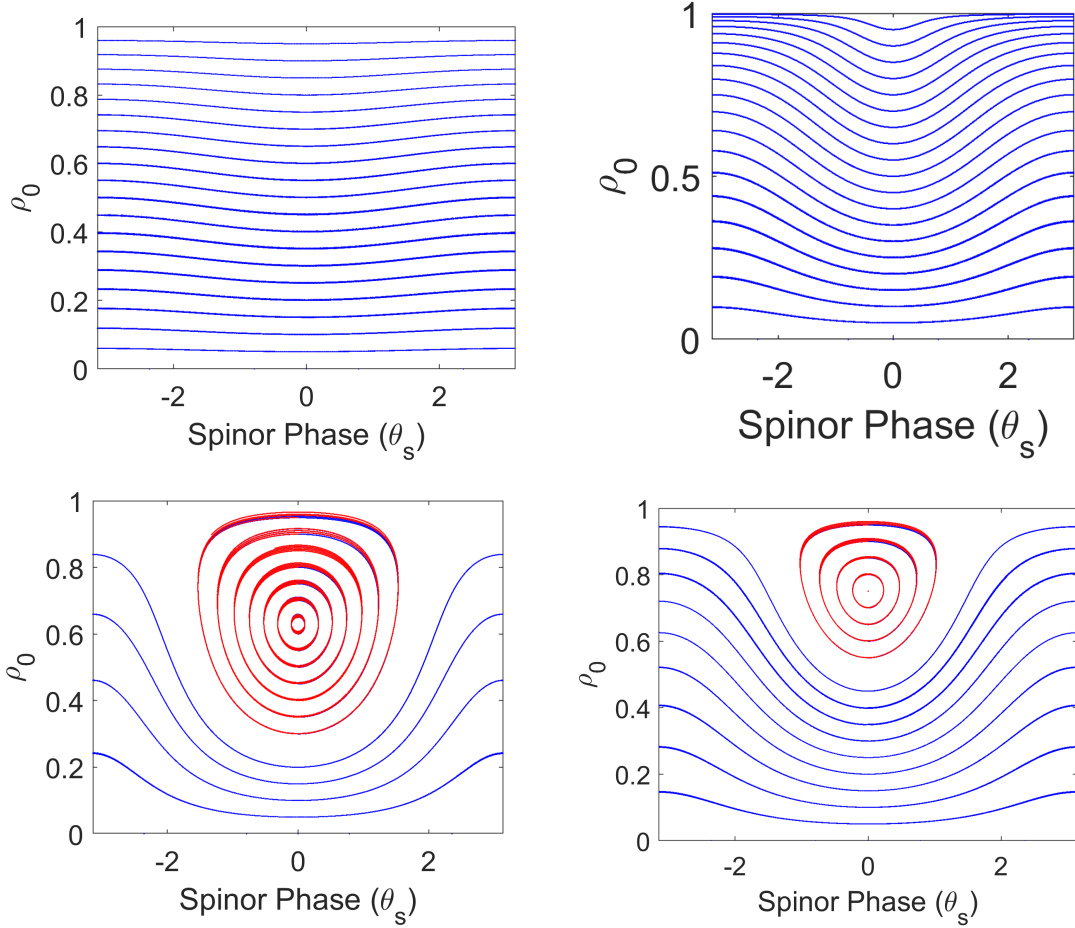


Figure 2.1: Energy contours in the spinor phase space  $(\rho_o, \theta_s)$  for different values of  $q/|c|$ . The plots in clockwise order, from top left to bottom left, show the contours for values of  $q/|c| = 10$ ,  $q/|c| = 2$ ,  $q/|c| = 1$ , and  $q/|c| = 0.5$ . Values for  $q/|c| > 2$  reside in the polar phase space, while values less than two belong to the broken-axis symmetry phase, where the oscillations away from the closed orbit ground state (shown in red) are characterized by larger phase-winding oscillations.

$$\begin{aligned}
S_x &= \langle \psi | S_x | \psi \rangle = 2\sqrt{\rho_0(1-\rho_0)} \cos \theta \cos \theta_L = S_\perp \cos \theta_L \\
Q_{yz} &= -2\sqrt{\rho_0(1-\rho_0)} \sin \theta \cos \theta_L = -Q_\perp \cos \theta_L \\
S_y &= -2\sqrt{\rho_0(1-\rho_0)} \cos \theta \sin \theta_L = -S_\perp \sin \theta_L \\
Q_{xz} &= -2\sqrt{\rho_0(1-\rho_0)} \sin \theta \sin \theta_L = -Q_\perp \sin \theta_L \\
Q_z &= 2\rho_0 - 1
\end{aligned} \tag{2.26}$$

This creates a projection onto a Bloch-type sphere and is useful for watching the evolution of the semi-classical space constructed from dipole-quadrupole operators defined as  $Q_{ij} = \hat{Q}_{ij}/N$ .  $Q_z$  is constructed in a way to maintain a range of  $[0, 1]$  for the variable  $\rho_0 - N_0/N$ . Together, the set of variables  $S_\perp$ ,  $Q_\perp$ , and  $Q_z$  don't create a proper  $SU(2)$  subspace of the  $SU(3)$  phase space, shown in [86], but they do allow us to visualize the dynamics in the higher, spin-1 space. Moreover, it becomes an excellent way to understand the squeezing dynamics which develop in the  $S_\perp, Q_\perp$  space, which we will demonstrate in the next section. Various values of  $q/|c|$  are shown on the spin-nematic spheres to show the energy contours for the various phases of the system.

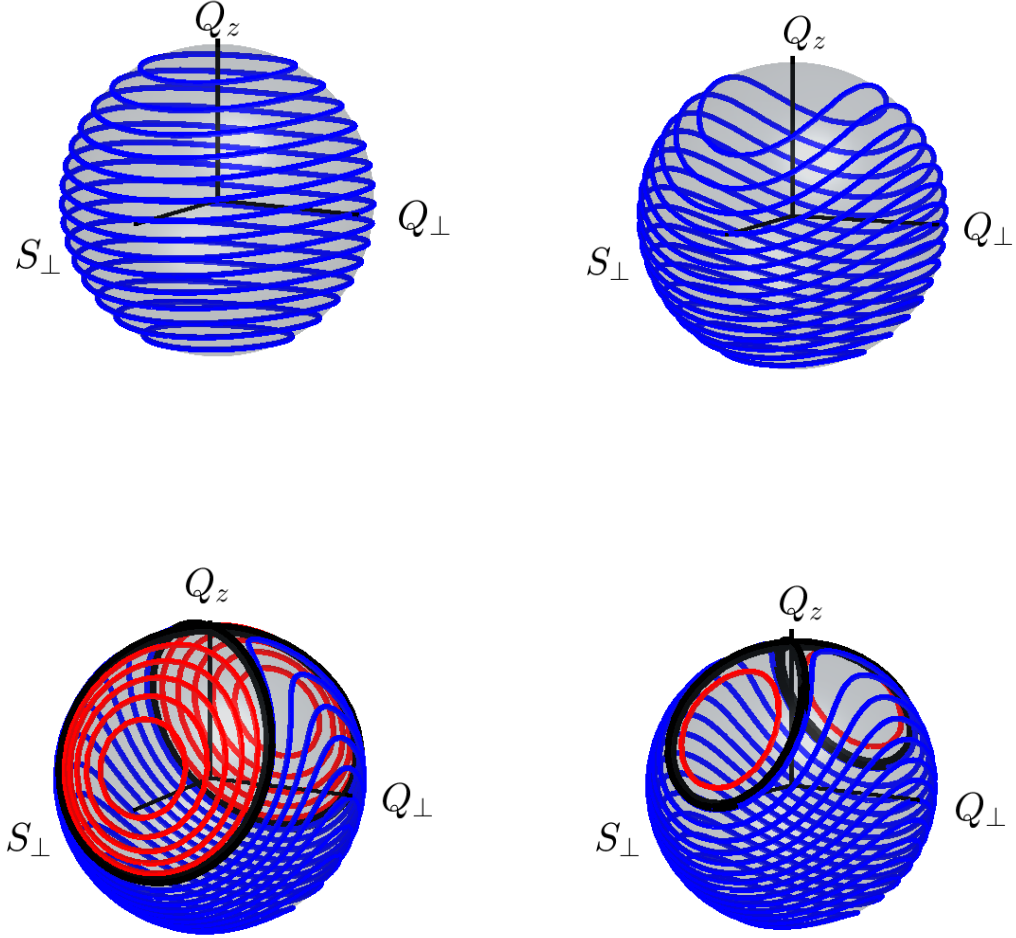


Figure 2.2: Energy contours in the spin-nematic phase space ( $\hat{S}_\perp$ ,  $\hat{Q}_\perp$ , and  $\hat{Q}_z$ ) for different values of  $q/|c|$ . The plots in clockwise order, from top left to bottom left, show the contours for values of  $q/|c| = 10$ ,  $q/|c| = 2$ ,  $q/|c| = 1$ , and  $q/|c| = 0.5$  as projected on the spin-nematic sphere. Values for  $q/|c| > 2$  reside in the polar phase space. As in the spinor phase space, values of  $q/|c| < 2$  are characterized by closed oscillations (in red) near the ground state, while phase winding oscillations appear in blue. The black line depicts the separatrix between these two types of oscillations.



## CHAPTER 3

### EXPERIMENTAL APPARATUS

In order to perform our particular flavor of spinor BEC studies, our experimental techniques rely on a number of generational advances, many of which are the by-product of many Nobel-worthy advances the field of atomic physics. The apparatus and techniques written about in this section also span several generations of graduate students in the Chapman laboratory, many of who's work is describe in other works [89, 81, 90, 91, 86, 92, 93].

This chapter will present an overview of the current apparatus used to create and perform the studies described in this thesis. We will briefly discuss the general types of techniques used to cool, trap, interact, and measure our BEC. We'll then outline how these tools are made to work practically in an experimental sequence to study spinor dynamics.

#### 3.1 Lasers

Lasers are a key part of our experiment, as they provide the cooling, trapping, and imaging of the atoms in the experiment. The sections below detail the setup and operation of these lasers, as well as their roles and layouts in the experiment.

##### 3.1.1 Experimental Diode Lasers

Diode lasers provide an economic and effective way to interact with rubidium [94], as its atomic transitions are in the near-infrared wavelength range of many diode lasers (for us  $\sim 780$  nm). These lasers are easy to make a stable frequency, or single mode, through appropriate temperature and current controls. In the previous versions of our experiment, the stability of our diode lasers were further strengthened through the use of an external grating. This grating is a standard technique which reflects the first order diffractive order back into the diode's internal cavity [94], allowing one to create a coherent laser beam of a

single, narrow frequency. This laser setup is referred to as an “external cavity diode laser” of ECDL. A schematic of a typical setup is shown below Figure 3.2.

A second type of diode laser newly introduced in the experiment is the distributed Bragg reflector laser or “DBR” laser. Similar to the conventional ECDL laser, it involves a grating to provide the single mode feedback for the laser; however instead of being located external to the diode housing, the grating is microfabricated to be located within the diode housing. This allows for more stable control of the temperature of the laser, and thus stability and tunability of the laser itself.

Our experiment currently employs both types of diode lasers. The former, ECDL type was used in the experiment for many decades. Within the last two years however, we added DBRs to our arsenal and after some testing, swapped out some of the ECDLs for equivalent DBR lasers. We’ll talk about how we use these diode lasers now in the experiment and some of their locking characteristics.

### 3.1.2 Frequency Stabilization of Diode Lasers Used in the Experiment

Our system uses a saturation absorption spectroscopy lock to electronically feedback to and lock our lasers onto a single frequency. First demonstrated in 1995 [95], it works by dithering the lasers’ current with a high frequency modulation ( $\sim$  MHz). This is then electronically mixed [86] to create an error signal using the signal from the photodiode signal and the input modulation (see Figure 3.2). Once the current and temperature settings are found to put the laser near resonance, the lines from the sub-Doppler peaks can be used to lock the lasers (see Figure 3.1).

A table for the modulation and locking settings used in the experiment is shown below in Table 3.1. Here the reported values are from Fall 2022. These modulations were later updated (circa Spring 2023) in our heterodyne studies of the DBR lasers to give smaller frequency spreads (FWHMs) of the output from the laser beams. Data presented in this thesis is taken primarily with the laser modulations listed in the table below.

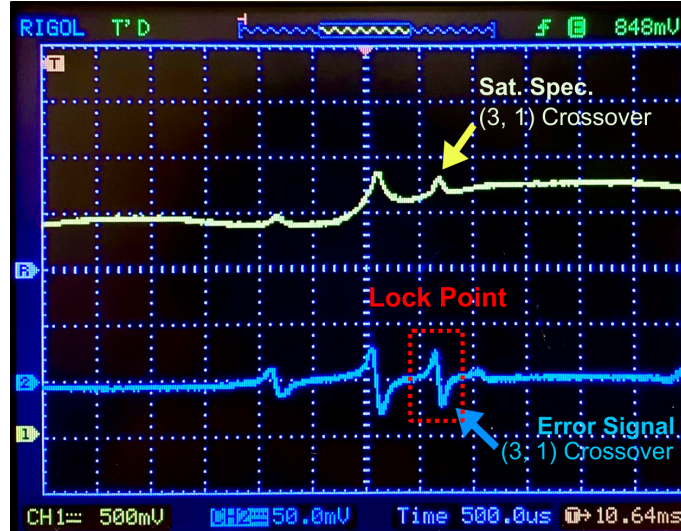


Figure 3.1: DBR cycling laser saturation absorption signal (yellow) and the DBR error signal (blue) depict the main signals used to lock the experimental cooling and imaging transition. Full schematic shown in the following figure to depict how this signal is used to stabilize our laser to a particular frequency to less than a 5 MHz linewidth [89].

Table 3.1: Experimental diode lasers listed with their modulation strengths and measured with heterodyne measurements to estimate the linewidth of the laser’s output when locked using the FM modulation.

Diode Laser	Est. FWHM	Modulation Freq.	Modulation Strength
Probe ECDL	3-4 MHz	0.3 MHz	+10 dBm
Cycling DBR	5+ MHz	1.8 MHz	-4.3 dBm
Repump DBR	5+ MHz	1.8 MHz	-4.1 dBm

Once this light is generated from the FM spectroscopy, it can be locked by the locking electronics using our home-built boxes [86]. Our locks use only proportional and integral feedback to the error signal to maintain the lock at its setpoint. In our older setup, the slower integral feedback went to the piezoelectric motor which controlled the grating position for the ECDL lasers, while the proportional feedback was applied to modulate the current of the diode itself. In the current configuration for the DBRs, we instead combine the proportional and integral outputs, with appropriate attenuation, to directly feedback to the DBR current (see Figure 3.3). In this configuration, the lasers can remain locked for most of the day, in the case of the ECDLs, and for many days, in the case of the DBR lasers. Additionally, while the ECDL lasers are temperature sensitive above a change of a few

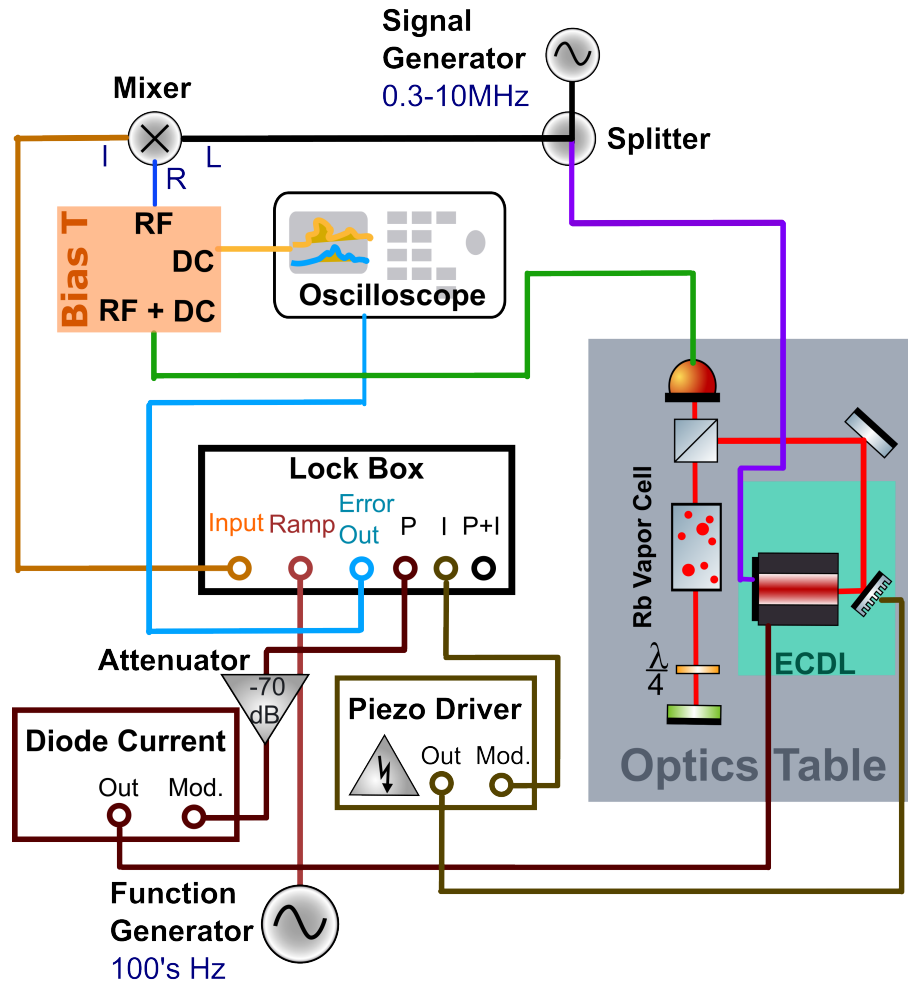


Figure 3.2: FM locking electronics circuit used to lock the ECDL laser on the experiment. Currently only used for the probe laser, as it incorporates a separate integral feedback for the piezo grating.

degrees in the room (as the external grating and experiences thermal shifts outside of the correctable range of the electronic feedback), the DBR lasers stay on resonance as the diode and grating are thermally and internally isolated from the environment.

A final point of consideration for the laser lock of the DBR lasers controlling what's known as the cycling or cooling transition of rubidium, is the frequency shifts provided by acoustic-optical modulators (AOMs). As will be discussed in the next section, the frequency shifts determine the output light's precise frequency used to cool or image the atoms. The AOMs for the DBR lasers, however lie within the laser locking path, and when the frequency of the AOM is changed, both the direction and amplitude of the outgoing

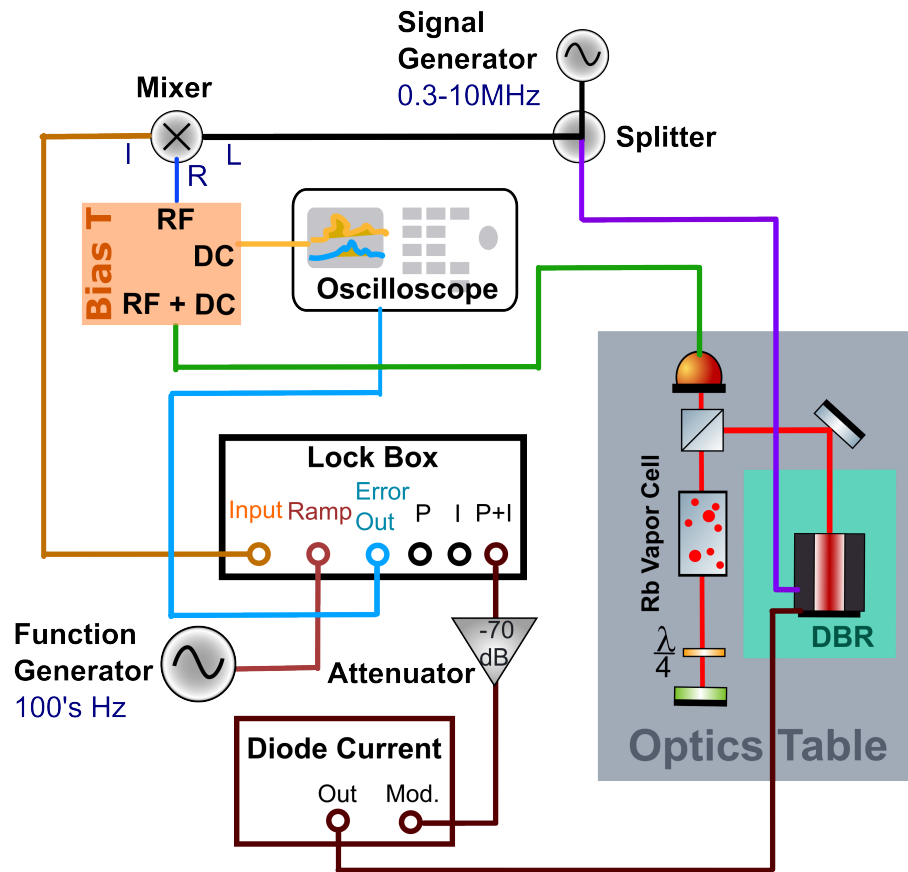


Figure 3.3: FM locking electronics circuit used to lock the DBR lasers used on the experiment. This circuit applies to both the cycling and repump DBR lasers and is used to stabilize the output frequency of the lasers.

beam is changed (see Figure 3.9 for optical layout). This inevitably changes the amount of light going to the saturation spectroscopy setup, effectively changing the error signal size (and offset to a smaller extent.) With appropriate gain settings, and a slow enough shift in the frequency, the DBR cycling laser can reliably follow the experimental cycle for the duration of the day. More details of the timing and size of the frequency shifts will be further discussed below.

### 3.1.3 MOT and Imaging Beams

As noted above, the diode lasers used in our experiment perform the initial stages of cooling and trapping for our rubidium atoms, and are used at the end of the cycle to image the atoms. The way we accomplish this is through a series of AOMs (mentioned above). As depicted in the level diagram shown below, the cycling transition ( $F = 2 \rightarrow F = 3$ ) is responsible for the initial cooling stage of the room temperature rubidium-87 atoms to the millikelvin range. This occurs in a process known as “Doppler cooling,” which originated in an Nobel-worthy advancement in the laser cooling of atoms [96]. Likewise, we use a simpler, though similar, locking scheme for the repump laser, which helps create a closed cooling system for our rubidium-87 system.

Rubidium is one of the easier atoms to cool because as an alkali atom, it is relatively simple to create a “closed” cooling system with two frequencies (the cycling and the repump, as mentioned previously). The cycling laser provides the

#### *Frequency Scanning of the Laser Detuning*

The so called “cycling laser” is called that as it is close in frequency to the “cycling” transition ( $F = 2 \rightarrow F' = 3$ , see Figure 3.4). This transition is used for both the main cooling mechanism in the first stage of the experiment (also known as the MOT phase). To cool and trap the most atoms we find a detuning of around -20 MHz to be the optimal detuning from the resonant, cycling transition. The second stage is used to further cool the lasers using a

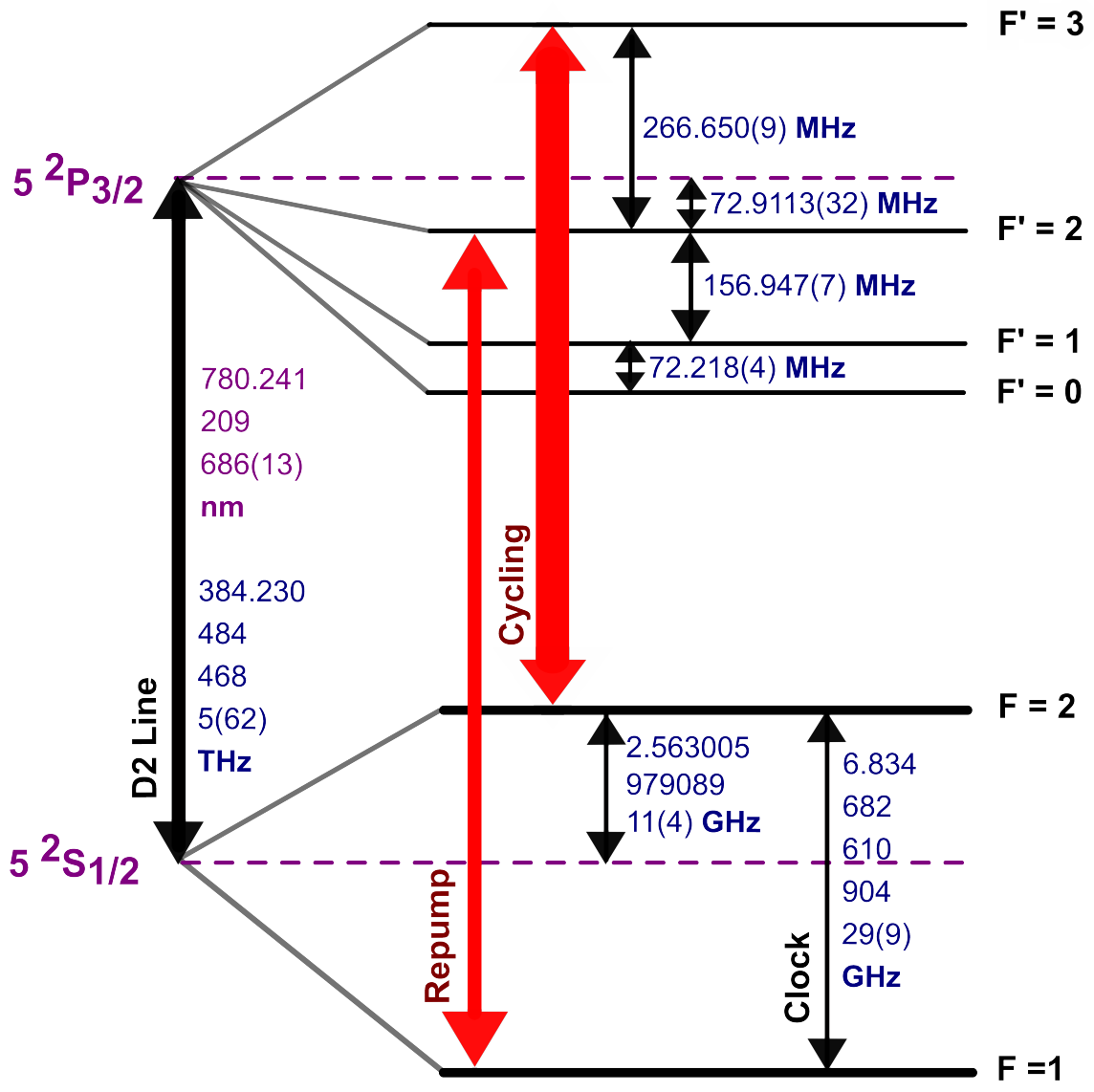


Figure 3.4: MOT Transitions in Rubidium-87

far-detuned, “dark” MOT setting, which is typically found to be optimal around -200 MHz from the cycling resonance. The final use of these lasers comes from In order to achieve a lockable laser capable of scanning over 200MHz, while staying locked, we use a series of AOMs and locking points to create a laser capable of reaching an on-resonance frequency.

We lock the cycling DBR laser, used for both the MOT and imaging light, to the “crossover” peak. This peak appears from the moving atoms that are resonant with either the incoming or reflected beam [95] and so produce a peak that lies between two resonant lines (here  $F = 2 \rightarrow F = 3'$  and  $F = 2 \rightarrow F' = 1$ ). The crossover we use is the “3-1” crossover, which is -211.8 MHz away from resonance. This peak is large enough to lock to and when combined with the available AOMs allow us to reach the cycling frequency. The locking point combined with the AOM shifts works out to:

Table 3.2: Frequency shifts for the cycling light used to generate the MOT and imaging light for the experiment. Shifts produced by a combination of the locking point and the shifts provided by various AOMs (depicted in optical outline below).

Frequency Shifts	MHz	Type
Lock Point	- 211.8	Fixed
Lock AOM	- 160	Fixed
Double Pass	+ (2x)(111.6 $\rightarrow$ 241.8)	Variable
Post-TA AOM	- 110	Fixed
<b>Net Shift</b>	<b>(-258.6 <math>\rightarrow</math> +1.8)</b>	<b>Range</b>

The range of output frequencies allows us to empirically optimize the frequencies for the MOT, dark MOT, and imaging stages. In the past, we could only scan up to a maximum of  $\sim$  -6 MHz. But when the new DBR lasers were installed, a 1.5x amplifier was added which allowed the control voltage from the computer (0-10 V output) to be increased. This allows a higher input to the voltage control oscillator (VCO), which changes the output of the AOM. In our case, the VCO-AOM driver circuit modulates the double-pass AOM, adding a variable frequency range to the output from this path. The plot of the net frequency shift is shown in Figure 3.5 for the new cycling DBR laser as a function of voltage input from the computer to the VCO. This however can be tricky, as the angle of deflection

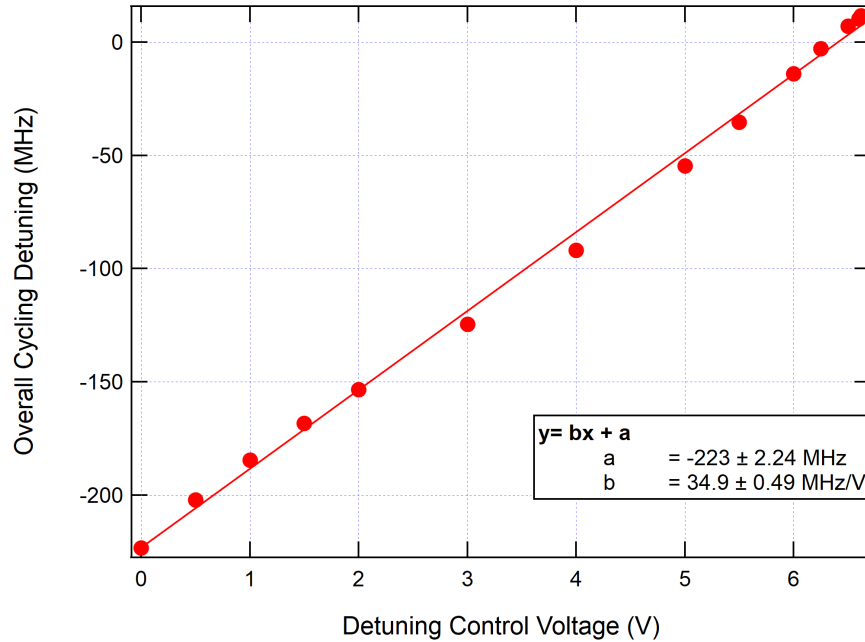


Figure 3.5: Net Frequency shift for the cycling DBR detuning as a function of experimental control voltage applied from the computer to the double pass AOM in the DBR cycling locking path. Shows wide tuning range used to tune between the dark MOT stages (around -200 MHz detuned) to imaging stages (around 0 MHz detuned) of the experiment.

of the frequency-shifted beam is dependent on the frequency. Thus, the amount of light downstream from the double pass AOM changes, changes due to the changing angle and efficiency for different frequencies.

For this reason, we try top optimize the double-pass AOM’s angle in the middle of the frequency range to ensure there isn’t a drastic change in the amount of light that makes its way to the saturation absorption setup used for locking. As a consequence, the saturation absorption spectra shifts by small amounts, due to the variable frequency settings, causing the error signal to have a slight DC offset and amplitude change. By using the appropriate locking settings (e.g. sufficient feedback, offset, etc.) and changing the detuning to be at a sufficiently slow rate (usually 20 - 40 ms for large detuning shifts), we can lock the cycling DBR laser for the entirety of the day without re-locking.

A similar procedure is done for the probe laser that is used in absorptive imaging of the BEC. It works by shining resonant light onto the condensate, which effectively gets totally

absorbed, creating a shadow of the cloud on the camera. In order for this to occur, the probe must be resonant with the cycling transition. To ensure this, we lock to the same transition as with the cycling DBR laser mentioned above (the (3,1) crossover, see Figure 3.6). The locking path also has a fixed -160 MHz AOM in it, as it was formerly the “master” or primary experimental cycling laser before we added the DBR lasers to the system. This gives a net detuning of around  $\sim -372$  MHz, before the light reaches the probe’s double-pass AOM. The frequency modulation of the AOM has a range of values it can be set to, but the exact frequency and strength of the modulation is determined quasi-empirically, as we look at the absorptive image. Usually this value is very close to the nominally expected value of  $186.0 \text{ MHz} \pm 0.1 \text{ MHz}$ . See Table 3.3 below for the summary of the frequency shifts for the probe laser.

Table 3.3: Frequency shifts for the probe produced by a combination of the locking point and the shifts provided by various AOMs (depicted in optical outline below).

Frequency Shifts	MHz	Type
Lock Point	- 211.8	Fixed
Lock AOM	- 160	Fixed
Double Pass	+ (2x)(186.0)	Set
<b>Net Shift</b>	+ 0.1	Set

The repump laser is simplest of all of the diode lasers, in terms of frequency shifts needed to make it resonant with the “repump” transition, as it only has one frequency shift involved. The repump laser itself is on resonance with the  $F = 1 \rightarrow F' = 2$  transition (see Figure 3.4). To achieve this, we lock the repump to the (2,1) crossover of the saturation absorption signal (see Figure 3.7). This proves to be a useful feature to lock to as it is one of the larger features on an already smaller signal (owing to the strength of the transition). It is also easily accessible with a fixed AOM shift of +80 MHz, as the crossover peak is located -80 MHz away from the true repump resonance.

A final function that our AOMs provide for all three of the lasers, is that the last AOMs in each of their respective paths have the ability to turn on and off with ns precision. This



Figure 3.6: Probe's scope trace of the saturation absorption signal (yellow) used to generate the error signal (blue) to lock the laser to a specific signal. Despite the noise seen on the trace, linewidth measured using heterodyne detection was measured to be within a few MHz [89].

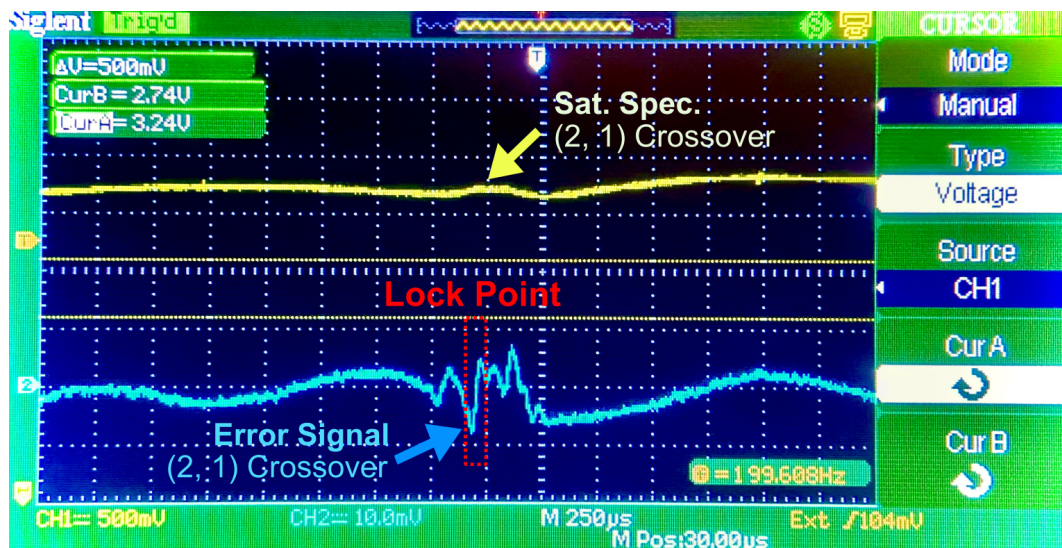


Figure 3.7: DBR Repump saturation absorption spectrum and error signal used to lock the repump laser on transition.

is used experimentally to turn on and off the lights on the experiment as needed. This and other features of the optical layouts for the diode lasers can be seen in the following section.

#### 3.1.4 Optical Layout

This section outlines schematics for the various diode lasers used on the experiment. For the last seven years or so, the optical setup for our experiment has been largely the same as we largely used the same types of diode lasers to provide the adequate powers and frequency stability the experiment requires. However, in the last couple of years, we have been testing out the use of a single high power DBR laser; this is as opposed to both a primary (master) ECDL laser for locking, and a secondary (slave) power laser that is seeded with the light from the primary. The light from the secondary laser would then become the seed light for the tapered amplifier (TA) which provides the high power amplification needed for the MOT.

Currently, we use a single DBR laser to replace the primary-secondary lasers system. Rather than completely scrap the lasers from the primary-secondary system, the optics were left in place and a nearly duplicate system was setup on a separate table for the DBR setup. In the previous system (shown in [89]), the primary ECDL was split off to send a portion of the light to both the injection path for the secondary laser and to a second path used to generate the probe beam used for absorption imaging. This was left in tact, and the layout is shown in Figure 3.8. The only addition to the former setup of the primary (master) ECDL is the addition of an extra path of variable power which we use for diagnostics of the laser to measure its frequency and linewidth.

The cycling DBR is composed of a high power diode which is capable of putting out 100's of mW. After testing the lock stability and laser linewidth, we switched from the primary-secondary diode laser system mentioned above. Other than that, the basic setup is identical in terms of the AOMs used. The main difference is that now the double pass AOM which was formerly located after the saturation absorption setup (used to generate the error

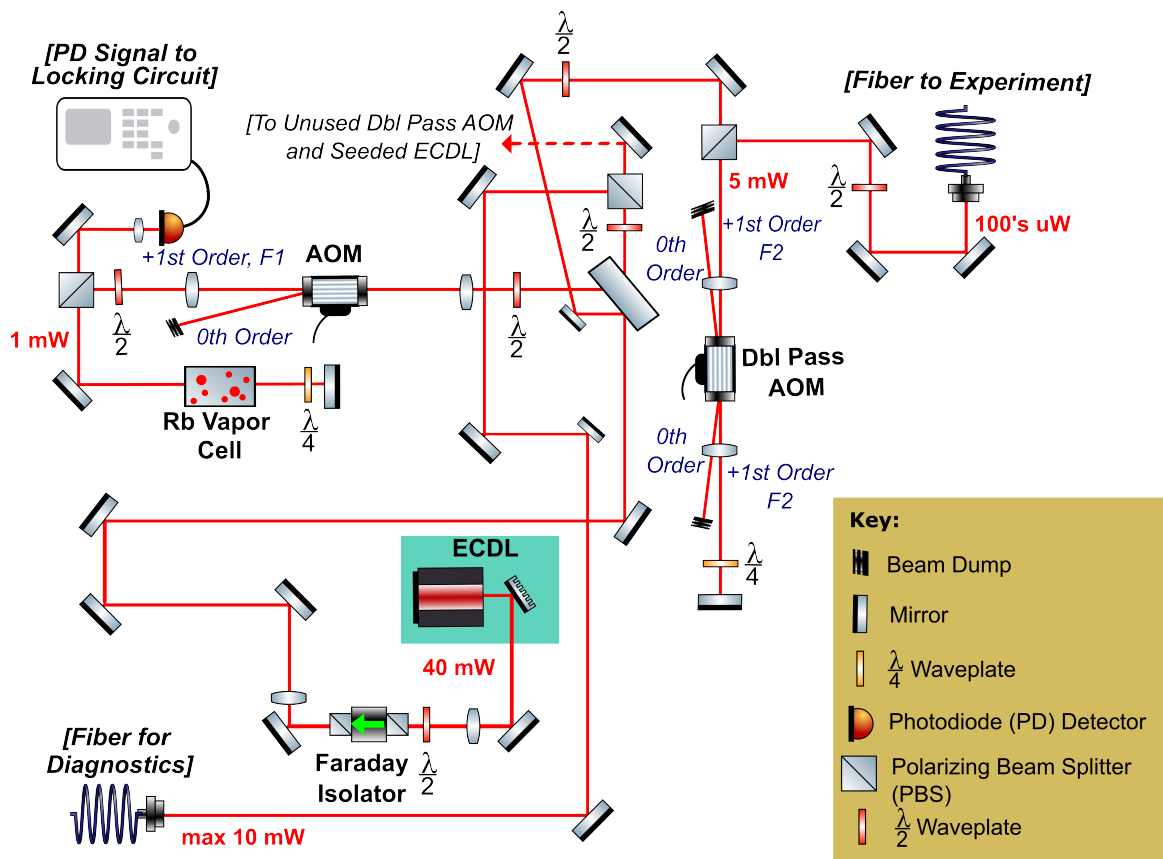


Figure 3.8: Probe Optical Layout

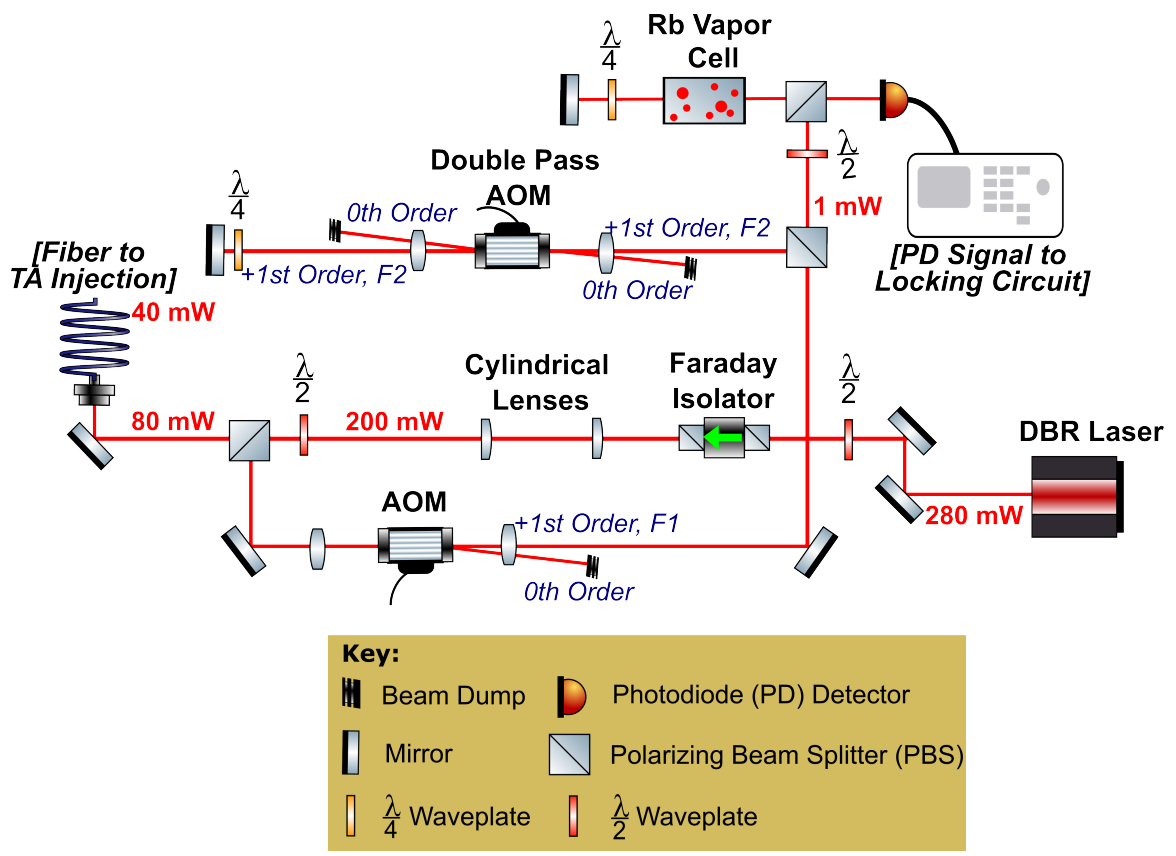


Figure 3.9: DBR Cycling Laser Optical Layout

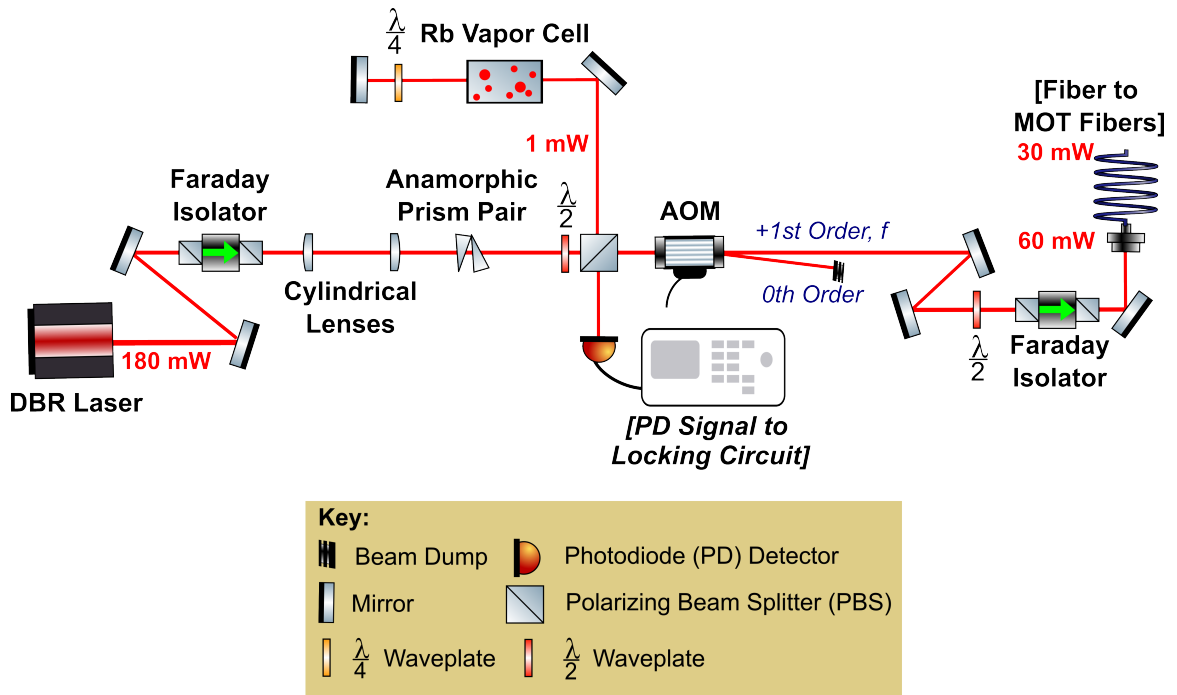


Figure 3.10: DBR Repump Laser Optical Layout

signal for locking), is now placed before it. Meaning the amount of light which reaches the locking path changes slightly in direction and magnitude, thus causing shifts in the error signal (as mentioned above). The layout for the cycling DBR is show in Figure 3.9. The output of the remaining laser light which is not used to generate the error signal is sent to the TA for amplification, providing enough light to send to the experiment to make a MOT and image the atoms.

The repump DBR layout, much like the cycling DBR, replaced the formerly used two-laser setup of a primary and injection-locked secondary diode laser. Many of the optics from the former setup were used to setup the repump DBR, as the testing for the repump had fewer constraints on the locking and dynamic frequency shifting needed. Just like the former repump layout, shown in [89], there is only one fixed AOM in the repump path which shifts the laser to be on resonance (as discussed above). The main difference in the former two-diode system and the current DBR system, is that now the light is input into a fiber where it is sent to the TA table to be coupled into the MOT fibers. An additional

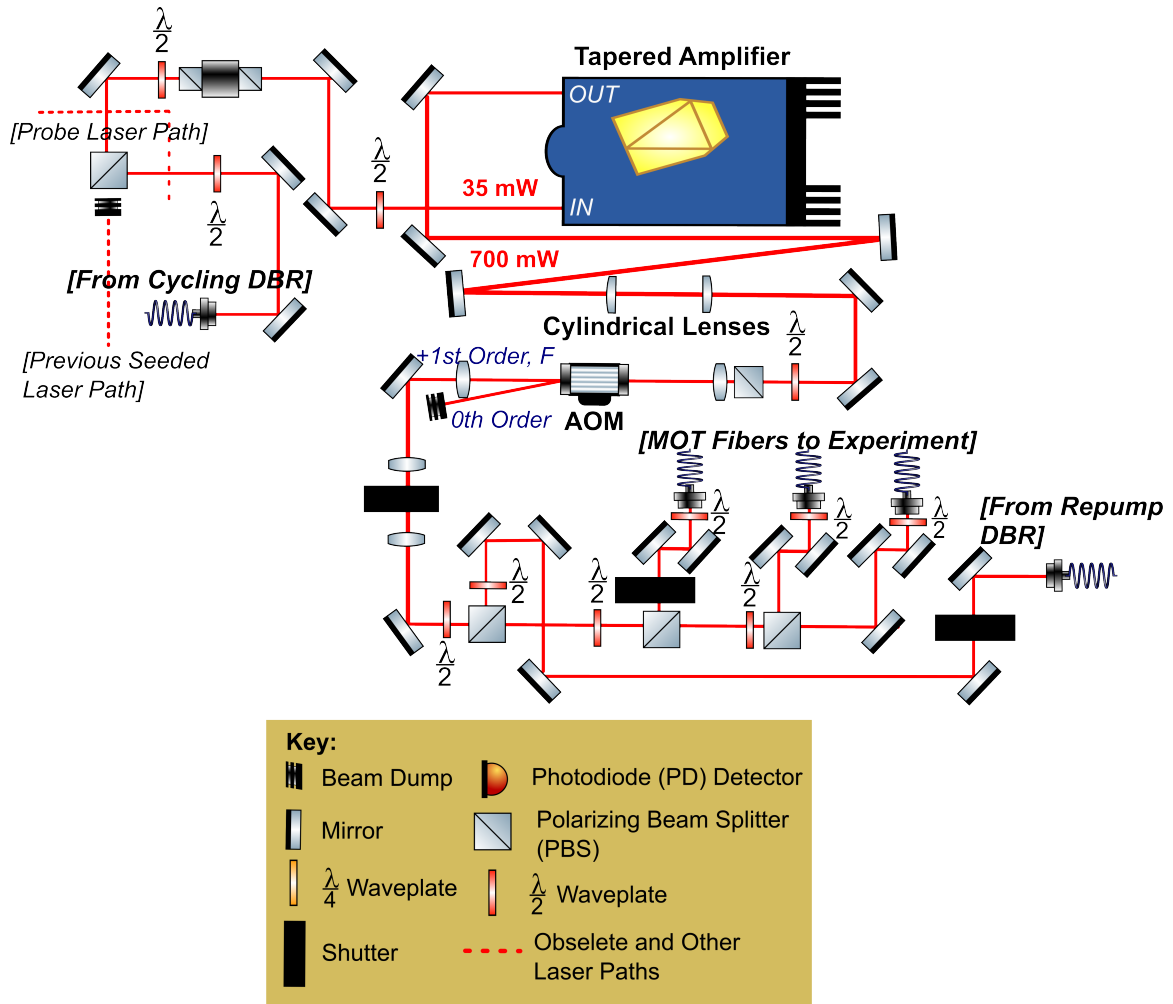


Figure 3.11: MOT and imaging optics that are used to send light to the experiment through optical fibers; seed light for the tapered amplifier (TA) and repump light come from the DBR lasers shown above.

isolator is placed in the path before the output to minimize any feedback that might enter the DBR repump diode from the fiber. Layout for the repump DBR system shown in Figure 3.10.

The final optics which prepare the MOT and imaging light from the DBRs to go to the experiment are shown in Figure 3.11. These optics are identical to those shown in [89]. The modifications to the system arise from the additional optics needed to bring in the light from the cycling and repump DBR lasers from fiber to the TA table and optics. As a precaution when putting in the DBR lasers, and not being sure of how the cycling DBR

scheme would perform, the fiber for this laser was added in situ and the former secondary (slave) laser and associated optics left in its place. They are still there, in the event that we might need some sort of backup lasers (should the DBRs fail or be out of use for a time). In the long-term, the DBRs could probably be moved to the TA table, avoiding the use of a fiber and the subsequent power loss through the fiber. Even more ambitiously, one could think about further changing the MOT and imaging light setup all together by by-passing the TA and using the light directly from the DBRs themselves. With the use of the high power DBR diodes, this makes this a more plausible proposition.

The repump optics are also the same, save for the introduction of a fiber coupler to bring in the DBR repump fiber from the other table. Both the cycling (after it has coupled into and amplified by the TA) and repump lights are combined on a cube a sent to the MOT fibers to the experiment. A table of typical powers from these fibers is shown below in Table 3.4.

Table 3.4: Typical powers as measured through the MOT fibers during the MOT loading stage. Same value is used for the imaging stage of the experiment.

Fiber	Cycling	Repump
MOT 1	42 mW	13 mW
MOT 2	42 mW	2.5 mW
MOT 3	43 mW	3 mW

### 3.2 Optical Trapping Lasers

Our experiment works on the principle that the atomic spins are free to interact with one another. This would not be possible in magnetic trap, typically used in traditional BEC experiments. Our group was the first to develop a way to achieve a BEC in an all-optical trap [31]. The heart of this apparatus focuses on our longest wavelength laser: the 10.6  $\mu\text{m}$  laser, or "CO<sub>2</sub>" laser. Traditionally used in metal cutting, this infrared, high power laser forms the main trap and evaporation potential for our condensate. Due to its tight focus we are able to efficiently evaporate the pre-cooled atoms in this trap alone to reach

condensation. Spin interactions in this “single beam” or “single focused” trap are dependent on the density of this trap. We can increase them by adding a second beam and increasing. We do so with a second-detuned trapping laser, the 850 nm diode laser. This configuration is known as the “crossed dipole trap” or “crossed trap.” These topics will be discussed further in subsection 4.2.2. Below will be shown the basic potentials for the traps and the optical layouts of the traps used in the experiment.

### 3.2.1 Trap Properties

Optical traps were first used to trap neutral atom in 1986 [97]. Since then, neutral atom traps have become an essential tool in atomic physics experiments. Also referred to as “dipole traps,” they operate by using the interaction of the dipole moment of the atom with the intensity of the light field. This interaction is given by:  $\vec{p} = \alpha \vec{E}$ , where  $\alpha$  is the complex frequency dependent atomic polarizability. The potential associated with this interaction is [92]:

$$U = -\langle \vec{p} \cdot \vec{E} \rangle = -\frac{1}{2} \langle \vec{p} \cdot \vec{E} \rangle = -\frac{1}{2\epsilon_0 c} \text{Re}(\alpha) I. \quad (3.1)$$

This is representative of the time-averaged potential, over one cycle of the light field, with light having intensity  $I$ .

From a Lorentz model of the damping ( $\Gamma$ ) due to the radiation loss from this atom-light interaction [92], the on-resonance  $\Gamma$  is estimated to be  $\Gamma = e^2 \omega_0^2 / 6\pi \epsilon_0 m_e c^3$ , where  $m_e$  is the mass of the electron and  $\omega_0$  is the cycling transition angular frequency. The potential and scattering rate, as a function of the angular frequency of the trapping light ( $\omega$ ), can be introduced to be [98, 92]:

$$U(r) = -\frac{3\pi c^2}{2\omega_0^2} \left( \frac{\Gamma}{\omega_0 - \omega} + \frac{\Gamma}{\omega_0 + \omega} \right) I(r) \quad (3.2)$$

and,

$$\Gamma_{sc} = \frac{3\pi c^2}{2\hbar \omega_0^3} \left( \frac{\omega}{\omega_0} \right)^3 \left( \frac{\Gamma}{\omega_0 - \omega} + \frac{\Gamma}{\omega_0 + \omega} \right)^2 I(r). \quad (3.3)$$

In the regimes that we are interested in, we can use the condition that  $\Delta = |\omega - \omega_0| \ll \omega_0$  to simplify Equation 3.2 and Equation 3.3 to:

$$U(r) = -\frac{3\pi c^2 \Gamma}{2\omega_0^2 \Delta} I(r) \quad (3.4)$$

and,

$$\Gamma_{sc} = \frac{3\pi c^2}{2\hbar\omega_0^3} \left(\frac{\Gamma}{\Delta}\right)^2 I(r) = -\frac{\Gamma}{\hbar\Delta} U(r). \quad (3.5)$$

This is known as the FORT (far off resonance trap) approximation. This is also the regime for our 850 nm trapping laser.

Our large and primary trapping laser is 10.6  $\mu\text{m}$ . In this regime, the relation  $\Delta = |\omega - \omega_0| \ll \omega_0$  is no longer valid, as  $\omega \ll \omega_0$ . This changes Equation 3.4 and Equation 3.5 to become:

$$U(r) \simeq -\frac{3\pi c^2 \Gamma}{\omega_0^4} I(r) = -\frac{\alpha_s}{2\epsilon_0 c} I(r) \quad (3.6)$$

and,

$$\Gamma_{sc} = \frac{2\Gamma}{\hbar\omega_0} \left(\frac{\omega}{\omega_0}\right)^3 U(r). \quad (3.7)$$

Here,  $\alpha_s = 6\pi\epsilon_0 c^3 \Gamma / \omega_0^4 = 5.3 \times 10^{-39} \text{ m}^2 \frac{C}{V}$ , and is the static polarizability of the rubidium atom. Because  $\omega \ll \omega_0$ , the single focused 10.6  $\mu\text{m}$  trap is essentially conservative based on the scattering estimation, making it especially useful in our studies.

Furthermore, the intensity in Equation 3.6 can be described as that of a focused Gaussian beam [92]. The transverse intensity of a TEM<sub>00</sub> Gaussian mode is:

$$I(x, y, z) = \frac{2P}{\pi w(z)^2} e^{-\frac{2(x^2+y^2)}{w(z)^2}}, \quad (3.8)$$

where  $w(z) = w_0 \sqrt{1 + \left(\frac{z}{z_R}\right)^2}$ .  $P$  is the power in watts of our single-focused trap, and  $z_R$  is the Rayleigh length,  $z_R = \pi w_0^2 / \lambda$  for wavelength  $\lambda$ . Referencing Equation 3.6, we insert the expression in Equation 3.8 for the intensity to obtain:

$$\begin{aligned}
U(x, y, z) &= -\frac{\alpha_s}{2\epsilon_0 c} I(x, y, z) \\
&= \left( \frac{1}{4\pi\epsilon_0} \right) \frac{4\alpha P}{cw(z)^2} e^{-\frac{2(x^2+y^2)}{w(z)^2}} \\
&= U_0 e^{-\frac{2(x^2+y^2)}{w(z)^2}}
\end{aligned} \tag{3.9}$$

where the trap depth,  $U_0$ , is defined as:

$$U_0 = \frac{1}{4\pi\epsilon_0} \frac{4\alpha}{cw_0^2} P. \tag{3.10}$$

This gives a useful relationship to relate the trap depth to the power in the laser beam for a given waist ( $w_0$ ).

### 3.2.2 CO<sub>2</sub> and Cross Trapping Lasers

The use of the “CO<sub>2</sub>,” or 10.6  $\mu\text{m}$ , laser is beneficial in many ways. In addition to the low scattering rate, the Rayleigh length ( $z_R$ , above) is quite small. This is useful for performing all-optical evaporation in, as we can tightly focus it. This is performed with the 38 mm lenses located at the entrance of where the CO<sub>2</sub> beam enters the vacuum chamber. This is then re-collimated at the output with a second 38 mm lens. Each is a zinc-selenide (ZnSe) lens capable of focusing infrared light and is discussed further in the next section.

This on its own is not sufficient to perform the full evaporation, as high densities are required to keep collisional rates high enough to allow evaporation to occur [93]. In order to do this a moving telescope is inserted into the 10.6  $\mu\text{m}$  trap earlier in the path (see Figure 3.12). The moving stage starts in a position that allows for the ODT trap to have the largest trap volume to encourage atoms to load from the MOT to the ODT with the greatest efficiency. Once the trap is loaded, the moving stage that contains one of the ZnSe lenses in the moving 1:1 telescope, begins to move. It takes around  $\sim 1$  second to nonlinearly move 10 mm. As this occurs, the power of the beam going to the telescope is

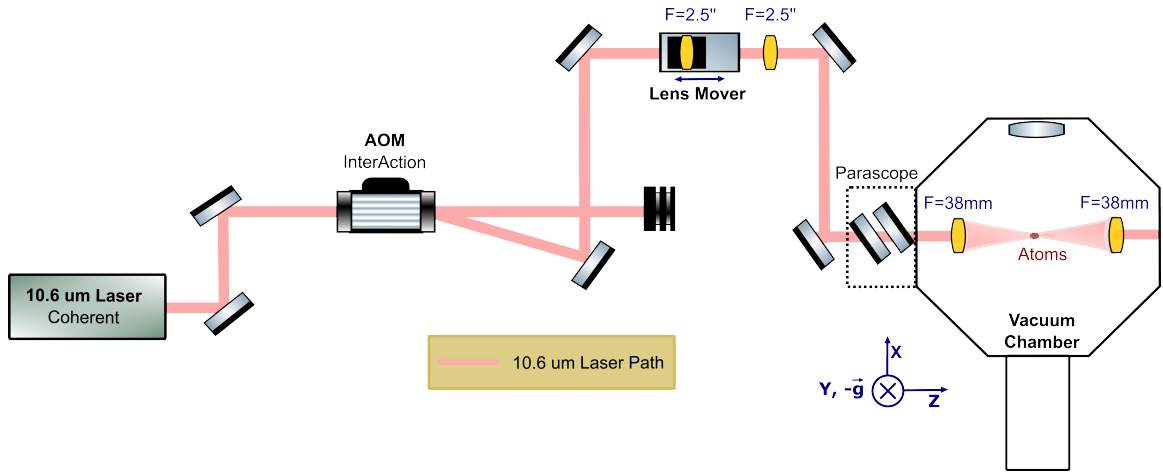


Figure 3.12: Optical layout for the 10.6  $\mu\text{m}$  trapping laser.

lowered. This creates a trap potential that is being lowered (according to Equation 3.10), but because of the moving telescope, the waist going to the chamber changes, creating an even tighter confinement. The minimum waist ( $w_0$ ) achieved in this configuration has been estimated to be around 25-30  $\mu\text{m}$ . This allows the atoms to continue to thermalize in the trap with the lowering power, while still maintaining sufficiently high density. The level of axial confinement from the laser is such that we can perform a full evaporation in the cigar-shaped, single focus trap.

The maximum power the laser (Coherent CX-10L) can output out of the laser head is around 165 W. With power losses however, the maximum power effectively going to the chamber (after the moving telescope and lens mover) is around 118 W. The power in the trap is lowered by changing the voltage that goes from the computer to the pre-amplifier (ZFL-100GH) to modify the RF power to it. The output is then sent to the  $\text{CO}_2$ 's AOM (InterAction) and amplifier (LZY-1). A switch (ZYSWA-2-50DR) allows the AOM (and thus beam going to the chamber) to be shut off quickly. This is used for time of flight applications and at the end of experimental cycles. By measuring the power after the AOM, as a function of computer voltage, we calibrate the computer voltage (RF power) to beam power in the deflected beam from the AOM. This function is input into our Labview program used to input the measured beam powers and fit them to a polynomial. The resulting calibration

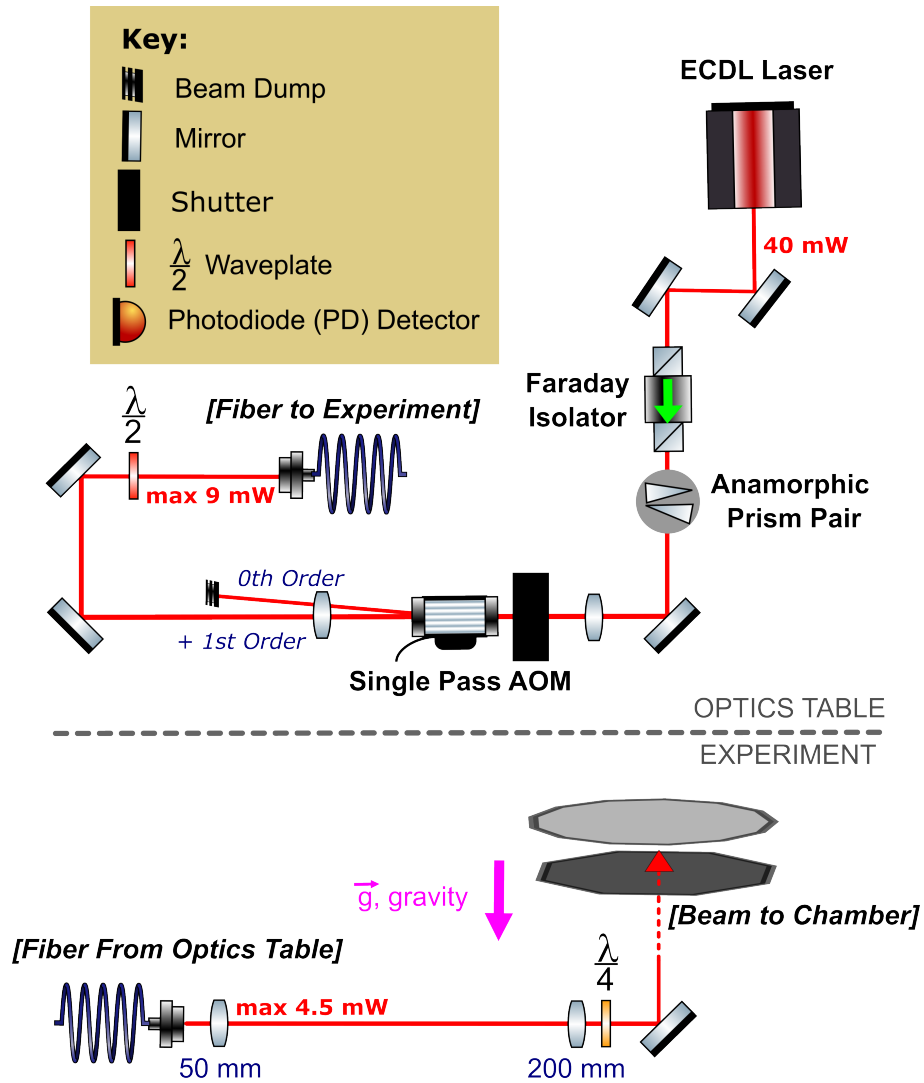


Figure 3.13: Crossed dipole trap layout

can then be used to output a laser power for a given computer input. The nominal values put into the computer range from 122 W to 18 mW, but have a voltage output that goes from 0-5 V [89]. When the trap power is lowered to perform the evaporation, it typically takes four to six seconds to go from loading ( $\sim 180$  W) to condensate ( $\sim 50$  mW). More will be said about this in the next section in discussing the experimental procedure.

The second trapping laser used in this setup is the 850 nm diode laser. Because the majority of the confinement is performed by the single focus trap, the second ODT is used to intersect with the CO<sub>2</sub> laser, once evaporation has occurred, forming a crossed trap

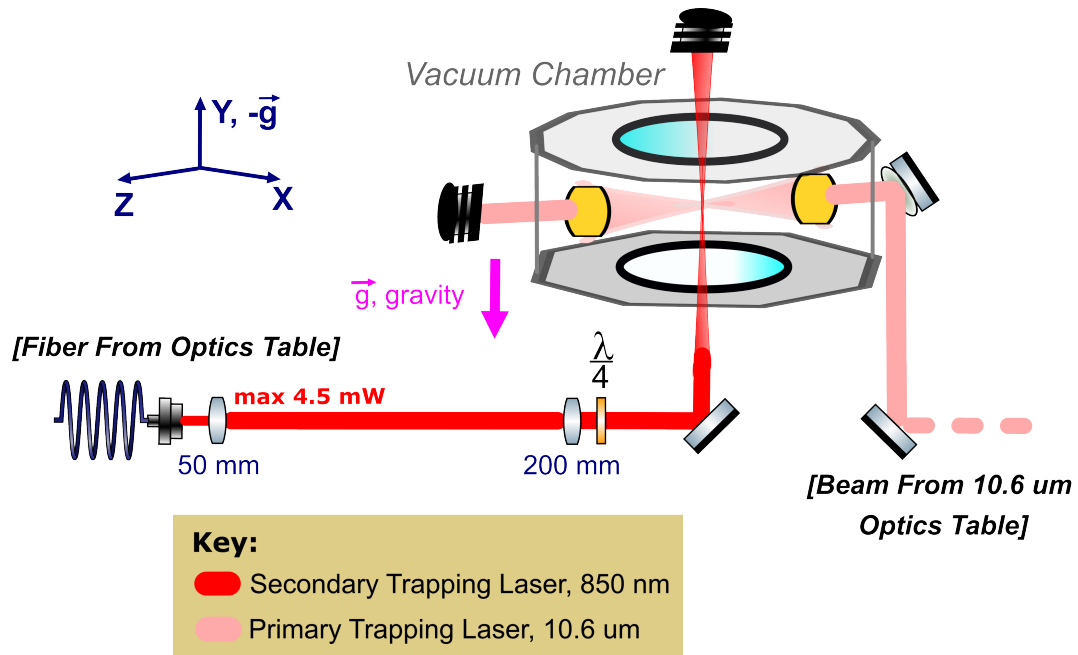


Figure 3.14: Schematic showing crossing of the 10.6  $\mu\text{m}$  laser and the secondary crossed trap 850 nm beam in the vacuum chamber. Waists are comparable for the trap making alignment very important for the condensate.

Figure 3.14. The 850 nm laser does not need much power for the aforementioned reason. The range of powers through the fiber to the experiment currently range from 0 to 4.5 mW. Its layout is shown in Figure 3.13. It is focused so that it has a waist that is around the same size of that of the single focused trap (the 10.6  $\mu\text{m}$  laser).

The single focus trap is aligned with the internal lenses on the chamber. We can do this by using a HeNe (helium-neon) laser which is made to overlap with the infrared, 10.6  $\mu\text{m}$  beam. This visible wavelength laser (not depicted in Figure 3.12) can then be safely aligned by eye with the ZnSe lenses for the different positions of the lens mover telescope. After this is done, the  $\text{CO}_2$  beam can be aligned using thermal paper at low power, and then thermal image plates (Macken Instruments) for intermediate powers. When the two trapping lasers are overlapped, the cigar trap becomes approximately spherical, providing even higher densities ( $\sim 2\text{-}4\times$  higher). This is achieved by moving the output of the 850 nm fiber beam coupler that is mounted on a translation stage. Equipped with micrometers, we can move the cross trap with fine precision to observe the cloud shape change in absorption

imaging. The change in aspect ratio of the cloud from vertical cigar to circular cloud for long times of flight, let us know our alignment is accurate. This can be further confirmed by measuring the density ( $|c|$ ) in the trap (see Figure 3.38).

### 3.3 Vacuum Chamber

One of the first and most fundamental parts of our apparatus is the ultrahigh vacuum (UHV) chamber where our rubidium atoms reside. A schematic of the vacuum chamber is shown in Figure 3.15. The pressure in the chamber is so low enough that the mean free path, the average length a particle could travel without colliding with another, is  $\approx 500$  km for a nitrogen molecule at room temperature. If you compare that with normal atmospheric pressure, where the mean free path becomes  $\approx 70$  nm, one can understand why lower pressure is necessary for us to study trapped rubidium atoms that would be free from spurious collisions with any background gas.

This pressure is achieved from a series of high vacuum techniques starting with good vacuum design (such as choosing vacuum-compatible materials and providing the largest amount of conductance needed to achieve the desired pressure), followed by a “bake out” achieved by pumping down on a chamber that has been heated up to the highest temperature allowed by the materials and vacuum parts. If the chamber is assembled correctly, the design is sound, and the bake out is sufficiently long enough, UHV is readily achieved and will last for the lifetime of the experiment or the experimental pumps attached to the chamber (such as an ion pump or NEG getter pump, etc.).

The current vacuum chamber Figure 3.15 consists of a Kimball Physics spherical octagon with two 6" conflat viewports on the top and bottom. These large glass viewports provide optical access and are anti-reflection (AR) coated for the 780 nm light. Likewise, eight 2.75" conflat flanges surround the sides of the chamber, and allow optical access for two of the three retro-reflected MOT beams, which occupy half of these viewports and are AR-coated. Two of the remaining four 2.75" viewports are used for both camera ac-

cess and probe beam access. Sometimes termed the "imaging access," these windows are across from each other. One end goes to the ANDOR iKon CCD camera which we use for all our imaging. The iKon window is AR-coated and also contains an in-vacuum, high aperture, aspheric lens (Thorlabs AL3026-B) which has an NA of 0.51 and focal length of 26mm. More can and will be said about the iKon and aspheric lens in the section discussing imaging below. Opposite this vacuum port is the one that goes to the pumping arm of the chamber which connects a tee-with a viewport for the probe laser used for absorption imaging and a smaller CMOS camera, called the Blackfly or FLIR camera, typically used to monitor the MOT. All will be discussed again in the later Imaging section. Finally, the last two viewports are made not from glass, as it is opaque to  $10.6 \mu\text{m}$  light, but from a single zinc-selenide (ZnSe) crystal. These are located along the axis where the  $10.6 \mu\text{m}$  trapping laser beam enters and exits the chamber. This axis is also naturally where the lenses for the large trapping laser are. The input lens is a 27.94 mm diameter, 38.1 mm effective focal length, aspheric lens from II-VI Infrared, Inc. The outgoing lens is a zinc-selenide meniscus lens from Thorlabs (LE7981-F). Each of the viewports and ZnSe lenses have anti-reflection coating for  $10.6 \mu\text{m}$ .

Our current BEC chamber was built in 2016, when it was found that the previous vacuum chamber was no longer operational. It was at that time that Matthew Boguslawski and Bharath H. M. began rebuilding and modifying what is now the current BEC chamber. This is the same design as shown in Figure 3.15. The layout is very similar to previous versions of the experiment, however some modifications were added to hopefully improve some of the issues seen in the earlier versions. One main problem that was observed was the proximity of the rubidium source (a SAES brand getter) to the  $10.6 \mu\text{m}$  lenses. Previous iterations would inadvertently leave a deposit of these atoms stuck to the surfaces of these lenses. Over time, this would build up and get burnt by the incoming high power  $10.6 \mu\text{m}$  laser beam causing the lenses to heat up. The new design puts the getter above the high numerical aspheric lens, further away from the  $10.6 \mu\text{m}$  ZnSe lenses to prevent this

rubidium build up.

Rounding out the tour of the vacuum chamber itself are several pumping ports and feed-throughs. The tee'd off section from the spherical octagon is where many of the pumping attachments are located. The initial 2.75" conflat tee has the wire feed-through for the getter where Near the top of the structure is an all-metal valve used to separate the chamber from the pumping station connected during the initial bakeout. This is where a pump could be hooked up again, should the need arise. Along this same 4.5" to 2.75" reducing conflat teem there are the titanium sublimation pump feed-throughs. This section provides a surface area for the titanium to stick to when the filaments are fired up at around 50A for a few minutes. This allows the newly sublimated titanium to effectively "pump" residual hydrogen in the chamber by capturing it as it sticks to it. This is particularly useful in UHV, stainless steel chambers, where usually the only residual gases are the harder to pump ones such as hydrogen. Connected to this is a 2.75" six-way conflat cross, which has both an ion gauge and an ion pump (Varian Starcell, 40 L/s). The ion pump is run continuously to pump on the chamber and its current is used to monitor the vacuum pressure, while the ion gauge is fired on occasionally when a more precise reading of the high vacuum is needed. When the newly-rebuilt chamber was put in place, pressure on the ion gauge read  $1 \times 10^{-10}$  Torr. This pressure has been confirmed recently and still remains the base pressure of the current BEC chamber.

### **3.4 Magnetic Coils**

The study of atomic spins, necessitates a precise control of the magnetic field. Our experiment uses six pairs of coils to accomplish (see schematic below of coil layouts on the experiment Figure 3.16). Using a series of procedures, we can apply fields from each of the coils to reliably cancel out any ambient magnetic fields, as well as apply an arbitrary bias field to manipulate the state of the atoms. Gradient fields allow us to initially trap and then separate the atoms for imaging. Below, I'll touch on some of the particulars of the coils

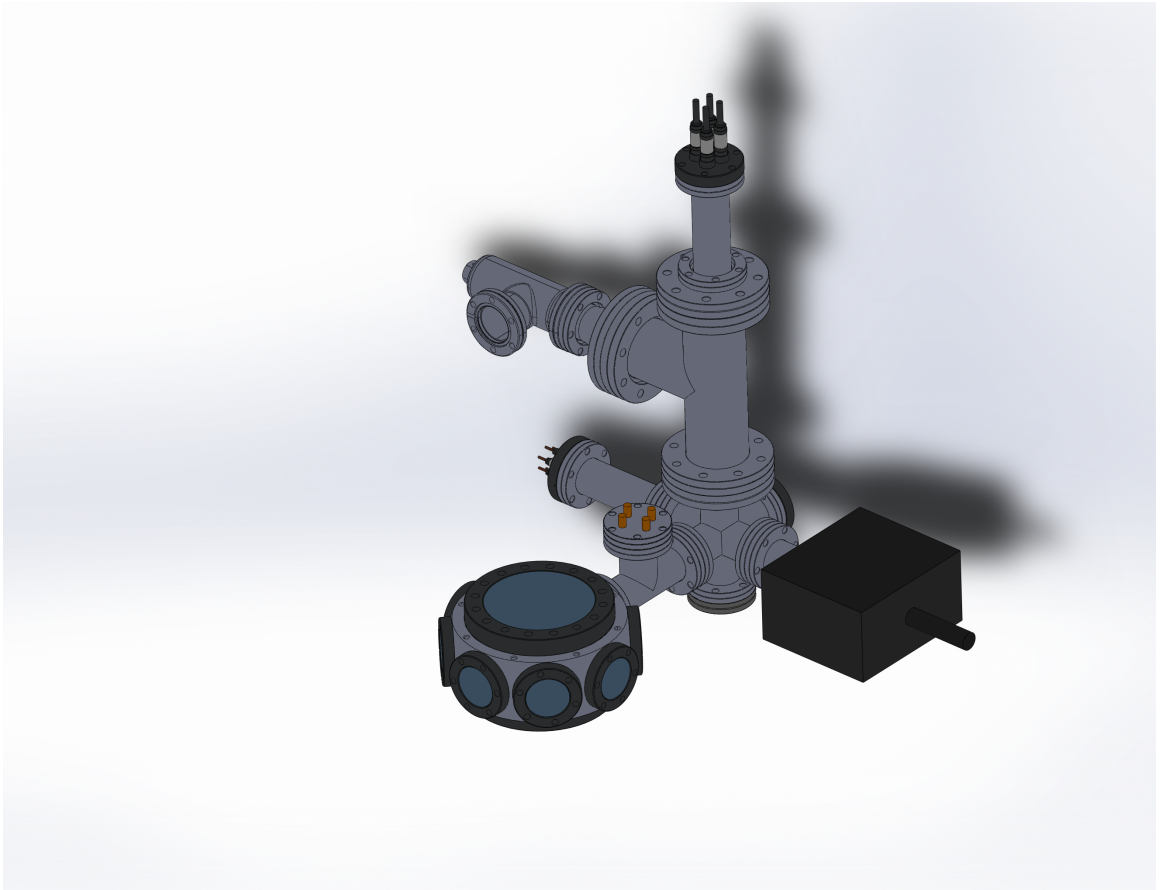


Figure 3.15: Schematic of current BEC experiment.

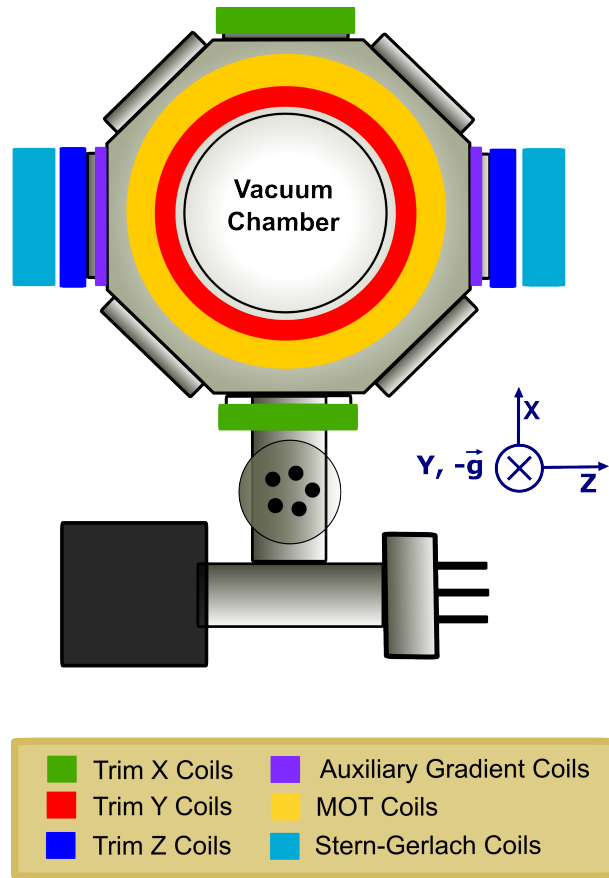


Figure 3.16: Schematic of coil layouts on the BEC experiment showing Helmholtz, bias field coils used to zero the field, as well as MOT gradient and Stern-Gerlach gradient coils used during the loading and imaging of the clouds, respectively. Auxiliary gradient coils also pictured and provide a small gradient offset to the magnetized chamber (more details in the Auxiliary Gradient section).

and describe their function.

### 3.4.1 MOT Coils

A pair of coils located along the vertical ( $\hat{y}$ ) direction, and above the large six inch view-ports of the vacuum chamber, are responsible for helping create the magneto-optical trap (MOT). As was described previously, the MOT is the initial cooling stage of the atoms as room-temperature atoms are cooled to  $\sim 1$  mK. In addition to the Doppler cooling described earlier, the MOT provides a restoring force to the atoms that creates a linear force to the atoms to push them to the center of the MOT. This is achieved from large MOT

coils which can provide a gradient of 10-20 mG/cm. The coils must also be in an anti-Helmholtz configuration, such that a quadrupole potential is created and there is zero field at the center of the trap.

We achieve this conditions with MOT coils made out of 1/4" hollow copper tubing. This allows us to water cool the coils with tap water from the building. There are nine turns per coil, which add up to give a total resistance of  $R_{tot} = R_{coils} + R_{leads} = 20 \text{ m}\Omega + 6.7 \text{ m}\Omega = 26.7 \text{ m}\Omega$  for both coils. In order to achieve a strong enough of gradient, we typically ran 113 A through the coils with the EMS supply, to get a calculated gradient of 13.5 G/cm. This was close to the peak current allowed from the supply. Recently however, we were able repair an older, higher power supply, which has the ability to increase this value, and thus the gradient. As of now however, there seems to be only small improvements for increases of the gradient MOT coil current; it plateaus after a small increase and is no longer optimal for the MOT loading.

### 3.4.2 Trim Coils

Three of these coils apply a bias field and are in a Helmholtz configuration. We call these the "trim" coils. They use smaller gauge wire and are closer to the chamber. These coils can be "zeroed" at the point where the atoms are at a field as low as  $\sim 1 \text{ mG}$ , by using the atoms themselves to measure the Larmor response to an applied magnetic field. We do this by applying a voltage to each of the trim coils, and sometimes a combination of the trim coils and measure the atom's response to that field (see Radio-Frequency section for more on this). The frequency with which the atoms respond to the applied field can be converted to give the magnetic field at the atoms. Doing this for a number of different points (usually around 10 or so) for all of the trim coil pairs, we can find the corresponding offsets to put in the control settings to "re-zero" what the zero field voltages for each coil pair is. The conversion from voltage to magnetic field is also calculated. This also gets put into the control parameters (talked about later in the Data Acquisition Section), and used

to apply a reliable bias field in any direction. The three main axes on the experiment that have these trim coils are geometrically orthogonal, as they are close to and in some cases wrapped onto the chamber. Trim X and Trim Y each have 15 turns per coil, while Trim Z has 90 turns per coil. Trim Z produces the largest field of the trim coils, and it helps define the quantization axis for the atoms, along with the  $10.6 \mu\text{m}$  trap beam.

### 3.4.3 Auxiliary Gradient Coils

The auxiliary gradient coils are a smaller but important gradient field. This pair of coils provides a small field which counteracts the permanent magnetization of the field along the  $\hat{z}$  axis (the axis where the  $10.6 \mu\text{m}$  laser enters and exits the chamber). The permanent magnetization of the chamber itself, which arises from the magnetization of the magnetic components created from the strong gradient applied by the Stern-Gerlach gradient coils, needs to be cancelled out. This extra, auxiliary gradient should be on during the state "interaction" or "preparation" time of the atoms (see sections below for more details). These are the times when the atoms have been purified into the polar ground state (see chapter 2 for details), and we are ready to either transfer atoms out of the  $|F = 1, m_F = 0\rangle$  sublevel or allow the state to evolve naturally via a magnetic quench (e.g. spin mixing, number squeezing, etc.). In the latter case, it is particularly important that there is no extra gradient to interfere with the evolution of the state during the interaction of the atoms, hence the application of an appropriate auxiliary gradient to eliminate the extra gradient.

In the past, we would zero the gradient by eye. Looking in absorption, one would either quench the magnetic field (with Trim Z) above and below the critical point of the condensate ( $q = 2|c|$ ) and allow the clouds to evolve for some time. When the clouds were separated during imaging with the Stern-Gerlach (SG) gradient, spin domains would be observed. A similar process was done by transferring atoms from  $|F = 1, m_F = 0\rangle$  to  $|F = 1, m_F = \pm 1\rangle$  such that all sub-levels have equal amounts, and then allow the state to interact for several 100 ms. The shape of the domains after either procedure would

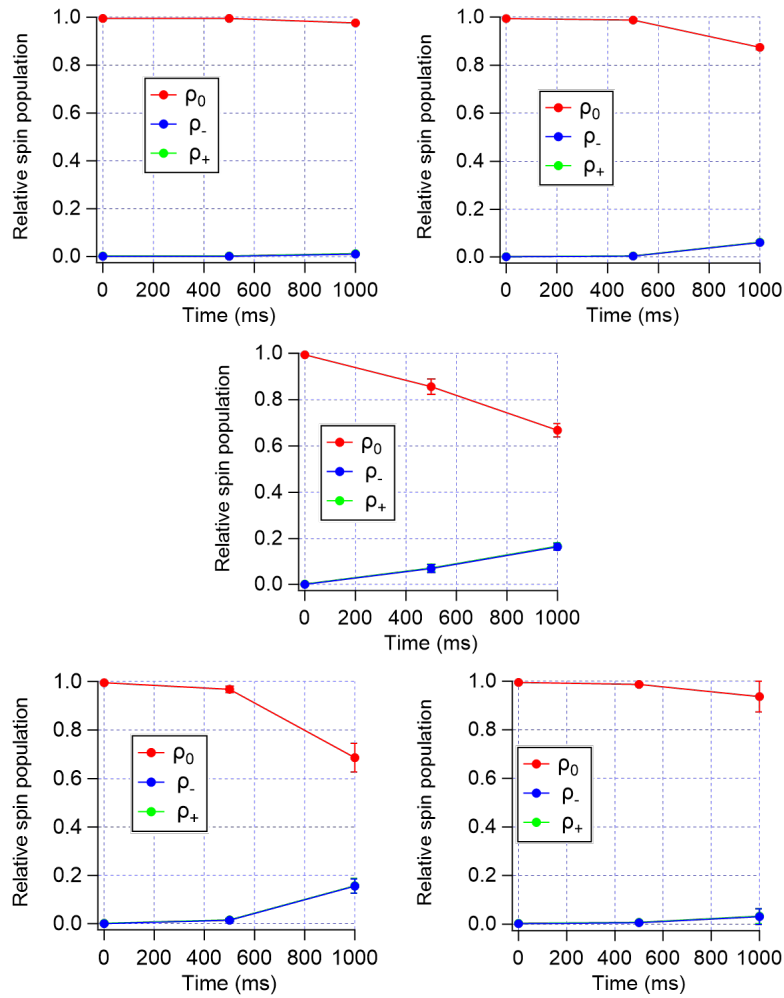


Figure 3.17: Amount of spin mixing observed in the primary ODT trap as a function of supplied voltage to the auxiliary gradient coils for one second of evolution time. One volt here corresponds to 250 mA. Fractional population in  $\rho_0$  shown in figure below. Moving clockwise from top left and ending bottom left, the voltage (and current) is increased. As can be seen when the auxiliary gradient is near the optimal value ( $\sim 5$  V), the degree of spin mixing is increased.

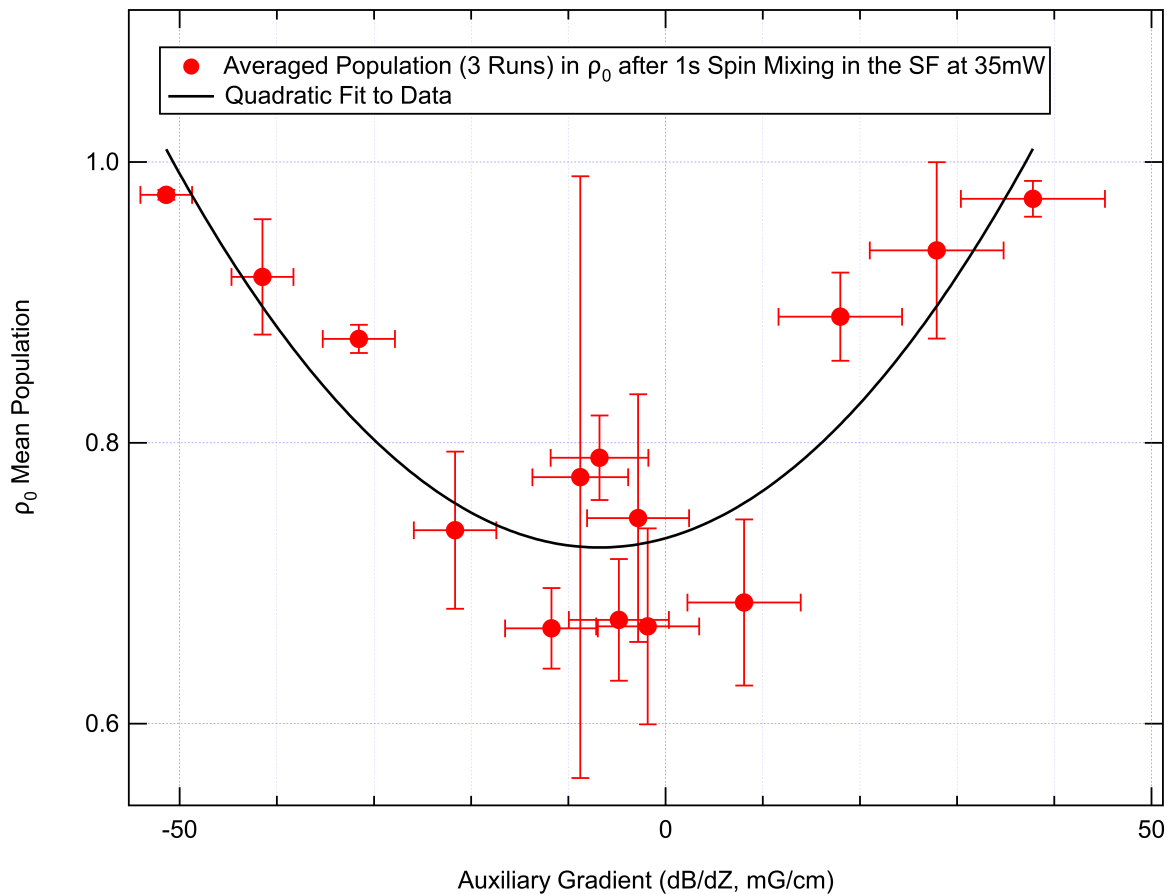


Figure 3.18: Plot of amount of evolution away from  $\rho_0 = 1$  (spin mixing) in the single focus,  $10.6 \mu\text{m}$  trap, after one second evolution. Shows a minimum value when the gradient is zeroed, indicating large degree of evolution from the initial state. This result was confirmed using the method described later in this section. The ability to see good spin mixing in the single focus trap seems to be due to the auxiliary gradient set to an appropriate value (i.e. when the auxiliary gradient cancels out the permanent gradient present in the experiment).

indicate whether or not the gradient was zeroed. If the clouds were facing outward, the auxiliary gradient would be in the same direction as the SG gradient. For example the  $|F = 1, m_F = -1\rangle$  sub-level for example, would be shaped like a backwards, capital letter “D”, while the  $|F = 1, m_F = +1\rangle$  would be shaped like a capital letter “D”. If the clouds are facing inward ( $|F = 1, m_F = -1\rangle$  looks like a capital “D” and  $|F = 1, m_F = +1\rangle$  like a backwards “D”), then the auxiliary gradient is in the opposite direction to that of the SG gradient. If no discern-able hard edges are observable, and the  $m = 0, \pm 1$  clouds just look like a bunch of lines of domains, this would indicate a near zeroing of the permanent gradient and the auxiliary gradient would be set to that value.

More recently, my contemporary graduate student, Lin Xin, thought of a way of zeroing the residual gradient by instead moving the atoms along the gradient axis and measuring the change in field. By adjusting the position of the second lens of the moving  $10.6 \mu\text{m}$  telescope, the condensate’s final position changes by a small amount. Applying a known field at various positions of the lens, one can measure the field at different points along the trap axis ( $\hat{z}$  axis). Doing this for different auxiliary gradient, a slope can be fit for the change in field as a change in position. Plotting the values of these slopes allows one to see when the change in field is unchanged as a function of position for a certain position of the lens, thus zeroing the auxiliary gradient with a greater precision. This has been performed on the experiment several times over the course of a year, and gave stable and consistent values for the auxiliary gradient. Most recent data for this measurement was performed by myself and is included in this thesis.

#### 3.4.4 Stern-Gerlach Gradient Coils

The Stern-Gerlach (SG) coils are experimentally important as they provide a gradient along the quantization ( $\hat{z}$  or  $\text{CO}_2$ ,  $10.6 \mu\text{m}$ ) axis. This is used in two ways on the experiment. The first comes from the “purification” stage of the cycle. At this stage, atoms are already loaded into the optical dipole trap and the evaporation stages have begun. While the trap power

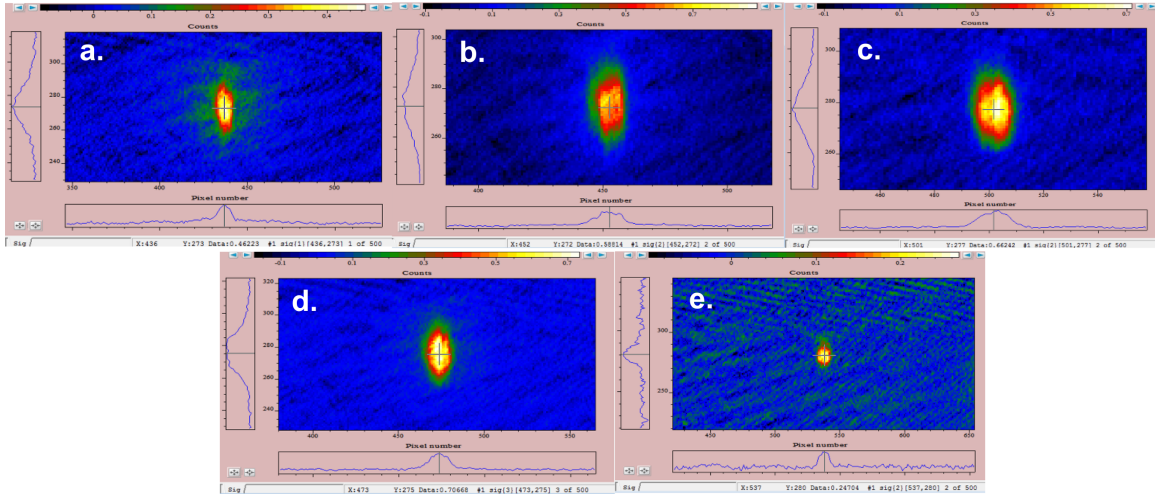


Figure 3.19: BEC cloud position as a function of second lens mover displacement distance. 10mm is the normal amount the lens mover (Newport LM3000) is programmed to move, and the location where we typically zero the ambient magnetic field with the trim coils. Different images are for different distances that the lens mover is displaced with a) at 10 mm, b) at 9 mm, c) at 8 mm, d) at 7 mm, and e) at 6 mm.

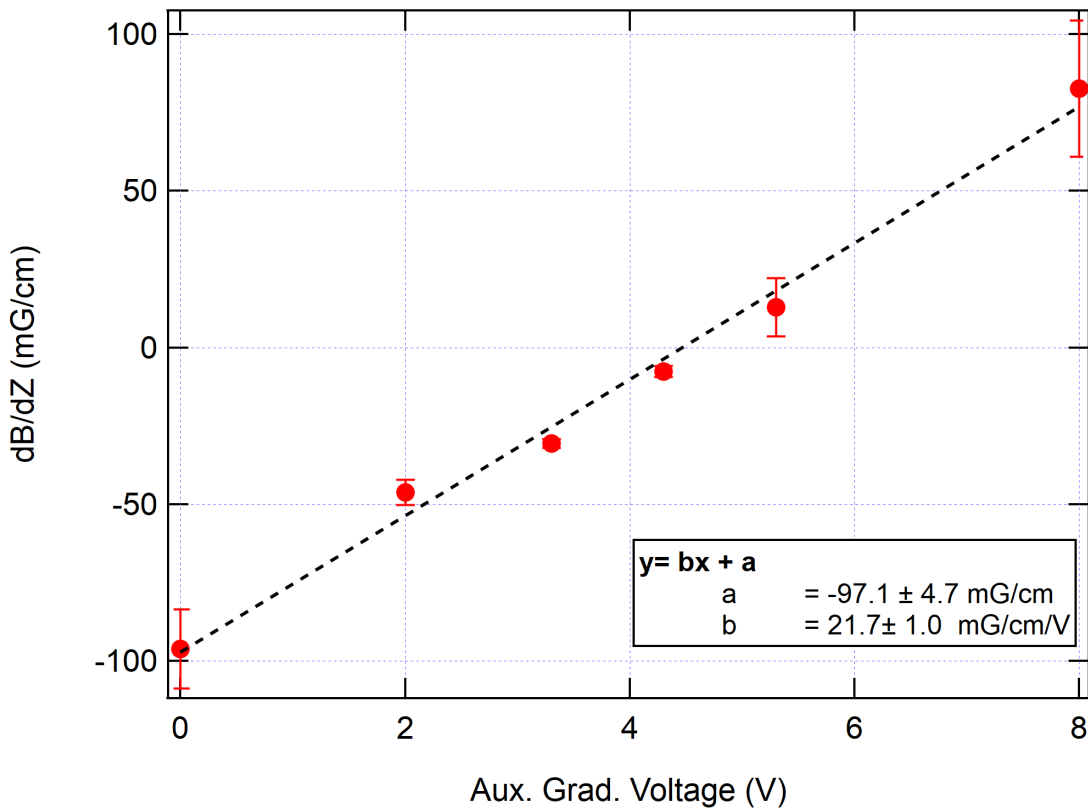


Figure 3.20: Auxiliary gradient fit to measured magnetic field gradients for different currents (here shown as a function of computer voltage) through the auxiliary coils. Result is consistent with previous measurements [91, 89].

(and depth) are dropping, the purification field is ejecting atoms from the  $m_F = \pm 1$  states. This leaves us with a cloud whose initial state is  $|F = 1, m_f = 0\rangle$ . This simplifies the experiment, as conservation of angular momentum applies, such that the magnetization,  $M$ , is defined to always equal 0. Thus, pairs that are created in later portions of the experiment through interactions, must be created in equal numbers in  $\pm 1$ . The gradient comes on at a moderate current (around 170 amps for around four seconds), and is turned off before the final stages of condensation.

The second key role of the SG or "gradient" coils is to apply a strong, short pulse to separate the final condensate for imaging with either fluorescence or absorption. This typically happens when the trap is shut off and released for free-fall to allow the condensate to expand. The longer we can apply a SG field, the further apart the clouds will be. There are a few limitations with that limit the SF pulse time however. As discussed in the section on imaging, allowing the condensate to fall for too long means it falls outside the range of the imaging optics for the camera. A comfortable upper bound for this time is around 22 ms. The second limitation revolves around turn on and off time. Ideally, we would like to image in a "zero-field" environment, as additional fields can create a magnetically-induced detuning from the resonant light, thus limiting the counting efficiency needed for accurate imaging. In order to ensure this we need to turn off the SG fields in a finite amount of time such that there is near-zero residual field from the SG coils. This pulse uses the maximum current available from the supply, for us around 460 amps.

Pulsing on and off for the SG coils is achieved using an IGBT (insulated-gate bipolar transistor). IGBT's are able turn on and off a large amount of current in less than one  $\mu$ s. While this does not matter much for the purification pulse, it is something we consider for the SG pulsing before imaging. The IGBT however, is not the main limitation for the SG pulse timing. The coils themselves have are natural inductors with a measured inductance of 72  $\mu$ H. The resistance for our current circuit is around 43 mOhms, with 35 mOhms being from the coils alone. This gives a natural decay time of around 1.7 ms (see Figure 3.21),

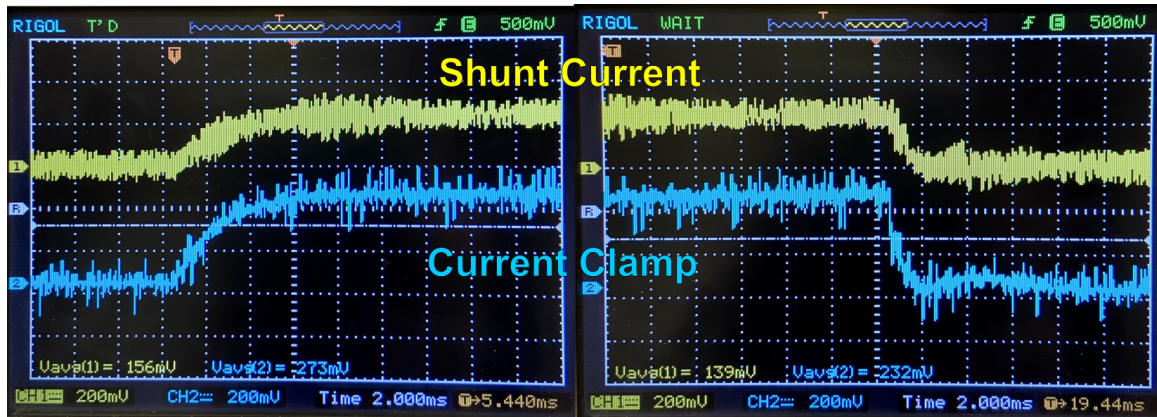


Figure 3.21: SG pulses taken with the new and current IGBT circuit as measured through a current clamp over the returning negative lead (blue), and the current measured through a shunt resistor (yellow).

meaning this is the minimum amount of time the circuit can turn on or turn off. This is taken into account by turning off the SG coils approximately 2 ms before imaging is to occur to insure any stray fields are extinguished by the time we image the atoms.

Previous and current versions of the IGBT and SG coil circuit are shown in Figure 3.22. The gradient coil circuit was updated when we received a new power supply and the old SG power supply had died circa February 2022. We wanted to develop a circuit that would prevent damage to the new supply, which we had at the time suspected might have contributed to the death of the old supply. (We later were told the old supply was repaired by repairing the four internal inverters which tend to die over time.) Modifications we made to the old circuit to include an additional varistor (S20K20) instead of one, and the removal of a flyback diode (1N4005). This was done as it was found that the varistors were the most effective at preventing large voltage spikes from reaching the IGBT and power supply, during the fast turn off of current for the SG pulse, but still allowed for a small voltage drop across them during normal operation. Two varistors were and are currently used, instead of one, as the voltage spike from the back EMF of the coils was quite large. In the future, we would like to improve this even further by adding varistors with higher voltage tolerances that can individually handle the potential back EMF. In the long term, there have been talks of using a similar but perhaps more robust solution with power MOSFETs. This has not

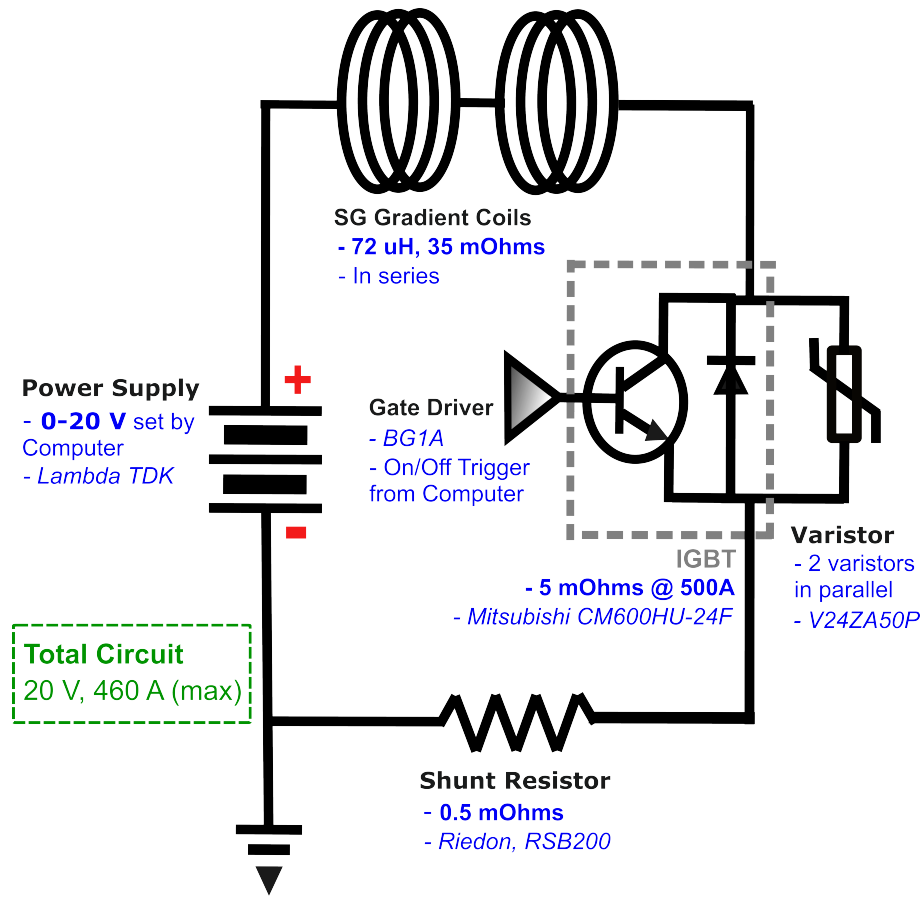


Figure 3.22: Schematic of current IGBT circuit on experiment that controls the SG pulses for imaging.

been looked into in depth, but is done in the neighboring Parker lab, and is a future project a student might want to look into.

The Stern-Gerlach gradient is important for our experiment as it allows us to separate the clouds into their magnetic sub-levels. The current separation for a 20 ms SG pulse at  $\sim 460$  amps is around 1.45 mm (see absorption image of cloud separation in Figure 3.23). Currently, there's a degeneracy between the  $|F = 1, m_f = 0, \pm 1\rangle$  and  $|F = 2, m_f = 0, \mp 1\rangle$ , as the  $F = 1$  and  $F = 2$  manifolds have differing signs for their Landé g-factors. For most of our purposes, this is okay, as we expect to be in the ground state  $F = 1$ , due to our efficient purification. However, imaging without the repump beam allows us to image the  $F = 2$  manifold. This is particularly useful for when we image the microwave population transfer from the clock state ( $|1, 0\rangle$  to  $|2, 0\rangle$ ).

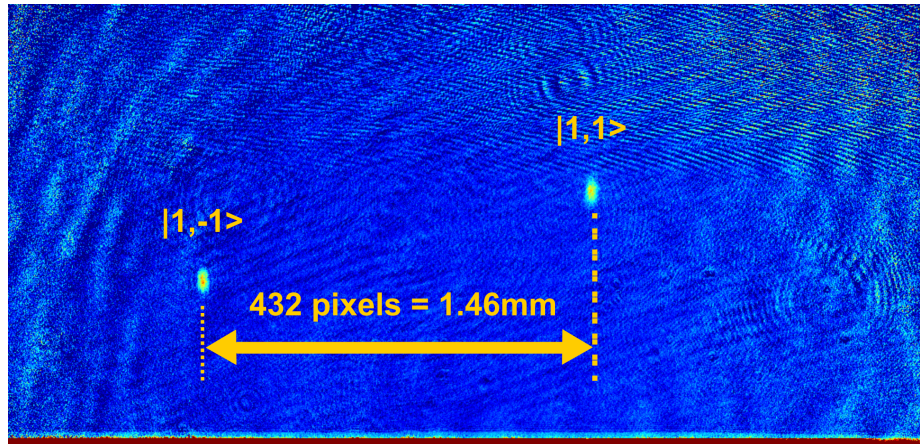


Figure 3.23: Cloud separation in absorption with new SG circuit at maximum current for 20 ms pulse time, and a 22 ms time of flight.

### 3.5 Control System

Our experiment runs off of two separate computers. One for data acquisition, and one for data analysis. The two are asynchronous, and must be manually initiated together to start and stop relevant data. This section outlines a basic overview of the experimental and data computers. The same basic setup has been in use for several generations of the lab. Updates and additions have been made organically over the years as devices or parts were replaced. I'll first talk about how the data is taken before touching on how we analyze it.

#### 3.5.1 Data Acquisition

Our control computer or data acquisition computer runs all of the controls for our experiment. This is done in Labview through the use of National Instrument (NI) cards. These cards provide a series of voltages at specific timings; the latter of which, originates from an editable Excel spreadsheet which outputs a table of values for each control channel. Labview reads in this table and uses it to operate the experimental channels. The timing resolution of these cards is  $10 \mu\text{s}$ . The cards are all synchronized by on a 60 Hz trigger from an AC line source. There are currently two analog cards used on the experiment ("A01" and "A02" boards). These have a voltage output of 0-10 V with eight BNC channels per card.

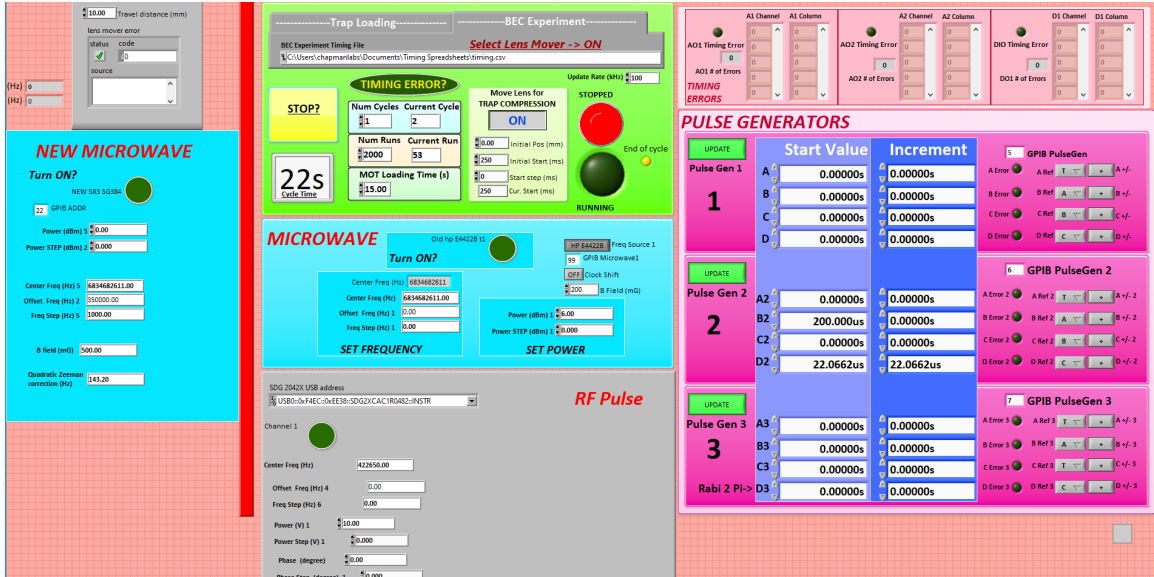


Figure 3.24: Labview front panel of control computer

A digital NI card has 24 BNC channels with either 0 or 5 V outputs, used mainly as trigger pulses for various switches, shutters, etc. In addition to these three cards, one is used to control the GPIB devices in the lab. This involves the microwave sources, the pulse generators, and the lens mover. The GPIB devices are slower than the desired pulses needed on the experiment, so their settings are updated in the Labview front panel and applied before the experimental run. The main labview also contains several special subVIs which operate the CO<sub>2</sub> power ramp parameters (as discussed in subsection 3.2.1), the microwave and RF generators, and the lens mover.

### Common Errors

As the system gets older, there are several types of errors which have seemed to appear as the most likely reason for the experiment to stop cycling and have issues running. The first type, is caused by a lack of connection with the “A01” analog NI card. This can occur when there has been a power outage and the PCI chassis for the NI cards has not been shutdown properly. Another cause of this disconnection can arise from moving any of the direct or adjacent cables attaching the AO1 BNC’s to the AO1 board in the PCI chassis.

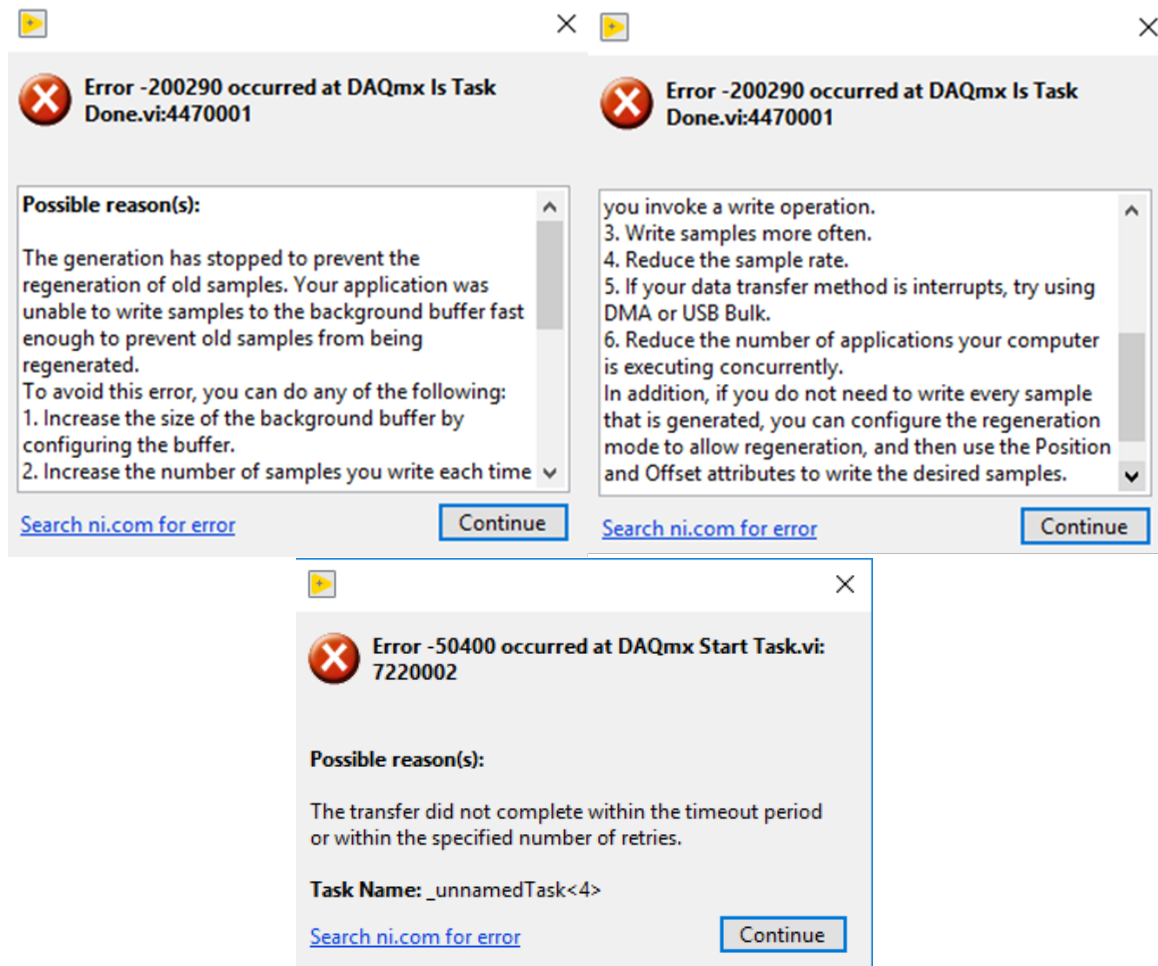


Figure 3.25: Since AO1 board controls and receives the timing signal from the computer, a failed connection to the chassis often can produce varied error, such as the ones shown. These are easily fixed by reestablishing the physical AO1 board connection and power cycling the chassis.

Some example errors that can appear are shown in Figure 3.25. A disconnection from the AO1 board will stop the whole Labview, as the VI (program type for Labview) will not be able to initialize the AO1 board. The AO1 board is special because it is the lead board in the daisy-chain of connections for the other PCI boards (AO1, AO2, and Digital boards), and is the one the program will use to initialize and execute timings when trying to execute the csv timing table for all the channels. If a response is seen from the AO1 board (BNCs output correct voltages when changed), then the board is connected and shouldn't be the issue the VI isn't running.

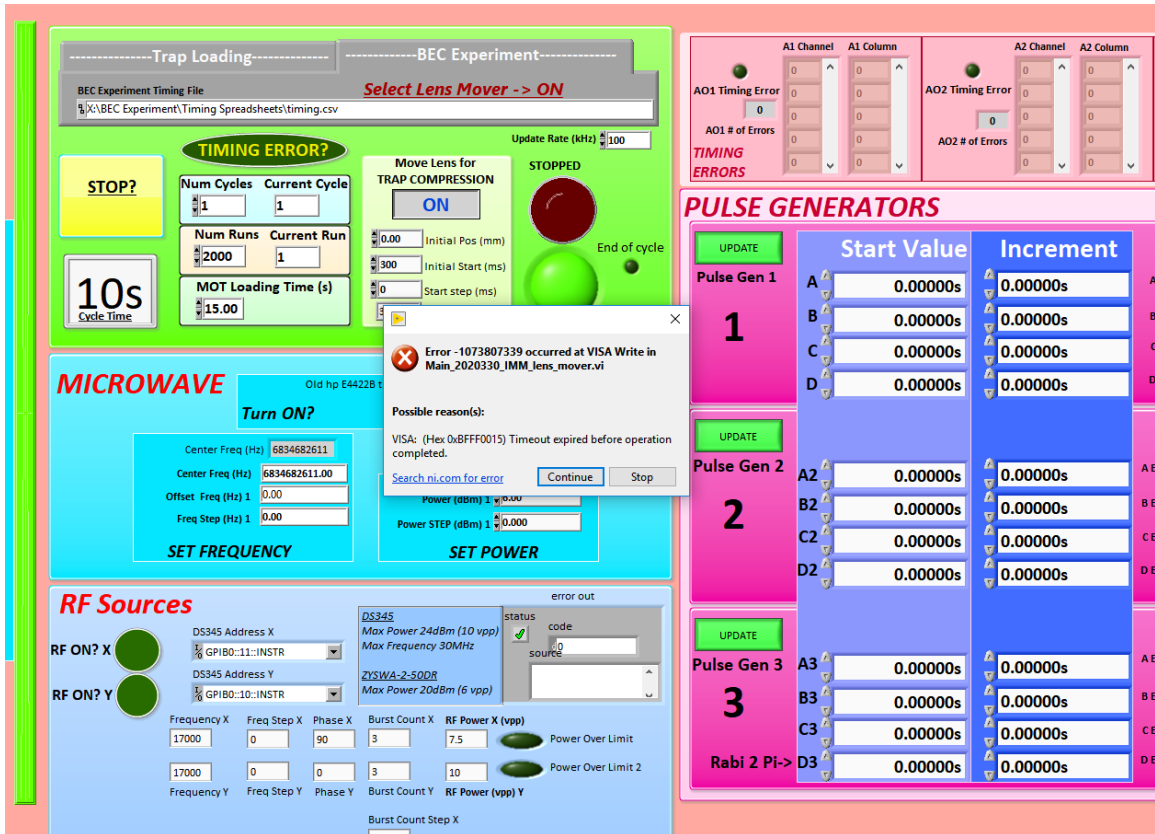


Figure 3.26: Demonstration of lens mover error, which is a very common, though not frequent problem on the experiment. It is caused by the age of the current lens mover and lack of local memory, that from time to time fails to store the settings that Labview sends to it.

Another common error encountered in running the experiment pertains to the lens mover. Because of the age of the linear motor stage for the moving 1:1 telescope, used to compress the  $10.6 \mu\text{m}$  trap, it struggles at times to "write" the requested setting to the local memory of the device. This will allow the experiment to run, but will produce an error when the program tries to initialize the lens mover (after MOT loading), forcing one to stop the experiment. The message presented by the computer is shown in Figure 3.26. This error can usually be easily cleared by turning off the lens mover linear stage driver, clearing the error messages, and resetting the GPIB address (to 26).

This isn't a long term solution. Ideally, we'd be able to replace the old motor with a newer one. We tried to do this last year, but were unsuccessful as the linear stage was not

compatible with our stage type. The Labview sub-VI did work however, so we would need to only replace the motor with one that is compatible for our moving stage. This remains a task for future work.

### 3.5.2 Data Analysis

As mentioned above, our two computers are asynchronous and must be manually synced by starting the data analysis computer after the settings have been input into the data acquisition computer and the run starts. The data analysis computer controls the cameras for the experiment. When these are triggered to take images, usually from a digital signal from the control computer, an image is taken with either the iKon, iXon ("Top camera," or FLIR (see discussions on imaging section 3.6). The iKon and iXon camera are a CCD camera from ANDOR. ANDOR comes with its own programming language. Historically, we relied on the programs we wrote to do more of the reporting of the number of atoms in each region, in addition to controlling the camera settings. Currently, the ANDOR programs are used primarily to produce the images during acquisition, perform basic background subtraction, and create a text file which lists the number of images in a run (more on this later). The program used for absorption is a little more complicated as it converts the camera counts from several images to make a composite image in units of "optical depth" (see section 3.6 below). The third camera, a BlackFly USB 3.0 by FLIR, is used to image the MOT and early stages of the evaporation ramp. It has the ability to run triggered or untriggered, making useful especially to measure the MOT loading during a normal experimental run.

Once we obtain the desired images from the camera(s), they can be imported into a software program called IGOR for analysis. Various IGORs are used for different cameras. The standard form of the IGOR programs uses the imaging parameters from the camera (pixel number, binning, etc.), and reads in the images from the designated folder where the aforementioned text file, denoting the number of images taken, resides. If the number of images is greater than zero, but less than the number requested (e.g. 20), the IGOR

program will continue to import images from the specified folder until the number (here, 20) is reached. Thus, there exists the opportunity to re-import old images and analyze data that is not being actively taken by the experiment. Since the IGOR has no knowledge of the experimental settings or operations being performed, the user must be aware of what parameters are being measured or used to input them into IGOR correctly when plotting or measuring various runs. Some of the standard operations programmed into the IGOR include spectrum and rate measurements for the microwave and RF, as well as statistical measurements used for RF calibration and noise measurements.

## **3.6 Imaging**

### 3.6.1 Imaging Optics and Masks

We rely on two primary, standard atomic physics techniques to image the state of our BEC: fluorescence and absorptive imaging. These measurements involve a form of projective measurement in which the Zeeman sublevels are separated and counted, giving information on the state of the condensate. Clouds are separated by magnetic sublevel using the Stern-Gerlach coils discussed above. Based on the imaging technique used, there are advantages and disadvantages to either method, and at times they are useful for different types of measurements. These will be laid out below in brief, but can be found more explicitly in the thesis of Eva Bookjans [99]. There will also be a discussion of how noise estimates are made for our imaging system. These noise calculations play an important role in how we take data, and also in our estimate of the noise limits of our system which dictate the minimum number of atoms we are able to image.

### 3.6.2 Fluorescence Imaging

Fluorescence imaging relies on scattering and collection of scattered light of the atoms. This requires near-resonant light at sufficiently high intensities to saturate the cycling D2 ( $F = 2 \rightarrow F = 3'$ ) transition. This condition, when met, creates a maximal value of

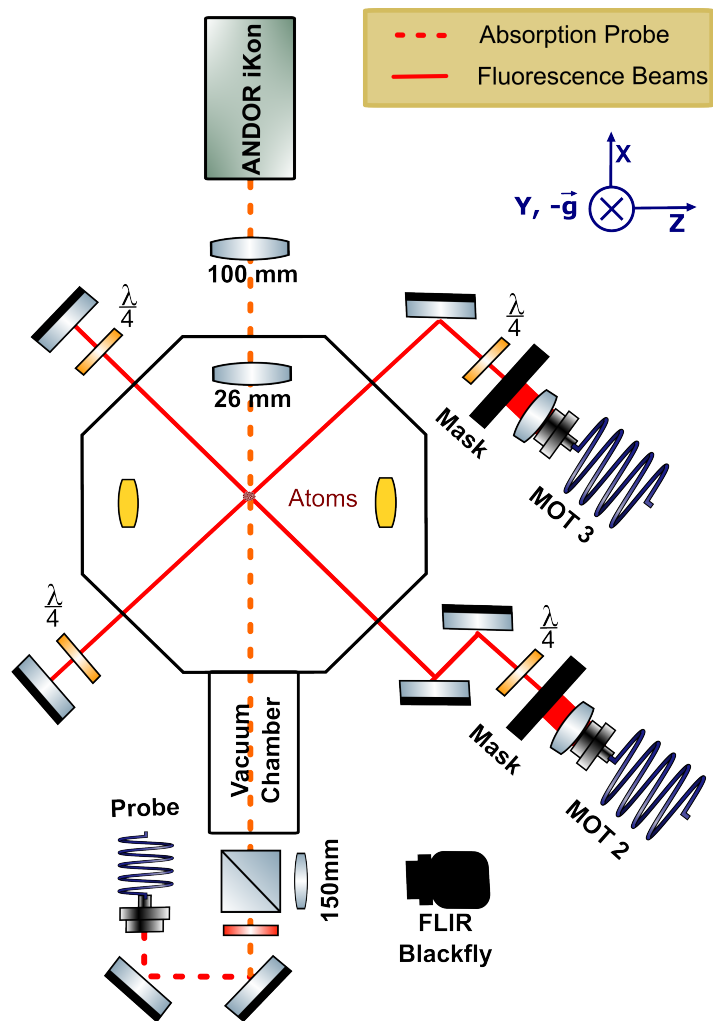


Figure 3.27: Top down view of BEC experiment and the imaging beam layout and setup. Probe beam for absorption imaging is denoted by red dashed line.

$\Gamma/2 = (2\pi * 6.065 \text{ MHz})/2 = 19.1 \text{ MHz}$ , where  $\Gamma = 1/\gamma$ , with  $\gamma$  being the natural lifetime of the transition [100]. More will be discussed in the following sections about the calculation for the CPA and the amount of light scattered.

The same beams used to create the MOT are the same beams used to illuminate the condensate while imaging. Instead of using the full size of the beams though for imaging, a homemade, pneumatic aperture is used to restrict the size of the beams from a one inch circle to a  $\sim 2 \times 2 \text{ mm}$  square. This leaves the intensity of the beams the same, but minimizes the scatter off of the internal optics of the chamber. In this masked configuration, only the horizontal beams are used for imaging, with the vertical beam being blocked by a separate shutter. A quantitative analysis of the noise from the masked, scattering beams is presented later in this section.

The beams are also tuned from the dark MOT detuning ( $\sim -170 \text{ MHz}$ ), to the imaging detuning ( $\sim -2 \text{ MHz}$ ). Before we installed the DBR lasers on the BEC experiment, the lasers locking scheme we used required a series of AOMs to bring us close to resonance for imaging. However, this only brought us to  $\sim -7 \text{ MHz}$  (see subsection 3.1.3 above). The possible effects of this are discussed quantitatively below. The amount of light scattered depends on this detuning, and thus affects the light available for collection for the fluorescence measurement.

The amount of light received by the camera is affected by the camera collection optics. The numerical aperture (NA) provided from aspheric lens inside the vacuum chamber (see Figure 3.28), provides a technically-specified NA of 0.51. This factors into the way we calculate the numbers of atoms in our system. In a simple estimate, the amount of light collected is given by a calculation for what we call the "counts per atom." This is done to estimate the amount of light we expect to collect and register on our camera, from the scattered light from the atoms. This naturally depends on the fractional solid angle of light we can collect optically ( $\Omega$ ), the camera specifications and efficiency ( $\eta$ ), the rate of scattering of light from the atoms ( $\Gamma/2$ ), and the time we expose the atoms to the resonant

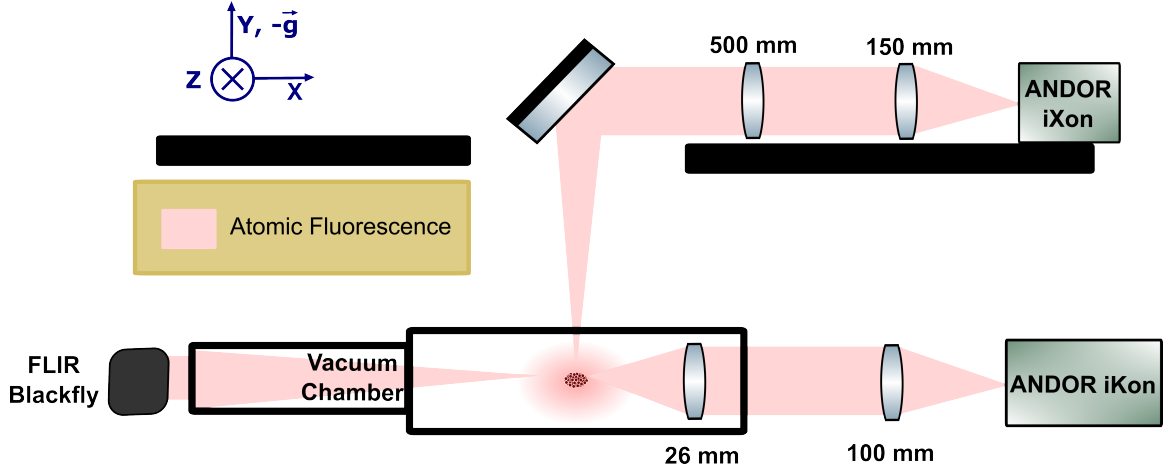


Figure 3.28: Schematic of BEC fluorescence imaging setup depicting three sources of fluorescence imaging using the iKon, iXon and FLIR cameras. Not all are useful at all stages of the experiment, as the cloud location and size changes within the experimental cycle.

light ( $\tau$ ). This gives the equation:

$$CPA = \left(\frac{\Gamma}{2}\right) \Omega \eta \tau. \quad (3.11)$$

It's from this we can estimate the conversion of the number of collected photons to the number of atoms detected. Here the solid angle,  $\Omega$ , is related to the limiting numerical aperture of our system when imaging with the iKon camera, for the aspheric imaging lens mentioned above. This is represented by the relation  $\Omega = \frac{(NA)^2}{4} = \frac{(0.51)^2}{4} = 0.065$ . Using the iKon camera settings and specifications for detecting light at 780 nm, we find an overall camera efficiency of  $\eta = (\text{quantum efficiency})/(\text{gain}) = (0.91 * 0.77)/1 = 0.693$ , where 0.91 is the specified quantum efficiency for 780nm light for the camera; 0.77 comes from the 780nm line filter placed in front of the camera to eliminate non-780nm light from entering the camera, and 1 is the specified gain for the iKon camera given the imaging settings (rate and internal preamplifier settings). Naturally, these numbers would change for different cameras and imaging optics (see subsection 3.6.4 below). The value of  $\Gamma/2$  as mentioned above is 19.1 MHz. This value is well defined for imaging light intensities well above the saturation intensity for the D2 transition. More realistic adjustments to this

number will be discussed later in the section for our setup. If we assume however that it is accurate, and we use a standard imaging exposure time for  $\tau = 200$  us, we obtain an upper-bound for the counts per atom (CPA) conversion:

$$CPA = 172. \tag{3.12}$$

Several other imperfections can affect the system. These mainly occur from the finite sizes of the clouds and the effects of the imaging radiation on the cloud appearance. One of the benefits of fluorescence imaging is that the counts detected are proportional to the time the atoms are exposed to the light (as can be seen in Equation 3.11). In theory this can lead to larger amounts of photons for longer exposure times, however the camera itself has a saturation limit per pixel which can be exceeded with too much light. Additional constraints arise with large exposure times, as clouds the clouds which absorb and scatter the radiant light are heated and pushed over time. This leads to a distortion and growth of the cloud sizes, which can make imaging difficult when looking for distinct regions of the camera for counting of the individual populations. To help with this, we allow the clouds to free fall, separate, and expand for as long as possible given the constraints of the Stern-Gerlach (SG) fields and the camera optics. Typically, we let the atoms fall for 22 ms, and apply the SG gradient for 20 ms. This gives us close to the maximal amount of cloud separation for our setup.

Another consideration which was mentioned earlier arises from our imaging with small apertured beams. While it does allow for less spuriously scattered photons to enter the camera, they also make imaging large clouds difficult as the separation size of the clouds ( $\sim 1.4$  mm) is close to the width of the imaging apertures and beams ( $\sim 2$  mm). Meaning, for sufficiently long exposure times, the imaging masks don't evenly hit all the sublevel-separated clouds, limiting our detection accuracy. This leads to the need for the adjustment of the masks periodically, particularly when we are looking to calibrate the imaging, as discussed

in the subsequent section on RF calibrations. Despite these constraints, fluorescence offers us the most accurate counting of the atoms, we believe, so it is the primary work-horse in the lab when performing noise-limited and sensitive spin measurements.

### 3.6.3 Absorption Imaging

While fluorescence is currently our preferred method for taking quantitative data, it can be difficult to use to gather spatial or structural information about the cloud, as fluorescence tends to blur and distort the cloud shapes. Enter absorptive imaging. Absorptive imaging involves shorter pulses, and relies on the absorption of a beam based on the atomic density. This provides a means to observe any internal structures of the condensate, which are particularly useful when looking for domains in the condensate, or when aligning the cross trap. It works on the principle that for a resonant beam, our atomic cloud will absorb the light. If we direct this light onto a camera, the camera sees a beam, with a shadow in it where the atoms interacted with the beam (see Figure 3.29). The atoms will become heated and scatter away once they have absorbed the light from the probe and re-emit it, thus there will be no atoms in the probe's path if it is pulsed again and another image taken. If one were to reference the difference in the image with the hole in the middle from the second image taken after the atoms have been excited away, then the composite would appear as a positive signal which would be inversely related to the amount of light absorbed by the atoms in the original image.

Quantitatively, this relationship is related to the optical depth (OD) of the cloud [99], and the column density ( $\tilde{n}(x, y)$ ) of the atoms as imaged on the camera:

$$\sum_{x,y} OD(x, y) \equiv \sigma_0 \tilde{n}(x, y). \quad (3.13)$$

Here,  $\sigma_0$  is the on-resonance absorption cross-section for the atoms. Likewise, in the limit of low-intensity imaging (probe beam typically around 50-100  $\mu\text{W}$ ), the optical density (OD) can be written in terms of the transmission ( $T(x, y)$ ) [99]:

$$OD(x, y) = -\ln \left( \frac{S'(x, y) - S_b(x, y)}{S_0(x, y) - S_b(x, y)} \right) = -\ln (T(x, y)). \quad (3.14)$$

Here  $S_i(x, y)$  refer to different signals measured on the camera for atoms and the probe beam ( $S_0(x, y)$ ), just the probe beam ( $S'(x, y)$ ), and no atoms or probe beam ( $S_b(x, y)$ ). Thus, based on the absorption property, we can infer the local density and distribution of the atoms in the cloud from a single absorptive image.

Experimentally, each of these signals are taken as a separate image as described briefly above. The background is taken separately at the start of acquisition, while the signal (image with atoms) and reference (image with probe, but no atoms) are taken for each experimental run. Because the signal strength is dependent on the probe beam intensity, it is important to take these images as close together as possible. Our CCD camera has some limitations on how quickly an image can be transferred from the sensor to the readout. To enhance the readout time, we cover half of the camera sensor (1024 pixels by 1024 pixels) so that its size is halved. This leaves the upper half of the sensor exposed for acquiring images, while the second, masked half of the sensor can receive the image while it is being shifted and transferred for readout. This effectively allows the readout time to be halved. The typical time between readout of the signal and subsequent reference images is typically around 5-10 ms. If this time were much shorter, portions of the signal image will enter the reference image frame, messing with the composite image made from the subtraction of the two.

To estimate the number of atoms detected in an absorption image, we can sum over the pixels in a composite image, given the measured optical depth (net transmittance,  $T(x, y)$ ).

This gives us a relation of the form:

$$\begin{aligned}
N &= \int \tilde{n}(x, y) dx dy \\
&= \sum_{pix} \tilde{n}_{pix} dA_{pix} \\
&= \frac{A_{pix}}{\sigma_0} \sum_{pix} OD(pix) \\
&= \frac{-A_{pix}}{\sigma_0} \sum_{pix} \ln(T(pix)).
\end{aligned} \tag{3.15}$$

The summation over the effective pixel area for the measured transmittance,  $T(x, y)$ , and is equivalent to measured “counts” over the pixel area. This then equates to a CPA proportional to  $A_{pix}/\sigma_0$ .  $A_{pix}$  is the effective pixel size after magnification ( $m$ ) is taken into account, such that  $A_{pix} = A_{pix}^{act}/m^2$ , with  $A_{pix}^{act}$  is the area of they physical camera pixel ( $13 \mu\text{m} \times 13 \mu\text{m}$ ). Using the on-resonance, absorption cross-section  $\sigma_0$  from [100], and the magnification for our imaging setup (3.846) we find the counts per atom (CPA) conversion for our current imaging setup is:

$$CPA = A_{pix}/\sigma_0 = \frac{(13 \times 13 \mu\text{m}^2)/(3.846)^2}{2.907 \times 10^{-9} \text{ cm}^2} = 0.0245. \tag{3.16}$$

This number is independent of exposure times, as well as camera settings, but only relies on the cloud being not too dense, the light to be resonant, and the intensity to be sufficiently below the saturation limit. As it stands now, the ANDOR software program for absorption already takes the signal and reference images and combines them into a composite image. The signal is also displayed in units of optical density as described above. Typically, peak densities don’t go above 1.5 OD for the condensate. Keeping the OD to less than two is a best practice, as it helps limit errors associated with imaging a cloud that is too optically dense.

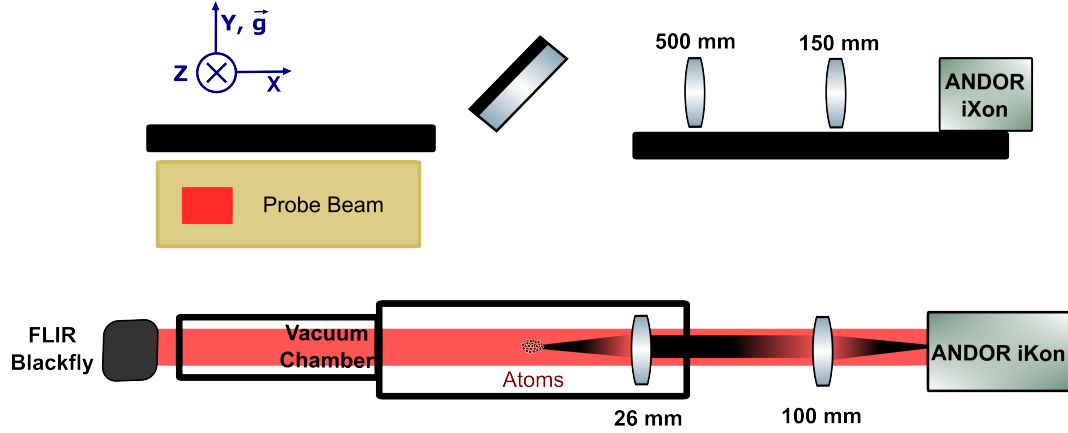


Figure 3.29: Schematic of BEC absorption imaging setup

### 3.6.4 Realistic Fluorescence Imaging Calculations

As discussed above in the fluorescence section, we can calculate the amount of atoms detected by our imaging system given the amount of counts collected. This is known as our “counts per atom conversion.” This was presented in Equation 3.11 for our iKon imaging system, assuming the light we image with is well above the saturation intensity, such that  $I \gg I_{sat}$ , where  $I_{sat} = 3.58 \text{ mW/cm}^2$  ([100]). In this limit, the scattering rate reaches its maximum value of  $\Gamma/2$ . Practically however, there is a finite limit to the intensity of light that we shine on the atoms during imaging. Currently, the imaging beams we use are masked versions of the MOT beams, which have around 42 mW per beam, are retro-reflected, and have a one inch diameter. This would give us an intensity ( $I_{beam}$ ) of 8.29 mW/cm<sup>2</sup> per beam. If we use the fact that we image using four beams (two input beams that are retro-reflected), the total intensity becomes:  $I_{tot} = \sum_{n=4} I_{beam,i} = 4 \times 8.29 = 33.2 \text{ mW/cm}^2$ . This would give us a ratio of total intensity to saturation intensity of:  $I_{tot}/I_{sat} = 9.04$ .

In a similar vein, the amount of light being used to image the atoms is also not quite on resonance ( $\omega_0$ ), but is slightly detuned by an amount,  $\Delta = \omega_{laser} - \omega_0$ . This would thus give us a photon scattering rate that is less than the maximum value for a given intensity. Using these experimentally realistic considerations, we can write a more accurate equation

for the counts per atom (CPA) determination using a realistic rate of light scattered during imaging ( $R_{sc}$ ):

$$\begin{aligned} N_{atoms} &= \frac{N_{counts}}{(CPA)_{real}} \\ &= \frac{N_{counts}}{(R_{sc}\Omega\eta\tau)} \end{aligned} \quad (3.17)$$

where,

$$R_{sc} = \left(\frac{\Gamma}{2}\right) \frac{(I_{tot}/I_{sat})}{1 + 4(\Delta/\Gamma)^2 + (I_{tot}/I_{sat})}. \quad (3.18)$$

For a detuning of  $\Delta/2\pi = -0.831$  Hz, and  $I_{tot}/I_{sat} = 9.04$  as mentioned above, this gives an  $R_{sc}/(\Gamma/2) = 0.894$ , meaning the realistic scattering rate is 89.4% of the maximum scattering rate at our density and detuning. If we assume an imaging (exposure) time of  $200 \mu s$ , this would give us a more realistic conversion between the counts to atoms, as shown by:

$$\begin{aligned} N_{atoms} &= N_{counts} \left[ \frac{(1 + 4(\Delta/\Gamma)^2 + I_{tot}/I_{sat})}{(\Gamma/2)(I_{tot}/I_{sat})\Omega\eta\tau} \right] \\ &= \frac{N_{counts}}{153}. \end{aligned} \quad (3.19)$$

Compare this to Equation 3.11, where an estimation of the CPA was shown to be 171 for a  $200 \mu s$ . As can be seen, the decrease in the CPA is directly proportional to the decrease in the amount of scattered light due to the finite intensity of the imaging beams, and the light's detuning subsection 3.6.4. This is an important consideration to investigate, especially as we think of future ways to image the BEC (see section 5.3). And while the CPA is an important number to compare to, we have for some time (for the last couple of years) relied on an experimentally obtained number measured using an RF calibration. This will be explored in the next section.

### 3.6.5 RF Calibration

The RF calibration is an important tool for calibrating the imaging conversion of counts to atoms using fluorescence. It works by measuring the quantum projection noise (QPN) of the system, which is Poissonian in nature, and naively should scale as  $\sqrt{N}$ . We can use our RF system to transfer atoms from  $|1, 0\rangle \rightarrow |1, \pm 1\rangle$  in various amounts. Since  $M = N_+ - N_-$ , we can calculate noise in this parameter by measuring the variance of this number.

Beyond the typical CPA calculated in subsection 3.6.4, we also need to take into account other noise sources. This can be represented by:

$$\sigma_{QPN}^2 = \Delta^2 M - \sigma_{PSN}^2 - \sigma_{BKG}^2. \quad (3.20)$$

Here  $\sigma_{QPN}^2$  is the noise of the quantum projection noise,  $\sigma_{PSN}^2$  is the noise associated with the photon shot noise of the imaging light, and  $\sigma_{BKG}^2$  is the noise associated with the imaging system (e.g. camera noise, etc.). These are subtracted from the magnetization noise estimate, as they obscure the atom noise in the populations themselves and are isotropic to each of them. More details on quantifying noise estimates for the imaging system is outlined in [99].

If our conversion of the counts to atom number is close to accurate for the system the slope between  $\Delta^2 M$  and the number of pairs of atoms should be close to one. Figure 3.30 shows an example of a good calibration taken throughout the day and following an estimation of the CPA to be 157.911 for a 200  $\mu s$  exposure time. The error bars in the plot are derived from the uncertainty in the measurement due to the limited sampling size of the measurement. For a finite number of samples, this can be represented by:

$$\text{std. dev.}(\sigma_{QPN}^2) = \sigma_{QPN}^2 \sqrt{2/(N_s - 1)}. \quad (3.21)$$

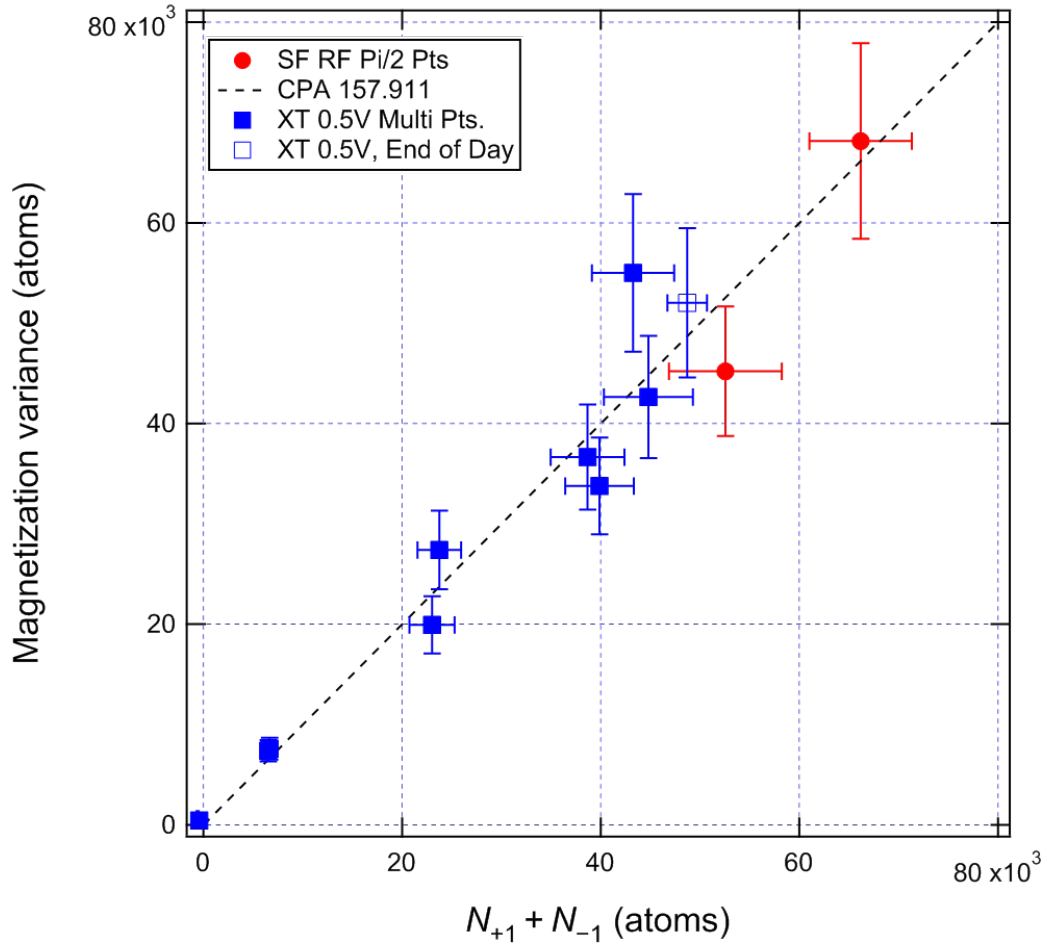


Figure 3.30: RF Calibration for  $200 \mu\text{s}$  at 500 mG. 50 shots per point are averaged. Data was taken in a single day and agrees with historical measurement [89]. This measurement produces a fit to a slope of one, indicating that the imaging conversion of 157.91 counts/atom is an accurate number. This data was also confirmed on other occasions, and especially when sensitive data, such as number squeezing data, is being taken.

### *Mask Adjustment*

The imaging masks used in the system are pneumatic and are used on the experimental MOT beams to make the beams smaller and reduce the scatter noise seen on the camera. The mask positions are independent of the MOT beams and from time to time need to be optimized to make sure the small beams ( $\sim 2$  mm by 2 mm) are hitting the condensate optimally. This is done by performing our normal experiment and applying a  $\pi/2$  RF pulse to transfer the atoms into the  $|1, \pm 1\rangle$  states. By looking at the magnetization for each of the masks individually, the position of each can be moved to minimize the noise and cloud imbalance between the populations. This is done in the vertical location of the masks to optimize the atom number, and in the horizontal direction to adjust the imbalance of atom  $\pm 1$ . In general, it should be possible to make the population imbalance between  $|1, +1\rangle$  and  $|1, -1\rangle$  fall within a few percent.

### **3.7 State Interaction and Preparation**

Light fields described earlier can drive the repump and cooling transitions in rubidium. Other electromagnetic fields however can be used to drive smaller transitions within the finer levels of rubidium. Using microwave and RF frequencies of radiation we are able to drive between the hyperfine levels of the  $5^2S^{1/2}$  level. These frequency ranges lie in the GHz and kHz range for the microwave and RF fields, respectively. These are particularly useful in control applications [81] and measurement of the quantum states we generate. We also use them to calibrate the imaging system and to zero the magnetic field.

#### 3.7.1 Microwave Fields

The microwave is useful in driving between the  $F=1$  and  $F=2$  manifolds themselves. The primary transition of note is the clock state (see Figure 3.4), which goes between the two  $m_f = 0$  levels:  $|F = 1, m_f = 0\rangle \rightarrow |F = 2, m_F = 0\rangle$ . This value (6.83468261090429(9)

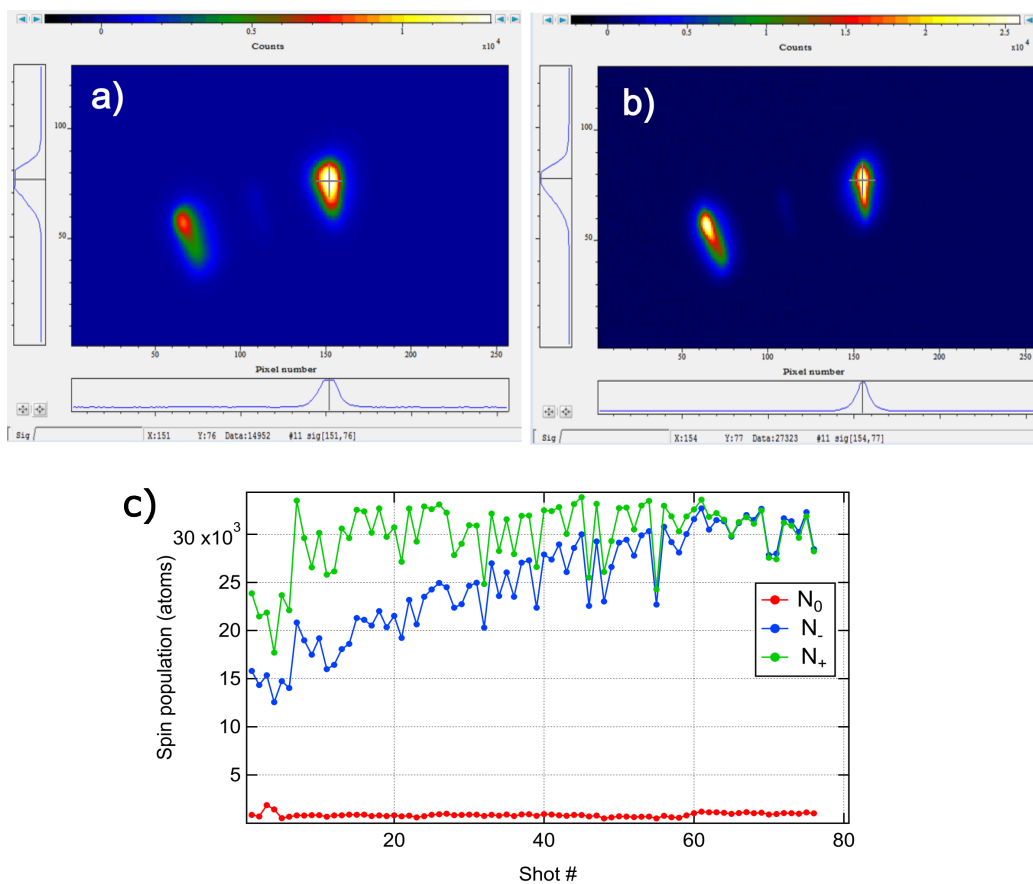


Figure 3.31: Imaging mask adjustments made on the experiment to optimize position of imaging light with respect to the condensate. This effect can be made more noticeable when blocking one of the beams and measuring the difference between the  $\pm 1$  clouds in the rubidium ground state. Initially unbalanced clouds (a) can become balanced (b) by adjusting the masks positions finely, such that the magnetization or difference in atom counting between the two states is equal (c).

GHz) is precisely known to many digits and is synthesized by an HP function generator. This transition is magnetically insensitive to first order, and has a frequency shift of  $575\text{Hz}/G^2$  to second order. Of course each hyperfine level also has sublevels. These transitions are magnetically sensitive to first order and are detuned from the clock state by  $\Delta = 700\text{ Hz/mG}$  for each  $m_F = 1$ . For example, a transition between  $|F = 1, m_f = 0\rangle \rightarrow |F = 2, m_F = 1\rangle$  would be detuned by the clock frequency plus  $\Delta$ , and  $|F = 1, m_f = -1\rangle \rightarrow |F = 2, m_F = -2\rangle$  would be detuned from the clock by  $(-2 + -1 =) -3\Delta$ .

We can fit the microwave resonance spectrum using the function:

$$\rho_{+1}(\omega) = \Omega^2 \left( \frac{\sin\left(T\sqrt{\Omega^2 + (\omega - \omega_0)^2}\right)}{\sqrt{\Omega^2 + (\omega - \omega_0)^2}} \right)^2 \quad (3.22)$$

$T$  is the microwave pulse length,  $\Omega$  is the microwave Rabi rate,  $\omega_0$  is the resonant frequency and  $\omega$  is the detuning frequency. We can fit both rate and spectra for the clock and “delta” transitions using our analysis software to determine the driving strength and field at the atoms’ location. In previous years, this was used to zero our magnetic field, but in the last two years we have switched to doing this with the RF, which is also magnetically sensitive. Circuits for the microwave circuit can be seen in [81, 89].

### 3.7.2 Radio-Frequency Fields

Much like the microwave fields, the RF fields are magnetically sensitive. RF transitions however are driven with the manifold itself (e.g. between  $m_F = 0$  and  $\pm 1$  for the  $F=1$  transitions). The frequencies between the sublevels for each manifold are nearly identical, but differ by a small amount due to the differing Landé factors. The shift for the  $F = 1$  manifold is  $\Delta_1 = 702.4\text{ Hz/mG}$ , and the shift for  $F = 2$  manifold is  $\Delta_2 = 699.6\text{ Hz/mG}$ .

$$\rho_0 = \left( 1 - \frac{\Omega^2}{\Omega^2 + (\omega_0 - \omega)^2} \left( 1 - \cos\left(T\sqrt{\Omega^2 + (\omega_0 - \omega)^2}\right) \right) \right)^2 \quad (3.23)$$

Circuits for the microwave circuit can be seen in [89].

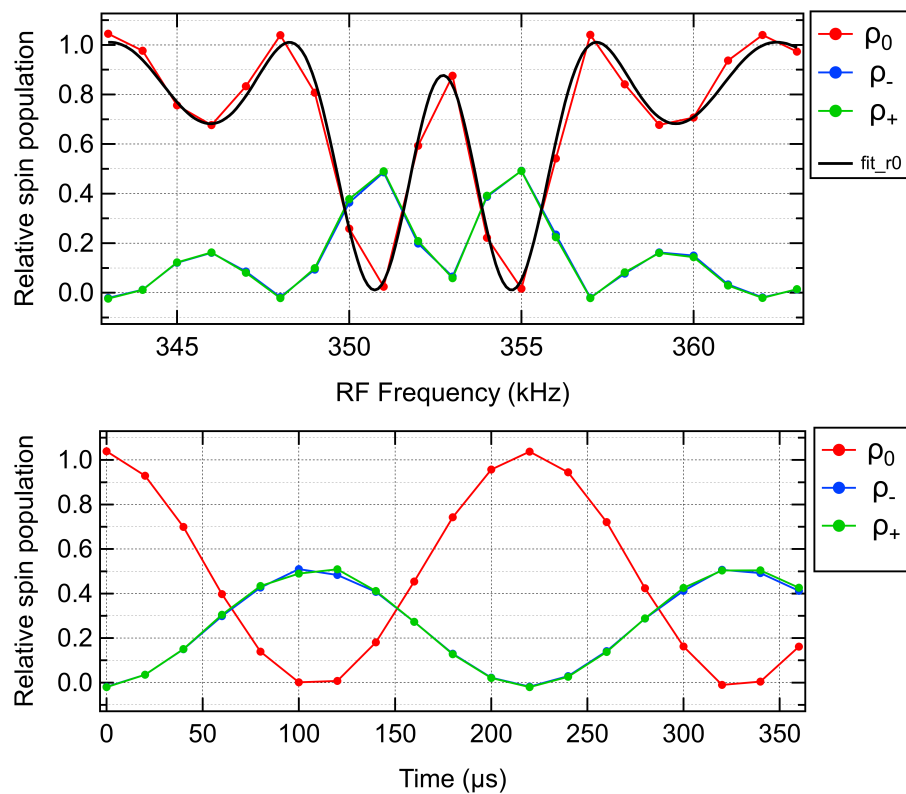


Figure 3.32: RF spectrum and rate taken at 500 mG at full power (10V). Fit parameters output for the black trace are for the resonance ( $\omega_0$ , kHz, Rabi rate ( $\Omega$ , kHz), offset, and pulse length (T,  $1/\pi$  ms).

### 3.8 BEC Experimental Stages

The following briefly outlines the experimental procedures by step. Some key, pertinent details are included for each stage. The process from no atoms, to thermal cloud, to pre-cooled atoms, to condensate, then imaging, takes around 21 seconds.

#### 3.8.1 MOT

Our MOT is loaded for 15s at the start of the experimental cycle with the initial values specified in the spreadsheet which controls the values for the experiment channels. The atoms are loaded from a getter (SAES). There are two getters available to use on the experiment. One is called the "old getter" and is the getter that has been primarily used on the experiment. With this getter operating between 4-5 A, we can load the MOT to around 12 million atoms for 15 seconds (as measured by the FLIR camera). This number can fluctuate from day to day, but a number of around nine million to 15 million is considered adequate for the "old getter" for 15 seconds of loading. The other getter called the "new getter" is typically unused, but has been tested for times when atom number loading seems to be an issue. In this case, a current of around four amps can be used to load the MOT for comparable atom, but in a much shorter time ( $\sim$  seven seconds of loading time).

The getter also contributes a small magnetic field that can be seen to have an effect on the atoms. This should be taken into account when zeroing fields or switching between getters, as the bias field and thus MOT cloud location changes slightly. Residual fields from the getter can be shut off by turning off a relay switch connected to the "blue lights." The blue lights are used as a desorption mechanism for the rubidium atoms, as they tend to coat the surfaces of the vacuum chamber when released from the getter. The blue lights prevent rubidium atoms from sticking to the viewports, via photo-ionization with the near UV light. The lights are left on during the majority of the MOT time and have a large effect on the MOT atom number.

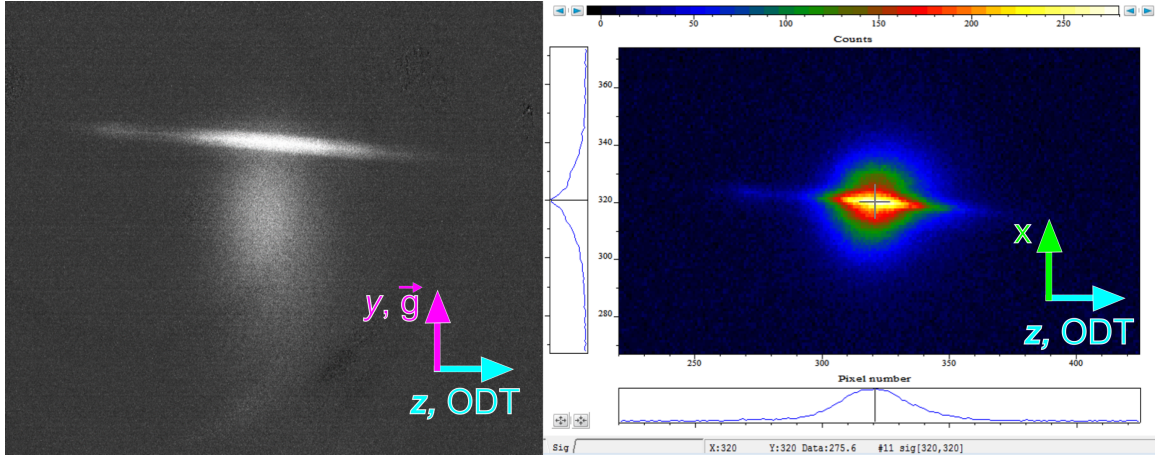


Figure 3.33: DarkMOT images with top (iXon) and FLIR cameras showing dark MOT intersecting with the initial optical dipole trap for loading.

The light shown on the atoms is around  $-20$  MHz detuned from the cycling transition. For around  $42$  mW and one inch diameter beams, the light has a total intensity of  $\sim 14x I_{sat}$ . Once the MOT loading is completed after 15 seconds, the experiment begins the running of the spreadsheet values. The temperature of the MOT at this stage is usually around  $80 \mu\text{K}$ . This includes changing the MOT gradient and the light detuning to what will be needed in the dark MOT sequence.

### 3.8.2 Dark MOT

The dark MOT is the phase of the sub-doppler cooling stage that the experiment undergoes. The detuning increase and gradient decrease for the dark MOT allow the MOT to be further cooled to below that of the MOT. The detuning is typically detuned to a range between  $-150$  MHz to  $-190$  MHz. This range is not very sensitive and needs to be done at a finite rate ( $\sim 10$ 's of ms), due to the locking configuration (see subsection 3.1.3). It also is helpful to decrease the available light going to the dark MOT, typically about half. The MOT coils are typically also decreased to near zero. The combined effects of these decrease the temperature around a factor of 3-4 (typically around  $25 \mu\text{K}$ ).

The repump also plays an important role at this stage, as its power is also decreased during the dark MOT stage. The optimal value for this stage is fairly sensitive in determin-

ing the final amount of atoms that make it into the optical dipole trap (ODT). The value is also more or less consistent day to day. This is because the final value of the repump power during the dark MOT seems to determine the vertical ( $\hat{y}$ ) height of the cloud, likely due to the majority of the repump light going into the “MOT 1” fiber (which is aligned vertically). Thus, it is a useful diagnostic for the experiment, and usually indicates the MOT light powers or the repump fiber coupling needs to be touched up.

Measured number of atoms in the darkMOT also typically shows a small number decrease from the MOT, typically by around 20 %. The dark MOT typically loads directly into the ODT. In order to optimize this loading, the various trim values are typically scanned in the spreadsheet to move the cloud by small amounts to adjust its location relative to the incoming 10.6  $\mu\text{m}$  beam. The dark MOT stage typically takes around 40ms in total. The ODT typically overlaps with part of the dark MOT stage, due to the loading time needed for the dark MOT into the trap.

### 3.8.3 Optical Dipole Trap and Evaporation

The ODT, formed from the 10.6  $\mu\text{m}$  laser, is turned on near the end of the MOT phase and is on during the dark MOT phase. The decrease in temperature from the additional sub-Doppler cooling stage aids in the efficient loading of the ODT. The final amount loaded is estimated to be between 2-4 million atoms. The compression of the trap starts during the loading and dark MOT stage (currently around 250 ms after the end of the MOT stage). This historically was meant to occur at 400 ms, after the dark MOT and ODT stage was completed, but recent (in the last two years) empirical measurements of the atom number stability points to it being more beneficial to start compression at this earlier time.

The trap compression lasts for a little longer than one second. After the trap compression begins, the so-called purification stage begins (around 400 ms after the MOT). This is so named as we use the Stern-Gerlach coils to preferentially keep atoms that are to first order, magnetically insensitive. This leaves atoms in the ground state of  $|F = 1, m_F = 0\rangle$

and forces atoms in the  $|F = 1, m_f = \pm 1\rangle$  out of the trap. The purification must be strong enough that atoms are forced out of the trap, but not so strong that too many atoms are made to leave the trap, limiting the number of atoms available to maintain a high enough density to make a condensate. The exact timing, strength, and duration of the purification gradient is determined empirically and typically is on for around four seconds, and turns off around one second before the final powers of the ODT are reached and condensation is reached.

As explained in subsection 3.2.2, the  $10.6 \mu\text{m}$  laser starts at maximum power (118 W) and is ramped down to a final power of around 40 mW. This produces a condensate of around 50,000 atoms in the single focus, almost all of which are in the condensate (as noted in absorption). The entire ramp takes around five seconds to complete, with the final powers taking the longest amount of time (the last two stages take around 1-2 seconds). The individual times between the different power steps from 118 W to 40 mW are determined via fluorescence and absorption imaging. The typical early stages (118 W to 4 W) are optimized using the atom number, meaning the power from one step to the next is ramped down in the shortest amount of time that produces the maximum amount of atoms. The later stages are typically optimized by ensuring that the cloud's temperature is equilibrated at each stage (see Figure 3.35), and that it reaches the predicted temperature for the predicted trap depth (trap depth determined by Equation 3.10 and temperature should be  $1/10k_B$  of that, where  $k_B$  is the Boltzmann constant). This is hard to measure for the final stages of evaporation when the clouds is not longer thermal, but has reached condensation. At the end of the evaporation ramp a condensate of atoms in the  $m_F = 0$  ground state should be prepared, and after letting the condensate stabilize for a few 100 ms, is ready for further state preparation.

### 3.8.4 State Preparation and Cross Trap

Some of the state preparation is performed through the purification stage described above. In order to make sure the condensate is in the polar ground state however, we apply a large bias field along the quantization axis (“Trim Z” along the  $\hat{z}$  axis, see Figure 3.16) of around 1.1 Gauss. Once the condensate is formed however, we are ready to begin our desired experiment. For faster and enhanced interactions, the crossed dipole trap can be used to add additional confinement to the single focus trap (subsection 3.2.2). To do this, the 850 nm trap beam power is ramped up to its chosen power (typically 0.5 - 1.0 W) at a slower rate (100’s ms) near the end of the single focus evaporation ramp.

After this, the Trim Z bias field can be lowered to its desired quench field. This ramp takes a finite amount of time, but is chosen to be as short as possible to minimize the amount of evolution of the state away from the polar ground state. The typical time used for us to ramp from the high field applied during purification to the final quench field is about four milliseconds, with three milliseconds of wait time. While the noise in the magnetization ( $\Delta M^2$ , for magnetization  $M = N_+ - N_-$ ) grows fairly quickly (see subsection 3.6.5), the mean value of  $\rho_0 = 1$  still holds for the duration of the quench (and for  $\sim 100$  ms after, see Figure 3.42). Once the final bias field is reached, we can apply any microwave or RF field as needed. This is done typically as the trap(s) is (are) released and the atoms are sent into free fall for imaging.

### 3.8.5 Imaging the BEC

To image the BEC, we allow the cloud(s) to free fall. The fall allows the clouds to expand, decreasing the density, preventing the chance that clouds that are too optically dense for accurate imaging. Our typical imaging time-of-flight is 22 ms. For 20 of those milliseconds, the Stern-Gerlach gradient is applied at full strength. This allows any clouds that are in the  $\pm 1$  or 2 sublevels to separate from the force felt from the gradient field. This creates adequate separation so that when we image the atoms, there is sufficient separation

between the various sublevels to allow for accurate counting of each region.

Imaging time is set by the pulsing on of the apertured MOT beams for a variable set exposure time. The apertures are the masks described in subsection 3.6.5. The light is shifted to be near resonance (around 1-2 MHz detuned). The light is pulsed on by AOMs and are accurate to the several nanosecond level. Shutters are used as well to ensure the light is completely shut off when cloud is not being actively imaged. These are inherently slower, mechanical shutters so are preemptively turned on and off a few milliseconds before needed. Typical exposure times range from 100  $\mu\text{s}$  to 300  $\mu\text{s}$ . 100  $\mu\text{s}$  is on the shorter end, and hasn't been the most reliable time. This is suspected to be due to clouds that are too optically dense. Longer exposure times tend to blur the clouds too much. 200  $\mu\text{s}$  tends to be a good median value, and is used for most of the data taken in this thesis.

Once imaging is complete, the experiment pauses for about 1/2 a second and resets to the MOT loading values. If the experiment is being cycled continuously, the MOT begins loading after the reset and a new run begins. The current total time needed to complete one cycle is around 21 seconds, with 15 of those seconds owing to the MOT.

### **3.9 Typical Experiments and Diagnostics**

Below are a list of typical experiments on the BEC. The ability to perform each is often used on the experiment to check the health and stability from time to time. These times often occur when things on the experiment are not performing as expected, or when a disruption has occurred in the normal operation of the experiment (e.g. power outage, diode replacement, etc.). The listed experiments here range from simple to more complicated, with some being the result of previous students' thesis work.

#### 3.9.1 Measuring the Temperature of the Cloud

The measuring of the temperature of the cloud is a useful tool for ascertaining which or if certain stages of the experimental cycle are achieving the expected temperature at that

stage. As discussed, we take room temperature atoms and cool them to condensation, leading to several distinct stages in the experiment where we can reliably check and confirm the final temperature at the end of that stage. The basic principle behind this is that the temperature ( $T$ ) of the cloud expands at a rate which is proportional to the square of its measured (Gaussian) width ( $\sigma$ ) [92]; this takes the form of:

$$T = \frac{m}{k_B} \left( \frac{\sigma}{t} \right)^2. \quad (3.24)$$

This works best for thermal clouds, but we use it as a rough estimate for the condensate at times when trying to diagnose the experiment. Further, we can allow the cloud to fall for different amounts of time and fit the profile of the clouds for different amounts of time. The increase in spread of the thermal cloud's density distribution can be solved to show expansion in time ( $t$ ) with:

$$\sigma(t)^2 = \sigma_i^2 + \frac{k_B T}{m} t^2. \quad (3.25)$$

Here, the temperature of the cloud can be fit to the measured Gaussian widths ( $\sigma(t)$ ) of the cloud, starting with the initial cloud width ( $\sigma_0$ ). An example of a TOF measurement of a thermal cloud is shown in Figure 3.34. Temperature of a single width measurement is used to estimate the initial cloud temperature and density distribution. As can be seen from the longer wait times, the cloud expands and the density decreases.

This can be done after all experimental stages and as mentioned, is useful in diagnosing the efficiency of each stage in terms of producing a cold cloud with high enough atom number. Figure 3.35 illustrates the usefulness of this diagnostic performed in the single focus optical dipole trap. Atom number changes for different powers and loading times, but the temperature should be roughly the same. The measurement of different ramps to a fixed power show different numbers, but the temperatures are in pretty good agreement, implying the atoms at that potential have reached their equilibrium temperature.

Measurement of the cloud temperature is best done with absorption imaging, where

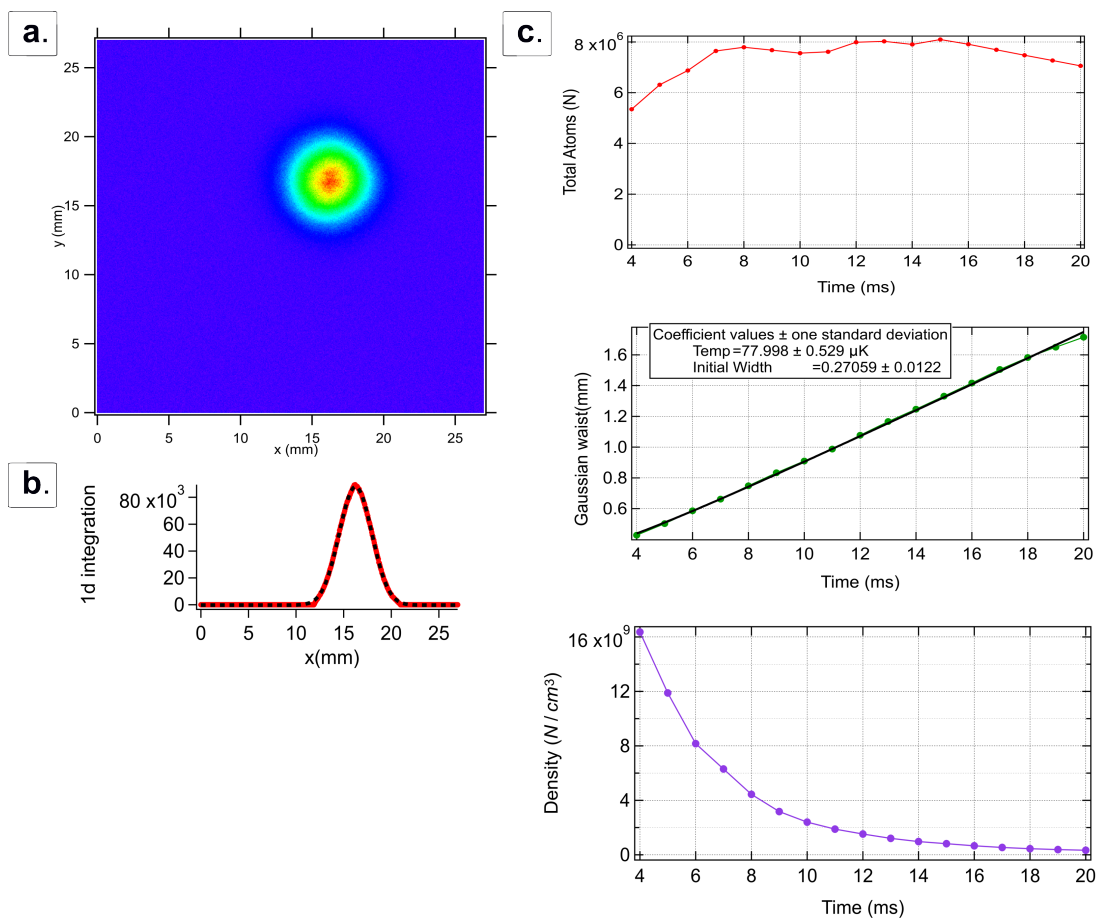


Figure 3.34: Images of the MOT taken from the iXon or “Top” camera; fit to the integrated cloud profile to estimate the Gaussian width of the cloud. MOT numbers, density and temperature during a time of flight measurement; shows a fit to the width of the cloud expansion to give a temperature of  $77 \mu\text{K}$ . Data is taken with the Top (iXon) camera.

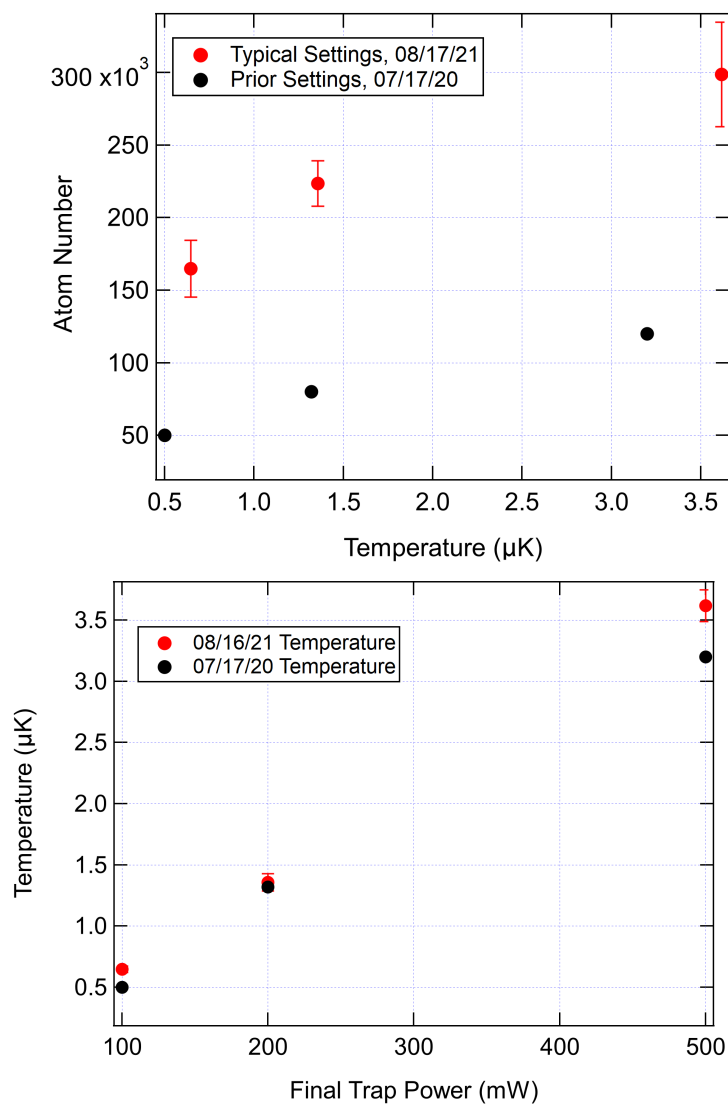


Figure 3.35: Numbers and temperature measurements for different 10.6 μm trap ramp settings for powers approaching condensation, but after compression has occurred, in the single focus optical dipole trap.

the spatial structure of the clouds is more pronounced, and less blurry than fluorescence imaging.

### 3.9.2 Lifetimes

Lifetime measurements measure the longevity of the condensate or cloud of atoms in a trap. Many aspects can affect these measurements, such as the vacuum and the density of the clouds being trapped. We typically rely on the measurement of the lifetime of the trap as a diagnostic for the vacuum health of the chamber, as we believe that density-related (three-body) losses do not play a role in our measurement of the condensate's lifetime when trapped in the single-focused trap. Typical lifetimes for the SF and XT are shown below. The lifetime in the single-focused,  $10.6 \mu\text{m}$  optical dipole trap is usually around  $15 \pm 1$  seconds. The lifetime for the second-crossed dipole trap varies quite a lot, and seems to be limited by the density of the trap. Depending on the power of the second trap laser, the lifetime can range from several seconds to less than a second. Lifetime shown here for the "crossed trap" is for a moderate power of the second laser ( $\sim 1 \text{ mW}$ ).

### 3.9.3 Critical Field Scan

The critical field scan (colloquially called the "B-crit" scan) is usually performed before, during, and after experiments involving atomic interactions, as it indicates the density of the cloud, which thus affects the amount of interaction the atoms will undergo when held at certain fields. Critical field scans were a method developed in our lab to help ascertain when the system had crossed the critical point ( $q_c = 2|c|$ ) from the polar phase to the broken-axis symmetry phase. It works by measuring the population in the polar ground state ( $\rho_0 = 1$ ) after a quench and hold (of around 100-500 ms) to a final magnetic field. If the final field is above the critical point, the state measured will remain at  $\rho_0 = 1$ . If pairwise creation occurs though (meaning  $\rho_0 < 1$ ), then the system has passed into the broken-axis symmetry phase and the critical field has been determined. Using the relation

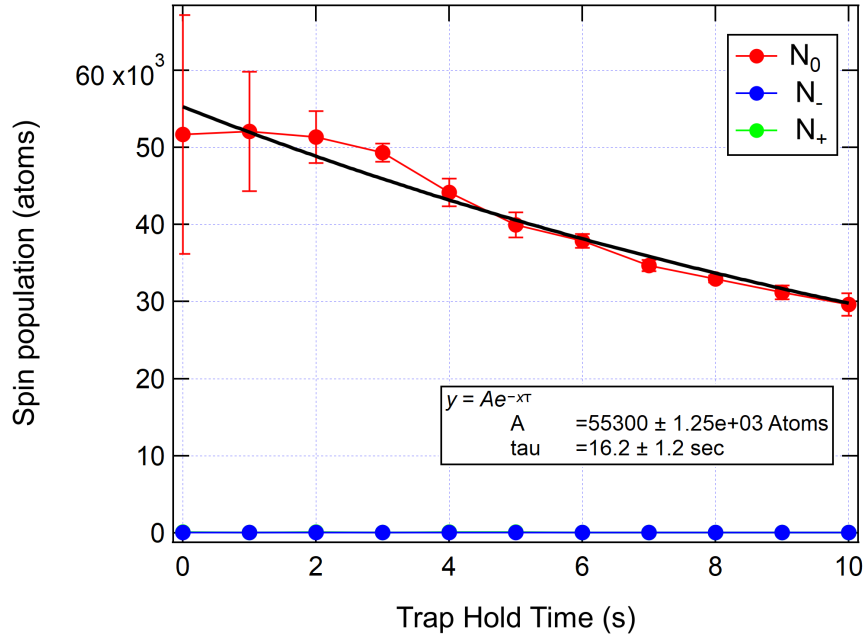


Figure 3.36: Single focus trap lifetime measurements averaged over three runs. Similar is done in the 850 nm “crossed trap” configuration to give a smaller lifetime (due the increased confinement). This can range from three to less than a second in length at maximum 850nm power.

for the critical point ( $q_c = 2|c| \Rightarrow |c| = 71.6 \text{ Hz/G}^2 \cdot B^2/2$ ) and the value of the field right before pairwise creation or interaction occurs, the value of  $c$  can be determined. This can be done with acceptable accuracy ( $\pm 0.1 \text{ Hz}$ ).

The  $c$ -value for the single-beam dipole trap ( $10.6 \mu\text{m}$ ) is usually found to be between 2-3 Hz. Anything smaller than this could indicate that the auxiliary gradient is not correct for the interactions to take place (see Figure 3.18), or that enough time has not been allowed for the dynamics to appear. The crossed-dipole trap has a wide range of  $|c|$  values, dependent on the power of the second (850 nm) trap laser. This value typically ranges anywhere from 3-11 Hz. It is usually consistent throughout the day, unless the alignment of the cross trap changes or the atom number changes drastically; thus it is generally a useful measure of the quality of the cross trap alignment throughout the day. This  $|c|$  value is usually in good agreement with our simulations of the dynamics, so we believe it to be fairly accurate. Agreement with other measurements (see subsection 3.9.4) can also confirm the measured

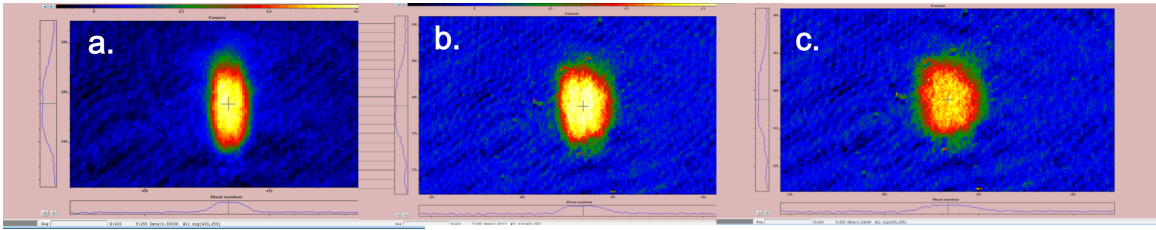


Figure 3.37: Absorption images of the cloud shown for the increasing confinement with a) being the primary ODT, b) being the crossed dipole trap with the 850 nm at low power, and c) being the crossed dipole trap with the 850 nm at higher powers. These images are used to align the crossed trap finely by adjusting the 850 nm location to get the cloud dispersion to change appearance. All images taken at 22 ms time of flight.

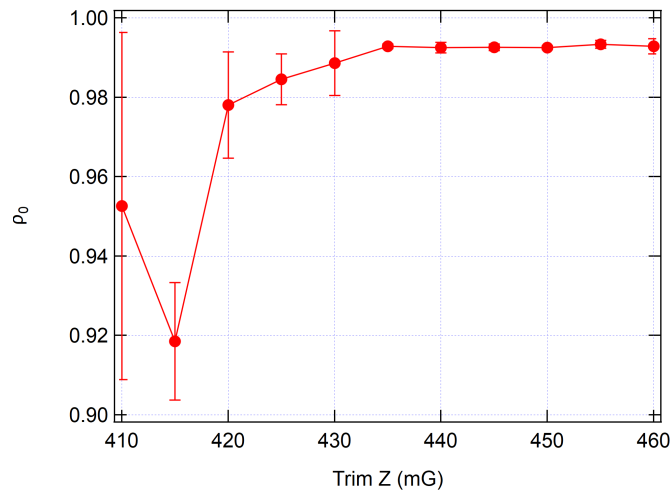


Figure 3.38: Typical critical field scan shown in crossed trap for different bias fields and a fixed amount of wait time (usually a few 100 ms for the crossed trap measurements). Here, deviation away from ground state occurs between 435 mG and 430 mG, leading us to put the critical field at 435 mG. This has shown great accuracy experimentally.

$|c|$  value.

### 3.9.4 Coherent Oscillations

Coherent oscillations are measurements of the oscillations of the phase space of our mean-field system. These oscillations have predicted frequencies given a specific spin interaction energy ( $c$ ) and quadratic Zeeman shift ( $q$ ). These are described in [69], and are based on the Bogoliubov approximation for the ground state oscillation and are represented in Equation 3.26:

$$\begin{aligned}\Delta_P &\equiv f_P = 2\sqrt{q(q+2c)}, \\ \Delta_{BA} &\equiv f_{BA} = 2\sqrt{c^2 - q^2/4}.\end{aligned}\tag{3.26}$$

Example oscillations for coherent oscillations near the ground state are shown in the figure below.

By following the procedure outlined in [69], we can initiate a small perturbation away from either the polar or broken-axis ground state to determine the approximate  $c$  value given the oscillation frequency. The ground states for each of these regimes are:

$$\rho_{0,GS} = 1 \text{ (Polar)}\tag{3.27}$$

$$\rho_{0,GS} = 1/2 + q/(4|c|). \text{ (Broken-Axis)}\tag{3.28}$$

Taking a number of oscillations near the ground states for both the polar and broken-axis phases, we can plot the measured oscillation frequencies,  $\Delta_P$  and  $\Delta_{BA}$  with example shown in Figure 3.39 as a function of  $q$  to obtain Figure 3.40. The measured frequencies can then be fit to give a prediction for the  $c$  value we expect given the oscillation frequencies. This provides another measure of the value of  $c$  other than that outlined in the critical field scan outlined in subsection 3.9.3. It also can help show the stability of the system as it is

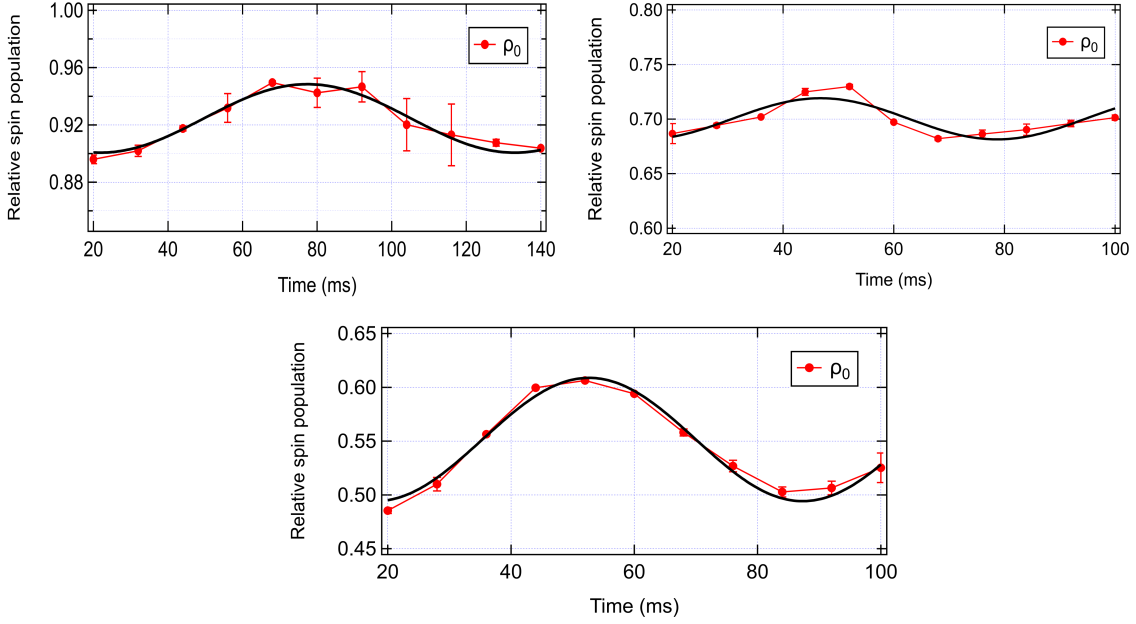


Figure 3.39: Coherent oscillations are shown in the crossed dipole trap; starting upper left and moving clockwise, we have coherent oscillations taken in the broken-axis symmetry phase for  $q/|c| = 1.5, 0.75,$  and  $0.25,$  respectively. Sinusoidal fits used to obtain frequencies, which are plotted in Figure 3.40.

averaged over multiple oscillations.

### 3.9.5 Spin Mixing

Spin mixing is a phenomenon observed early in spinor physics history [38, 71]. Nonetheless, it is a fundamental and essential experiment to be able to perform. Similar to the critical field measurement, we measure the population in  $\rho_0$  and watch the evolution of the spins away from the polar ground state ( $\rho_0 = 1$ ). However, now we keep the field set to a single quench value (below the critical field,  $q = 2|c|$ ), and measure the state for various lengths of interaction time. This involves pair-wise creation in the  $\pm 1$  clouds, which oscillate in time. Due to damping and atom losses, these oscillations are damped [99]. The rate at which the oscillations occur depends on the density of the atoms. The point where the fraction of the atomic pairs ( $\pm 1$ ) is the highest is typically the time chosen to perform our number squeezing experiments [99] (see below).

Typical spin mixing plots shown in Figure 3.42 for the crossed dipole trap for various

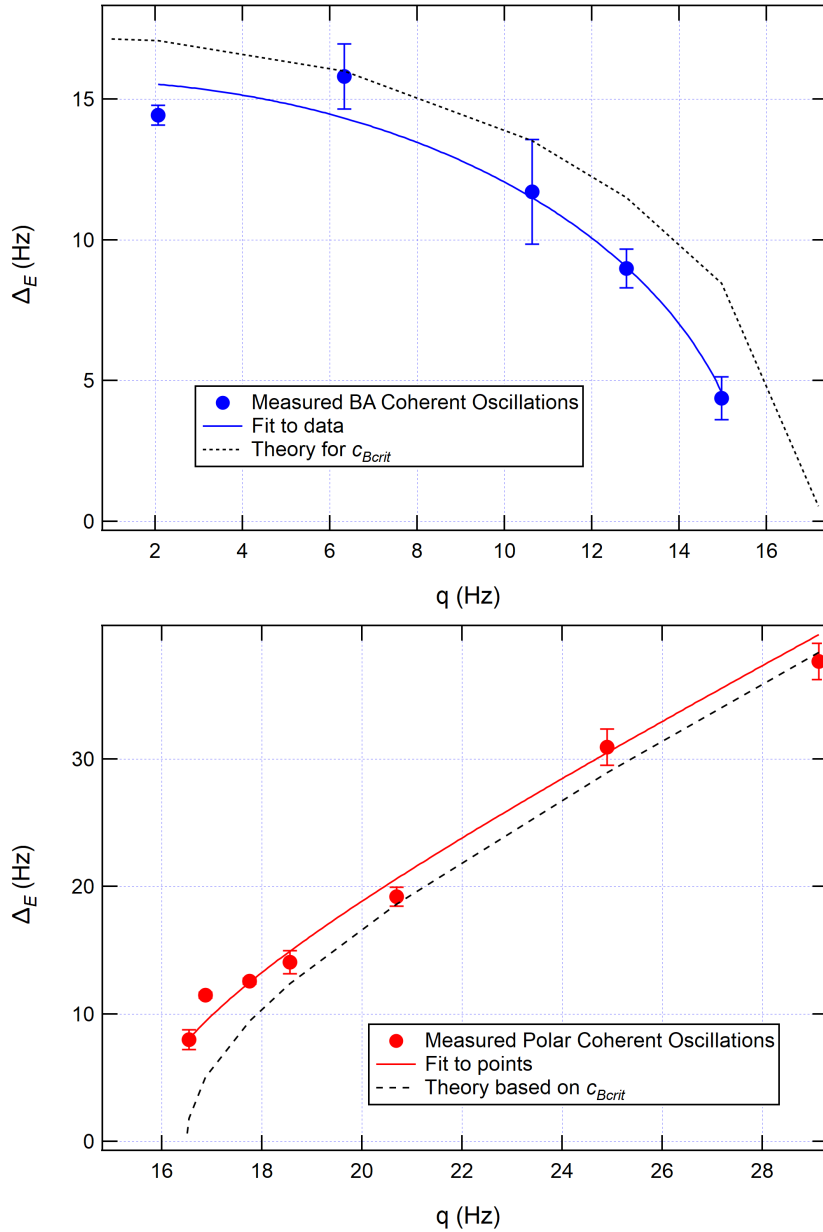


Figure 3.40: Coherent oscillations are measured for the polar (red) and broken-axis (blue) phases. These measurements are fit to give a predicted  $|c|$  value (solid blue and red lines). The two sets of data were taken on different days, but both show good agreement with the critical field predictions for  $|c|$  on each day (as indicated by the dashed line). Predicted broken-axis critical field value was  $8.6 \pm 0.1$  Hz, while fit yielded  $7.8 \pm 0.1$  Hz. Predicted polar critical field value was  $8.2 \pm 0.1$  Hz, while fit yielded  $7.8 \pm 0.1$  Hz. Discrepancies in the measurement are likely due to the coherent oscillations not being exactly at the true ground state, but some small excitation away from it. Data near the critical point  $q/|c| = 2$  also is particularly sensitive, leading to further potential sources of error for fast quenches [79, 69].

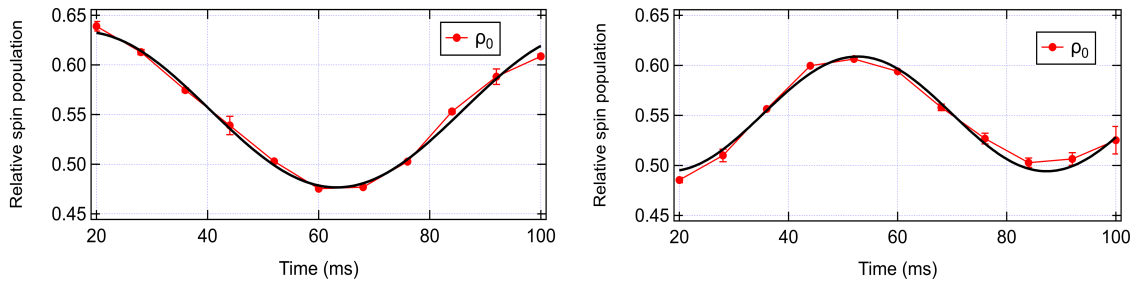


Figure 3.41: This example shows the effects of the RF pulse on the measurement of the coherent oscillations; example here shows oscillation at the same nominal  $q/|c| = 0.25$  but with an RF pulse differing by 20 ns. Oscillation on the left has the wrong phase and a larger amplitude and period, while the oscillation right (used in Figure 3.40) is smaller in amplitude and period.

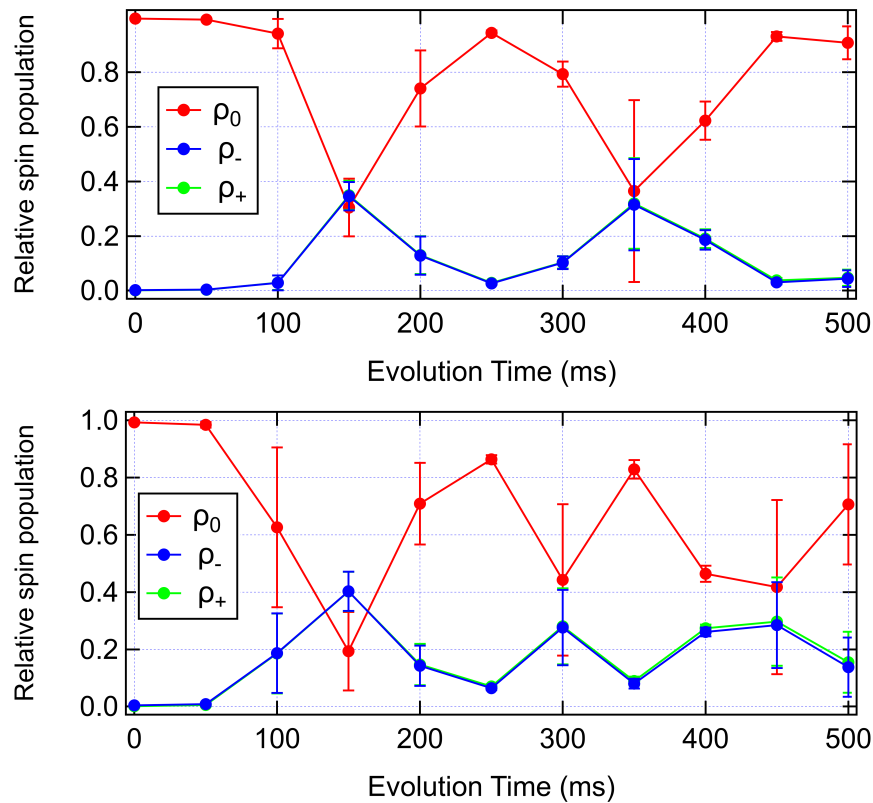


Figure 3.42: Spin mixing in the crossed trap for different crossed trap powers. Both runs here are quenched well below the critical field and points are averaged over three runs. Top plot is taken with a slightly lower crossed trap power ( $\sim 2$  mW), so the dynamics are slightly slower than that of the bottom plot (with 850 nm at  $\sim 2.5$  mW).

second trap (850 nm) powers. As can be seen, the dynamics are slightly faster for the higher trap power, given the increased density of the cloud of atoms. Similar dynamics can be seen in the single (10.6  $\mu\text{m}$ ) trap, however the density is much lower so the dynamics are slower. Likewise, the decreased density means the gradient zeroing is even more important, and the auxiliary gradient field must be sufficiently close for the spin mixing dynamics to be observed in the single trap (see Figure 3.17).

### 3.9.6 Number Squeezing

As described above, the atoms, when quenched below the critical point, exhibit pair-wise creation of  $m_F = \pm 1$  from the  $m_F = 0$  state. This was shown to lead to squeezing in the magnetization noise ( $\Delta M^2$ ) [99, 101]. This means that fluctuations in this parameter are lower than that of what would be expected in a coherent state, say as in an RF rotation from  $|1, 0\rangle \rightarrow |1, \pm 1\rangle$ , which has a noise of  $\sqrt{N_+ + N_-}$ . The noise can be measured in the magnetization and compared with that of a coherent state to produce a ratio of the noise suppression. This in terms of decibels is written as:  $\xi_{S_z}^2 = (\Delta M)^2 / (N_+ + N_-)$ .

This data is obtained by allowing the evolution of spin mixing to occur for a fixed amount of interaction time and then measuring the amount of pairs created in  $|1, \pm 1\rangle$  (see Figure 3.43). From there the data can be binned by the numbers of pairs of atom and the measured magnetization converted into decibels. After subtracting off the measured detection noise of our imaging system, the limit in squeezing we observe is close to -8 dB. When the RF calibration is well behaved, this is the level of detection we should expect from our other squeezing measurements.

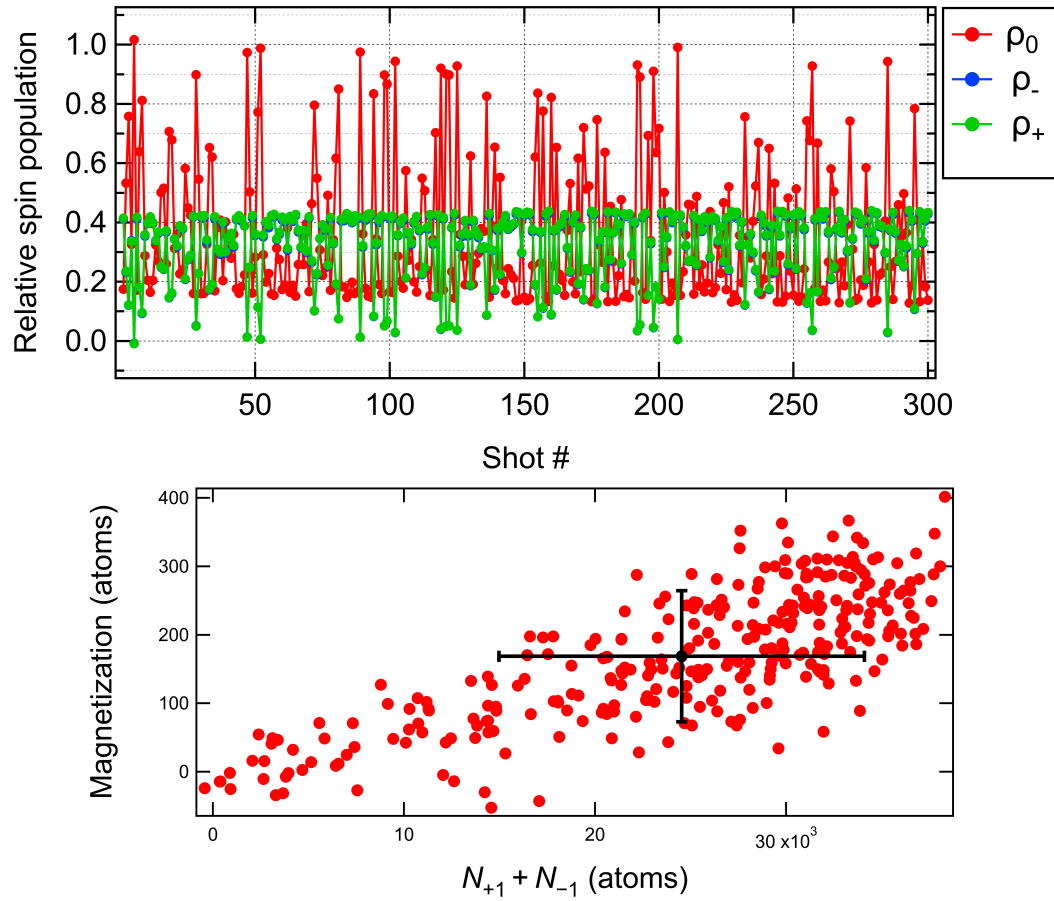


Figure 3.43: Number squeezing data in the cross trap taken for 300 shots. Magnetic field is quenched to well below the critical field and spin mixing is allowed to occur for a few hundred milliseconds.

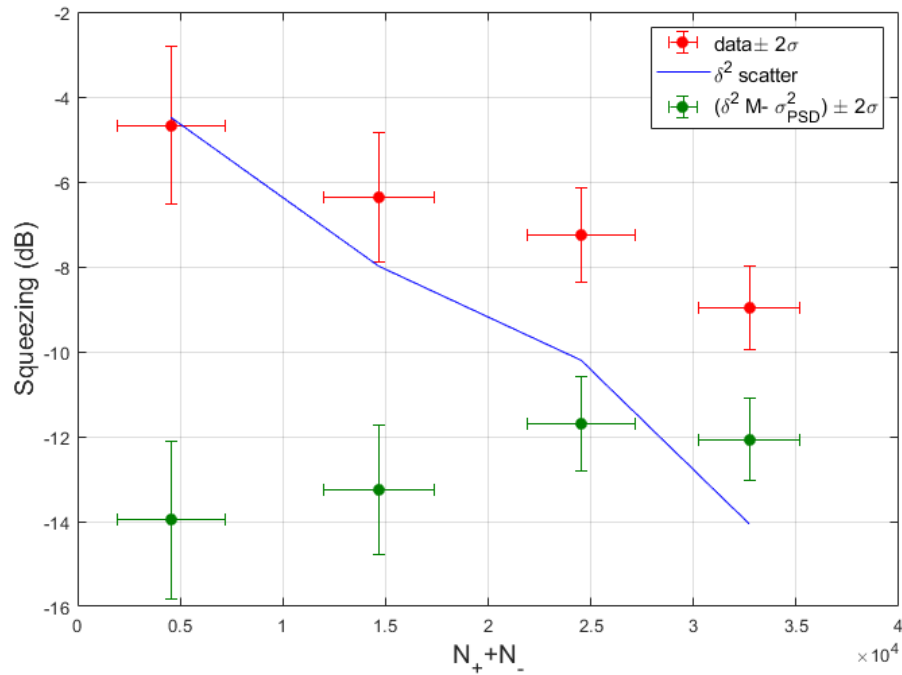


Figure 3.44: Number squeezing data analysis shows good amount of detectable squeezing and confirms predicted detection limit. RF calibration data also taken on this day and show good agreement with CPA estimate, making this a reliable value. Red points are raw amounts of detected squeezing, meaning they do not have the estimated detection noise subtracted off (see green points). Points are binned and then data is averaged to compute squeezing amount; Data here represents 300 shots divided into four bins.

## CHAPTER 4

### DENSITY-INDUCED SQUEEZING

As mentioned previously chapter 1, the concept of pressure-tuning of a quantum phase transition is quite prolific in condensed matter systems, but has yet to be fully realized in a cold atom context. Here we take this idea of pressure-tuning and translate it to our system by modifying the cloud density. In doing this we effectively move the quantum critical point (QCP) to cross our quantum phase transition (QPT). We do this by modifying the trap power of our system, dynamically changing the trap density. In doing so, we are able to push our system into an interacting phase, allowing the system to undergo spin mixing and even spin-nematic squeezing. We characterize the shift in the energy gap, and are able to observe squeezing of up to  $-8.4 \pm 0.8$  dB. The hope is that this technique can be used further in our studies and used to generate other forms of quantum phenomenon such as parametric squeezing and the engineering of a Dicke state.

#### 4.1 Quantum Phase Transitions

Quantum phase transitions (QPT's) are distinguished from traditional phase transitions in that they occur at or near zero temperature. Thus, the crossing of the transition is accomplished by quantum fluctuations, as opposed to thermal fluctuations. In our case, the zero dimensionality of our system (see subsection 2.1.2), leaves the spin interactions as the relevant part of the dynamics. Many phase transitions are characterized as first-order or continuous phase transitions. In the latter case, typically an order parameter is defined for the system and denotes the change from one phase to another. For our system, the relevant order parameter is that of the transverse spin,  $S_{\perp}$ . The values of  $S_{\perp}$  on either side of the

phase transition are [69]:

$$\begin{aligned}
 S_{\perp} &= 0, \text{ for } q > 2|c| \text{ the polar phase} \\
 S_{\perp} &= \sqrt{1 - \frac{q^2}{4|c|^2}}, \text{ for } q < 2|c| \text{ the BA phase.}
 \end{aligned}
 \tag{4.1}$$

Here we recall that the quantum critical point for our system occurs at  $q = 2|c|$ , and BA denotes the broken-axis symmetry phase. The polar phase is where we initialize our system to be entirely in the ground state  $|F = 1, m_F = 0\rangle$ , see Equation 3.27.

Furthermore, the expressions shown in Equation 3.26, are a result of using Bogoliubov theory to approximate the excitations created when crossing the phase transition. The spin-1, ferromagnetic ground state can be shown to contain three such excitation modes; one of which, has an non-trivial eigenvalue [57, 102]. We define this as the energy gap, or the excitation energy,  $\Delta_E$ , between the ground and first excited state. These are the expressions shown for our coherent oscillations shown in Equation 3.26. With this in mind, we can begin to explore how one might cross the quantum phase transition from the polar phase to the broken-axis phase.

## 4.2 Ways to Cross our Quantum Phase Transition

Here, we explore the crossing of a quantum phase transition in a spin-1, ferromagnetic BEC. By changing the relationship between the quadratic Zeeman energy and the density of the BEC, we can control the spin dynamics across the critical point between a polar phase to a broken-axis phase. Typical experimental procedures traverse the two quantum phases through a magnetic field quench. This has its drawbacks however experimentally, as it can lead to changes in field stability while the field is quenching in a finite amount of time. Our technique instead performs the “quench” by changing the density of the cloud itself, inducing the interaction phase for the spinor atoms.

If we recall, the relevant dynamics of our spin-1 system can be reduced to a two-term

Hamiltonian represented by a competition between the spin interaction energy of the atoms and the effect of the magnetic field. Taking  $\hbar$  to be 1, and a magnetic field to be aligned along the  $\hat{z}$ -axis, we reference the Hamiltonian described earlier in Equation 2.12 with:

$$\hat{H} = \frac{c}{2}\hat{S}^2 - \frac{q}{2}\hat{Q}_z. \quad (4.2)$$

Here again,  $c$  is known as the spinor dynamical rate and describes the spin interactions. For rubidium the value of  $c$  is negative, making the condensates ferromagnetic in nature. Moreover, the exact value of  $|c|$  for the condensates is also density-dependent subsection 4.2.2, with  $|c| \propto N^{1/3}$ , where  $N$  is the number of atoms in the condensate. The combination of this value with the total spin vector operator ( $\hat{S}^2 = \hat{S}_x^2 + \hat{S}_y^2 + \hat{S}_z^2$ ), make up the full spin interactions for the system. The value of  $q$  corresponds to the quadratic Zeeman energy for a given magnetic field magnitude,  $B$ , expressed by  $q = q_z B^2$ , where  $q_z \approx 71.6 \text{ Hz/G}^2$ .  $\hat{Q}_z$  again takes the form of  $\hat{Q}_z = 2\rho_0 - 1$ , where  $\rho_0$  is defined as the fractional population in the  $m_F = 0$  hyperfine sublevel, normalized to the total number of atoms. Using the relation  $1 = Q_z^2 + Q_\perp^2 + S_\perp^2$ , with  $Q_\perp^2 = Q_{xz}^2 + Q_{yz}^2$  and  $S_\perp^2 = S_x^2 + S_y^2$  defined earlier in Equation 2.26, the combination of these mean-field terms yield an expression for the energy of the system, and dictate which mean-field phase we are in.

#### 4.2.1 Conventional Magnetic Field Quenching

As can be seen from Equation 4.2, crossing the QPT from the polar phase into the BA phase can be achieved by either decreasing  $q$ , or increasing  $c$ . Our typical experimental procedure uses many magnetic fields to prepare and initiate the state. The condensate is initialized at a high bias field along the  $\hat{z}$  axis, where the polar phase dominates, until we are ready to allow atomic interactions to take place.

For the reasons noted above, decreasing  $q$  is fairly straightforward by simply lowering the magnetic field ( $B$ ), as  $q \propto B^2$ ; but this when implemented experimentally tends to add

restrictions to the rate at which the bias magnetic field can be changed, due to the hysteretic nature of the coils. Additionally, because we in general use linear ramps for our magnetic fields, the ratio of  $q(t)/|c|$  changes quadratically as the field changes, making the dynamics even more sensitive to changes in the field. Nonetheless, we have found this to be workable for many experiments, even for those that require sensitive and stable dynamics, such as spin-nematic squeezing and spin mixing.

### *Conventional Spin-Nematic Squeezing and Spin Mixing*

As seen in a previous section (subsection 3.9.5), this leads to an oscillating population in  $\rho_0$ . These dynamics can be modeled for the given quench field and measured  $|c|$  value. The damped oscillation of the atoms is faster for higher densities in the cloud and are shown below (Figure 4.1) for a normal magnetic quench at high densities. The quench from high

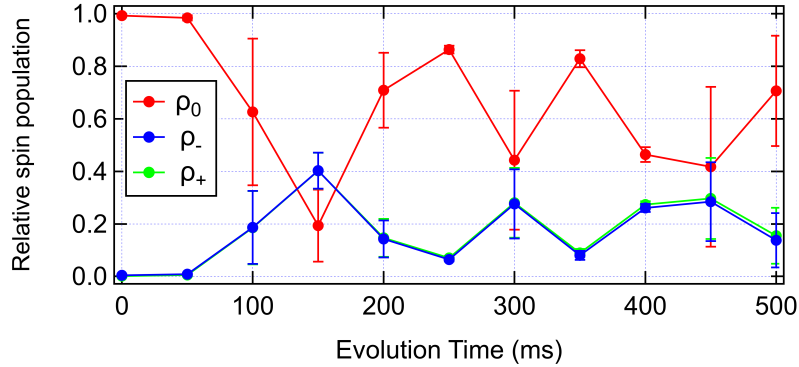


Figure 4.1: Normal high density spin mixing from a magnetic quench

field to low field takes around 7 ms to change, with 4 ms being used to change the field itself, and 3 ms used to wait for the field to stabilize. The time in the spin mixing axis shows the evolution time for the atoms held in the trap after the magnetic quench. The crossing of the QCP leads to pairwise creation out of  $m_F = 0$  to  $m_F = \pm 1$  as discussed earlier.

This pairwise creation leads to squeezing, as the created pairs are correlated, due to the conservation of the initial angular momentum of  $M = 0$ , where  $M = N_+ - N_-$  and represents the magnetization for the system. The noise fluctuations of this parameter change

exponentially and vary as a function of spinor phase,  $\theta_s$ . The spinor phase is defined as the relative phase between the spin-1 components:  $\theta_s = \theta_+ + \theta_- - 2\theta_0$ . In our discussions of the spin-1 space (section 2.4), the “spin-nematic sphere” was discussed. This is comprised of the sphere with axes  $(\hat{S}_\perp, \hat{Q}_\perp, \hat{Q}_z)$ . The initial state is centered at the pole of  $\hat{Q}_z$ , and the total noise of the state has a noise of  $1/\sqrt{N}$  in both the  $\hat{S}_\perp$  and  $\hat{Q}_\perp$ . Once the QCP

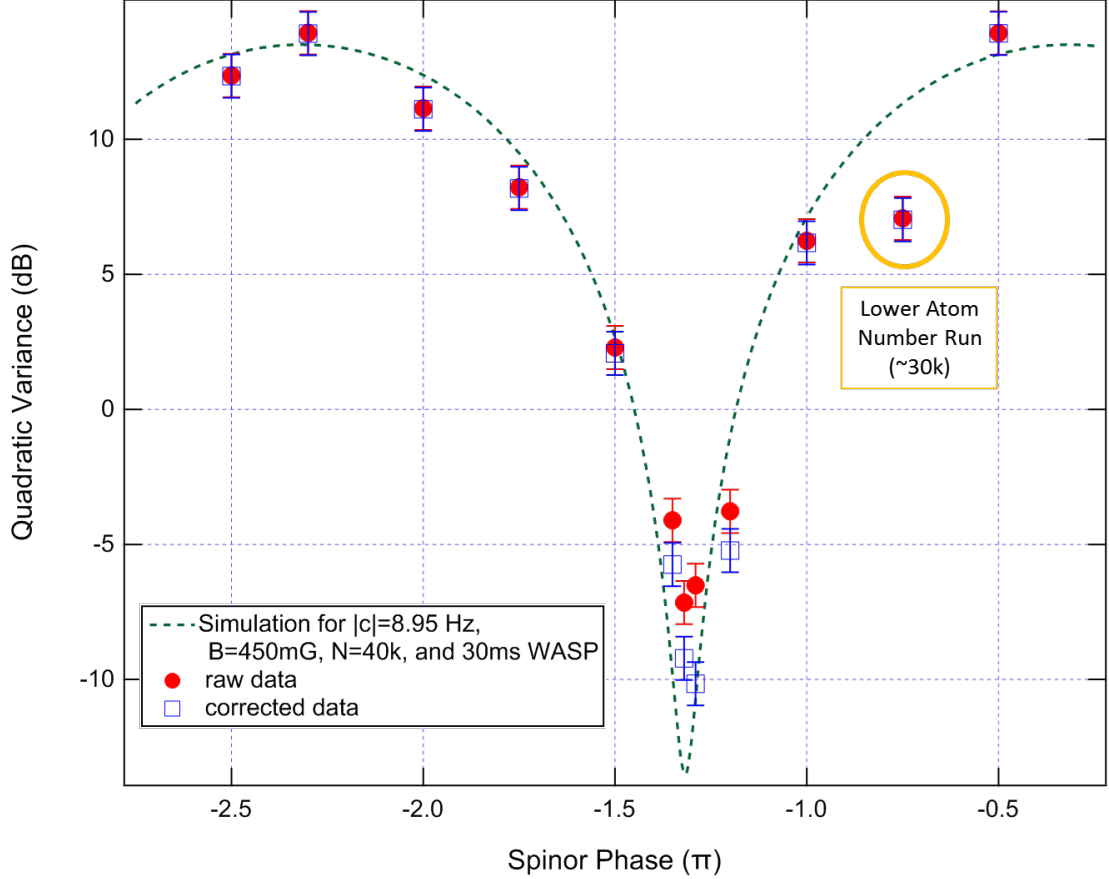


Figure 4.2: Normal SN squeezing in the crossed dipole trap

is crossed with a magnetic field quench, the noise grows exponentially in the variance of  $\hat{S}_\perp$  and  $\hat{Q}_\perp$  variables. The quadratic variance relative to the initial unsqueezed state can be expressed as the squeezing parameter [75]:

$$\xi_\theta^2 = 10 \log_{10}(\Delta^2 M_{meas} / \tilde{N}_{meas}), \text{ decibels} \quad (4.3)$$

where  $\tilde{N}$  is the average number of detected atoms in the condensate. This expression is the

one plotted in Figure 4.2 for various spinor phases. The figure shows a simulation using a mean-field representation of the variables. Despite this being a quantum process, the large number of atoms make the simulation a good fit to the dynamics. More will be said about this type of simulations in the next sections.

Interestingly, we see an atom number effect on the squeezing data. In runs where the atom number is temporarily lower by 25%, the dynamics change in an appreciable way. This is a prelude to the effect atom number can have on the density, and shows an alternative way in which we can cross the QCP. We hope to replicate the experiments shown here using a traditional magnetic field quench, with that of a new form of quenching technique.

#### 4.2.2 Optical Trapping Modulation

While magnetic field quenches affect the quadratic Zeeman term in the Hamiltonian, the spin interactions, governed by the  $cS^2$  term, typically are taken to be unchanging or slowly decaying, due to the finite lifetime of the trap. However, we can intentionally change  $c$  independently by noting that  $c$  itself is dependent on the atom number, and more precisely the integrated density over the cloud [92]. Thus in order to change  $c$ , there are two main options: changing the number atoms in the condensate, or decreasing the volume of the existing cloud to increase its density. The former was attempted in several ways and is described in section 5.1. The latter was explored in various ways, but eventually found success in a two-trap laser configuration.

Recall from subsection 3.2.1 that the single focus trap potential of our 10.6  $\mu\text{m}$  laser is given by:

$$U_{QUEST}(0) = \frac{1}{4\pi\epsilon_0} \frac{4\alpha}{c\omega_0^2} P, \quad (4.4)$$

and the potential for the cross trap laser is given by:

$$U_{FORT}(0) = \frac{3\pi c^2}{2\omega_0^2} \frac{\Gamma}{\Delta} I(0). \quad (4.5)$$

Here,  $\omega_0$  is the D2 resonance line for rubidium,  $\Gamma = \omega_0^2 e^2 / 6\pi\epsilon_0 c^3 m_e^2$ , and  $\Delta$  is the difference in the laser's frequency from resonance;  $I(0) = 2P/\pi w_0^2$  for power ( $P$ ) and waist ( $w_0$ ) of the intensity of a focused Gaussian beam [98]. Combining these potentials gives,  $U_{tot} = U_{QUEST} + U_{FORT}$ .

Additionally, we note that the spin collisional term,  $c$ , in the trap can be written as being proportional to [92]:

$$c = c_2 N \int |\phi(\vec{r})|^4 d^3r, \quad (4.6)$$

where  $|\phi(\vec{r})|^2$  is the normalized Thomas-Fermi density profile and  $c_2$  is spin interaction coefficient presented previously in subsection 2.1.1 and is the spin interaction energy given by:  $c_2 = 4\pi\hbar^2\Delta a/3m$  [92] for the difference in the s-wave scattering lengths for rubidium,  $\Delta a = a_{F=2} - a_{F=0}$ . From this it is easy to see how  $c$  relates to density  $n(r)$  when we note that:

$$N \int |\phi(\vec{r})|^4 d^3r = \frac{4}{7}n_0, \quad (4.7)$$

as  $n_0$  is defined as the peak density of the condensate. This is important as the equation for the peak density is  $\propto \mu$  (the chemical potential for the condensate). We can calculate  $\mu$  by calculating the average trap frequencies from our combined potential,  $U_{tot}$ . Noting that the trap potential can be approximated like a harmonic potential in each direction for sufficiently low temperatures such that,  $\omega_i \propto \sqrt{U_{tot}}$  for the high and low frequencies of the trap [92]. Since  $U_{tot} \propto P$ , this gives  $\omega_i \propto \sqrt{P}$  as well. The average trap frequency is equivalent  $\omega_{avg}^- = (\omega_L\omega_H^2)^{1/3}$  for the geometry of our trap. Using this, we can use the relation for the peak density of the condensate, defined as:

$$n_0 = \frac{15N}{8\pi R_L R_H R_H}, \quad (4.8)$$

where  $N$  is the number of atoms in the condensate;  $R_L$  and  $R_H$  are the radii associated with the low and high trap frequencies defined as  $R_i = (15Nc_0/4\pi m\omega_i^2)^{1/5}$ , with  $c_0 = 4\pi\hbar^2\bar{a}/m_{Rb}$  being the two-body, spin-dependent interaction term for rubidium with average

scattering length  $\bar{a} = (a_{F=0} + 2a_{F=2})/3$  [92]. Combining these relations we find that  $R_i \propto \omega_i^{-2/5}$  and thus  $R_i \propto P^{-1/5}$ . Furthermore, with  $n_0 \propto 1/R_i^3$ , we find the peak density in the trap is related to changes in power by:  $n_0 \propto P^{3/5}$ .

These relations are important as we care about the effect that the trap properties, such as the power, has on the value of  $c$ . The relationship between the peak density and  $c$  is straightforward, using Equation 4.7:

$$\begin{aligned}
 c &= \frac{4n_0c_2}{7} \\
 \rightarrow c &\propto n_0 \\
 \rightarrow c &\propto P^{3/5}.
 \end{aligned}
 \tag{4.9}$$

Thus, we can find a way to modify  $c$  by changing the trap potential  $U_{tot}$  via the trap power(s). The easiest way to do this is by directly changing the trap power. The experimental implementation of this will be demonstrated below.

### *Experimental Implementation of Density Modulation*

Our condensate is created in a single optical dipole trap (ODT), with a 10.6  $\mu\text{m}$  wavelength, and is tightly confined enough to abide by the single mode approximation. We can however add a second laser to intersect with the primary ODT and overlap with the trapped condensate to create a crossed dipole trap. We typically do this in our normal interacting experiments to create a cloud with higher density, which increases the rate at which dynamics occur after a typical magnetic quench to a lower field.

If instead, we modify the crossed laser's power, we can change the waist of the laser, and thus the trap volume. The initial state of our condensate is prepared by performing an evaporative ramp with the 10.6  $\mu\text{m}$ , while applying a strong magnetic field gradient to purify the condensate's ground state to be in the magnetically-insensitive sublevel of  $|F = 1, m_F = 0\rangle$ . This can also be written as  $\rho_0 = 1$ , where  $\rho_0 \equiv N_0/N_{total}$ , representing the number of atoms in the  $|F = 1, m = 0\rangle$  ground state, normalized to the total number of

atoms. Near the end of the evaporative ramp, we add an 850 nm diode laser as a second trap and overlap it with our 10.6  $\mu\text{m}$  trap. From there, the 850 nm trap power is ramped up to increase the density of the cloud. This is ordinarily where the condensate state preparation would end, and where typical magnetic field quench experiments would begin.

Instead, we hold the crossed trap at high density for several 100 ms until the atom number decays to a certain value. This is done to allow the cloud to have approximately the same atom numbers when we perform a second ramp up of the 850 nm laser to different final powers to create different densities for the final cloud. Figure 4.3 depicts a schematic of the relevant experimental timings. The initial crossed laser is first ramped up to high power while the bias magnetic field is still high. The intensity of the second trap beam is then dropped, followed by a magnetic field quench to finite field 100 ms after and before the second trap is lowered and raised respectively to its lowest and final powers. The reasons for doing this are two-fold, and are primarily chosen to illustrate the technique of ramping the density. Firstly, the lowest final power of the 850 nm laser is chosen to give an appreciable increase in the density and appearance from our traditional single trap condensate. Secondly, we would like to demonstrate the effect of our technique by showing that the final state of the condensate does not evolve greatly from the initial state after we perform the field quench to a finite level. (This is demonstrated further in our spin mixing experiments shown in Figure 4.7).

### 4.2.3 Simulation of Density-Quench

We can measure the effect of our density ramp protocol by looking at the state evolution of the cloud. This can be done by holding the cloud in the dual laser trap for a various amount of time ranging from 150 ms to 400 ms at a chosen magnetic bias field. Given our system, the state will evolve once a ratio of  $|q|/c < 2$  is reached, or when we have crossed the phase transition. The state of the condensate is projectively measured at each field value to see if there is any evolution away from the ground state. In our case, this will result in a

departure of the state from  $\rho_0 = 1$  (the ground state of the polar phase), to  $\rho_0 < 1$  when the field is below the critical field. This point where evolution takes place allows us to calculate the value of  $|c|$  for the system. Since we know the critical field occurs at  $q/|c| = 2$ , we can measure the impact the second laser's power has on the condensate's density. For our procedure, the sequence in Figure 4.3 is followed, and the final bias field is quenched to a finite value. If we use the 850 nm at its lowest trapped setting, and measure the state for different fields, we find evolution away from the ground state starts at around 390 mG ( $\pm 5$  mG) with a calculated  $|c|$  value of around  $2\pi * 5.4 \pm 0.1$  Hz. When we increase the second laser power to a higher power, the evolution from the ground state for this setting occurs around 535 mG, giving a  $|c|$  value of  $2\pi * 10.2 \pm 0.1$  Hz. This demonstrates the effect our technique can have on the density of the cloud. As we will show next (subsection 4.3.1), it also affects the long term behavior of the dynamics.

### *Mean-Field Simulations of Density-Induced Quench*

To simulate the dynamics of the density-induced quench, we need to first generate an ensemble of atoms which mimics the quantum distribution. For the number of atoms we have in the condensate (around 20,000-25,000 for these studies), we may use semi-classical, mean-field estimations to perform the simulations with good accuracy. We first define a distribution with coherent or Poissonian noise distribution proportional to  $1/\sqrt{N}$ . This can be done by noting the uncertainty relationship between the spin-nematic variables that we introduced in section 2.3.

A further important test of the system's ability to cross the quantum phase transition is the generation of a spin-nematic squeezed state. Squeezing involves the measurement of the noise in a conjugate pair of variables. Looking at an example of a coherent, spin-1/2 system with Pauli spin matrices,  $\hat{S}_i$ , the commutation relation from such a pair of variables is:

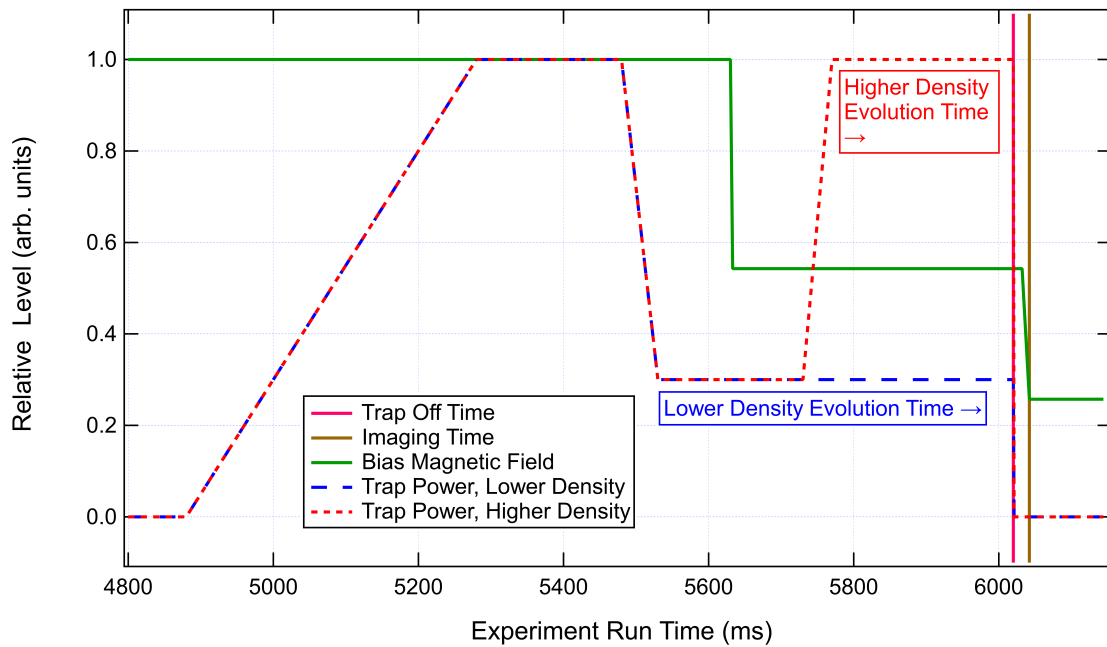


Figure 4.3: Experimental timings used to generate mean-field spin mixing dynamics for both the simulations and the spin mixing data shown below. Shows the experimental procedure used to generate higher densities for the condensate. A magnetic field quench occurs 100ms before a 40 ms final ramp of the second trap’s power, which is used to increase the density of the condensate past the critical point. An extended hold time is shown here to depict how long the evolution time is for the critical field measurements shown below Figure 4.6.

$$\left[ \hat{S}_i, \hat{S}_j \right] \geq i\epsilon_{ijk} \hat{S}_k. \quad (4.10)$$

This equates to an uncertainty relation of:

$$\langle \Delta \hat{S}_i^2 \rangle \langle \Delta \hat{S}_j^2 \rangle \geq |\langle \hat{S}_k \rangle|/4. \quad (4.11)$$

This works in the case where non-commuting variables have a non-zero expectation value. To compare this to a spin-1, we look at the two non-commuting variables of our system:  $\hat{S}_y$  and  $\hat{Q}_{xz}$  (or equivalently up to a minus sign,  $\hat{S}_x$  and  $\hat{Q}_{yz}$ ). The commutation relationship between these two operators is [86]:

$$\left[ \hat{S}_{y(x)}, \hat{Q}_{xz(yz)} \right] \geq (-)2iN. \quad (4.12)$$

This then gives us an uncertainty relation of:

$$\langle \Delta \hat{S}_{y(x)}^2 \rangle \langle \Delta \hat{Q}_{xz(yz)}^2 \rangle \geq N. \quad (4.13)$$

This is the uncertainty in the number basis ( $|N_{-1}, N_0, N_{+1}\rangle$ ). It should be noted that the previous presentation of these variables Equation 2.26 used in the construction of the spin-nematic sphere were of the form:  $Q_{\perp}^2 + S_{\perp}^2 + Q_z^2 = 1$ . These are for the normalized variables,  $S_i$  and  $Q_{jk}$ . They have a noise spread of  $\Delta S_y$  and  $\Delta Q_{xz} \sim 1/\sqrt{N}$  and in the mean-field,  $\{\rho_0, \theta_s\}$  space.

Additionally, we used expressions for the transverse as represented by  $\hat{S}_{\perp}^2 = \hat{S}_x^2 + \hat{S}_y^2$  and  $\hat{Q}_{\perp}^2 = \hat{Q}_{xz}^2 + \hat{Q}_{yz}^2$ . These relations are useful and help us simplify the representations for the expected squeezing of the state. As was noted in the work of Chris Hamley [86], the spin-nematic spaces of  $\{\hat{S}_y, \hat{Q}_{xz}, \hat{Q}_z\}$  and  $\{\hat{S}_x, \hat{Q}_{yz}, \hat{Q}_z\}$  are degenerate and the dynamics in each space are equivalent and related by an oscillating phase. As such, we can reduce the dynamics to one scalar value for both the  $S_{\perp}$  and  $Q_{\perp}$ . These are the variables used in

the simulations, using the normalized and mean-field variables,  $\rho_0$  and  $\theta_s$ .

The initial state of our condensate can be modeled as a coherent state, created in the polar ground state,  $\rho_0 = 1$  (as described above), leaving no atoms in the  $m_f = \pm 1$  states. Due to this experimental approach, we note that the magnetization of the system is equal to zero, as it is defined as  $m = M/N_{total} = (N_+ - N_-)/N_{total}$ . This means the magnetization will be conserved throughout our experiment, and simplifies some of the simulations. We can use the mean-field expressions described in section 2.4. Looking at the energy functional for the mean-field representation in Equation 2.19, the setting of  $m = 0$  simplifies the expression to:

$$\mathcal{E}(m = 0) = c\rho_0(1 - \rho_0)[1 + \cos\theta_s] + q(1 - \rho_0). \quad (4.14)$$

Taking the canonical derivatives of this expression,  $\dot{\rho}_0 = \frac{2}{\hbar} \frac{\partial \mathcal{E}}{\partial \theta_s}$  and  $\dot{\theta}_s = \frac{2}{\hbar} \frac{\partial \mathcal{E}}{\partial \rho_0}$ , we can find the dynamics around the  $\rho_0, \theta_s$  space for  $\hbar = 1$  to be:

$$\dot{\rho}_0 = 2c\rho_0(1 - \rho_0) \sin \theta_s \quad (4.15)$$

and,

$$\dot{\theta}_s = -2q + 2c(1 - 2\rho_0)(1 + \cos \theta_s). \quad (4.16)$$

We generate our initial state by specifying a coherent distribution, as described earlier for  $S_\perp$  and  $Q_\perp$  with a standard deviation of  $\sqrt{1/N}$ . A random value is generated within this normalized distribution for each. This is then substituted in to the mean-field expressions, shown in Equation 2.24 and section 2.4, to give the initial  $\rho_0$  and  $\theta_s$  states:

$$\begin{aligned} 1 &= Q_{\perp,ini}^2 + S_{\perp,ini}^2 + Q_{z,ini}^2 \\ 1 &= Q_{\perp,ini}^2 + S_{\perp,ini}^2 + (2\rho_{0,ini} - 1)^2 \\ \Rightarrow \rho_{0,ini} &= (1 + \sqrt{1 - S_{\perp,ini}^2 - Q_{\perp,ini}^2})/2. \end{aligned} \quad (4.17)$$

Likewise,

$$\theta_{s,ini} = \arctan Q_{\perp,ini}/S_{\perp,ini}. \quad (4.18)$$

The initial random values are then inserted into Equation 4.15 and Equation 4.16 and numerically integrated at each time step (for a total time of 500 ms with a time step of 50  $\mu$ s). This is done 1000 times to obtain statistics and standard deviations for the dynamics. The value of  $c$  in Equation 4.15 and Equation 4.16 is written to start after the quench from highest field to a finite field (which is still well above  $q > 2|c|$ , as  $q/|c| \sim 10$ ). The ramp of the density follows what is depicted in Figure 4.3, except for the squeezing protocol which has a faster final ramp of the density (10 ms ramp as opposed to 40 ms for the spin mixing experiments). During the times at finite field, when the density is being ramped to higher value or being held at its lowest value, a lifetime of  $c_{real} = ce^{-2t/5\tau}$  is used to reflect the realistic atomic decays from the trap. The lifetime  $\tau$  is measured for each experimental crossed trap power used and is put into the simulation for each stage. As can be seen in Figure 4.4, the dynamics show good agreement with the measured spin mixing data depicted in Figure 4.8. Likewise, the simulation curves depicted in Figure 4.9, also show excellent agreement with the measured experimental data. This shows that our simulation of the mean-field dynamics is well-captured using the density ramp procedure described here.

### 4.3 Checking for Effects of the Density-Increasing Ramp

Now that we can model and describe the changing effects of our experimental sequence on the atoms, we can try observing the dynamics and behaviors of the atoms in a number of typical experiments we perform in our typical experimental protocol involving a magnetic field quench. The quench will instead be performed by the increase in atomic density to move the system between two quantum phases.

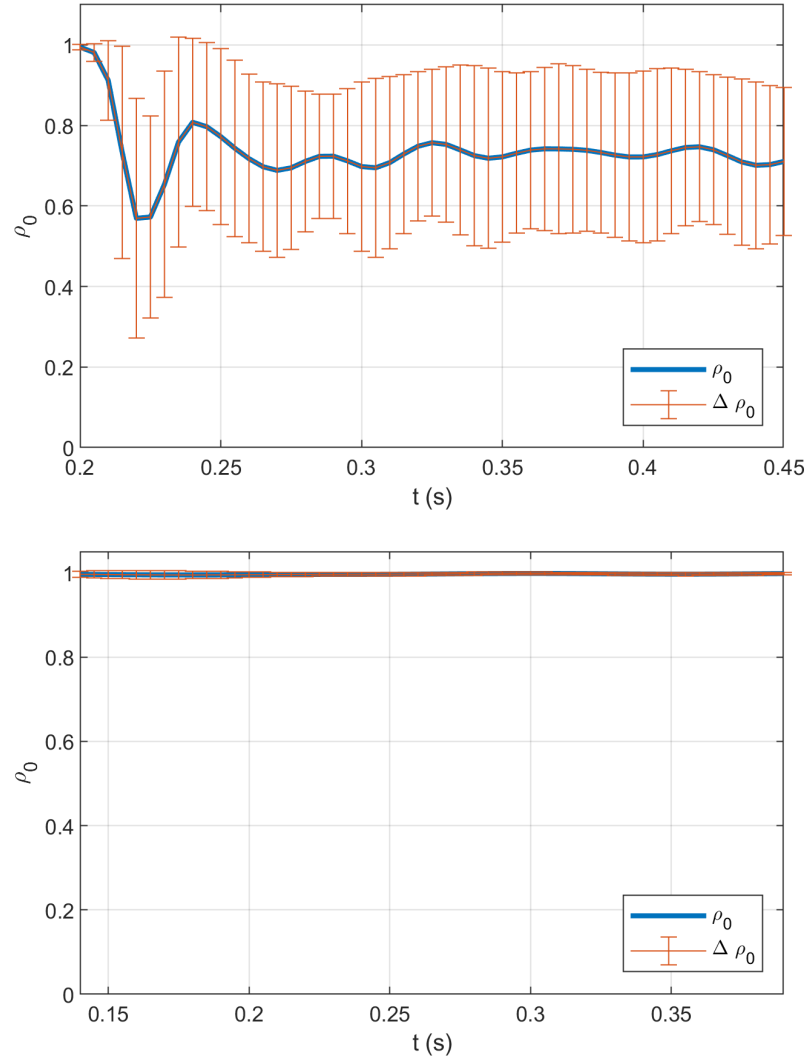


Figure 4.4: Mean-field spin mixing simulations for over 1000 samples and 27,000 atoms. Experimental values of the magnetic field, cloud density ( $|c|$ ), and evolution time for low and high densities used to compute  $\rho_0$  population for longer evolution times. Optical trap power ramp for 850 nm follows procedure depicted in Figure 4.3. Good agreement is found between these simulations and the spin mixing data in Figure 4.8.

### 4.3.1 Coherent Oscillations of Energy Gap

As introduced in subsection 3.9.4, we can use the Bogoliubov approximation and mean field theory to write an expression for the energy gap between the ground and first energy level of the condensate [43, 57]. The equations for this can be written (as noted in Equation 3.26) as:

$$\begin{aligned}\Delta_P &\equiv f_P = 2\sqrt{q(q+2c)}, \\ \Delta_{BA} &\equiv f_{BA} = 2\sqrt{c^2 - q^2/4}.\end{aligned}\tag{4.19}$$

This energy gap for both the polar and broken-axis phase is defined for a given quadratic Zeeman energy ( $q$ ) and spinor interaction energy ( $c$ ). Thus by changing  $|c|$ , we can shift the location of the quantum critical point, and change the atomic interaction to be interacting or non-interacting, depending on whether the chosen bias field is below or above  $q = q_{critical} = 2|c|$ , respectively.

To measure our ability to reliably shift the quantum critical point and energy gap of our system, we take a series of coherent oscillation measurements with the same procedure as relayed in subsection 3.9.4. The results of this are shown in Figure 4.5. By initializing the state in the polar ground state, we can perturb it slightly away from this state and measure the population oscillations in the mean-field observable  $\rho_0$  (see subsection 4.3.1). The fit to the rate of this oscillation gives us a prediction for the value of  $c$ , given a known value of  $q$ . We average over three runs for three different values of  $q/|c|$  all residing in the polar phase. This is done for two different power ramps of the crossed dipole trap (850 nm) laser, which produce a lower and higher density trap, increasing  $|c|$  for higher powers of the laser. The ramp is the same as shown in Figure 4.3. In doing this, we can see that the energy gap of our system can be definitively shifted to produce a noticeable shift in the quantum critical point, meaning we can shift the system between the polar and broken-axis symmetry phases by increasing the crossed dipole trap power for a given, fixed bias field. The increase in

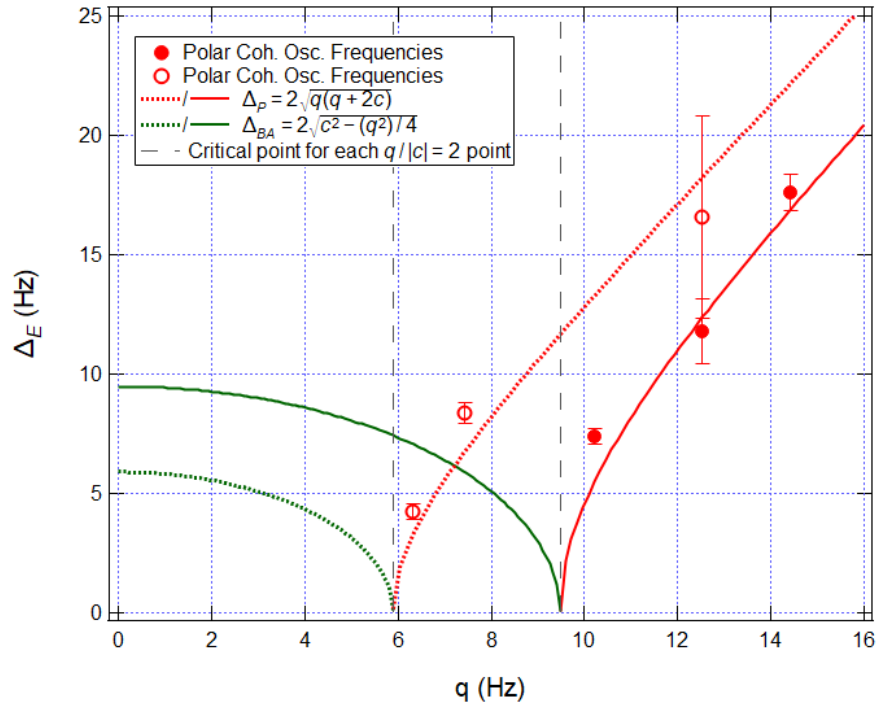


Figure 4.5: Shows stability of phase-space dynamics after the optical trap ramp of the 850 nm laser. The  $|c|$  values from the coherent oscillation fits are good predictions that are in agreement with the critical field scans shown in Figure 4.6. Ability to change density of cloud, allows us to tune and shift the quantum critical point (dashed lines) of the condensate. Green and red curves depict the broken-axis and polar energy gap predictions from the critical field measurements.

$|c|$  is measured to be nearly double ( $|c_{high}|/2\pi = 10.2$  Hz) that of the lowest 850 nm laser potential ( $|c_{low}|/2\pi = 5.4$  Hz).

A second test of the density is done, involving a critical field scan (see subsection 3.9.3). This procedure is another standard technique typically performed by holding the atoms in the trap for a set amount of time and watching their evolution in  $\rho_0$ , while the bias magnetic field is quenched to different values. For fields that are below  $q = 2|c|$  for a respective  $|c|$  value, pairwise creation of atoms in  $|F = 1, m_F = 0\rangle$  (or  $\rho_0$ ) into  $|F = 1, m_F = \pm 1\rangle$  is seen and the fractional population of  $\rho_0 = N_0/N_{total} \approx 1$  starts to decrease. This allows us to extract the value of  $|c|$  by observing the field at which this occurs. Of course, we are interested in what value will be found for a density quench, instead of a magnetic field quench. This is achieved by following the same crossed dipole trap ramp as shown in Figure 4.3, and used in the coherent oscillations discussed above. We quench the magnetic field to a set value above the critical point, and then perform a ramp up of the crossed dipole trap power to increase  $|c|$  to a point where pairwise creation can begin to occur.

If we prepare a condensate that is held for 390 ms at low power and 290 ms at high power (times which are sufficiently long to observe the evolution away from the ground state of  $\rho_0 = 1$ ), we observe a critical field at 390 mG for the crossed dipole trap's lowest density. For the highest trap density, we find a critical field of 535 mG (see Figure 4.6). This corresponds to a calculated density of  $|c_{low}|/2\pi = 5.4$  Hz  $\pm 0.1$  Hz and  $|c_{high}|/2\pi = 10.2$  Hz  $\pm 0.1$  Hz. Comparing this to the fits given by the coherent oscillations, we find good agreement. In fact, if we use the  $|c|$  values obtained in the critical field measurements, we can plot the energy gap shift (as seen in subsection 4.3.1), and find that the measured coherent oscillation points and their error bars confirm the reliability of the shifting of the energy gap for various quenches to differing cross trap powers.

As an aside, if we numerically estimate the density of the trap by using the formulas specified in Equation 4.4 and Equation 4.5, we also predict a similar, significant increase in the trap density for the given experimental parameters. However, there is a bit of an over-

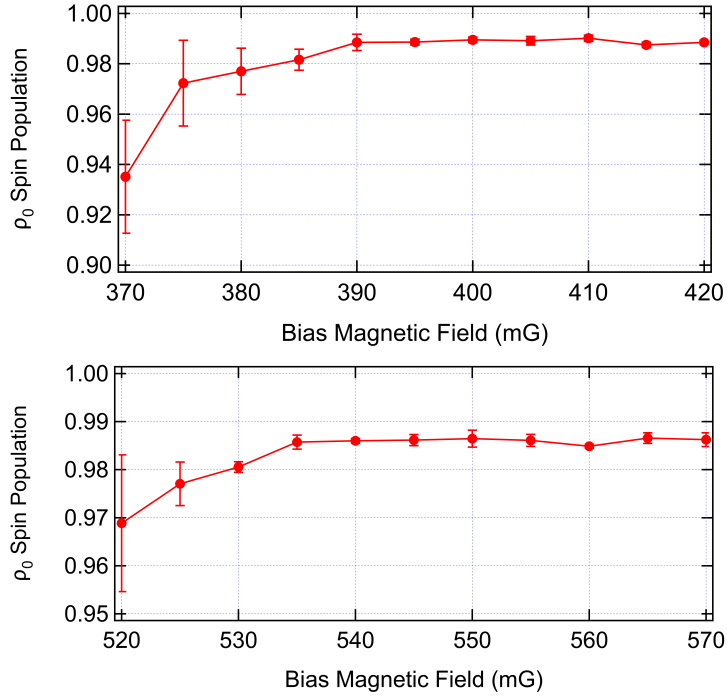


Figure 4.6: Depiction of the relevant experimental parameters for the density quench performed using a second laser trap to confine the spin-1 condensate, and eventually cross the critical point. **Above** depicts critical field measurements for the lowest and highest density of the condensate. Here a 40 ms ramp to the highest second trap laser power is shown to increase the measured condensate density (or  $|c|$ ) value by nearly a factor of two, with the lowest density in the second trap having  $|c| = 2\pi \cdot 5.4 \pm 0.1$  Hz and the highest density having  $|c| = 2\pi \cdot 10.2 \pm 0.1$  Hz. This value is atom number-dependent and obtained after 200ms of evolution time (for highest density second trap power), averaged over three runs.

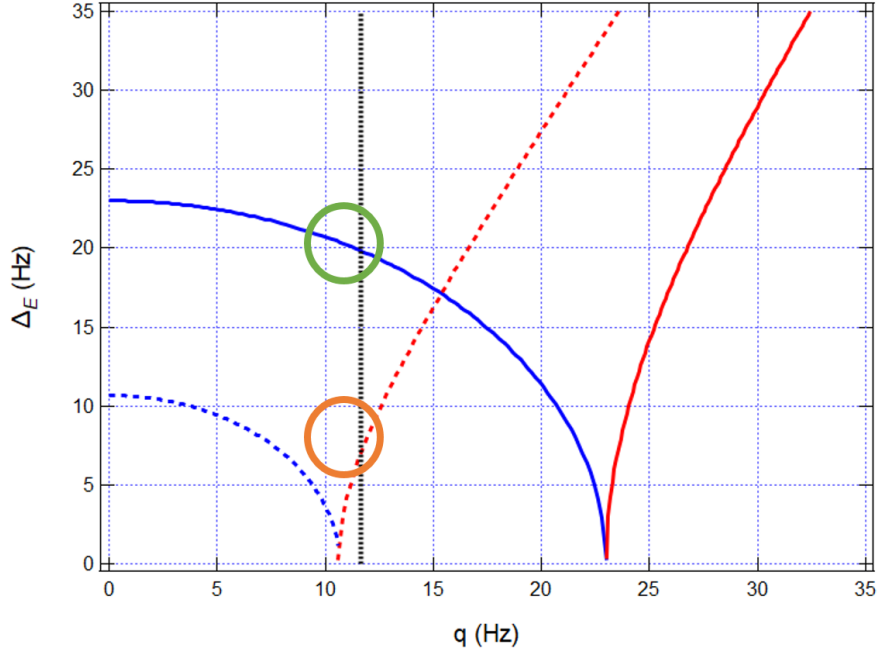


Figure 4.7: The energy difference ( $\Delta$ , red solid line) delineates the polar phase and the broken-axis symmetry phase of the system. The critical point occurs at the value  $q/|c| = 2$  (dashed line). In general, the phase transition can be crossed by either lowering the magnetic field,  $q$ , or increasing the density of the system,  $|c|$ . Spheres depicted here show the energy contours for the spin-1 system above and below the critical point.

estimation in the predicted density for the highest cross trap laser power ranging anywhere from 15-30% over the estimate given from the critical field measurement. This discrepancy is largely attributed to an inaccuracy in the estimation of the waist and the exact atom number, due to the finite lifetime of the high density trap. Overall however, the dynamics and stability of  $|c|$  are consistent from run to run and moreover, show good agreement with the mean-field simulations described above. This will be shown in greater detail in the section below.

#### 4.3.2 Density-Induced Spin Mixing

To show that the effects of the increased trap density can extend to the effects in the spin dynamics, we perform a series of canonical spin interactions. The first of these is the process of spin mixing. Spin mixing occurs in a spin-1 BEC once the critical point has been crossed. When looking at equation Equation 4.2, this occurs as the spin-collisional

energy dominates, giving rise to spin-changing collisions. Because we start in the initial state of  $|F = 1, m_F = 0\rangle$ , angular momentum-preserving collisions between two  $m_F = 0$  atoms produces a pair of atoms with new spin states of  $m_F = \pm 1$ . This process is also reversible, leading to an oscillating process of spin-exchange. This can be seen occurring in Figure 4.8. Normally, the move to spin interactions would be accomplished by lowering the magnetic field and letting the trapped cloud interact. But as described above, interactions can be engineered instead by increasing the trap power, and keeping the field constant.

To study the effect our density ramp has on the spin mixing interactions, we follow the procedure outlined in the previous section. A field is chosen to be just above the critical point, here around 400 mG, at  $q/|c| = 2.2$  for the lowest 850 nm power and density used in this study ( $|c| \approx 5.4$  Hz). We then allow the cloud to evolve for various amounts of time before projectively measuring the state. We expect no evolution of the state away from the ground state ( $\rho_0 = 1$  for all time), when the field is above the critical field for a given  $|c|$  (see Figure 4.8). However if, as shown above, we increase the second trap's power, resulting in an increased cloud density and  $|c|$  value, we can cross the critical point, and we begin to see evolution of the state from  $\rho_0 = 1$ . For the spin mixing experiments performed for the given field (Figure 4.7), the value of  $q/|c|$  for the low density is around 2.2, whereas the high density value is around 1.2 – well below the critical point for the phase transition. The evolution times shown in Figure 4.8 are offset by 100 ms, since this is the time between the magnetic quench to a finite field and the final power ramp up for the second dipole trap, used to increase the density past the critical point (see Figure 4.3). An additional 40 ms of time is added to the start of the evolution time for both of the plots in Figure 4.8, as this is the power ramp up time for the second trap laser. As can be seen in the figure, the state clearly evolves away from the ground state and oscillates. Spin mixing in general is a noise-driven process, so we average the points over fifty runs. The change in the density can also be noted by the decreased lifetime for the higher density cloud due to the increased collisions between the atoms. The higher final density cloud has a lifetime

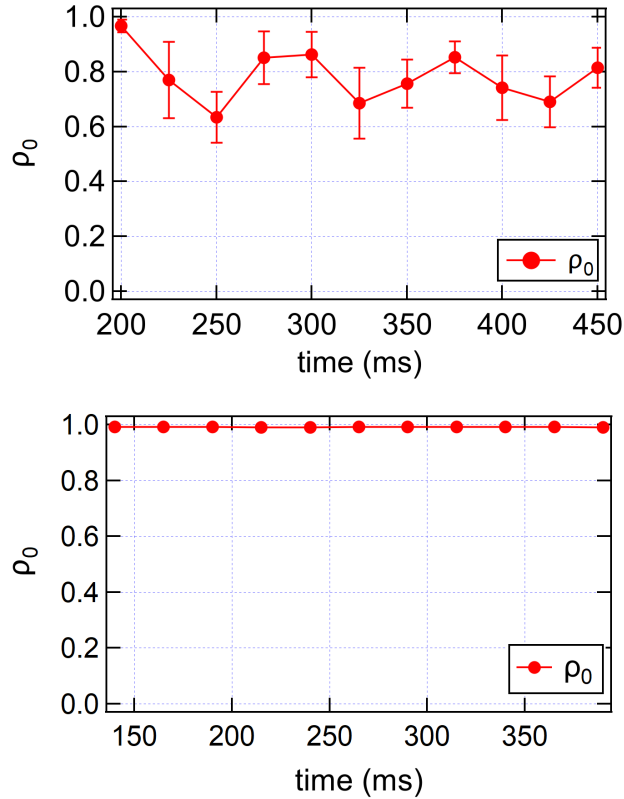


Figure 4.8: Spin mixing evolution for two clouds confined to two different final densities. Dynamics occur only when the density is increased enough to cross the quantum critical point, allowing state to evolve away from  $\rho_0 = 1$ . **Top** shows the evolution for the lowest density cloud averaged over 50 runs, with the evolution time starting from the start of the magnetic field quench. Bias magnetic field is chosen to be above the critical point for the lowest density cloud, so evolution away from  $\rho_0 = 1$  does not occur. **Bottom** shows what occurs when the cloud density is instead ramped to give a ratio of  $q/|c| < 2$ , crossing the critical point. Here evolution time starts when the second trap laser has started to ramp up to its final, higher value (ramp ends at 40ms). This is also averaged for 50 runs. Lifetimes are measured for the decaying atom numbers while the clouds are allowed to evolve. Lower density cloud has a longer lifetime of around 3.7 seconds, while the higher density cloud has a lifetime of around 0.81 seconds.

of 0.8 s, while the lower final density cloud has a lifetime of  $\sim 3.7$  s.

#### 4.4 Density-Induced Spin-Nematic Squeezing

In previous studies in our lab, this was again, produced using a magnetic field quench, followed by a time held in the trap, and a measurement protocol [75]. The evolution time in the trap is typically a shorter length scale than is needed to observe relative population changes (as seen in the spin mixing measurements above). To accommodate this, we changed the procedure to ramp up to the final density in 10 ms, as opposed to the 40 ms used in the previous spin mixing studies shown above. Other than this change, the remainder of the procedure remains the same as outlined in Figure 4.3.

The mean field simulation used was adjusted to use this shorter ramp of the crossed laser trap. Times scales of longer than  $\sim 50$ ms tended to evolve past the maximum squeezing. An evolution time of 35 ms was chosen for the amount of predicted squeezing it gives from the simulation for the highest density. Time starts when the power of the crossed trap is ramped up, leaving 25 ms at a steady-state high cross trap power. After this time has passed, a microwave pulse detuned from the clock state ( $|F = 1, m_F = 0\rangle \rightarrow |F = 2, m_F = 0\rangle$ ) is applied for a desired amount of time, in order to perform tomography on the state by changing the spinor phase of the system [86]. To finish the measurement of the state, we need to projectively measure the populations in the  $F = 1$  ground state of the system. This is performed in our system by rotating any transverse spin populations (i.e. any atoms present in  $S_{\perp}$ ) into our measurement basis of  $S_z$ , or the axis in which our Stern-Gerlach gradient is applied to separate the magnetic sublevels. We rotate the spin populations by applying a resonant  $\pi/2$  RF pulse at the chosen bias field. The trap is then nearly simultaneously released, and the atomic clouds are allowed to fall for 22 ms, while the gradient is applied for 20 ms of the fall time. This sequence constitutes one “shot” of the experimental run. A run is performed for each of the points in Figure 4.9. Each of these runs is composed of 50 shots and the resulting numbers for the measured atomic

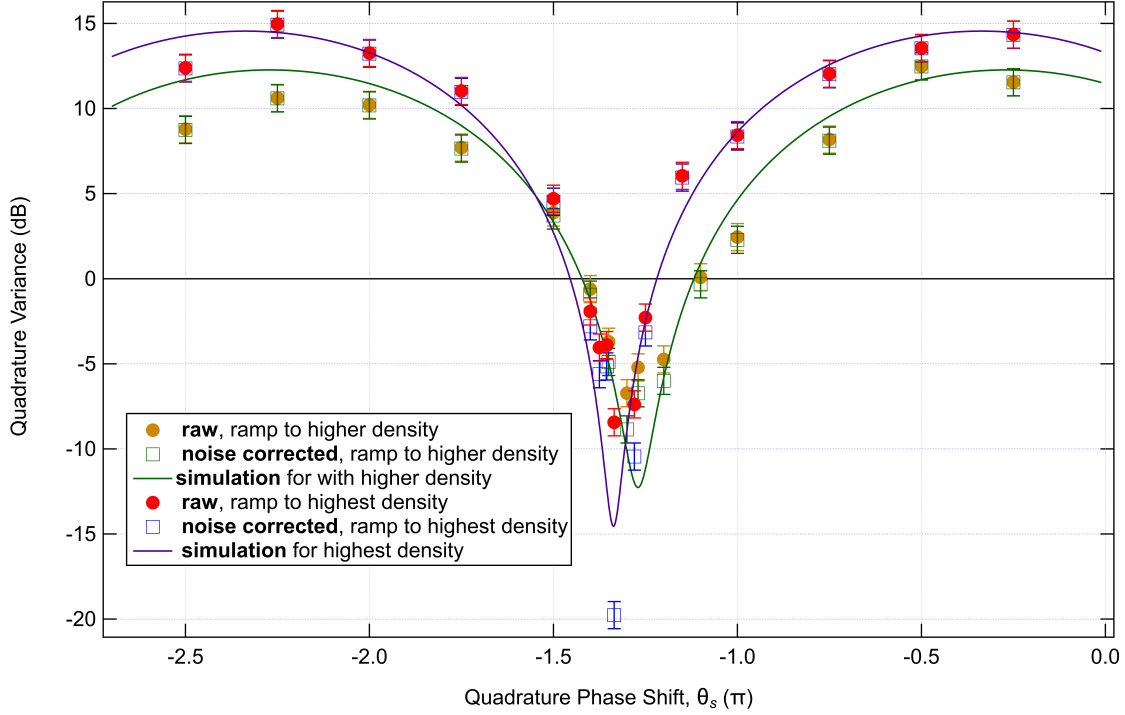


Figure 4.9: Spin-nematic squeezing performed for condensates ramped up to different final densities, allowing the system to cross the quantum critical point. Simulations performed to account for the experimental parameters such as evolution time (35 ms), magnetic field, and cloud density ( $|c|$  value). These simulations show good agreement with data. Each point represents statistics from 50 runs. Circle points depict “raw” measured data, while the “corrected” data is depicted by the square points in the plot, and have the detection noise subtracted from the raw, measured points. Lowest level of raw squeezing measured was around  $-8.4 \pm 0.8$  dB for the highest density ramp (red circles).

populations are averaged over these shots.

We endeavor to test the squeezing stability and control of the density ramp to different final powers. Taken over the course of two days, we perform the shorter, 10 ms density ramp (final cross trap laser power increase) to different final powers and take the spin-nematic squeezing data for the two different final powers, as described above. This leads to the data shown in Figure 4.9. The red circles and blue squares show the data extracted for the highest density ramp runs ( $|c| \approx 10.6$  Hz), and correspond to the noise from the raw data and noise-corrected data points respectively (more on this below). The second set of runs are shown with the yellow circle and green square points. This set of runs is performed at a slightly less dense cloud ( $|c| \approx 9.3$  Hz) than the red and blue points. The solid blue and

green lines reflect the mean-field simulation results described in subsection 4.2.3 using the measured  $|c|$  values mentioned above, as determined by critical field measurements similar to Figure 4.6. These simulations also include the shorter, 10ms ramp. Using these values, we find the data points for both density ramps are in great agreement with the mean-field predictions.

The amount of squeezing (or “anti-squeezing”) measured in the system comes from the measured noise in the magnetization, as noted in Equation 4.3, relative to that of the shot noise limit ( $\sim \sqrt{N}$  for a total number of atoms  $N$ ). The now conventional unit of reported squeezing is in decibels. In our measurements, we were able to measure a raw, uncorrected squeezing of around  $-8.4 \pm 0.8$  dB, which is at the range of our detection limit. The corrected levels of squeezing correspond to squeezing points which have the noise from the detection subtracted off of the measurement (i.e. the photon shot noise and the background camera noise; see discussion below in subsection 4.4.1). These points did not show large amounts of correction near the anti-squeezed regions, but did in the regions exhibiting squeezing, where the system is more sensitive to noise (see Figure 4.9). Error bars for the data points are determined by the number of shots taken for each run. The finite sample size ( $N_s$ ) leads to an error bar given by [86]:  $\xi^2 = 10 \log_{10}(1 + \sqrt{2/(N_s - 1)})$ . For 50 shots, this equates to an error bar of  $\pm 0.8$  dB for the raw and corrected squeezing points.

Additionally, the corrected noise data all seemed to be in good agreement with the simulation curves. The only major discrepancy lie for the maximally squeezed point where squeezing is most sensitive to noise. The corrected point, when the detection noise is subtracted off, shows larger than predicted squeezing (nearly  $\sim -20$  dB of squeezing!) This points to there being a large amount of noise in the background regions of this run, which lead to a relatively large correction when subtracted off, and may not be actually present in the actual data regions (regions where the raw data is taken from). All in all, the system shows remarkable and reliable amounts of spin-nematic squeezing using our density ramp

protocol indicating that we are in fact able to push the system into the spin interacting phase of our quantum phase regions, independent of the bias magnetic field environment. Moreover, we are able to do so in a way that doesn't modify the delicate nature of the squeezing process, which will be important for future work in this direction.

#### 4.4.1 Imaging Calibration

As noted earlier in the RF calibration section in subsection 3.6.5, the CPA for experiment was found to be around 157.91 for 200  $\mu\text{s}$  of exposure time. We measured the RF calibration during days where the squeezing data was being taken to ensure the system was behaving and consistent with previous calibration measurements. This is important as was mentioned above, because it is how we establish the standard quantum limit of the noise to be measured and the correction for the photon shot noise from the system.

In general, there are several key noise sources we consider when calculating the amount of squeezing measured by the system. Many of these noise sources were discussed in depth in [99]. We reference them previously in this thesis in subsection 3.6.5. The key noise sources for our measurement are in descending order: the scatter from the imaging light, the photon shot noise, and the readout noise from the imaging system. The background scatter of our system, taken by shining the imaging light in the chamber without atoms, and measuring the noise in each of the regions typically used when measuring the  $N_+$  and  $N_-$  populations. Measuring the difference between these regions gives us the measured background scatter we would typically detect when taking the squeezing or calibration data. The standard deviation ( $\Delta M_{scatter}$ ) measured for 50 shots, taken at 200  $\mu\text{s}$  exposure time, between the detection regions of interest equates to 49 "atoms" for a CPA of 157.911, which was previously calibrated for our system [89]. Thus, the variance ( $\Delta^2 M_{scatter}$ ) amounts to around 2400 atoms. For a cloud of 25,000 atoms evenly distributed in the  $|1, \pm 1\rangle$  states with a CPA of 157.91, this leads to a baseline level of squeezing of  $\xi^2 = 10 \log_{10} 2400 \text{ atoms}/25,000 \text{ atoms} = 10.2$  decibels.

The next largest noise source in our imaging is the photon shot noise (PSN). The noise from this source can be represented as:  $\sigma_{PSN}^2 = \sigma_{PSN,electrons}^2 N_e / CPA^2 = q(N_+ + N_-) / CPA$ , where  $q$  is the number of pixels binned together to create a one-super pixel,  $\sigma_{PSN}^2(N_e)$  is the photon shot noise for the detected number of electrons, and the number of photons detected is equal to the number of electrons divided by the binning number (here, 4). The conversion of camera counts to atoms is still given by the CPA. Using the experimental CPA of 157.91 for a 200  $\mu s$  exposure time on 25,000 atoms, we can estimate the photon shot noise to be around  $\sigma_{PSN}^2 = 4 * 25,000 / 157.91 = 630$  atoms. Finally, the read out noise (RO) is the smallest contribution of noise in the system. It pertains to the noise associated with the camera's collection and conversion of photons to electrons and counts. The per-pixel (pp) noise can be represented as [99]:  $\sigma_{RO,pp,atoms}^2 = \sigma_{RO,pp,electrons}^2 / CPA^2$ . The single pixel electron standard deviation noise is given by the specification sheet for the camera and equates to 8.1 for the iKon camera. To calculate the total readout noise, we need to sum over the entire region where the clouds are imaged ( $A_{pix,total}$ ). Using the same experimental CPA as before for a 200  $\mu s$  exposure time, we can estimate the total readout noise from the camera to be:  $\sum_{pp} \sigma_{RO,pp,atoms}^2 = \sigma_{RO,pp,electron}^2 / CPA^2 \times A_{pix,total} / n_{bin} = (8.1 / 157.91)^2 \times (2 * 10^2) / 4 = 13$  atoms. This of course estimates the two regions (or regions of interests (ROIs)) used for imaging the ground state populations for the  $|F = 1, \pm 1\rangle$  clouds, and includes a 4x4 binning with  $n_{bin} = 4$ .

If we combine all these noise sources, we can estimate the overall limit of our detection system, given our experimental settings. The readout noise can be combined to include the scattered light noise, as we measure the scattering indirectly by looking at background regions of interest (ROI). We can empirically measure the noise from the regions selected near the  $|1, \pm 1\rangle$  clouds and get an estimate for the total noise that the scatter and camera read out noise contribute to the measured, overall signal. We refer to this combined noise as  $\sigma_{bkg}^2$ . If we were to calculate the minimum level of squeezing detectable from the es-

timated noise sources above, given the scatter level above and the experimental values of 25,000 atoms, a CPA of 157.91, and a binning of 4x4, the minimum detectable limit for our measurement becomes:

$$\begin{aligned}
\xi_{detection}^2 &= 10 \log_{10}(\Delta^2 M_{scatter} + \sigma_{PSN}^2 + \sigma_{RO}^2)/(N_+ + N_-) \\
&= 10 \log_{10}(\sigma_{PSN}^2 + \sigma_{bkg}^2)/(N_+ + N_-) \\
&\approx -9.16 \text{ decibels.}
\end{aligned}
\tag{4.20}$$

Conversely, we can also subtract this noise to extract what we believe the noise from just the atoms is. Combining all this with our estimates for the photon shot noise, we can calculate a “corrected” noise level for the dynamics themselves. In the case of squeezing this correction takes the form of:

$$\xi_{corrected}^2 = 10 \log_{10}(\Delta M_{meas}^2 - \sigma_{PSN}^2 - \sigma_{bkg}^2)/(N_+ + N_-).
\tag{4.21}$$

The corrected forms of this data are plotted in Figure 4.9. This data can be useful in attempting to reveal the extent of the atomic dynamics on the measured noise levels. Ideally the noise floor could be further decreased by limiting the primary sources of noise in the system, such as the residual scatter to lower the noise floor and allow for higher levels of squeezing to be directly observed without correction.

## 4.5 Outlook and Conclusion

The ability to utilize a changing laser potential to modify the density of the cloud has shown clear results in being able to reliably and consistently change the quantum phase of our system. By increasing the density of our system, we are able to shift the quantum critical point independent of the magnetic bias field to create and modify spin interactions. This shift has been shown to occur in both our critical field measurements and our coherent oscillations of the energy gap itself.

The shift into the spin-interacting regime is demonstrated further by examining the spin mixing and spin-nematic squeezing behavior of the atoms. In both cases, the dynamics are reliably captured by the mean-field simulations describing the density ramp performed in the trap. Furthermore, we find a high degree of both spin mixing and spin squeezing using our density ramp method. Using our technique, we are able to measure an uncorrected noise at a level of  $-8.4 \text{ dB} \pm 0.8 \text{ dB}$ . This demonstrates the ability to reliably create and control interactions to a low noise level using our modulated potential.

The future applications could include further quantum interactions using multiple or faster ramps. One interesting aspect to this would be the ability to perform parametric excitation of the quantum cloud. This was done previously in our group by modulating the bias magnetic field by two times the coherent oscillation frequency [103]. If we instead performed this modulation and applied it to the trap potential, perhaps via the acoustic optical modulator for the laser, we can perform the same parametric excitation of the system and observe parametric squeezing.

## **CHAPTER 5**

### **OTHER EXPERIMENTAL PURSUITS**

This chapter details some ongoing and potential future experiments that are useful to the future direction of the lab. The main thrusts of these topics involves various techniques to improve the experimental performance, as well as explore more ways to traverse the quantum phase transition within our experiment. In terms of longer term projects, we first explore the effects of small numbers of atoms on the nature of the quantum phase transition. We will describe the basic theoretical concept behind the finite atom number effects, as well as their applications. These types of experiments have less room for technical error however. This leads to the proposal and suggestion for future upgrades to the experiment, including a new atomic loading system and a dedicated imaging beam setup. This will touched on in the latter sections of this chapter and illuminate a path forward for the future of our spinor BEC experiments.

#### **5.1 Finite Energy Gap for Small Numbered Condensates**

As discussed in Chapter 2, large numbered condensates are easily described by mean-field or semi-classical methods. However, quantum effects owing to a finite number of atoms is an interesting path forward for its deviation away from the mean-field description of the phase transition. It has also been shown in similar types of experiments to allow for higher fidelity of the quantum state (due to the preservation of the cloud away from experimental noise) [104, 69]. Recent work has used these smaller systems to their advantage. Examples of some of these avenues of research include the pursuit of exotic quantum states such as squeezed states, twin-Fock states, and Dicke states [105, 106] to name a few. Much like the current research being done in other spin-1 systems, the broken-axis symmetry phase of our QPT can be crossed in such a way as to be adiabatic. This has been shown to create

a highly entangled quantum ground state called a Dicke state [107, 104, 108, 109].

As mentioned in our previous work [69], crossing the QPT adiabatically to create a highly entangled state is very difficult to do. However, more recent work has been done which has demonstrated the effect that small numbers of atoms can have in generating exotic quantum states in condensates of around 10,000 atoms [110, 111]. There they were able to create both a twin-Fock state [110] and a balanced spin-1 Dicke state [111] in rubidium, relatively close to the ideal ground states. If creating smaller numbered condensates can achieve these highly sensitive and entangled states, this would open up many more possibilities for fundamental studies of the adiabatic transition, as well as applications such as adiabatic quantum computation [112, 113].

Other recent work being done with antiferromagnetic condensates in spin-1 sodium atoms, condensates on the order of 100-1000 atoms have been shown to create a “fragmented condensate” [114]. This has been a long-predicted and sought-after state since the early days of BEC creation [115]. It relies on the degeneracy of several spin energy levels within the BEC, which can be accomplished at very low magnetic fields, making it technically very challenging. The Gerbier group was able to experimentally achieve this, however, through a further opening of the energy gap between the BEC and fragmented phases, allowed by the small number of atoms. In the same group, a similar study was conducted by passing through their QPT with a faster quench or drive across the QCP. This led to the observation of increased correlations in the overall spin observable for the atoms [116]. The latter study informs future tests of the connection between statistical and quantum mechanics.

### 5.1.1 QPT for Finite Numbers of Atoms

As discussed in the last chapter, mean-field theory accurately describes many of our experiments. The key to this lies in the fact that the theory is semi-classical, and thus is more accurate as the number of atoms approaches the thermodynamic limit of  $N \rightarrow \infty$ . How-

ever, as the number of atoms decreases in the cloud, the finite number of atoms begins to have a noticeable deviation from the mean-field prediction. We can simulate this by using the quantum solution. While more computationally intensive, it is achievable. To do this we use the quantum form of our Hamiltonian presented in Equation 2.14:

$$\begin{aligned}
H_{k,k'} = & (2\tilde{c}_2 k (2(N - 2k) - 1) + 2qk) \delta_{k,k'} \\
& + 2\tilde{c}_2 [(k' + 1) \sqrt{(N - 2k')(N - 2k' - 1)} \delta_{k,k'+1} \\
& + k' \sqrt{(N - 2k' + 1)(N - 2k' + 2)} \delta_{k,k'-1}].
\end{aligned} \tag{5.1}$$

From the above equation, we note again that our experimental sequence gives  $\Delta M = 0$  and the initial state for the atomic cloud is  $|F = 1, m_F = 0\rangle$ . These elements form a symmetric, tridiagonal matrix. The energy gap between the first excited and ground state of the system comes from diagonalizing Equation 5.1. Doing this for various numbers of atoms and starting with our initial ground state, we can see the effect that the finite atom number has on the energy gap. As can be readily seen in Figure 5.1, the increasing atom number creates a vanishingly small energy gap at the critical point. For our experiments of tens of thousands of atoms, this gap is near zero at the QCP and nearly identical with the mean-field limit.

We can observe the dynamics of this Hamiltonian as well by numerically integrating the Schrödinger equation of the form  $i\hbar \frac{\partial}{\partial t} \psi = H\psi$ . This is also done in the  $|N, m = 0, k\rangle$  basis, where  $N$  is the number of atoms,  $k$  is the number of pairs of atoms in the  $|F = 1, m_F = \pm 1\rangle$  state, and  $m$  is the magnetization. This process is greatly simplified if we take the number of atoms and magnetization as conserved quantities to first order. This leaves  $k$  as the determining parameter ranging from zero to  $N/2 + 1$  values.

### 5.1.2 Adiabatic Crossing of the QPT

The investigation on the finite number effects in the purely quantum system is of interest as the finite energy gap has direct implications on our ability to adiabatically cross the

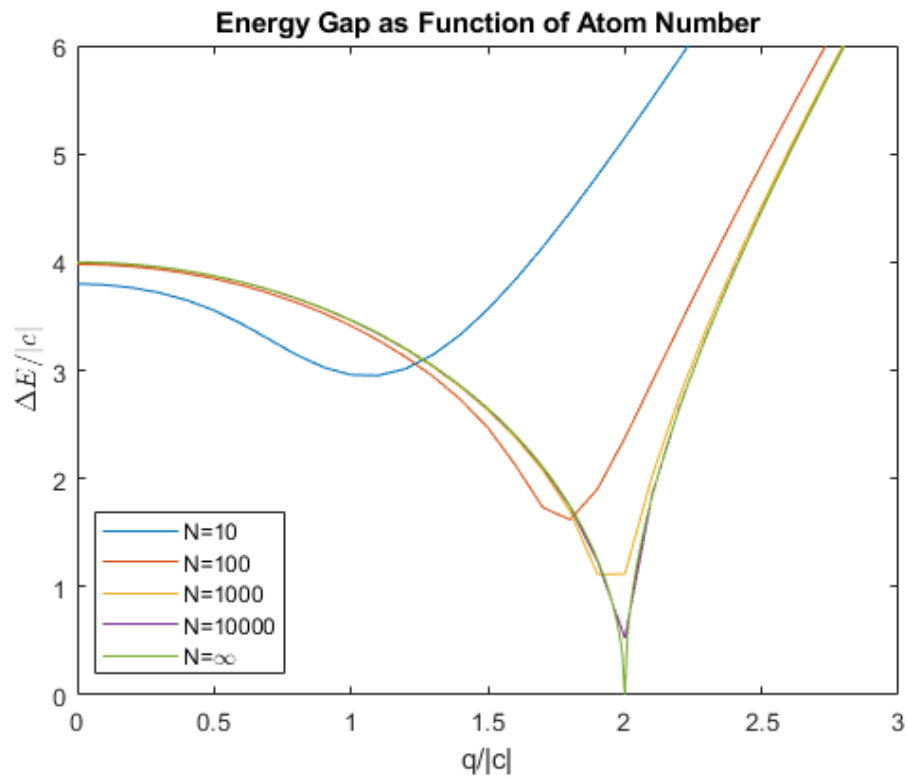


Figure 5.1: Quantum calculated energy gap for finite numbers of atoms shows gap appearing for finite atom numbers.

quantum critical point of the system.

We previously touched on the work done in our lab involving the rapid crossing of the critical point in our quantum Kibble-Zurek experiment [79], as well as our exploration of our ability to adiabatically cross the QCP [69]. These experiments were concerned with the speed with which the QCP was crossed. Faster quenches led to a higher probability of the atoms in the ground state being excited to a higher energy level. The ability of the system to remain in the ground state can be represented by as the probability for the system to be in the ground state, shown as:

$$P_E = 1 - |\langle \Psi_f | \Psi_{GS} \rangle|^2. \quad (5.2)$$

For an adiabatic transition, this probability should be close to zero. Assuming a low level of excitation, the energy gap shown in Figure 5.1 is a good representation between the ground and first excited state for the system [69]. Equation 5.2 is the equivalent lower bound of the Landau-Zener transition probability for a simple linear-quench across the QCP [78, 117, 118].

An alternative description of the adiabatic limit, that doesn't rely on a simple linear quench through the QCP, involves the spinor phase space variables  $\rho_0$  and  $\theta_s$ . We can consider an adiabatic invariant in the form of the action using these canonical variables [119]. This can be represented as:

$$I = \frac{1}{2\pi} \oint \rho_0 d\theta_s. \quad (5.3)$$

A Taylor expansion of the orbits around the ground state from our mean field energy written in Equation 2.19, give elliptical orbits from which we can derive a measure of the action to find [69]:

$$\Delta\rho_0^2 \approx \frac{\sqrt{1 - q^2/(4|c|^2)}}{4N}. \quad (5.4)$$

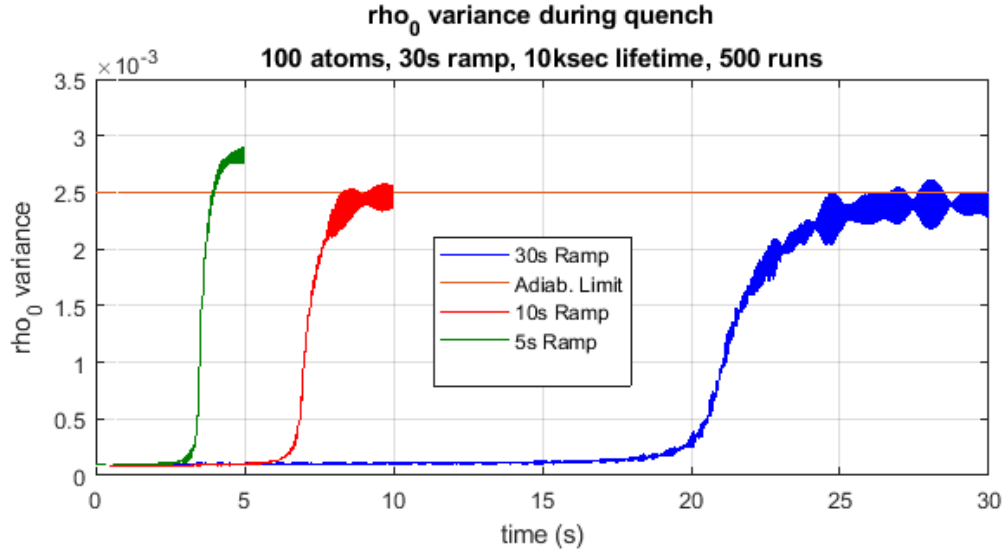


Figure 5.2: Noise estimates for crossing the quantum critical point with different ramp speeds of the magnetic field ramping from around 1 G to zero field. Finite numbered condensates opens up the energy gap allowing easier crossing of the QCP adiabatically. For 100 atoms, it can be shown that even a normal linear quench in ten seconds time would be sufficient to cross the QCP adiabatically. This is important because this is shorter than the lifetime of the single focused trap, allowing for less atoms to be lost in the process.

This value defines the maximum rate of a given quench across the QCP to maintain an adiabatic following. This was an important metric in picking the optimal ramp speed near the critical point in our previous energy gap measurement experiment [69].

Conversely, instead of asking how fast a quench can be performed to maintain adiabaticity for a certain number of atoms, one can ask how the fluctuations might scale for a given ramp speed with different, smaller atom numbers. If we use a standard, non-adiabatic, linear ramp, and plot out the fluctuations or variance in  $\rho_0$ , we can see that lower numbers of atoms correspond to higher values of the variance in the  $m = 0$  population (see Figure 5.2). This means that the gap, which goes as  $\Delta_H = 4\Delta\rho_0^2|c|$  for  $q < 2|c|$  [69], will also be larger, leading to an easier adiabatic condition to fulfill for the ramp speed.

A simulation of this type of non-adiabatic, linear quenches (here using the magnetic field) is performed for a condensate of one hundred atoms, and assuming no decay from the trap. We can see that even for short ramps on the order of ten seconds we are in within the adiabatic limit. This is an important result, as our longest lifetimes in the experiment

tend to be on the order of tens of seconds (see Figure 3.36). Losing atoms out of the trap affects the overall degree of entanglement we can create as we lose correlated pairs of atoms. The degree of entanglement is given by the formula [72]:

$$\xi = \left( \langle \hat{S}_x^2 + \hat{S}_y^2 \rangle \right) N / \left( 1 + 4 \langle \left( \Delta \hat{S}_z \right)^2 \rangle N^2 \right). \quad (5.5)$$

This is pertinent for the measurement of the generation of macroscopic entanglement. If we are able to cross the QCP adiabatically, then the end result at zero magnetic field is a massively entangled Dicke state [120, 107]. These states are interesting for their exotic nature, but also their possible applications to quantum computation.

### 5.1.3 Preliminary Data for Making Small Condensates

Given this incentive to create small condensates, the challenge becomes two-fold: how do you create small atom clouds, and how do you maintain dynamics in the trap. We would like to change the atom number to take advantage of the finite atom effects, but would like to maintain the spin interactions,  $c$ . The rate of the spin dynamics is dependent on the atom density, so maintaining a high enough spin-interaction term,  $c$ , is essential. One way to do this is to turn up the trap power to increase the potential, and thus the mean trap frequency and density, at a rate that would maintain a stable and sufficient  $c$  value. As mentioned in chapter 4, we can modify  $|c|$  by either decreasing the number of atoms, or changing the trap potential. There the value in Equation 4.9 for  $c$  as a function of the power of the laser was shown to be:  $c \propto P^{3/5}$ .

We attempted to create this effect by trying a number of different procedures to 1) lower the atom number and 2) maintain a sufficiently high  $|c|$  value. From our studies we found that if we raised the final power of our primary, 10.6  $\mu\text{m}$  trapping laser, we could change the trap potential enough to observe trap dynamics. By performing the normal condensate creation procedure, we create a normal-sized condensate in the single focus trap of around

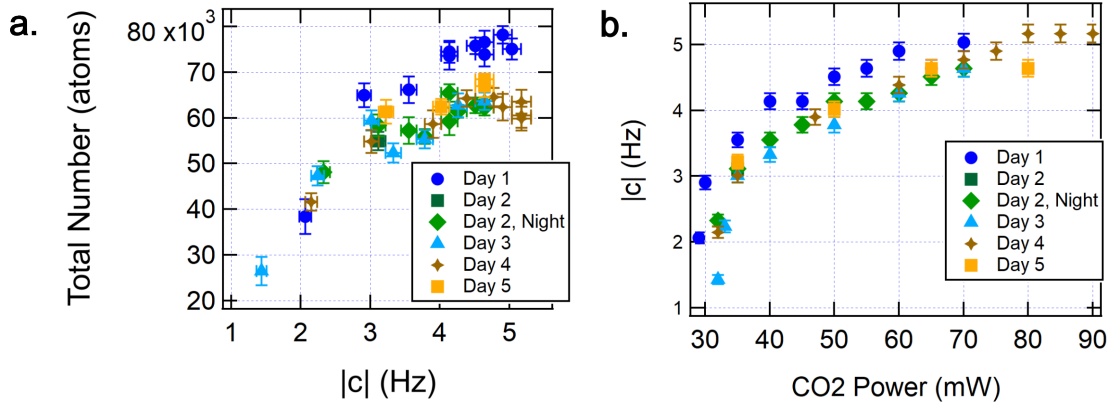


Figure 5.3: Measured  $c$  values for different final  $10.6 \mu\text{m}$  powers and final atom numbers over several days. Data shows a clear and consistent pattern to the change in measured critical field values or  $|c|$  values for given final  $10.6 \mu\text{m}$  power. As expected, increases in the final  $10.6 \mu\text{m}$  power lead to increased density in the trap, however this seemed to plateau for certain values. Ramp times up to these high power was not looked at much, so this could also have something to do with the measured dynamics of  $|c|$ .

60,000 atoms. From there, we can raise the trap power quickly to increase the trap depth and peak density. This allowed us to ramp up the final  $10.6 \mu\text{m}$  trap laser quickly enough to avoid too much thermalization, but sufficiently high enough to appreciable increase the  $c$  (see Figure 5.3).

For sufficiently high densities, this leads to collisional losses within the trap, allowing us to go to smaller numbers of atoms. While performing these tests we were able to decrease the atom number to several thousand. These clouds were very stable and showed clear coherence via coherent oscillations. Additionally, when looked at in absorption, these clouds were still very cold, and didn't show much evidence of being thermal. However, there did appear to be some domain formation for very short ramp times (see Figure 5.5). This appeared to plateau for sufficiently slow ramp times (usually in the in hundreds of milliseconds, see Figure 5.4).

However, to get to the hundreds of atoms level, we had to lower the trap power enough that atoms began to be lost from the trap. This had a dual effect of allowing only very cold atoms to remain in the trap, and also allowed us to lose enough atoms before increasing the final power to increase the density of the trap. Several tests were done to test the coherence

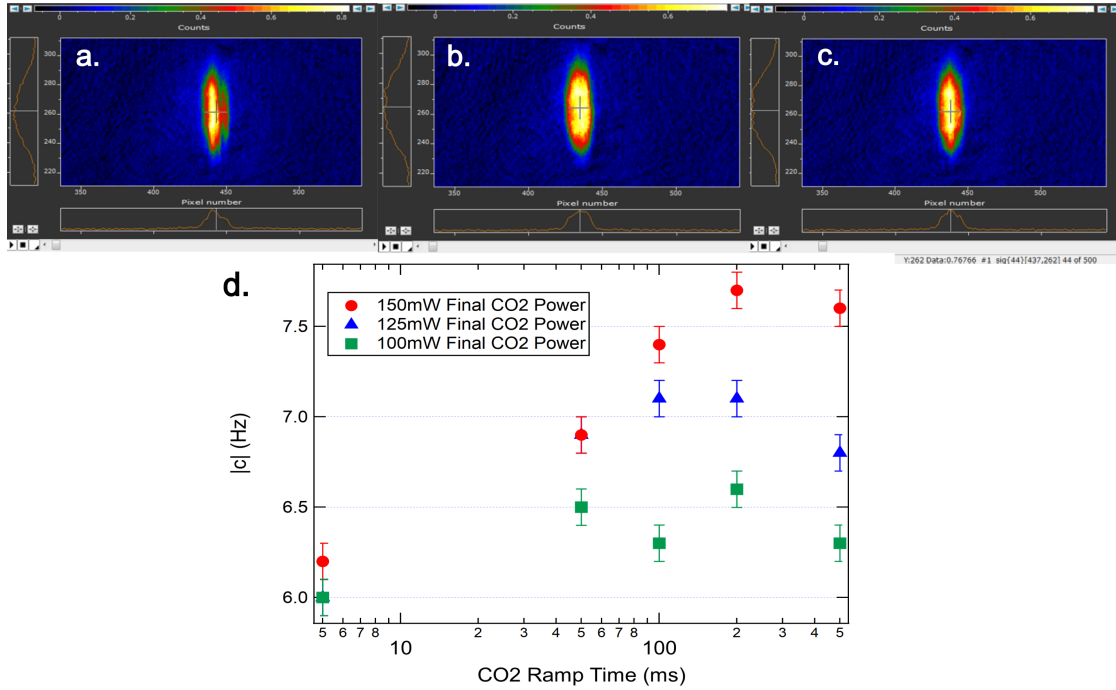


Figure 5.4: a)-c) shows absorptive images for the  $10.6 \mu\text{m}$  final power ramps up to 150 mW at different rates. Measured critical field values for these different ramp times is shown in d) for several final high power of the  $10.6 \mu\text{m}$  laser. This seems to suggest that the speed of ramp plays a role in the effective dynamics in the trap. Moreover, ramping too fast to high power will not allow the full dynamics to be observed (see ramp times of 5 ms in d)). This is shown in the absorptive images as well, as a) shows a cloud ramped to 150 mW in 5 ms, that has multiple domains to it, whereas slower-ramped clouds such as b), done in 50ms, and c), done in 500ms, don't seem to show as much spatial or dynamical deviation.

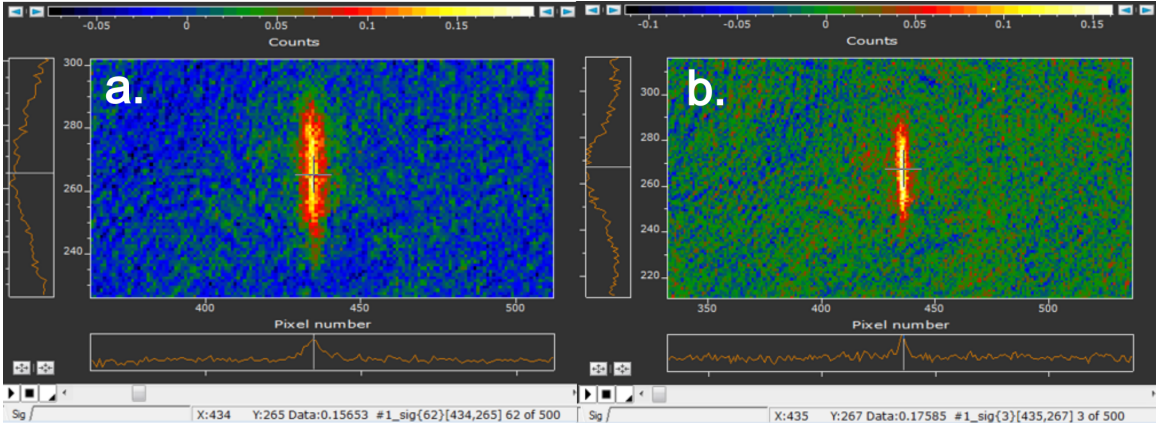


Figure 5.5: Absorptive images small condensates (2-5 thousand atoms) created with the single-focused,  $10.6 \mu\text{m}$  laser. Difference between a) and b) is the minimum power the  $10.6 \mu\text{m}$  laser is lowered to: 28 mW and 27 mW respectively. Ramping the condensate back up allows the condensate to become tightly confined (note the aspect ratio). The difference in atom number is a few thousand, with b) being the smaller of the two.

and stability of the final system. Images were also taken with absorptive imaging to look at the structure of the cloud. This revealed that the cloud was very cold and highly compressed at high powers (see Figure 5.5).

The ultimate goal of these type of experiments would be to create a small and stable cloud of atoms that could exhibit coherent oscillations and other signs of spin interaction. We found that using the atom ramp to generate small clouds with the single-focused,  $10.6 \mu\text{m}$  on its own led to final condensates in the hundreds of atoms, but they were largely unstable due to lowest power needed for the  $10.6 \mu\text{m}$  laser to allow atoms to spill out of the trap. The final atom clouds would not be stable throughout the day, and settings that were found to generate clouds with a set number of atoms would drift away and no longer be ideal.

We attempted to mitigate this by adding a second trapping laser to the protocol by using the 850 nm, cross-trapping laser to aid in atom losses due to increase density collisions. This did help add some stability to the process. Through this technique we were able to create some more stable atom numbered-clouds that were less amenable to experimental drifts. One of the successful runs we had is shown in Figure 5.6. This run, which was

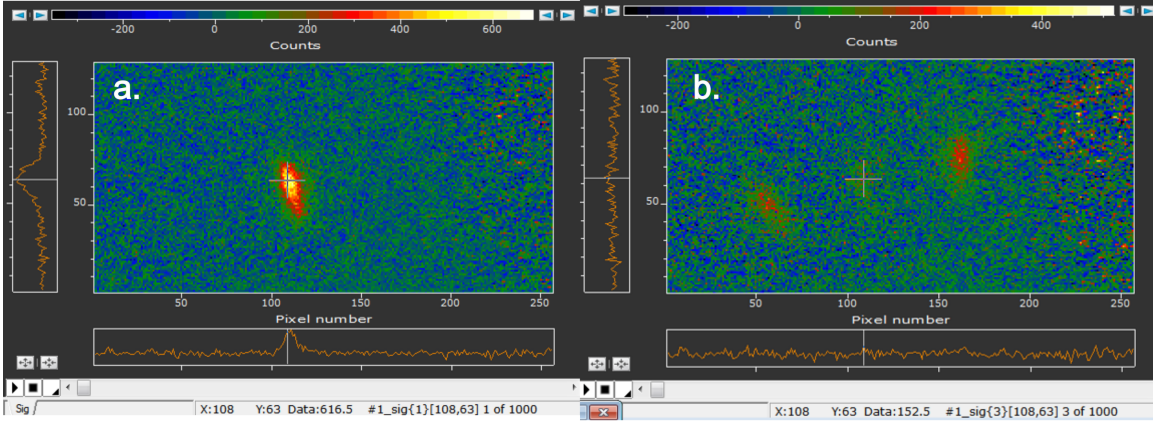


Figure 5.6: Spin mixing in the SF trap with crossed trap-assisted atom losses and a final high power single-focused  $10.6 \mu\text{m}$  ramp; spin mixing dynamics observed for 100's of atoms in the final high power single focus trap. Image a) shows the initial cloud at zero evolution time, while b) shows the clouds at 150 ms of evolution time. Spin mixing is measured and plotted in c) for three runs averaged.

averaged three times shows about 100-200 atoms interacting in the single focus,  $10.6 \mu\text{m}$  trap at 3 Watts. The dynamics are surprisingly quick, due to the very high power potential, despite the low number of atoms.

At this level, detection becomes very difficult, and even small amounts of drifts in the imaging light leads to drifts in the detected scattered light; this makes the final atom hard to accurately measure. Many of the imaging tests we performed indicate that we are near the edge of our detection limit with the current imaging system. More potential improvements will be discussed in section 5.3. If these improvements are made, this series of investigations can be revisited and hopefully improved upon to fully realize and measure the change in the energy gap that finite numbered condensates can bring.

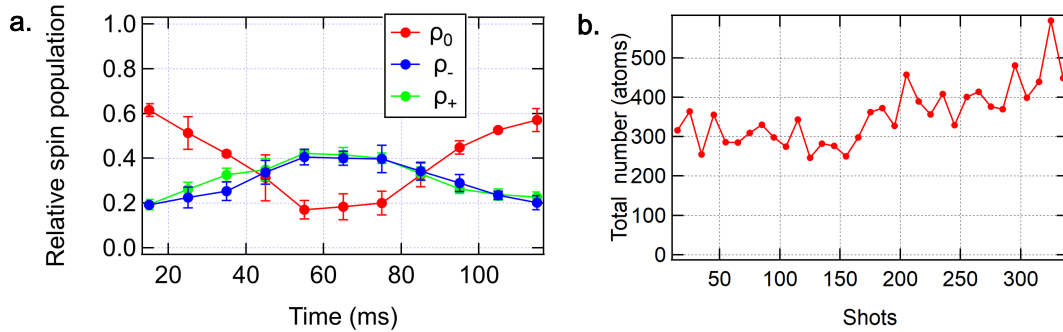


Figure 5.7: Coherent oscillations in the SF trap with crossed trap-assisted atom losses and a final high power single-focused  $10.6 \mu\text{m}$  ramp; coherent oscillations observed for 100's of atoms in the final high power single focus trap. Image a) shows the coherent oscillations averaged over three runs, while b) shows the atom numbers during the run. Large instabilities seen for very small atom numbers.

## 5.2 2D-MOT

Two-dimensional magneto-optical traps (2D-MOT's) are an atom loading technique that have been around for a couple of decades. Developed in the late 1990's and early 2000's [121, 122, 123, 124, 125, 126], 2D-MOTs are a way to provide slow, pre-cooled atoms to an experimental apparatus, at a rapid (few seconds) rate. Other techniques exist for this including low-velocity intense source (LVIS, [124]) and Zeeman slowers [127], though they are not as ubiquitous as the 2D-MOT, as it is the generally accepted best way to compactly construct a sufficiently fast and cold source of atoms. In addition to their loading abilities, they also allow one to have two different vacuum regimes, as the cold atom beam of the 2D-MOT is readily aimed through a differential pumping tube. This allows the 2D-MOT to be loaded with relatively high vapor pressure, while the downstream, target area for the atom beam can be at a much higher vacuum, affording this side a longer lifetime for the atoms once they are trapped again.

Below we will discuss the results obtained from our lab's own studies of the 2D-MOT (termed the "Double MOT" experiment in our lab), loading into a 3D-MOT. These studies were meant to inform our own future experimental upgrades, and potentially a second experiment involving an all-glass, science chamber for studies at low magnetic field. We'll

discuss the main observations and outlook for a future prospect for using the 2D-MOT on a future version of the BEC experiment.

### 5.2.1 Preliminary 2D-MOT Experiments

2D-MOTs work in nearly identical ways as a conventional magneto-optical trap (3D-MOT). They use detuned light from the cycling transition to cool the atoms transversely with four beams (hence the “2D” moniker). They also utilize a quadrupole magnetic field to create a confining force on the atoms; this is done in our experiment using two pairs of anti-Helmholtz coils. The third axis, or longitudinal axis, is free for the atoms to propagate along in both directions. This is known as a traditional “2D-MOT”. One can stop the propagation along one of these directions however by adding a “push” beam which is aligned along the desired direction for the atom beam to travel. This effect can be further enhanced by creating a “2D<sup>+</sup>-MOT” in which cooling along the longitudinal axis does take place as two beams are added: one stronger in the desired direction for the cooled atoms to travel and another weaker, counter-propagating beam to slow and cool the atoms traveling in that direction. This is accomplished in the existing setup discussed here with a laser beam shown on a polished copper mirror with a hole, through which the cooled atoms from the 2D<sup>+</sup>-MOT travel.

Another key feature and advantage of the 2D-MOT, is that it is able to be loaded at a higher pressure, which is typically better for faster loading, up to a certain point. This is due to the fact that most 2D-MOTs are separated from the final capture region by differential pumping. This mechanism is usually accomplished by a very small aperture or a moderately small tube (a few millimeters). This creates two different pressure regions on either side of the differential pumping. If a UHV or non-evaporable getter (NEG) pump is pump on one side of the differential pumping, the second region will have a decreased pumping effect on its side. The factor with which this side will be pumped to is the factor dictated by the geometry of the differential pump. Likewise, if one side, say the 2D-MOT

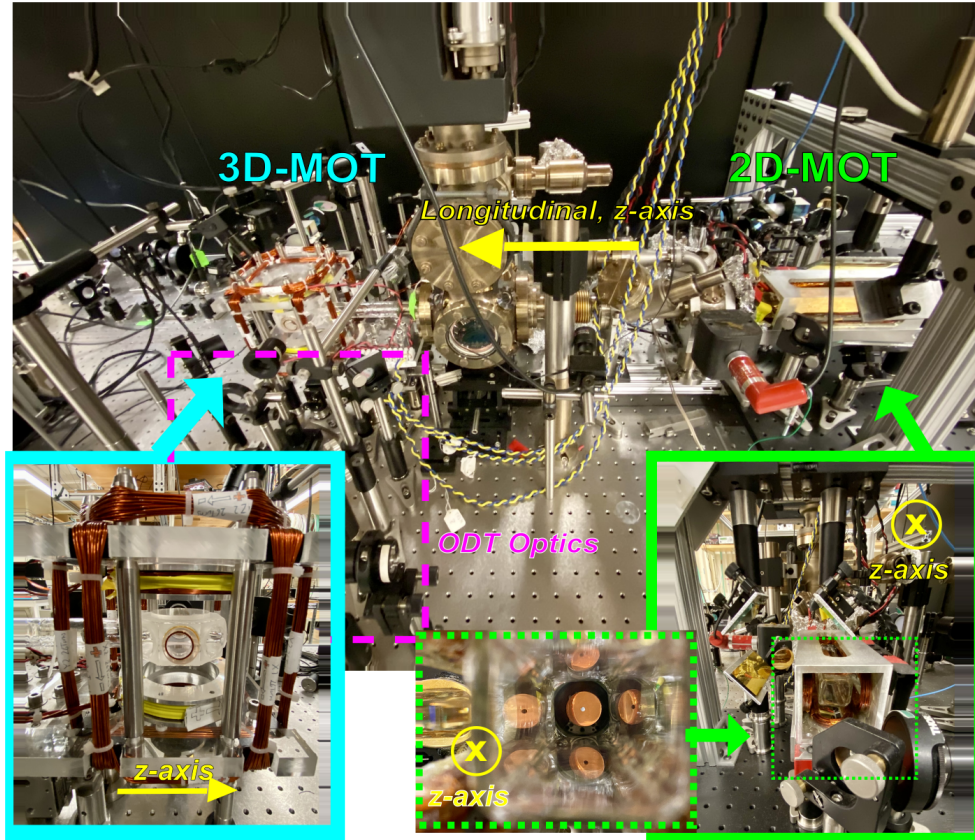


Figure 5.8: Existing double-MOT experimental setup

side is at a higher pressure due to high rubidium vapor pressure, the capture side's pressure will be less affected by the differential pumping factor. In our case, this is achieved by a flange and adaptor, to which the polished copper mirror is attached (see Figure 5.8). The hole is visible through the copper mirror and continues for a specific length which gives a differential pumping factor of about 1000x. This isn't an issue in general, but can add some complications when try to steer the atomic beam through the differential pumping region. This was particularly challenging in our case, as the MOT region was so far downstream from the 2D-MOT formation. The radial divergence of our beam was therefore set by the geometric configuration of our differential pumping region, so atoms that were not cold enough did not make it through this region.

The full apparatus used in these tests is shown in Figure 5.8. This was an apparatus built

by a former graduate student, Chris Hamley, circa 2013. It was built using spare vacuum parts. This was built to test the efficiency of the 2D-MOT as a future experimental cold atom source. It however had not really full operation when the revival of the 2D-MOT began in Spring 2016. After several semesters of work, the 2D-MOT was fully operational in the winter of 2017, and being captured efficiently in a 3D-MOT downstream in the “science” side of the apparatus (see Figure 5.8). From January 2016 to May 2016, we achieved at 2D-MOT but were unable to see a 3D-MOT capture. This led to many tests including lifting the 2D-MOT side of the vacuum chamber, optimizing the push beam to create a 2D-MOT+, optimizing the laser powers to the 2D- or 3D-MOT sides, and changing the rubidium pressure on the 2D-side – just to name a few parameters.

For awhile, the expected atom number collected in the 3D-MOT from the 2D-MOT was several orders of magnitude smaller than expected. We thought this could be from the atoms lost between the 2D-MOT and the science chamber due to the small width of the differential pumping tube, as it may exclude atoms that were lost due to the distance fallen from gravity, or the radial divergence of the atom beam out of the 2D-MOT. After much consternation, it was found that the ANDOR iXon camera was focused on the reflection of the MOT from the chamber window, as opposed to the MOT itself. Adjusting this gave us around the atom numbers we expected.

One thing that we found that greatly optimized the loading from the 2D<sup>+</sup>-MOT to the 3D-MOT was the optimization of the push beam, likely due to the increase in the amount of atoms from the 2D<sup>+</sup>-MOT that were slowed enough to have a longitudinal velocity that was within the capture velocity of the MOT, or were cooled long enough to have a radial velocity which was slow enough to allow the beam to not diverge so much that it didn't make it out of the differential pumping tube. The atom beam divergence, which for us is given by the length of the differential pumping tube and the distance from the end of the 2D-region to the beginning of the 3D beams, is slightly smaller than most 2D-MOT experiments (see Table 5.2), due to the length of the chamber and the long distance between

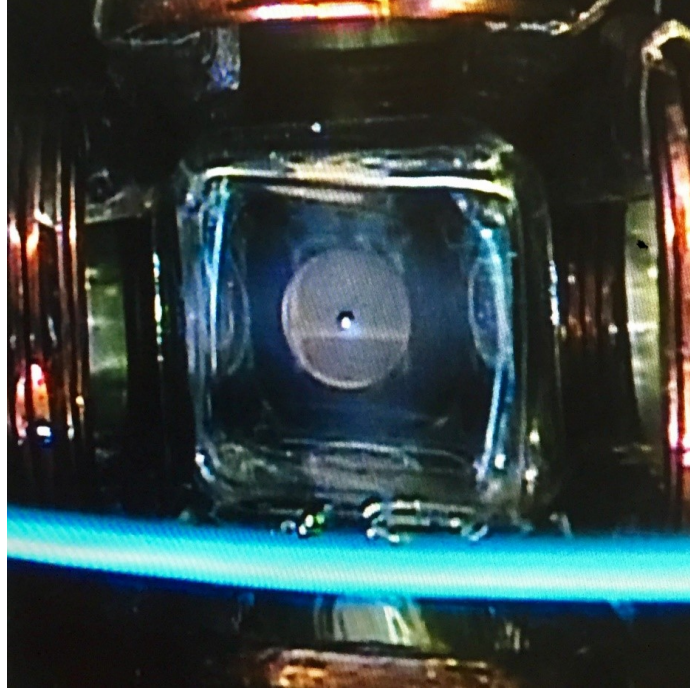


Figure 5.9: 2D-MOT beam looking down the longitudinal axis of the 2D-MOT to 3D-MOT experiment.

the 2D and 3D regions. This makes steering the beam and sufficient cooling of the beam very important, and would be something we would like to design better in the future. An additionally important parameter was just high enough loading pressures on the 2D-MOT side. Pressures on the low to mid  $10E-7$  Torr tended to not yield as good of loading as the high  $10E-7$  Torr to low  $10E-6$  Torr. Higher or lower than that led to poor loading (and lifetime in the case of the too high of loading pressure). The pumping differential was about a factor of 1000x, so having high  $10E-6$  Torr would mean a pressure of  $10E-9$  Torr in the science chamber, which is consistent with the ideal pressures needed to make a MOT [96].

The max loading observed at this time was close to 400 million atoms/s, but due to the finite resources in laser power, this sometimes led to smaller max numbers of atoms in the MOT. Best set of settings we found for the experiment led to around 300 million atoms per second loaded in the MOT for a loading time of 1.7 seconds. This had a lifetime of 20 seconds, and a total MOT number of around 900 million atoms in the MOT. An example table of measurements taken during a near optimal 2D-MOT vapor pressure. Two sets of

measurements, shown in Table 5.1, are taken around thirty minutes apart, while optimizing different parameters. When every parameter is near optimal for the given experimental resources (i.e. for the total available laser power), the loading rate is within a few seconds and on the order of 100’s of millions of atoms per second. In order for our system to load at an efficient rate, we need the push beam power and counter propagating beam to be optimized in power. This leads to change in loading time from tens of seconds to seconds (see Table 5.1 Settings 1 and 2).

Table 5.1: Loading, lifetime, and total number of atoms from the 2D-MOT+ into the 3D-MOT.

Settings	Loading (s)	Lifetime (s)	Load. Rate (N/s)	Max Number (N)
1) no opt.	$19 \pm 1.0$	$33 \pm 2.8$	$12 \times 10^6$	$200 \times 10^6$
2) push opt.	$1.8 \pm 0.42$	$20 \pm 2.9$	$280 \times 10^6$	$280 \times 10^6$
3) wait 30 min.	$1.8 \pm 0.99$	$29 \pm 0.99$	$280 \times 10^6$	$930 \times 10^6$
4) wait and 3D opt.	$29 \pm 1.7$	$11 \pm 0.45$	$140 \times 10^6$	$2,400 \times 10^6$

Similarly, if we optimize the power in the 3D-MOT, we sacrifice the power available for the 2D-MOT to efficiently cool atoms. Therefore, while we can capture more atoms in the MOT, the loading rate from the 2D-MOT is slower and the density of the MOT itself starts to play a role (as reflected in the lifetime of the MOT itself). The third run shown in Table 5.1 shows an example of Goldilocks-type of settings, where the loading into the 3D-MOT is very quick, and we are still able to achieve a fairly high final atom number of nearly one billion atoms in the MOT. These factors are important considerations for a future 2D-MOT setup, but it is unclear how sensitive the system will be to these particular settings. Ideally, the 2D-MOT source to be used in the future builds will be much more compact in terms of the distance between the source (2D-MOT) and the capture (3D-MOT) regions. Additionally, we used a vapor cell source on the 2D-MOT side, which was hard to control, and seemed to play a significant role in the efficient loading of the 2D- and 3D-MOTs. In the future we would hope to use a getter much closer to the 2D-MOT to ease this requirement and more reliably control the rubidium vapor pressure.

A comparison of many of the initial 2D-MOT studies and their reported settings are

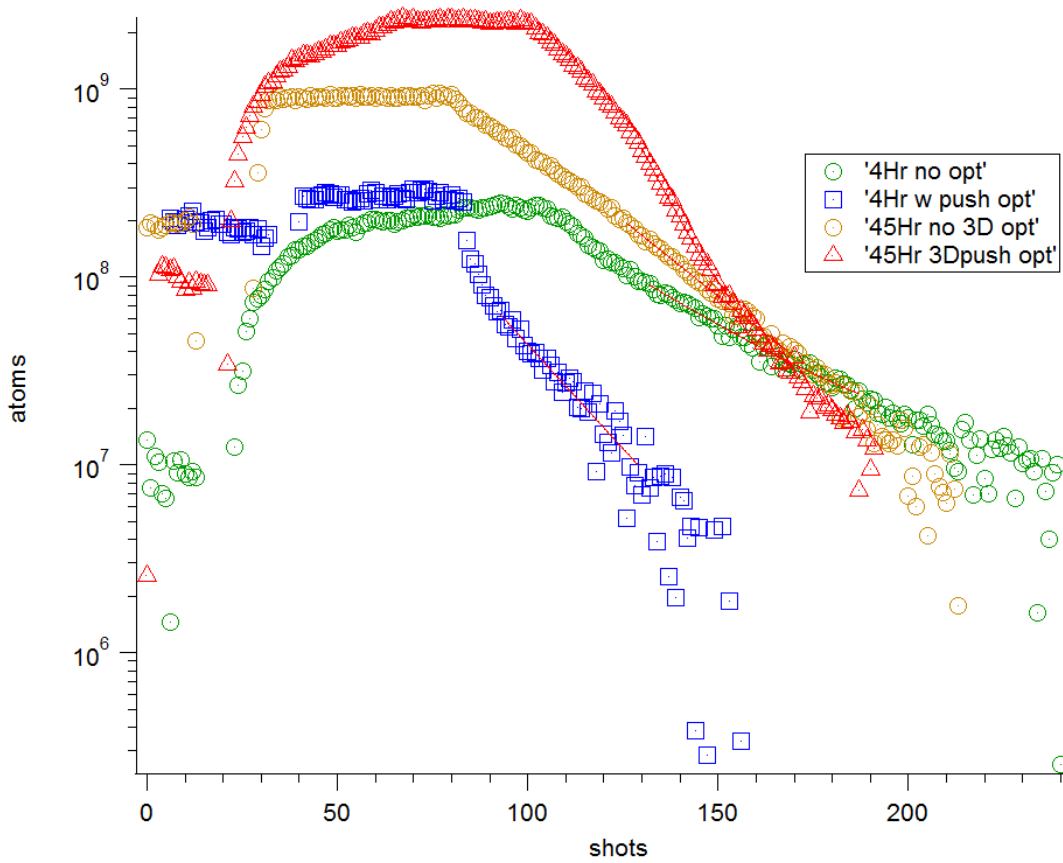


Figure 5.10: Loading and lifetime curves taken at a 1 Hz sampling rate, illustrating the number of atoms captured in or leaving a 3D-MOT downstream from a 2D<sup>+</sup>-MOT. “No opt.” refers to no optimizations performed, whereas “3D opt” or “push opt” refers to the atom number being optimized using the 3D-MOT parameters (e.g. powers, etc), or the push beam optimized (e.g. power or polarization, etc.). What can be seen is that the atom number can be brought up to be very high with 3D-MOT optimizations (>1 billion atoms), but that the loading and lifetime are best optimized using the push beam to get a few seconds of loading time, and tens of seconds of lifetime. As an aside, the “4Hr” and “45Hr” refer to the amount of time (four hours and four and a half hours respectively) since the rubidium vapor source was left open to the 2D-MOT cell. Pressure also has a big effect in the extremes, namely when there are too many or not enough atoms around.

summarized in Table 5.2. Our experiment is comparable to those reported in the earlier works referenced earlier, while still being on the lower end of the atom flux rate. This is likely due to the small geometric divergence allowed by the experimental apparatus itself. Despite these limitations, the loading rate and maximum number of atoms loaded into our 3D-MOT in the end was still very good, and definitely an order of magnitude faster than what is currently used on the main BEC experiment (15 million atoms in 15 seconds).

The double-MOT setup described here was later tested on by Lin Xin [89] to see if we could use a 1064 nm laser to make a condensate in the science side of the chamber using the 3D-MOT to load into an optical dipole trap. It was found that this was very challenging using the fiber laser we had on that table at that time. While atoms were observed in the trap, there was determined to be not enough of a trap depth and density to evaporate or create a condensate. The future use of the 2D-MOT seems to lie in a future rebuild of the BEC experiment. Several ideas and possible designs have been floated for the experiment. I describe some of them in the section below, incorporating the 2D-MOT in their schematics.

Table 5.2: Table of 2D-MOT varieties compiled from References [121, 122, 128, 124, 125, 126]. This table summarizes the key experimental quantities noted in these papers and theses. The “transverse” column denotes the amount of power in the transverse beams used to cool the 2D-MOT. Similarly, the “push beam” column denotes the amount of power in the push beam for the 2D-MOT. “Beam size” denotes the size of the light beams used to cool the 2D-MOT. Some of the key values we are concerned with are the longitudinal velocity ( $v_{long.}$ ), as it relates to the MOT capture velocity, and the atom flux, as it relates to the loading rate of the MOT. The asterisk under the “divergence” column denotes the value that is the geometrically allowed tolerance from the vacuum chamber of the 2D-MOT to the capture region. Some experiments measure the atom flux directly out of the 2D-MOT, and not by using the MOT loading rate (which is denoted in the table with “#”).  $P_{2D}$  refers to the pressure on the 2D-MOT side. The values obtained in our experiment are listed on the bottom row of the table.

Type	Transverse (mW)	Push (mW)	Detuning ( $\Gamma$ )	Beam Size (mm)	$v_{long.}$ (m/s)	Diver- gence (mrad)	$P_{2D}$ (mbar)	Gradient (G/cm)	Flux (atoms/s)
2D+, Rb [121]	44	11	2	96x9	17	26	3E-7	15	2E10
2D, Rb [122]	320	N/A	1.9	96x15	50	–	1.8E-6	17	6E10
2D w/push, Rb [122]	50/beam	3-30	1.9	96x15, 5 push	25	32; 59*	1.8E-6	17	–
2D, Rb [128]	34	NA	1.7	24 x 7	12	46*	2E-7	17.7	5E9
2D+, Rb [128]	30	2.1, 0.6 retro	3	24x7, 7 push	8	43*	1.5E-7	12.6	9E9
2D, Rb [124]	48	N/A	3	25	–	–	3E-7	6	2E8
2D+, Rb [124]	48	10	3	25	9	–	3E-7	6	8E9
2D w/push, K [126]	175	0.75	2.6; 0 push	80x40	–	50*	1.5E-7	8.7	6E9#
2D, Ca [125]	220	N/A	1.5	30	27	40	4E-8	1-1.5	1E10
2D+, Ca [125]	220	2	1.5	30, 20 push	20	–	4E-8	1-1.5	1.3E10
2D+, Rb Us	90-100	0-10	2	95x16	–	33*	4E-6	11	4E8#

### 5.2.2 New Vacuum Designs with 2D-MOT Source

As mentioned above, we would like to use a 2D-MOT on the experiment as a new source of cold atoms. This would provide us with a fast and reliable atomic source, which would not affect the vacuum in the region where we form the condensate. We believe this is one of the main limiting figures in the lifetime of our condensate. This therefore could greatly add to the length of time we would be able to perform our experiments, as well allow us to retain more atoms in the trap for a given time frame, thereby preserving more of the coherence of the quantum states of our atoms.

In addition to the increased coherence and longer trap lifetimes, the speed at which the 2D-MOT would load our (3D-)MOT would greatly experimental run time. The current run time on the experiment is around 22 seconds, with 15 seconds of that having to do with waiting for our traditional vapor cell MOT to load to a high enough number for us to begin the transfer to the optical dipole trap and begin the evaporation sequence. If this could be instead shortened to one to two seconds of loading time, this would cut our run time in half and allow us to take twice as many shots in a day. This is useful in an experiment where we rely on repeated measurements of a set of experimental parameters to acquire statistical averages and measurements. This would also help the experiment perform better, as day-long drifts in the experiment would have less affect on optimized settings for a given measurement over the course of a day.

There are many ways in which we could easily incorporate a 2D-MOT into our existing setup with very minimal perturbation. One of these plans entails simply replacing one of our imaging viewports with a compact 2D-MOT (readily purchased from companies like ColdQuanta). Using the current absorption probe location as the location of the new 2D-MOT source, see Figure 5.11, the cold atom source already has direct line of sight to the locations of the current MOT and optical dipole trapping location. The 2D-MOT is also far enough away that if permanent magnets are used to create the quadrupole fields for the 2D-MOT, it would be far enough away from the dipole trap location to not greatly impede

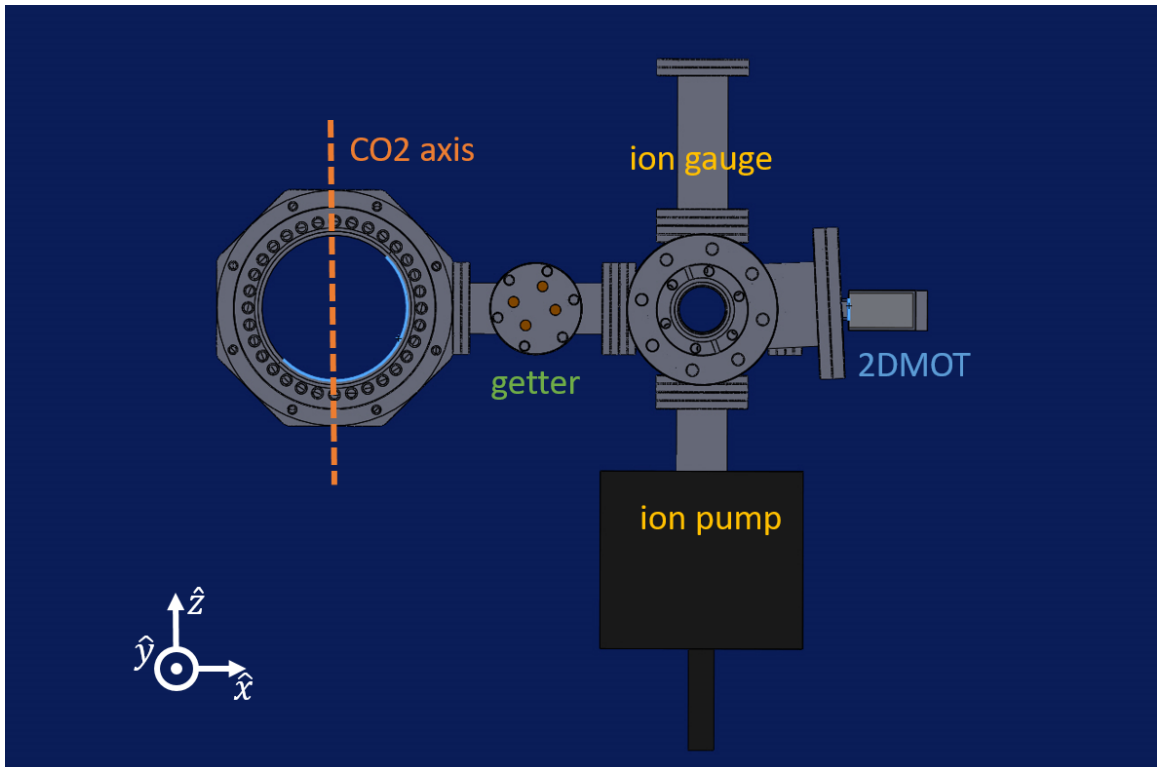


Figure 5.11: Possible new double MOT design featuring the smallest change to the current system: the addition of the 2D-MOT to the existing absorption probe port.

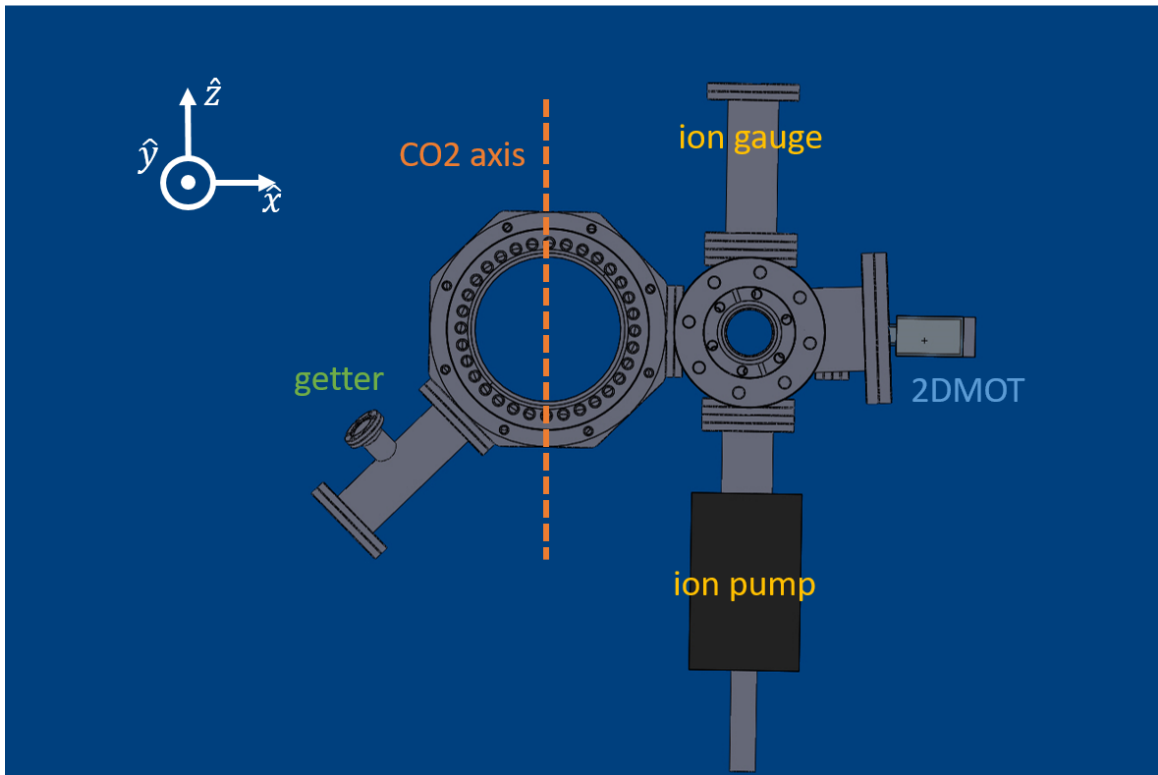


Figure 5.12: Possible new double MOT design with a slight modification to the current chamber which involves moving the getter to another port, bringing the 2D-MOT and ion pump closer to the chamber center. This will hopefully improve vacuum performance, as well as speed of loading.

the magnetically sensitive operations performed on the atoms. The only larger drawback of this system is having to find a new home for the absorption probe path, which requires line of sight to one of our ANDOR cameras. Luckily, we have a camera over the large viewport of the spherical octagon (the “Top” camera, or iXon camera), to which an absorption probe could be added, perhaps even at or near the current location of the current 850 nm cross trap. Doing this, would require some work on the Top camera to increase the magnification to be able to more closely examine the structure of the condensate. Additional adjustments can be made, such as using the push beam from the 2D-MOT setup or another imaging beam in its place as the probe beam, which would shine through the differential pumping tube to illuminate the condensate on the existing ANDOR iKon camera. A more radical approach might involve moving the existing, main imaging access ( $\hat{x}$ ) from its current location to that of the vertical ( $\hat{y}$ ) axis, as it has the most optical axis and doing our absorption imaging in that way. More will be said about such schemes in the section 5.3.

Another adjustment to the aforementioned design involves moving the getter and associated feedthroughs out of the path of the 2D-MOT proposed location (see Figure 5.12). This decreases the distance the atom beam needs to travel to reach the current MOT and dipole trap location, while still maintaining a far enough distance to allow the magnetic fields from the 2D-MOT to have a minimal effect. Furthermore, it still offers the ability to use our experiment in its existing capacity by utilizing auxiliary getters that could be used to create a vapor-loaded MOT, in the event that we needed to. All in all, there are many other ways we could devise adding a 2D-MOT to our system, such as loading from above the chamber and having the atoms from the 2D-MOT fall down into the existing spherical octagon and dipole trap location. Additionally, rotating the experiment vertically and mounting the spherical octagon on its side could allow more optical access and less detection-limiting scatter in the experiment. In which case, there are even more ways we could envision utilizing this previously explored technology to our advantage.

### 5.3 Imaging Improvements

In our earlier discussions on the detection of our system (subsection 3.6.5 and subsection 4.4.1), we noted that the limiting factor to our detection limit was the scatter from the imaging beams currently used to image the atoms. We'll touch on the current experimental restrictions and work that's been done to improve our imaging. We'll also propose some simple changes that we believe could improve the scattering limit as well.

#### 5.3.1 Current Imaging Limitations

Our current fluorescence imaging involves two of the MOT beams that are retro-reflected back into the chamber. These are apertured with imaging masks that are approximately two by three millimeters. This is a hard aperture as the size of the beams is nearly the same width as the end-to-end cloud separation of the magnetic sublevels in our normal experimental procedure. We do this to minimize the scattered light which dominates our noise floor. The means that a slight misalignment can affect our detection accuracy by not imaging both clouds evenly. One way we could mitigate this is by adding a third beam oriented vertically, which would pass through the largest viewport on the vacuum chamber. This would ideally eliminate most of the background scatter, as we believe most of it arises from the scatter off of the lens mount, located near the horizontal beam's entry and exit. Using the larger, unobstructed viewport could also mean we can use a larger beam, as opposed to the few millimeter apertures used on the horizontal beams, which might be more robust against any misalignment or cloud movements.

An additional beam could also increase the CPA of the imaging system as it introduces more beams to the system, thus increasing the counts per atoms emitted by the atoms, assuming the overall intensity is below the saturation limit (see discussion in subsection 3.6.4). Moreover, the addition of a third pair of beams also creates the potential for the cloud to be trapped, as opposed only in the transverse direction with the horizontal

imaging beams. This leads to the possibility of increasing the experimental exposure time to much longer. While both the photon shot noise and the scattering noise scale as  $1/\tau$  [99], and thus the noise from the scatter can't be reduced to lower the noise floor independently, the long exposure time does allow for longer interrogation time, which may be useful for collecting more fluorescence from smaller numbered condensates.

As expressed in subsection 4.4.1, we can write the combined noise measured from the magnetization as:

$$\xi_{detection}^2 = 10 \log_{10}(\sigma_{PSN}^2 + \sigma_{bkg}^2)/(N_+ + N_-), \quad (5.6)$$

where  $\sigma_{bkg}$  is the empirically measured background noise detected which includes the scatter noise plus the noise associated with the read out from the camera. When we measure this noise,  $\sigma_{bkg}$  or  $\Delta M_{bkg}$ , we measure the standard deviation in the measured magnetization. Using ROIs used on the experiment for the  $\pm 1$  regions from our projective measurement, we can extract what the measured noise would be for a combination of imaging beams. Measurements for the top MOT beam (MOT 1) and the horizontal MOT beams (MOT 2 and MOT 3), are performed in this manner and shown in Table 5.3. These measurements clearly denote the advantage using MOT 1 has as an imaging beam, as it produces much less detected scattering noise than the MOT 2 and MOT 3 beams. Even the MOT 1 beam on its own is still shown to produce the same order of magnitude noise as the masked horizontal MOT beams.

We attempt to test and use the vertical, MOT 1 beam to image the condensate with various masks ranging from 2 mm to 10 mm, but settle on a 5 mm mask for the tests shown here. Aligning it with the condensate (see Figure 5.13), we see that it alone is not saturating the cloud. Combining it with the other imaging beams (MOT 2 and MOT 3), we performed various long exposure tests and large-detuning tests using these clouds. While we were able to accurately predict the counts per atom (CPA) using the formula for non-resonant

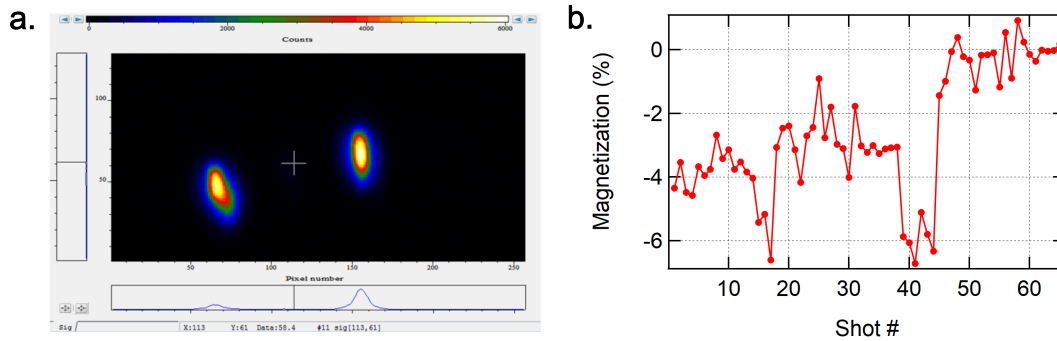


Figure 5.13: Vertical, MOT 1 mask adjustment showing the need to adjust masks even for the larger, vertical imaging beam. Image a) shows the balanced cloud after the magnetization has been balanced. Image b) shows the initial and final magnetization between the  $\pm 1$  clouds after mask adjustment.

and non-saturating imaging light (see subsection 5.3.2 below), the imaging became more difficult when attempting to image sizeable amounts of atoms in all three hyperfine levels. As can be seen in Figure 5.15, the clouds begin to bleed into each other when all three pairs of imaging beams are used, and it becomes difficult to accurately count each of the cloud populations. This was the case for even smaller exposures, such as our typical imaging time of  $200 \mu\text{s}$ . Moreover, the RF calibration points taken, even for separable clouds, seemed noisier than predicted and non-linear. For these reasons, after repeated attempts to improve this, we put the three MOT beam imaging on pause until we could revisit it with possibly smaller condensates.

In theory this or other imaging schemes should be investigated further, including incorporating the vertical MOT 1 beam again, and perhaps trying to modify its power. Likewise, other related schemes involving imaging through the large viewport on the chamber could be investigated, especially if large rebuilds of either the vacuum chamber or the imaging system is being undertaken. In the next section, we will motivate the use of a dedicated imaging system incorporating smaller, but more intense teams. This could further be done for all directions, as investigated and described here, allowing for longer exposure times and possibly more detuning, in order to interrogate the condensates for longer periods of time.

Table 5.3: Noise analysis by measuring the scattering noise with no atoms for the imaging beams to be tested.  $\Delta M$  computed from the noise between the  $\pm 1$  clouds using ROIs used in the experiment. Counts (and atoms) detected are displayed here without additional background subtraction, only that used in the ANDOR acquisition process is used here. Noise analysis performed under typical experimental imaging conditions: 200  $\mu\text{s}$  and 4x4 binning. CPA used to convert the counts to atoms is the empirical value of 157.91.

Beams Tested	$\Delta M_{bkg}$ (Counts)	$\Delta M_{bkg}$ (Atoms)
MOT 1, no mask	4148.4	26.3
MOT 2, no mask	72177	457
MOT 3, no mask	24245	154
MOT 1, 5 mm mask	876.09	5.54
MOT 2, 2 mm mask	1807.2	11.4
MOT 3, 2 mm mask	1227.2	7.77

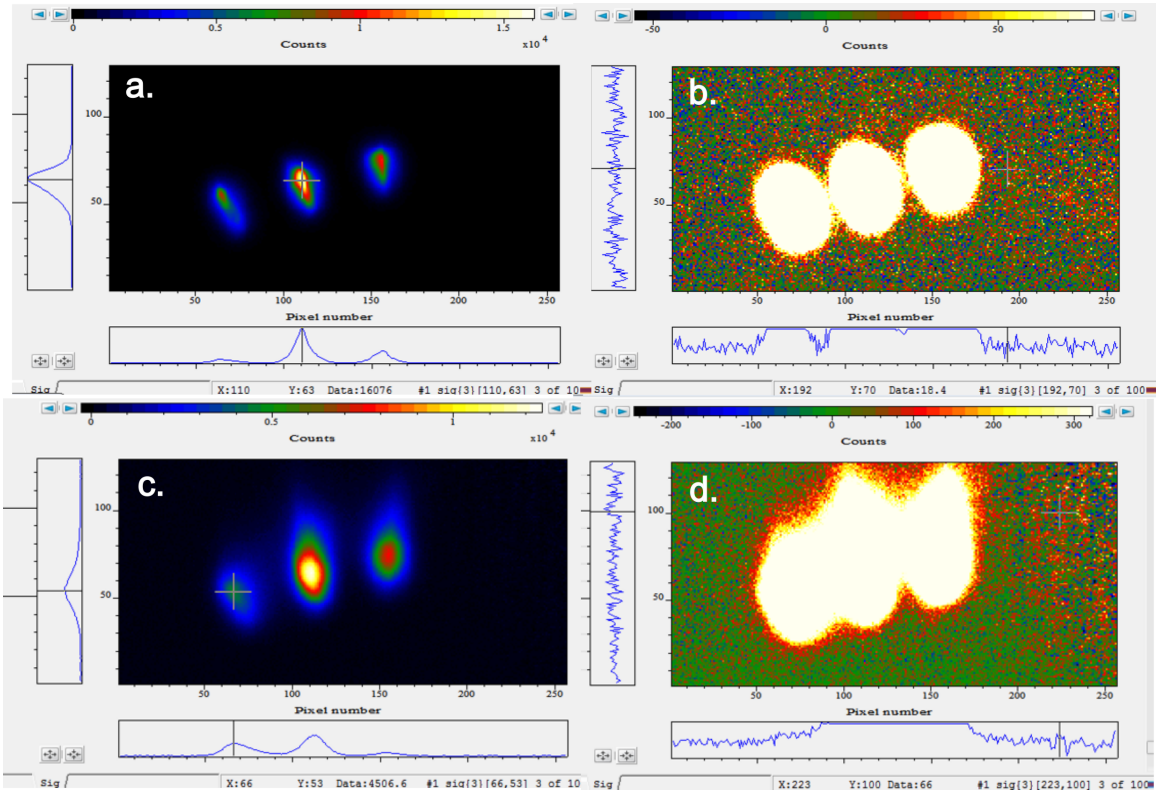


Figure 5.14: Imaging with all six beams, using short and long exposure times, we can see that the clouds are already broadened and indistinguishable at our normal imaging times. Images a) and b) are the same images, but on different scales, taken at our normal imaging parameters of 200  $\mu\text{s}$  and -7 MHz detuned. Likewise, clouds in c) and d) are also the same image, but on different scales. They are imaged at a much larger exposure time of 1.5 ms and -18 MHz, showing that these types of images can be taken, but that more work needs to be done to distinguish the different cloud regions, either with longer times of flight or smaller cloud sizes.

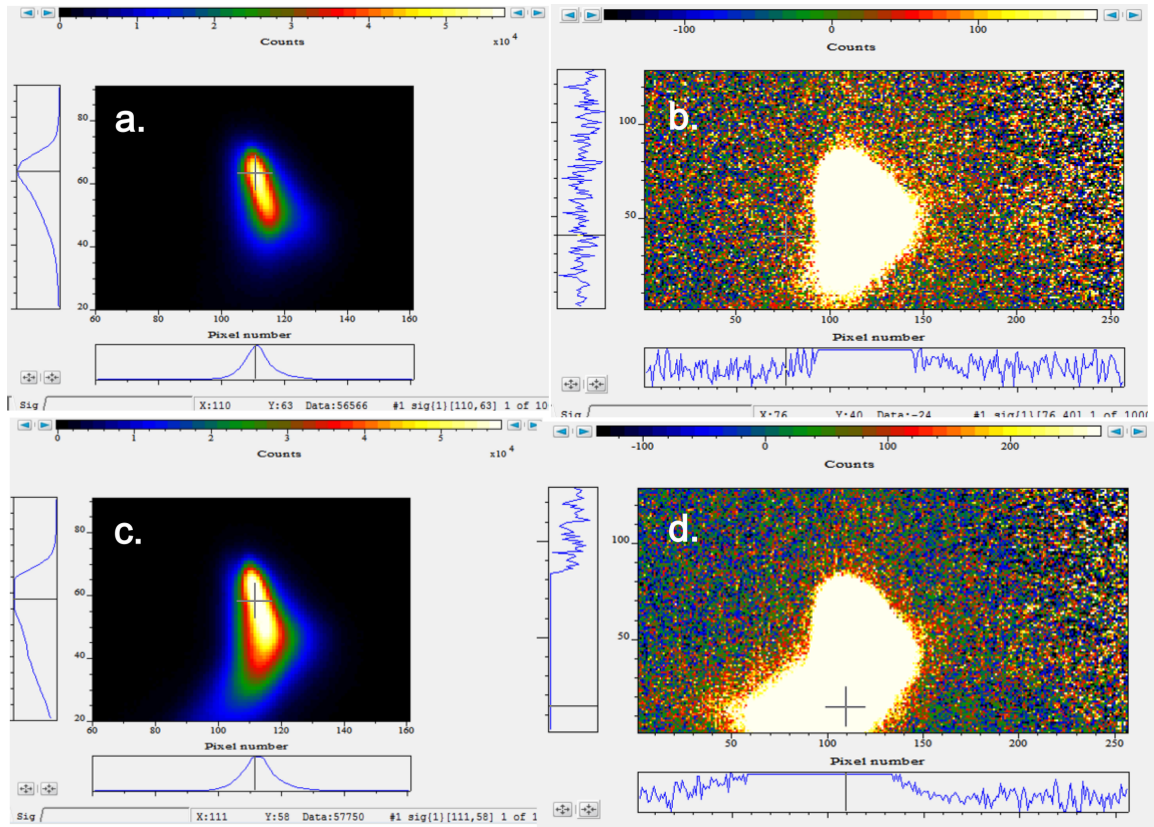


Figure 5.15: Imaging with all six beams, using long exposure times and large detunings, we can see that it is possible to us all image beams for a very long time (2 ms); we also find detuning the light helps confine the beam for longer exposure times, as one might expect. Images a)-b) are the same image but on different scales, and are imaged for 2 ms at around -29 MHz detuning. Images c)-d) are the same image but on different scales as well, and are imaged for 2ms at around -18 MHz.

### 5.3.2 Realistic CPA Estimates and Improvements

As discussed previously in section 3.6, we primarily use fluorescence imaging in our experiments as it seems to be the best calibrated at present. We presented in subsection 3.6.4 that the theoretical maximum value for the conversion of counts to atoms given a particular optical setup, is dependent on full saturation of the cycling transition (or  $I_{tot}/I_{sat} \rightarrow \infty$ ) on resonance ( $\omega_0$ ), such that  $R_{sc}(\omega_0) = \Gamma/2$ . In reality however, for our experiment and a detuning  $\Delta_{exp}/2\pi = -0.831$  Hz,  $I_{tot}/I_{sat} \approx 9$  and  $R_{sc}(\Delta) = (0.89)\Gamma/2$ . This leads to a decrease in the actual expected amount of scattered photons per atom. The general expression for this realistic CPA calculation can be written as:

$$CPA = R_{sc}(\Delta)\Omega\eta\tau. \quad (5.7)$$

where,

$$R_{sc}(\Delta) = \left(\frac{\Gamma}{2}\right) \frac{(I_{tot}/I_{sat})}{1 + 4(\Delta/\Gamma)^2 + (I_{tot}/I_{sat})}. \quad (5.8)$$

If we look at our current imaging system, we can calculate the deviation from the ideal conversion of counts to atoms. We can also use this to calculate what parameters could actually get us closer to the ideal case with very few experimental changes. One idea involves having dedicated imaging beams that are locked to the desired imaging transition and sent directly to the chamber. Currently our imaging beams consists of large, 1" diameter MOT beams with around 42 mW in each, that are apertured down for imaging to around 2 mm x 3 mm squares. This is done to limit the experimental scatter, which as discussed above, is the largest noise source in our system.

By having dedicated, small diameter imaging beams we can both mitigate the scatter limitations associated with using the alignment of the MOT beams being non-optimized for the condensate imaging, as MOT formation and final condensate locations occur at slightly different locations in the chamber. Additionally, the lasers locked to a singular set frequency have the potential to be more stable, as they are not associated with the other

Table 5.4: Table of possible CPA's for our current imaging system with  $200 \mu\text{s}$  exposure time and a detuning of  $\Delta/2\pi = -0.831 \text{ Hz}$ . The estimates for the expected counts per atom (CPA) is given in Equation 5.7.  $I_{tot} \equiv \sum_{i=N} I_i$  for a given intensity per beam of  $I_i$  and summed over the number of beams,  $N$ .  $I_{sat} = 3.2 \text{ mW/cm}^2$  and  $\Gamma/2 = 19.05 \text{ MHz}$ .

Imaging Beam Settings	CPA	$I_{tot}/I_{sat}$	$R_{sc}/\Gamma/2$
<b>Theoretical</b> maximum	172	$\infty$	1
<b>Current</b> (42 mW/beam, 4 beams, 25 mm)	154	9.3	0.90
<b>+2 Beams</b> (42 mW/beam, 6 beams, 25 mm)	159	14	0.93
<b>2x Power</b> (84 mW/beam, 4 beams, 25 mm)	162	19	0.95
<b>Small Beams</b> (10 mW/beam, 4 beams, 5 mm)	169	57	0.98
<b>Small Beams +2</b> (10 mW/beam, 6 beams, 5 mm)	170	85	0.99

cooling stages (i.e. MOT and dark MOT), and would no longer need to change frequency throughout the course of the experimental run. Finally, the smaller diameter imaging beams for a rather moderate power can achieve equal or greater light intensities, increasing the  $I_{tot}/I_{sat}$  ratio.

The values shown in Table 5.4 illustrate the experimental options available to us to impact the CPA for the experiment, and potentially even provide lower imaging scatter, as well as more stable imaging frequencies, if we choose to go to smaller beams. The biggest lever arm on improving the CPA is by increasing the intensity of the beams. For a set of smaller dedicated beams, with even moderate power, like 10 mW and only using horizontal pair of beams, we can increase the CPA nearly 10%. This could be a very powerful tool going forward, especially if the scatter can be reduced, as it would allow us to image for longer with higher signal, which will be an essential tool in improving our imaging for more sensitive measurements involving small condensates and higher squeezed states.

## CHAPTER 6

### CONCLUSION AND OUTLOOK

Since its inception, spinor BECs have been a very useful tool in exploring rich and more complex systems, both from the aspect of their controllability, as well as their ease of theoretical description. This ability is furthered by our lab's development of an all-optical creation of a BEC, whereby the spin degrees of freedom of the atom are free to interact. The ability to isolate the spin dynamics has led to rich descriptions in both the mean-field and quantum formalisms, as we have touched on in chapter 2, but most relevantly in our theoretical understanding of the mean-field phase space [72, 75] and experimental observation of coherent dynamics therein [71, 73, 70, 69].

Our previous works used our lab's understanding of the spin-1 formalism to generate highly entangled spin-nematic squeezing [75], parametric excitation [103], and number squeezing [129]. Moreover, we have been able to study these mean-field descriptions to make meaningful connections to quantum phase transitions in a spin-1 system, and explored crossing the quantum critical point in our system with our quantum Kibble-Zurek mechanism studies [79], as well as our studies of crossing it adiabatically [69]. Each of these techniques have comprised what has now been established as our understanding of the spin-1, rubidium BECs, and has become the metric with which we gauge the current experiment discussed in this thesis, as well as future endeavors.

In this thesis, we sought to explore a new way to cross the QCP. Analogous to condensed matter systems that utilize pressure and doping to change the QPT of the material, we use the modulation of the cloud's density to push the cloud through the QCP and into the interacting phase. We are able to do this without changing the bias magnetic field to perform the quench, as is traditionally done in similar spinor BEC experiments. We demonstrate not only that the QPT can be shifted, but that it can also be done reliably, as

the cloud exhibits coherent measurements of the phase space. Additionally, we are able to push the QCP such that we can engineer the emergence of spin mixing for a given magnetic field. Moreover, we can perform the shifting of the QPT in such a way that we can observe spin-nematic squeezing. We do so to a high degree, measuring  $-8.4 \pm 0.8$  dB of raw squeezing, not adjusted for the detection noise.

This is a useful technique that we hope we can build on more in the future by possibly modulating the cloud potential further, and thus the density, in such a way as to create parametric excitation, and eventually squeezing. Other further experiments we could perform are outlined below. The techniques devised and described in this thesis are further tools we have added to our spinor BEC toolkit, in the hopes that it can possibly be employed as an alternative quench method for future experiments.

## 6.1 Future Directions

We further highlight future experimental paths to explore, as well technical improvements that could create a more navigable terrain for these studies including a new vacuum system, an independent imaging system, and a means for studying small-atom number condensates.

### 6.1.1 New Atom Source and Vacuum Upgrades

We discussed in chapter 5 the experiments performed involving the development of a potentially new atom source in the form of a 2D-MOT to load a 3D-MOT, and eventually an optical dipole trap. Currently, we use a vapor cell MOT to load our experiment before transferring it to a  $10.6 \mu\text{m}$  dipole trap laser. This at present takes our experiment 15 seconds to load around 15 million atoms. The  $2\text{D}^+$ -MOT tests presented in this thesis showed that we could load nearly a billion atoms in  $\sim 1.8$  seconds. This was achieved even in non-ideal conditions, as the 2D-MOT source was loaded using an ampule (as opposed to a more controllable getter source) and was located very far away from the target location. The loading and total number of atoms is a drastic improvement over the current setup and

could nearly half our experimental run time. Using a 2D-MOT as our source would not only allow us to be able to take data faster, but potentially with more stability, as experimental drifts (e.g. magnetic field drifts, temperature changes, etc.) could become less of an issue as a given experiment would take less time to complete. An additional benefit would be the improved vacuum in the main experimental chamber as well, as we wouldn't need as high of a partial pressure of rubidium to make a decent MOT. The vacuum pressure could be maintained at a lower level conceivably, as the differential pumping in the 2D-MOT would allow for the loading to occur at a higher pressure and not impact the area where the condensate is formed. This would lead to longer lifetimes, and more time to study our condensates without major losses in coherence due to atoms leaving the trap.

Finally, a couple of low-impact designs have been proposed in Table 5.2, which could readily be implemented on the experiment with minimal change to the other parts of the experiment. Adding a compact pre-fabricated 2D<sup>+</sup>-MOT, or even using the cell used in the previous iterations of our tests could be used. If major rebuilds are being considered however, it would also be ideal to possibly incorporate upgrades to a new imaging system in tandem. These improvements are touched on in the next section.

### 6.1.2 Reducing Scatter and Improving Squeezing Detection

The imaging in our system is vital to our data-taking process, as we acquire many images to count and gather statistics on our atomic populations. As presented in subsection 3.6.5 and subsection 4.4.1, there are several key noise sources in our experiment that must be taken into consideration when we image, especially when taking low-noise data. This type of data is typical of the squeezing data we take, where the ratio between the detected atom noise and the noise from the total number of atoms is used to determine the amount of squeezing we measure. Thus any noise in the detection, either from scatter or camera-related sources, minimize the lowest level of atoms that we can detect. As we've stated, the current detection limit is set by the scatter noise associated with the imaging beams themselves. This

level was measured to be around  $\Delta M_{bkg} = 49$  atoms for our typical imaging system (see subsection 4.4.1). While this is not prohibitive for our current measurements, as we have large enough condensates that a noise of 49 atoms still allows us to measure a decent degree of squeezing, it would become a problem should we go to smaller and smaller cloud sizes.

In addition to this possible limitation, there is the fact that we are imaging with a lower intensity than the ideal ( $I_{tot}/I_{sat} \rightarrow \infty$ ). This was discussed in section 5.3. There we saw that imaging with a third beam oriented through our largest viewport afforded us lower scatter noise, but also had the potential to increase the overall intensity delivered to the atoms by hitting it with more beams. In our experiments with the additional imaging beams, we found it very challenging to count the other atomic regions independently. While in theory the extra pair of beams is helpful, especially in the prospects of possibly imaging for longer exposure times and increasing the signal to noise, it is in general not nearly as helpful as imaging with smaller beams with higher intensity. For even just a replacement of the horizontal imaging beams with 5 mm diameter width with 10mW of power in each, we can accomplish a ratio of  $I_{tot}/I_{sat}$  to be 10x higher than what we currently have. This could be achieved with a single diode laser dedicated to providing imaging beams. Additionally, these could be added to the experiment with greater precision of alignment to the cloud and with minimal additional optics, with perhaps pneumatic mirrors placed in the path of the current MOT beams. Likewise, the locking of a single diode laser to the imaging transition for the duration of the experimental cycle should help with the frequency noise and stability, which will aid in the accuracy of the imaging as well.

As stated, while not imperative for our tests described here, improving the fluorescence imaging in our system is important to all aspects of our work. In the case of future, more sensitive experiments such as small atom number condensates or higher levels of squeezing, an improved imaging system becomes imperative. The noise reduction and possibly higher CPA would afford us a smaller detection limit and better signal to noise, respectively.

### 6.1.3 Studying the Finite Energy Gap

Finally, we touched on means of creating a variety of small atom number condensates ranging from 100s to 1000s of atoms. We demonstrated these could be shown to exhibit coherence and interaction, however the experiments were limited by both the detection and the stability of the final atom number which seemed to drift throughout the day. Experiments using small numbers of condensates are interesting because of the finite-atom number effects. In our case, we would like to measure the magnitude of these effects for a variety of small numbered clouds. Doing so would allow us to continue the work began in [69] in attempting an adiabatic crossing of the QCP.

If achieved, this could lead to very interesting physics including creating a massively-entangled, macroscopic quantum state known as a Dicke state [104]. To our knowledge, this would be the first of its kind, and interesting in its own right. Opening up the energy gap via finite atom effects is also useful in that crossing the QCP adiabatically is much more achievable and can be done at a faster rate. This is important due to the finite lifetime of our condensates, as well, as the time needed to cross the transition adiabatically is inversely proportional to the energy gap. Faster quench times means more atoms that are left in the trap at the end of the quench, leading to the retention of correlated pairs. Previous adiabatic experiments tried to count the number of entangled atoms using the spin variables, but found the loss in atoms was so great that we were unable to accurately estimate this quantity [69]. Performing experiments with finite numbers of atoms could help us perform these and other types of metrologically interesting experiments, pushing us into new territory to explore.

## REFERENCES

- [1] S. Sachdev, *Quantum Phase Transitions*. Cambridge University Press, 1999.
- [2] R. Pathria and P. Beale, *Statistical Mechanics*. Elsevier, 1996.
- [3] G. A. Gehring, “Pressure-induced quantum phase transitions,” *EPL (Europhysics Letters)*, vol. 82, no. 6, p. 60 004, Jun. 2008.
- [4] Q. Zeng *et al.*, “Pressure-Driven Magneto-Topological Phase Transition in a Magnetic Weyl Semimetal,” *Advanced Quantum Technologies*, vol. 5, no. 4, p. 2 100 149, Apr. 2022.
- [5] D. B. McWhan and J. P. Remeika, “Metal-insulator transition in  $(V_{1-x}Cr_x)_2O_3$ ,” *Phys. Rev. B*, vol. 2, pp. 3734–3750, 9 Nov. 1970.
- [6] F. Kagawa, K. Miyagawa, and K. Kanoda, “Unconventional critical behaviour in a quasi-two-dimensional organic conductor,” *Nature*, vol. 436, no. 7050, pp. 534–537, Jul. 2005.
- [7] S. M. Stishov and A. E. Petrova, “Critical Points and Phase Transitions,” *Journal of Experimental and Theoretical Physics*, vol. 131, no. 6, pp. 1056–1063, Dec. 2020.
- [8] H. Kim, J. H. Shim, S. Kim, J.-H. Park, K. Kim, and B. I. Min, “Unusual Pressure-Induced Quantum Phase Transition from Superconducting to Charge-Density Wave State in Rare-Earth-Based Heusler LuPd 2 In Compound,” *Physical Review Letters*, vol. 125, no. 15, p. 157 001, Oct. 2020.
- [9] T. Hong *et al.*, “Evidence for pressure induced unconventional quantum criticality in the coupled spin ladder antiferromagnet  $C9H18N2CuBr4$ ,” *Nature Communications*, vol. 13, no. 1, p. 3073, Jun. 2022.
- [10] S. A. Zvyagin *et al.*, “Pressure-tuning the quantum spin Hamiltonian of the triangular lattice antiferromagnet  $Cs2CuCl4$ ,” *Nature Communications*, vol. 10, no. 1, p. 1064, Mar. 2019.
- [11] P. Limelette, A. Georges, D. Jérôme, P. Wzietek, P. Metcalf, and J. M. Honig, “Universality and Critical Behavior at the Mott Transition,” *Science*, vol. 302, no. 5642, pp. 89–92, Oct. 2003.
- [12] Y. Suzuki *et al.*, “Mott-Driven BEC-BCS Crossover in a Doped Spin Liquid Candidate  $\kappa$ - ( BEDT - TTF ) 4 Hg 2.89 Br 8,” *Physical Review X*, vol. 12, no. 1, p. 011 016, Jan. 2022.

- [13] T. Biesner and E. Uykur, “Pressure-Tuned Interactions in Frustrated Magnets: Pathway to Quantum Spin Liquids?” *Crystals*, vol. 10, no. 1, p. 4, Dec. 2019.
- [14] C. Rüegg *et al.*, “Pressure-Induced Quantum Phase Transition in the Spin-Liquid  $TlCuCl_3$ ,” *Physical Review Letters*, vol. 93, no. 25, p. 257 201, Dec. 2004.
- [15] J. Qiu *et al.*, “Pressure induced phase transitions of bulk  $CsGeCl_3$  and ultrafast laser pulse induced excited-state properties of  $CsGeCl_3$  quantum dots,” *Physical Chemistry Chemical Physics*, vol. 24, no. 36, pp. 22 038–22 045, 2022.
- [16] L. Kou, C. Tang, Y. Zhang, T. Heine, C. Chen, and T. Frauenheim, “Tuning Magnetism and Electronic Phase Transitions by Strain and Electric Field in Zigzag  $MoS_2$  Nanoribbons,” *The Journal of Physical Chemistry Letters*, vol. 3, no. 20, pp. 2934–2941, Oct. 2012.
- [17] M. H. Anderson, J. R. Ensher, M. R. Matthews, C. E. Wieman, and E. A. Cornell, “Observation of bose-einstein condensation in a dilute atomic vapor,” *Science*, vol. 269, no. 5221, pp. 198–201, Jul. 14, 1995.
- [18] C. C. Bradley, C. A. Sackett, J. J. Tollett, and R. G. Hulet, “Evidence of bose-einstein condensation in an atomic gas with attractive interactions,” *Physical Review Letters*, vol. 75, no. 9, pp. 1687–1690, Aug. 28, 1995.
- [19] K. B. Davis *et al.*, “Bose-einstein condensation in a gas of sodium atoms,” *Physical Review Letters*, vol. 75, no. 22, pp. 3969–3973, Nov. 27, 1995.
- [20] M. R. Andrews, C. G. Townsend, H.-J. Miesner, D. S. Durfee, D. M. Kurn, and W. Ketterle, “Observation of interference between two bose condensates,” *Science*, vol. 275, no. 5300, pp. 637–641, 1997.
- [21] I. Bloch, T. W. Hänsch, and T. Esslinger, “Measurement of the spatial coherence of a trapped Bose gas at the phase transition,” *Nature*, vol. 403, no. 6766, pp. 166–170, Jan. 2000.
- [22] M.-O. Mewes, M. R. Andrews, D. M. Kurn, D. S. Durfee, C. G. Townsend, and W. Ketterle, “Output coupler for bose-einstein condensed atoms,” *Phys. Rev. Lett.*, vol. 78, pp. 582–585, 4 Jan. 1997.
- [23] I. Bloch, T. W. Hänsch, and T. Esslinger, “Atom laser with a cw output coupler,” *Phys. Rev. Lett.*, vol. 82, pp. 3008–3011, 15 Apr. 1999.
- [24] E. W. Hagley *et al.*, “A well-collimated quasi-continuous atom laser,” *Science*, vol. 283, no. 5408, pp. 1706–1709, 1999.

- [25] M. R. Matthews, B. P. Anderson, P. C. Haljan, D. S. Hall, C. E. Wieman, and E. A. Cornell, “Vortices in a bose-einstein condensate,” *Phys. Rev. Lett.*, vol. 83, pp. 2498–2501, 13 Sep. 1999.
- [26] K. W. Madison, F. Chevy, W. Wohlleben, and J. Dalibard, “Vortex formation in a stirred bose-einstein condensate,” *Phys. Rev. Lett.*, vol. 84, pp. 806–809, 5 Jan. 2000.
- [27] J. R. Abo-Shaeer, C. Raman, J. M. Vogels, and W. Ketterle, “Observation of vortex lattices in bose-einstein condensates,” *Science*, vol. 292, no. 5516, pp. 476–479, 2001.
- [28] B. P. Anderson and M. A. Kasevich, “Macroscopic quantum interference from atomic tunnel arrays,” *Science*, vol. 282, no. 5394, pp. 1686–1689, 1998.
- [29] M. Albiez, R. Gati, J. Fölling, S. Hunsmann, M. Cristiani, and M. K. Oberthaler, “Direct observation of tunneling and nonlinear self-trapping in a single bosonic josephson junction,” *Phys. Rev. Lett.*, vol. 95, p. 010402, 1 Jun. 2005.
- [30] D. M. Stamper-Kurn *et al.*, “Optical confinement of a bose-einstein condensate,” *Phys. Rev. Lett.*, vol. 80, pp. 2027–2030, 10 Mar. 1998.
- [31] M. D. Barrett, J. A. Sauer, and M. S. Chapman, “All-optical formation of an atomic bose-einstein condensate,” *Physical Review Letters*, vol. 87, no. 1, p. 010404, Jun. 19, 2001.
- [32] H.-J. Miesner, D. M. Stamper-Kurn, J. Stenger, S. Inouye, A. P. Chikkatur, and W. Ketterle, “Observation of metastable states in spinor bose-einstein condensates,” *Phys. Rev. Lett.*, vol. 82, pp. 2228–2231, 11 Mar. 1999.
- [33] S. Inouye, M. R. Andrews, J. Stenger, H.-J. Miesner, D. M. Stamper-Kurn, and W. Ketterle, “Observation of feshbach resonances in a bose-einstein condensate,” *Nature*, vol. 392, no. 6672, pp. 151–154, Mar. 1, 1998.
- [34] D. M. Stamper-Kurn, H.-J. Miesner, A. P. Chikkatur, S. Inouye, J. Stenger, and W. Ketterle, “Quantum tunneling across spin domains in a bose-einstein condensate,” *Phys. Rev. Lett.*, vol. 83, pp. 661–665, 4 Jul. 1999.
- [35] J. Stenger, S. Inouye, D. M. Stamper-Kurn, H.-J. Miesner, A. P. Chikkatur, and W. Ketterle, “Spin domains in ground-state bose-einstein condensates,” *Nature*, vol. 396, no. 6709, pp. 345–348, Nov. 1, 1998.
- [36] E. A. Cornell, D. S. Hall, M. R. Matthews, and C. E. Wieman, “Having It Both Ways: Distinguishable Yet Phase-Coherent Mixtures of Bose-Einstein Conden-

- sates,” *Journal of Low Temperature Physics*, vol. 113, no. 3, pp. 151–165, Nov. 1998.
- [37] T. Ohmi and K. Machida, “Bose-einstein condensation with internal degrees of freedom in alkali atom gases,” *Journal of the Physical Society of Japan*, vol. 67, no. 6, pp. 1822–1825, 1998.
- [38] T.-L. Ho, “Spinor Bose Condensates in Optical Traps,” *Physical Review Letters*, vol. 81, no. 4, pp. 742–745, Jul. 1998, arXiv: cond-mat/9803231.
- [39] C. K. Law, H. Pu, and N. P. Bigelow, “Quantum spins mixing in spinor Bose-Einstein condensates,” *Physical Review Letters*, vol. 81, no. 24, pp. 5257–5261, Dec. 1998, arXiv: cond-mat/9807258.
- [40] H. Pu, C. K. Law, S. Raghavan, J. H. Eberly, and N. P. Bigelow, “Spin-mixing dynamics of a spinor bose-einstein condensate,” *Phys. Rev. A*, vol. 60, pp. 1463–1470, 2 Aug. 1999.
- [41] G. I. Mias, N. R. Cooper, and S. M. Girvin, “Quantum noise, scaling, and domain formation in a spinor Bose-Einstein condensate,” *Physical Review A*, vol. 77, no. 2, p. 023 616, Feb. 2008.
- [42] W. Zhang, S. Yi, and L. You, “Mean field ground state of a spin-1 condensate in a magnetic field,” *New Journal of Physics*, vol. 5, pp. 77–77, Jun. 2003.
- [43] W. Zhang, D. L. Zhou, M.-S. Chang, M. S. Chapman, and L. You, “Coherent spin mixing dynamics in a spin-1 atomic condensate,” *Phys. Rev. A*, vol. 72, p. 013 602, 1 Jul. 2005.
- [44] M.-S. Chang *et al.*, “Observation of spinor dynamics in optically trapped  $^{87}\text{Rb}$  bose-einstein condensates,” *Phys. Rev. Lett.*, vol. 92, p. 140 403, 14 Apr. 2004.
- [45] M.-S. Chang, Q. Qin, W. Zhang, L. You, and M. S. Chapman, “Coherent spinor dynamics in a spin-1 bose condensate,” *Nature Physics*, vol. 1, no. 2, pp. 111–116, Nov. 1, 2005.
- [46] H. Schmaljohann *et al.*, “Dynamics of  $F = 2$  spinor bose-einstein condensates,” *Phys. Rev. Lett.*, vol. 92, p. 040 402, 4 Jan. 2004.
- [47] J. Kronjäger *et al.*, “Evolution of a spinor condensate: Coherent dynamics, dephasing, and revivals,” *Phys. Rev. A*, vol. 72, p. 063 619, 6 Dec. 2005.
- [48] J. Kronjäger, C. Becker, P. Navez, K. Bongs, and K. Sengstock, “Magnetically tuned spin dynamics resonance,” *Phys. Rev. Lett.*, vol. 97, p. 110 404, 11 Sep. 2006.

- [49] A. Widera, F. Gerbier, S. Fölling, T. Gericke, O. Mandel, and I. Bloch, “Coherent collisional spin dynamics in optical lattices,” *Phys. Rev. Lett.*, vol. 95, p. 190 405, 19 Nov. 2005.
- [50] A. T. Black, E. Gomez, L. D. Turner, S. Jung, and P. D. Lett, “Spinor dynamics in an antiferromagnetic spin-1 condensate,” *Phys. Rev. Lett.*, vol. 99, p. 070 403, 7 Aug. 2007.
- [51] L. E. Sadler, J. M. Higbie, S. R. Leslie, M. Vengalattore, and D. M. Stamper-Kurn, “Spontaneous symmetry breaking in a quenched ferromagnetic spinor Bose–Einstein condensate,” *Nature*, vol. 443, no. 7109, pp. 312–315, Sep. 2006.
- [52] M. Vengalattore, S. R. Leslie, J. Guzman, and D. M. Stamper-Kurn, “Spontaneously modulated spin textures in a dipolar spinor bose-einstein condensate,” *Phys. Rev. Lett.*, vol. 100, p. 170 403, 17 May 2008.
- [53] C. Klempt *et al.*, “Multiresonant spinor dynamics in a bose-einstein condensate,” *Phys. Rev. Lett.*, vol. 103, p. 195 302, 19 Nov. 2009.
- [54] L. S. Leslie, A. Hansen, K. C. Wright, B. M. Deutsch, and N. P. Bigelow, “Creation and detection of skyrmions in a bose-einstein condensate,” *Phys. Rev. Lett.*, vol. 103, p. 250 401, 25 Dec. 2009.
- [55] E. M. Bookjans, A. Vinit, and C. Raman, “Quantum phase transition in an antiferromagnetic spinor bose-einstein condensate,” *Phys. Rev. Lett.*, vol. 107, p. 195 306, 19 Nov. 2011.
- [56] A. Lamacraft, “Quantum Quenches in a Spinor Condensate,” *Physical Review Letters*, vol. 98, no. 16, p. 160 404, Apr. 2007.
- [57] K. Murata, H. Saito, and M. Ueda, “Broken-axisymmetry phase of a spin-1 ferromagnetic Bose-Einstein condensate,” *Physical Review A*, vol. 75, no. 1, p. 013 607, Jan. 2007.
- [58] I. Bloch, J. Dalibard, and W. Zwerger, “Many-body physics with ultracold gases,” *Rev. Mod. Phys.*, vol. 80, pp. 885–964, 3 Jul. 2008.
- [59] M. Greiner, O. Mandel, and T. Esslinger, “Quantum phase transition from a superfluid to a Mott insulator in a gas of ultracold atoms,” vol. 415, p. 6, 2002.
- [60] L. Tarruell and L. Sanchez-Palencia, “Quantum simulation of the hubbard model with ultracold fermions in optical lattices,” *Quantum simulation / Simulation quantitative*, vol. 19, no. 6, pp. 365–393, Sep. 1, 2018.

- [61] A. B. Kuklov and B. V. Svistunov, “Counterflow superfluidity of two-species ultracold atoms in a commensurate optical lattice,” *Phys. Rev. Lett.*, vol. 90, p. 100 401, 10 Mar. 2003.
- [62] L.-M. Duan, E. Demler, and M. D. Lukin, “Controlling spin exchange interactions of ultracold atoms in optical lattices,” *Phys. Rev. Lett.*, vol. 91, p. 090 402, 9 Aug. 2003.
- [63] A. Imambekov, M. Lukin, and E. Demler, “Spin-exchange interactions of spin-one bosons in optical lattices: Singlet, nematic, and dimerized phases,” *Phys. Rev. A*, vol. 68, p. 063 602, 6 Dec. 2003.
- [64] S. Levy, E. Lahoud, I. Shomroni, and J. Steinhauer, “The a.c. and d.c. Josephson effects in a Bose–Einstein condensate,” *Nature*, vol. 449, no. 7162, pp. 579–583, Oct. 2007.
- [65] M. Trippenbach, E. Infeld, J. Gocałek, M. Matuszewski, M. Oberthaler, and B. A. Malomed, “Spontaneous symmetry breaking of gap solitons and phase transitions in double-well traps,” *Physical Review A*, vol. 78, no. 1, p. 013 603, Jul. 2008.
- [66] M. F. Riedel, P. Böhi, Y. Li, T. W. Hänsch, A. Sinatra, and P. Treutlein, “Atom-chip-based generation of entanglement for quantum metrology,” *Nature*, vol. 464, no. 7292, pp. 1170–1173, Apr. 2010.
- [67] C. Gross, “Nonlinear atom interferometer surpasses classical precision limit,” vol. 464, p. 5, 2010.
- [68] S. Morrison and A. S. Parkins, “Collective spin systems in dispersive optical cavity QED: Quantum phase transitions and entanglement,” *Physical Review A*, vol. 77, no. 4, p. 043 810, Apr. 2008.
- [69] T. M. Hoang, H. M. Bharath, M. J. Boguslawski, M. Anquez, B. A. Robbins, and M. S. Chapman, “Adiabatic quenches and characterization of amplitude excitations in a continuous quantum phase transition,” *Proceedings of the National Academy of Sciences*, vol. 113, no. 34, pp. 9475–9479, Aug. 2016.
- [70] M.-S. Chang *et al.*, “Observation of spinor dynamics in optically trapped  $^{87}\text{Rb}$  bose-einstein condensates,” *Phys. Rev. Lett.*, vol. 92, p. 140 403, 14 Apr. 2004.
- [71] M.-S. Chang, Q. Qin, W. Zhang, L. You, and M. S. Chapman, “Coherent spinor dynamics in a spin-1 Bose condensate,” *Nature Physics*, vol. 1, no. 2, pp. 111–116, Nov. 2005.

- [72] W. Zhang, D. L. Zhou, M.-S. Chang, M. S. Chapman, and L. You, “Coherent spin mixing dynamics in a spin-1 atomic condensate,” *Physical Review A*, vol. 72, no. 1, p. 013 602, Jul. 2005.
- [73] C. Gerving, T. Hoang, B. Land, M. Anquez, C. Hamley, and M. Chapman, “Non-equilibrium dynamics of an unstable quantum pendulum explored in a spin-1 Bose–Einstein condensate,” *Nature Communications*, vol. 3, p. 1169, 1 Nov. 2012.
- [74] Q. Zhai, L. Chang, R. Lu, and L. You, “Number fluctuation dynamics of a spin-1 atomic condensate,” *Phys. Rev. A*, vol. 79, p. 043 608, 4 Apr. 2009.
- [75] C. D. Hamley, C. S. Gerving, T. M. Hoang, E. M. Bookjans, and M. S. Chapman, “Spin-nematic squeezed vacuum in a quantum gas,” *Nature Physics*, vol. 8, no. 4, pp. 305–308, Apr. 2012.
- [76] J. Dziarmaga, “Dynamics of a quantum phase transition and relaxation to a steady state,” *Advances in Physics*, vol. 59, no. 6, pp. 1063–1189, Nov. 2010, Publisher: Taylor & Francis.
- [77] J. Dziarmaga and W. H. Zurek, “Quench in the 1D Bose-Hubbard model: Topological defects and excitations from the Kosterlitz-Thouless phase transition dynamics,” *Scientific Reports*, vol. 4, no. 1, p. 5950, May 2015.
- [78] W. H. Zurek, U. Dorner, and P. Zoller, “Dynamics of a Quantum Phase Transition,” *Physical Review Letters*, vol. 95, no. 10, p. 105 701, Sep. 2005.
- [79] M. Anquez, B. A. Robbins, H. M. Bharath, M. Boguslawski, T. M. Hoang, and M. S. Chapman, “Quantum Kibble-Zurek Mechanism in a Spin-1 Bose-Einstein Condensate,” *Physical Review Letters*, vol. 116, no. 15, p. 155 301, Apr. 2016.
- [80] B. H. M., M. Boguslawski, M. Barrios, L. Xin, and M. S. Chapman, “Exploring non-abelian geometric phases in spin-1 ultracold atoms,” *Phys. Rev. Lett.*, vol. 123, p. 173 202, 17 Oct. 2019.
- [81] M. Boguslawski, “All-microwave control of hyperfine states in ultracold spin-1 rubidium,” Ph.D. dissertation, Georgia Institute of Technology, 2019.
- [82] L. Xin, M. Barrios, J. T. Cohen, and M. S. Chapman, “Long-lived squeezed ground states in a quantum spin ensemble,” *Phys. Rev. Lett.*, vol. 131, p. 133 402, 13 Sep. 2023.
- [83] T. Ohmi and K. Machida, “Bose-Einstein Condensation with Internal Degrees of Freedom in Alkali Atom Gases,” *Journal of the Physical Society of Japan*, vol. 67, no. 6, pp. 1822–1825, Jun. 1998.

- [84] S. Yi, Ö. E. Müstecaplıoğlu, C. P. Sun, and L. You, “Single-mode approximation in a spinor-1 atomic condensate,” *Physical Review A*, vol. 66, no. 1, p. 011 601, Jul. 2002.
- [85] E. G. M. van Kempen, S. J. J. M. F. Kokkelmans, D. J. Heinzen, and B. J. Verhaar, “Interisotope determination of ultracold rubidium interactions from three high-precision experiments,” *Phys. Rev. Lett.*, vol. 88, p. 093 201, 9 Feb. 2002.
- [86] C. Hamley, “Spin Nematic Squeezing in a Spin-1 BEC,” Ph.D. dissertation, Georgia Institute of Technology, 2012.
- [87] C. Girving, “Dynamics of a spin-1 bec in the regime of a quantum inverted pendulum,” Ph.D. dissertation, Georgia Institute of Technology, 2013.
- [88] T. Hoang, “Quantum control of a many body system in a spin-1 bose-einstein condensate,” Ph.D. dissertation, Georgia Institute of Technology, 2013.
- [89] L. Xin, “Shortcut to target states in a spin-1 bose-einstein condensate,” Ph.D. dissertation, Georgia Institute of Technology, 2022.
- [90] B. H. M., “Geometry, topology and control of spin-1 quantum systems,” Ph.D. dissertation, Georgia Institute of Technology, 2018.
- [91] M. Anquez, “Kibble-zurek mechanism in a spin-1 bose-einstein condensate,” Ph.D. dissertation, Georgia Institute of Technology, 2015.
- [92] M.-S. Chang, “Coherent spin dynamics of a spin-1 bose-einstein condensate,” Ph.D. dissertation, Georgia Institute of Technology, 2006.
- [93] M. Barrett, “A quest for bec: An all optical alternative,” Ph.D. dissertation, Georgia Institute of Technology, 2002.
- [94] C. E. Wieman and L. Hollberg, “Using diode lasers for atomic physics,” *Review of Scientific Instruments*, vol. 62, no. 1, pp. 1–20, Jan. 1991. eprint: [https://pubs.aip.org/aip/rsi/article-pdf/62/1/1/8382797/1\\_1\\_online.pdf](https://pubs.aip.org/aip/rsi/article-pdf/62/1/1/8382797/1_1_online.pdf).
- [95] D. W. Preston, “Doppler-free saturated absorption: Laser spectroscopy,” *American Journal of Physics*, vol. 64, no. 11, pp. 1432–1436, Nov. 1996.
- [96] D. E. Pritchard, E. L. Raab, V. Bagnato, C. E. Wieman, and R. N. Watts, “Light traps using spontaneous forces,” *Phys. Rev. Lett.*, vol. 57, pp. 310–313, 3 Jul. 1986.
- [97] S. Chu, J. E. Bjorkholm, A. Ashkin, and A. Cable, “Experimental observation of optically trapped atoms,” *Phys. Rev. Lett.*, vol. 57, pp. 314–317, 3 Jul. 1986.

- [98] R. Grimm, M. Weidemüller, and Y. B. Ovchinnikov, “Optical dipole traps for neutral atoms,” in ser. *Advances In Atomic, Molecular, and Optical Physics*, B. Bederson and H. Walther, Eds., vol. 42, Academic Press, 2000, pp. 95–170.
- [99] E. Bookjans, “Relative number squeezing in a spin-1 bec,” Ph.D. dissertation, Georgia Institute of Technology, 2010.
- [100] D. Steck, “Rubidium 87 d line data,” University of Oregon, Tech. Rep., 2001.
- [101] E. M. Bookjans, A. Vinit, and C. Raman, “Quantum Phase Transition in an Antiferromagnetic Spinor Bose-Einstein Condensate,” *Physical Review Letters*, vol. 107, no. 19, p. 195 306, Nov. 2011.
- [102] J. Goldstone, “Field theories with « Superconductor » solutions,” *Il Nuovo Cimento (1955-1965)*, vol. 19, no. 1, pp. 154–164, Jan. 1961.
- [103] T. M. Hoang *et al.*, “Parametric excitation and squeezing in a many-body spinor condensate,” *Nature Communications*, vol. 7, no. 1, p. 11 233, Sep. 2016.
- [104] Z. Zhang and L.-M. Duan, “Generation of Massive Entanglement through an Adiabatic Quantum Phase Transition in a Spinor Condensate,” *Physical Review Letters*, vol. 111, no. 18, p. 180 401, Oct. 2013.
- [105] L. Pezzè, A. Smerzi, M. K. Oberthaler, R. Schmied, and P. Treutlein, “Quantum metrology with nonclassical states of atomic ensembles,” *Reviews of Modern Physics*, vol. 90, no. 3, p. 035 005, Sep. 2018.
- [106] B. Lucke *et al.*, “Detecting multiparticle entanglement of dicke states,” *Phys. Rev. Lett.*, vol. 112, p. 155 304, 15 Apr. 2014.
- [107] L.-M. Duan, J. I. Cirac, and P. Zoller, “Quantum entanglement in spinor Bose-Einstein condensates,” *Physical Review A*, vol. 65, no. 3, p. 033 619, Feb. 2002.
- [108] L.-M. Duan, “Entanglement Detection in the Vicinity of Arbitrary Dicke States,” *Physical Review Letters*, vol. 107, no. 18, p. 180 502, Oct. 2011.
- [109] G. Vitagliano, G. Colangelo, F. Martin Ciurana, M. W. Mitchell, R. J. Sewell, and G. Tóth, “Entanglement and extreme planar spin squeezing,” *Physical Review A*, vol. 97, no. 2, p. 020 301, Feb. 2018.
- [110] X.-Y. Luo *et al.*, “Deterministic entanglement generation from driving through quantum phase transitions,” *Science*, vol. 355, no. 6325, pp. 620–623, Feb. 10, 2017.

- [111] Y.-Q. Zou *et al.*, “Beating the classical precision limit with spin-1 dicke states of more than 10,000 atoms,” *Proceedings of the National Academy of Sciences*, vol. 115, no. 25, pp. 6381–6385, Jun. 19, 2018.
- [112] E. Farhi, J. Goldstone, S. Gutmann, J. Lapan, A. Lundgren, and D. Preda, “A Quantum Adiabatic Evolution Algorithm Applied to Random Instances of an NP-Complete Problem,” *Science*, vol. 292, no. 5516, pp. 472–475, Apr. 2001.
- [113] R. Schützhold and G. Schaller, “Adiabatic quantum algorithms as quantum phase transitions: First versus second order,” *Physical Review A*, vol. 74, no. 6, p. 060 304, Dec. 2006.
- [114] B. Evrard, A. Qu, J. Dalibard, and F. Gerbier, “Production and characterization of a fragmented spinor Bose-Einstein condensate,” *arXiv:2010.15739 [cond-mat]*, Oct. 2020, arXiv: 2010.15739.
- [115] E. J. Mueller, T.-L. Ho, M. Ueda, and G. Baym, “Fragmentation of bose-einstein condensates,” *Phys. Rev. A*, vol. 74, p. 033 612, 3 Sep. 2006.
- [116] B. Evrard, A. Qu, J. Dalibard, and F. Gerbier, “From many-body oscillations to thermalization in an isolated spinor gas,” *arXiv:2010.13832 [cond-mat]*, Oct. 2020, arXiv: 2010.13832.
- [117] T. Caneva, R. Fazio, and G. E. Santoro, “Adiabatic quantum dynamics of the Lipkin-Meshkov-Glick model,” *Physical Review B*, vol. 78, no. 10, p. 104 426, Sep. 2008.
- [118] A. Altland, V. Gurarie, T. Kriecherbauer, and A. Polkovnikov, “Nonadiabaticity and large fluctuations in a many-particle landau-zener problem,” *Physical Review A*, vol. 79, no. 4, p. 042 703, Apr. 2, 2009.
- [119] L. D. Landau and E. M. Lifshitz, *Mechanics*. Oxford: Butterworth-Heinemann, 1976.
- [120] A. S. Sørensen and K. Mølmer, “Entanglement and Extreme Spin Squeezing,” *Physical Review Letters*, vol. 86, no. 20, pp. 4431–4434, May 2001.
- [121] S. Chaudhuri, S. Roy, and C. S. Unnikrishnan, “Realization of an intense cold rb atomic beam based on a two-dimensional magneto-optical trap: Experiments and comparison with simulations,” *Phys. Rev. A*, vol. 74, p. 023 406, 2 Aug. 2006.
- [122] J. Schoser *et al.*, “Intense source of cold rb atoms from a pure two-dimensional magneto-optical trap,” *Phys. Rev. A*, vol. 66, p. 023 410, 2 Aug. 2002.

- [123] K. Dieckmann, R. J. C. Spreeuw, M. Weidemüller, and J. T. M. Walraven, “Two-dimensional magneto-optical trap as a source of slow atoms,” *Phys. Rev. A*, vol. 58, pp. 3891–3895, 5 Nov. 1998.
- [124] Y. B. Ovchinnikov, “Compact magneto-optical sources of slow atoms,” *Optics Communications*, vol. 249, pp. 473–481, 4 2005.
- [125] N. Castagna, J. Guéna, M. Plimmer, and P. Thomann, “A novel simplified two-dimensional magneto-optical trap as an intense source of slow cesium atoms,” *European Physical Journal: Applied Physics*, vol. 34, pp. 21–30, 2006.
- [126] T. Uehlinger, “A 2d magneto-optical trap as a high-flux source of cold potassium atoms,” Ph.D. dissertation, Swiss Federal Institute of Technology Zurich, 2008.
- [127] W. D. Phillips and H. Metcalf, “Laser deceleration of an atomic beam,” *Phys. Rev. Lett.*, vol. 48, pp. 596–599, 9 Mar. 1982.
- [128] K. Dieckmann, R. J. C. Spreeuw, M. Weidemüller, and J. T. M. Walraven, “Two-dimensional magneto-optical trap as a source of slow atoms,” *Phys. Rev. A*, vol. 58, pp. 3891–3895, 5 Nov. 1998.
- [129] E. M. Bookjans, C. D. Hamley, and M. S. Chapman, “Strong quantum spin correlations observed in atomic spin mixing,” *Phys. Rev. Lett.*, vol. 107, p. 210406, 21 Nov. 2011.

## VITA

Maryrose Barrios was born to parents Peter and Fidela on the Central Coast of California. She is a member of the Tule River Indian Tribe of California, and will be the first to obtain a PhD degree from her nation. She currently resides in Atlanta, but plans to follow her passions into teaching physics in higher education back in her home state of California. Her and her partner Rafael Araica plan to relocate west to be closer to their family and be reunited with their dog, Blue.